Mechanism of Antimicrobial Peptide Binding to Membrane-mimetic Systems: Insight from Molecular Dynamics Simulations

A Thesis
Submitted in Partial Fulfilment of the requirement for the Degree of

DOCTOR of PHILOSOPHY

by

Suvankar Ghosh

Under the Supervision of

Dr. Priyadarshi Satpati

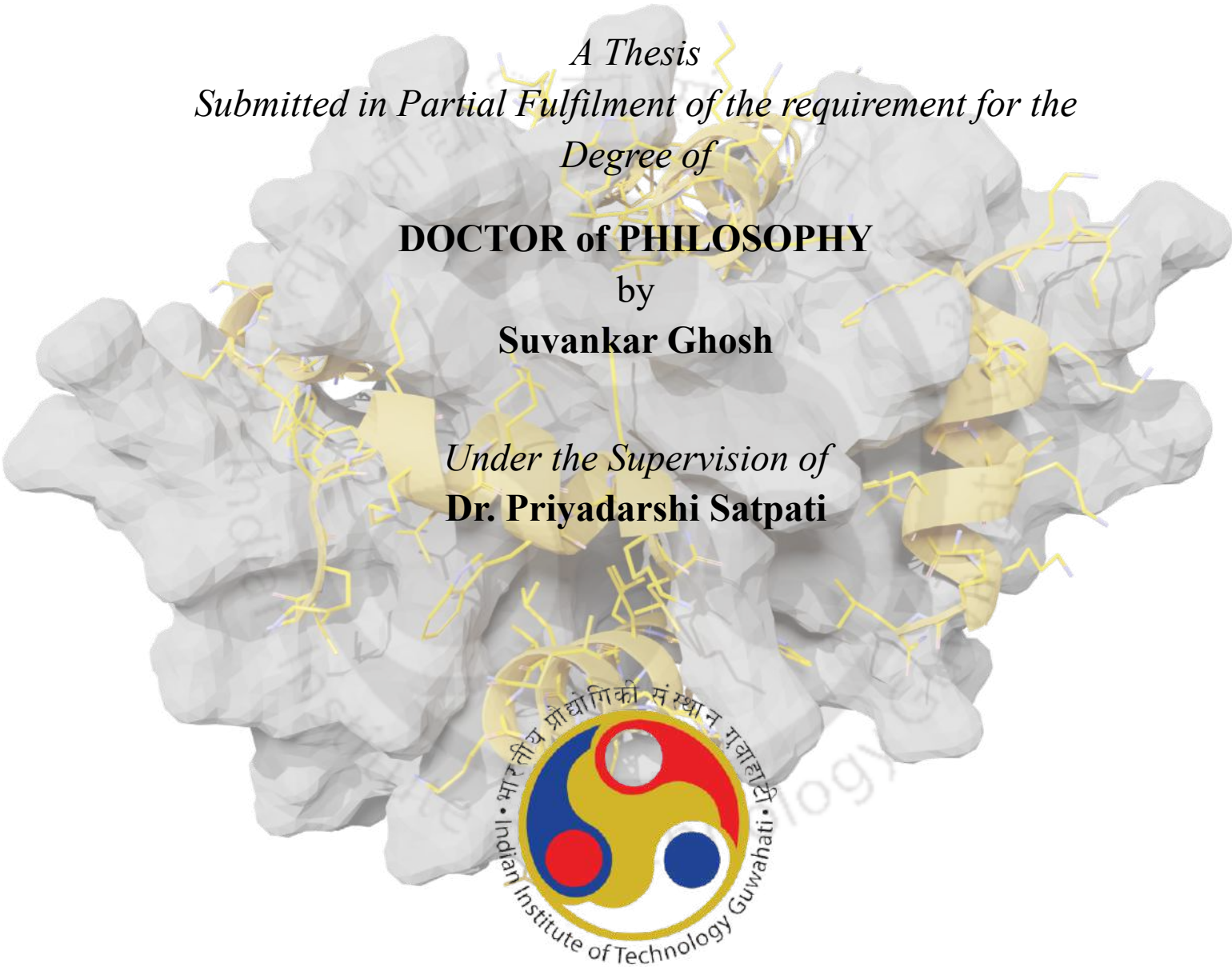

Department of Biosciences and Bioengineering
Indian Institute of Technology Guwahati, Guwahati,
Assam 781039, India

Dedicated to my family and friends

Indian Institute of Technology Guwahati
Department of
Biosciences and Bioengineering

DECLARATION

I do hereby declare that the content embodied in this thesis entitled "**Mechanism of Antimicrobial Peptide Binding to Membrane-mimetic Systems: Insight from Molecular Dynamics Simulations**" is the result carried out by me in the Department of Biosciences and Bioengineering, Indian Institute of Technology Guwahati, India, for the award of the degree of Doctor of Philosophy, under the supervision of Dr. Priyadarshi Satpati.

In keeping with the general practice of reporting scientific observations, due acknowledgment has been made wherever the work described is based on the findings of other investigators.

Date: 23.06.2023
Place: Guwahati

Suvankar Ghosh
Roll No. 166106105

Indian Institute of Technology Guwahati
Department of
Biosciences and Bioengineering

CEARTIFICATE

It is certified that the work described in this thesis entitled "**Mechanism of Antimicrobial Peptide Binding to Membrane-mimetic Systems: Insight from Molecular Dynamics Simulations**" by Mr. Suvankar Ghosh (Roll No. 166106105) for the award of the degree of Doctor of Philosophy is an authentic record of the results obtained from the research work carried out under my supervision in the Department of Biosciences and Bioengineering, Indian Institute of Technology Guwahati, India. This work has not been submitted elsewhere for the award of any degree or diploma.

Date: 23/06/2023
Place: Guwahati

Dr. Priyadarshi Satpati
(Thesis Supervisor)

ACKNOWLEDGEMENT

I feel immensely privileged to have the chance to work on this thesis research topic. I want to extend my gratitude to my thesis advisor, Dr. Priyadarshi Satpati, for his unwavering guidance, support, and invaluable insights throughout this project. His expertise, encouragement, and patience have been invaluable to me and have contributed significantly to the success of my research.

I would also like to express my sincere appreciation to my thesis committee members, Dr. Ananya Debnath, Prof. Harish Vashisth, Prof. Shankar Prasad Kanaujia (Chairman), Prof. Tamal Banerjee, Dr. Sunanda Chatterjee, Prof. Debapratim Das, and Dr. Sirisha Nagotu for their valuable feedback, suggestions, and support. Their insights and expertise have contributed significantly to the improvement of my research and my understanding of the field.

I am also grateful to my former lab colleagues Dr. Amit Kumar and Dr. Abhishek Kumar, and current lab colleagues Mr. S.R. Vignesh, Mr. Pallav Sengupta, and Mr. Mohd. Ayaz Siddique and the M.Tech. juniors for their encouragement and support throughout the research process.

I want to acknowledge the contributions of Gopal Pandit, Swapna Debnath, and Tanumoy Sarkar from The Peptide Laboratory (Group leader Dr. Sunanda Chatterjee). Without their experimental insight, this research would not have been possible. Their participation and support have greatly enhanced the quality of my research.

I am deeply grateful to my friends Mr. Pratap Chandra, Mr. Adhiraj Nath, Mr. Ratan Kumar, Mr. Dipak Kumar Kanaujiya, and Mr. Vineet Anand for their constant source of motivation and inspiration.

I also wish to appreciate the Department of BSBE's Bioinformatics Infrastructure Facility (BIF) and IIT Guwahati's supercomputing facility (PARAM-ISHAN) for providing High-Performance Computing (HPC) clusters. I also like to thank the Ministry of Human Resource Development and IIT Guwahati for supporting my Ph.D. financially.

I am deeply grateful to any other individuals whom I have not recognized by name but who gave their support and cooperation.

This research project has been an enriching experience, and I am deeply grateful for the support and guidance of these individuals. Thank you.

CONTENTS

Abbreviations iv
Symbols v
Synopsis **vii**
List of Tables xv
List of Figures xvi
Chapter 1: Introduction, Objective, and Methodology **1**
1.1 Antimicrobial Peptides 1
1.1.1 Activity of Antimicrobial Peptides 4
1.1.2 Overview of Bacterial and Mammalian Membrane 6
1.1.3 Drawbacks of Antimicrobial Peptides 7
1.2 Literatures relevant to this thesis 10
1.3 The Objective of the Thesis 18
1.4 Methods adopted in this thesis 19
1.4.1 Peptide models 20
1.4.2 Membrane mimetic models 20
1.4.3 Classical MD Simulation 21
1.4.3.1 Newtons Equation of Motion 21
1.4.3.2 Computational Algorithms 22
• Verlet integration 22
• Velocity Verlet integrator 23
1.4.3.3 Assigning Initial velocities 23
1.4.3.4 Potential Energy Function and force fields 24
1.4.3.5 Periodic Boundary Conditions 25
1.4.3.6 Long-range electrostatic interactions and Ewald Summation Method 25
1.4.3.7 Energy Minimization and Equilibration 27
• Temperature control 28
• Pressure control 28
1.4.4 Thermodynamic cycle and Free Energy calculations 29
1.4.4.1 Molecular Mechanics Poisson-Boltzmann Surface Area (MM/PBSA) 30
1.4.4.2 Steered Molecular Dynamics and Umbrella Sampling 32
1.4.4.3 Alchemical transformation 34
1.4.5 Software used in this thesis 35
REFERENCES 36
Chapter 2: Thermodynamics, Activity and pH Sensitivity of Cationic Hepta-Peptides **47**
2.1 Background 48
2.2 Materials and Methods 49
2.2.1 Computational Modelling of Synthesize Peptides 49
2.2.2 Micelle/Bilayer Modelling and Peptide Binding 50
2.2.3 MD Simulation Parameters 51
2.2.4 Steered Molecular Dynamics and Umbrella Sampling Simulations: Absolute Binding Affinity (ΔG) 52
2.2.5 Thermodynamic Cycle, Alchemical Free Energy Simulation, and Relative Binding Affinity (ΔΔG) 53

2.2.6 MM/PBSA Calculation and Absolute Binding Affinity (ΔG_{bind}) 54
2.2.7 Sampling and Convergence of the Free Energy Simulations 54
2.2.8 Materials used for peptide synthesis and antimicrobial assay 55
2.2.9 Synthesis and characteristic of peptides 56
2.2.10 Minimum Inhibitory Concentration (MIC) assay 57
2.2.11 FESEM imaging 57
2.3 Results 58
2.3.1 Energetics of peptide selectivity 58
2.3.2 Antimicrobial activity of P4, P5, P6, and P7 at pH 7.4 62
2.3.3 The pH-sensitivity of histidine-containing peptide P6 against *Escherichia coli* 62
2.4 Discussion 65
2.5 Conclusion 66
2.6 Supporting Information 67
REFERENCES 67
Chapter 3: Salt-Sensitivity of the fourteen residue long cationic anti-microbial peptide 71
3.1 Background 72
Part A: Molecular Dynamics simulations of LL-14 in presence and absence of micelle 73
3.2 Materials and Methods 74
3.2.1 Modelling the peptides (extended:P^c and α-helical:P^h) 74
3.2.2 Modelling of membrane-mimetic systems (SDS and DPC micelles) 74
3.2.3 Peptide:SDS/DPC micelle setup 74
3.2.4 Simulation specification 75
3.2.5 Sampling and convergence of MD simulations 75
3.2.6 Circular dichroism (CD) experiments 77
3.2.7 Fluorescence experiments 77
3.3 Results 77
3.3.1 Structural and dynamical properties of LL-14 and SDS micelle 77
3.3.2 Salt effect in peptide-micelle (SDS) binding 80
3.3.3 Structural insight into the sequential peptide-micelle binding event from MD simulations 82
3.3.4 Secondary structural insight from CD experiments 85
3.3.5 Fluorescence studies and tryptophan burial in the final peptide:micelle complex 86
3.4 Discussion 86
3.5 Conclusion 91
Part B: Thermodynamics of peptide:micelle binding 91
3.6 Material and Methods 91
3.6.1 Structure of the LL-14(P^h):SDS complex from Part A MD study 91
3.6.2 Steered molecular dynamics and umbrella sampling 92
3.6.3 Sampling and convergence 93
3.7 Results 94
3.7.1 MD simulations of center-of-mass (COM) pulling 94
3.7.2 Umbrella sampling simulations and energetics of LL-14 Dissociation from the SDS micelle 97
3.8 Discussion 99
3.9 Conclusion 102
3.10 Supporting Information 103

REFERENCES 103
Chapter 4: Stability of AMP:micelle system upon Leu/Val mutation 107
4.1 Background 108
4.2 Materials and Methods 109
4.2.1 System preparation 109
4.2.2 Free Energy Simulation 109
4.2.3 Sampling and convergence 111
4.3 Results 112
4.3.1 Energetics of Leucine/Valine-Containing 14-residue peptide to Micelle Surrogates 112
4.3.2 The link between Calculated Energetics and Structure 114
4.3.2.1 Discrimination of Peptides Differing at the N-Terminal (1^{st} Position: L1 or V1) 114
4.3.2.2 Discriminating of Peptide Differing at the C-Terminal (14^{th} Position: L14 or V14) 116
4.3.2.3 Discrimination of Peptides Differing at the Middle Positions (4^{th}, 7^{th}, 8^{th}, and 11^{th} position: Single- and Multiple-Site Mutations) 117
4.3.3 LL-14 vs VV-14 Discrimination 120
4.4 Discussion 120
4.5 Conclusion 124
4.6 Supporting Information 125
REFERENCES 125
Chapter 5: Peptide Selectivity by Membrane-mimetic-bilayers in Response to Spacer Length Modification of the Cationic Side-chains 129
5.1 Background 130
5.2 Materials and Methods 130
5.2.1 Peptide and Bilayer models 130
5.2.2 Absolute binding affinity 131
5.2.3 Thermodynamic cycle and Relative Binding Affinity 132
5.3 Results 133
5.3.1 Absolute peptide:bilayer binding affinity 133
5.3.2 Energetics of peptide binding to the membrane-mimetic-bilayer models from alchemical free energy simulations 135
5.3.3 MD structures and Energetics 137
5.3.3.1 Lysine versus Arginine peptide bound to Membrane-mimetic -bilayer 137
5.3.3.2 MD Structures of Homolysine peptide:bilayer complexes 138
5.3.3.3 MD Structures of Homoarginine peptide:bilayer complexes 139
5.4 Discussion 139
5.5 Conclusion 140
5.6 Supporting Information 140
REFERENCES 140
Chapter 6: Overall conclusion and future perspective **143**
Appendix I **147**
Appendix II **164**
Appendix III **179**
Appendix IV **189**
List of Publications **195**

Abbreviations

AMP	Antimicrobial Peptides
APD	Antimicrobial Peptide Database
BAR	Bennett Acceptance Ratio
CD	Circular Dichroism
CG	Coarse Grained
COM	Center of Mass
DPC	Dodecyl phosphocholine
DSSP	Dictionary Secondary Structure of Protein
FEP	Free Energy Perturbation
HREMD	Hamiltonian replica exchange Molecular Dynamics
HT-MD	High Temperature Molecular Dynamics
MD	Molecular Dynamics
MDFE	Molecular Dynamics Free Energy
MIC	Minimum inhibitory concentration
MM/PBSA	Molecular Mechanics/Poisson-Boltzmann Surface Area
PMF	Potential of Mean Force
POPE	1-palmitoyl-2-oleoyl-sn-glycerol-3-phosphoethanolamine
POPG	1-palmitoyl-2-oleoyl-sn-glycero-3-phospho-(1'-rac-glycerol)
POPC	1-palmitoyl-2-oleoyl-sn- glycerol-3-phosphocholine
RDF	Radial Distribution Functions
RMSD	Root Mean Squared Deviations
RMSF	Root Mean Square Fluctuation
SASA	Solvent Accessible Surface Area
SDS	Sodium Dodecyl Sulfate
SMD	Steered Molecular Dynamics
TI	Thermodynamic Integration
US	Umbrella Sampling
WHAM	Weighted Histogram Analysis Method
WSE	Weighted Solvent Exposer

Symbols

Å	Angstrom
α	α-helix
β	β-sheet
λ	Coupling coordinate
mM	millimolar
μM	micromolar
°C	Degree Celsius
μs	Microsecond
ns	Nanosecond
ps	Picosecond
fs	Femtosecond
ϕ	phi
φ	psi
t	time
T	Temperature
K	Kelvin
V	Volume
P	Pressure
ξ	Reaction coordinate
ΔG	Gibbs free energy
ΔΔG	Relative binding free energy
kJ	Kilo joule
kcal	Kilo calorie
nm	Nanometer
μL	Microliter

Synopsis

The rapid growth of antibiotic resistance in microbes is a serious concern for human health and urges for alternative therapeutics. For millions of years, antimicrobial peptides [AMPs composed of 5-50 amino acid residues] have been an integral part of the host defense system in various kingdoms of life (microbes, plants, animals) for combating infections (caused by viruses, bacteria, fungi, yeast, etc.). Antimicrobial activity of AMPs includes disintegration of microbial membrane architecture, disruption of intracellular pathways, immuno-modulation of host cells, etc. Various modes of antimicrobial activity of the AMPs hinder the fast microbial resistance. Moreover, AMPs are biocompatible, easily tuneable (variable amino acid side-chain), and non-toxic upon digestion. Thus, AMPs are promising as an alternative to conventional antibiotic treatments. However, clinical use of AMPs is very limited, primarily due to two key factors: salt sensitivity and short serum stability of the AMPs. The design of salt-tolerant, stable AMPs with high potency and selectivity demands the understanding of the mechanism of antimicrobial activity of the AMPs in terms of energetics, kinetics, molecular structure, and the link between them.

This dissertation explores the mechanism of synthetic cationic AMP (7 and 14 residues long) binding to the simplest membrane-mimetic systems [micelles: SDS/DPC and bilayers: (DOPE:DOPG and POPE:POPG)/POPC as bacterial/mammalian membrane-mimic] using classical Molecular Dynamics (MD) simulations. The structures of the free peptides in water and complex with the membrane-mimetic systems were obtained from conventional MD simulations and verified by experiments. Using the experimentally verified MD structures as a template, the energetics (ΔG_{bind}; absolute binding affinity and $\Delta\Delta G$; Binding free energy difference between two peptides to the membrane-mimetic system) of peptide: (micelle/bilayer) binding was estimated by employing various popular methods (Figure S1). The simulations of peptide binding to the simplest membrane-mimetic systems provide insight into the kinetics and establish a direct link between the calculated energetics and molecular structures. The predictions from the simulations were verified by our collaborator (performing CD, NMR, Fluorescence, ITC, Antimicrobial assays, FESEM, etc). This thesis is divided into six chapters.

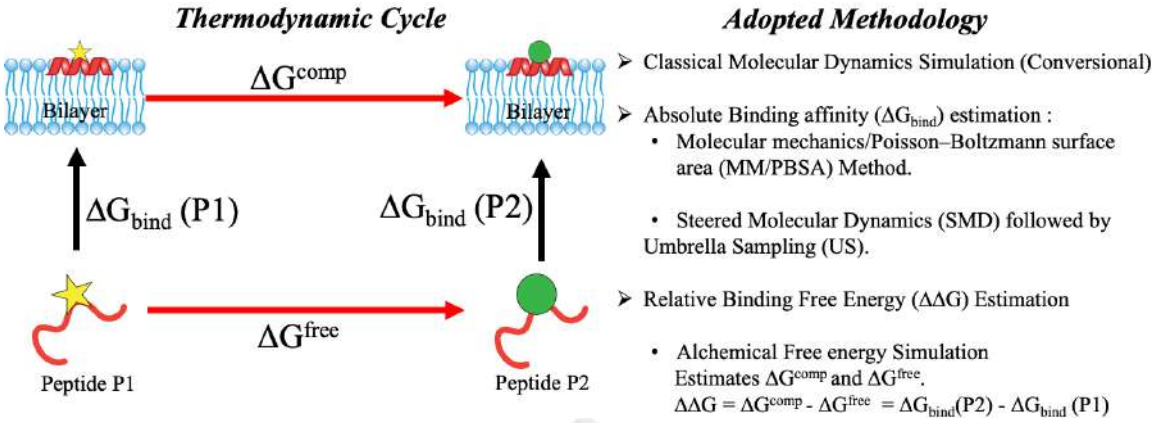

Figure S1: Thermodynamic cycle and adopted methodology for studying peptide:membrane binding.

Chapter 1 consists of a brief overview of the antimicrobial peptides and membrane-mimetic systems, the computational methodology adopted in this thesis.

Chapter 2 discusses the binding of cationic, non-toxic, non-hemolytic, and salt-tolerant heptapeptide (P4: NH_3^+-LKWLKKL-$CONH_2$, Charge +4 and analogs P5: Lysine's → Arginine's; P6: Lysine's → Uncharged-Histidine's; P7: Tryptophan → Leucine) to bacterial-membrane-mimetic models (SDS micelle and DOPE:DOPG bilayer). Hepta-peptides were unstructured in the presence or absence of the micelle (Figure S2). Thus, the

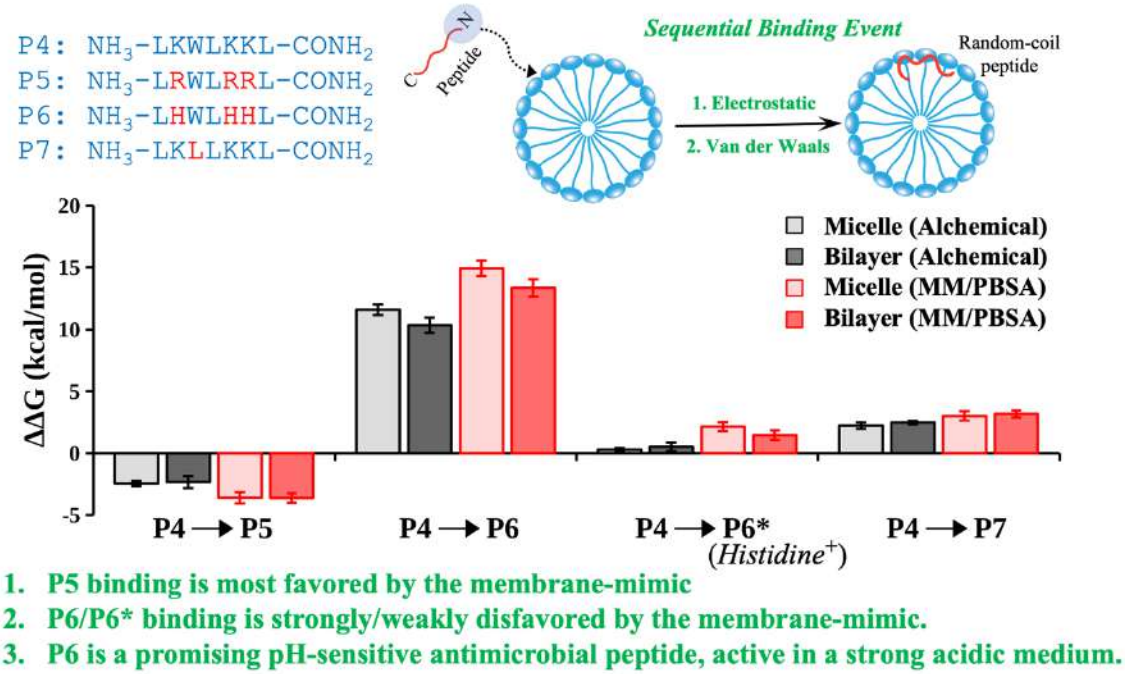

Figure S2: Cationic heptapeptides (P4, P5, P6*, P7: Charge +4; P6: Charge +1). The peptides are unstructured both in water and in a bacterial membrane-mimicking environment. Peptide binding to membrane-mimic is sequential (electrostatic interactions followed by hydrophobic stabilization stabilize the final complex). Aromatic amino acid (tryptophan, P6) substitution by leucine (P7) is disfavoured by micelle/bilayer. Error bars, 1 s.e.m.

secondary structure of the peptides (P4, P5, P6, P7) has no role in membrane binding. Peptide:micelle complex formation is sequential, electrostatic interactions (positively charged peptide and negatively charged surface of SDS micelle) followed by hydrophobic stabilization (placement of hydrophobic side-chains of the peptide into the hydrophobic lipid core of the micelle) stabilizes the complex. The reduction of overall positive charge or deprotonation at the C-terminal end ($-COO^-$) on the peptide resulted in inferior peptide:micelle interactions. The magnitude of the calculated absolute peptide binding affinity (ΔG_{bind} estimated from SMD-US and MM/PBSA methods) depends strongly on the model of the bacterial membrane-mimic (micelle and bilayer, the former being more favourable). However, the relative peptide binding affinities ($\Delta\Delta G$: P5/P6/P7 binding relative to P4, estimated from alchemical free energy simulations) are independent of the membrane model. The strength of favourable peptide binding affinity to the micelle/bilayer was predicted as P5 (most potent binder) > P4 > P7 >> P6. Minimal inhibitory concentration [MIC90%] assays confirmed that the antimicrobial activity against *P. aeruginosa* at physiological pH 7.4 was correlated [$MIC_{90\%}$: P5(30 μM) > P4(20 μM) >> P7(200 μM) >> P6 (inactive up to 200 μM)] with the calculated $\Delta\Delta G$'s. Substitution of the uncharged-histidine (P6) by charged-histidine (P6*) significantly favoured micelle/bilayer binding. Thus, P6 was proposed to be an effective antimicrobial peptide only at low pH. Noticeable improvement of the antimicrobial activity of the histidine-peptide-P6 against *E. Coli* (an acid-resistant bacteria which can survive in the low pH gastric environment) upon lowering of pH was demonstrated by experiments ($MIC_{90\%}$= 150 μM, 120 μM, 75 μM, 25 μM at pH = 7.4, 6.0, 4.0, and 3.0 respectively). The strength of the antimicrobial activity of the peptides against *E. Coli* at pH 7.4 [MIC: P5(50 μM) > P4(20 μM) > P6(150 μM) >> P7(inactive up to 200 μM)] also confirmed P5 as the most potent peptide whereas P6 showed inferior activity (as expected from calculated energetics). Field emission scanning electron microscopy (FESEM) experiments showed that the peptides were membranolytic, which is in line with the observed deformation of the micelle/bilayer in response to peptide binding in the MD study. Histidine-peptide (P6) was shown to be active against acid-resistant bacteria, thus, a promising membranolytic pH-sensitive AMP. The correlation between the calculated energetics ($\Delta\Delta G$) and the experimental activity has been highlighted.

Chapter 3 discusses the salt-sensitivity of 14 residue-long antimicrobial peptides (LL-14) obtained by doubling the length of peptide P4 (LL-14: NH_3^+-LKWLKKLLKWLKKL-

$CONH_2$, Charge = +7). Fluorescence and CD experiments confirmed that the LL-14 was unstructured in water, but attained α-helical (P^h) conformation in response to micelle binding. MD simulations were performed with LL-14 peptide (in two different conformations: (A) random coil or unstructured: P^c, and (B) amphipathic α-helical: P^h) in presence and absence of SDS-micelle in water with varying monovalent salt (NaCl) concentrations (0.0%, 0.5%, 1.0% w/v).

Simulations showed that free LL-14 in water preferred random coil (P^c) conformation in lines with fluorescence and CD experiments. However, peptide conformational change in response to micelle binding (LL-14(P^c):SDS → LL-14(P^h):SDS) was not observed within the time scale of the simulations. Thus, the structure of LL-14(P^h):SDS complex was proposed from the MD simulation α-helical (P^h) LL-14 binding to SDS micelle, which was verified by the fluorescence experiments (Figure S3a).

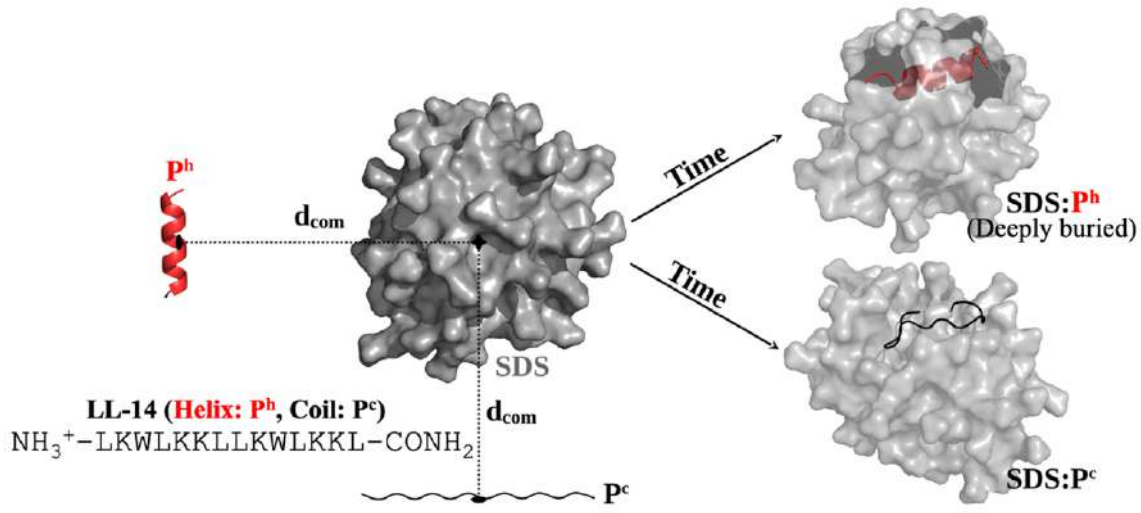

Figure S3a: Simulation setup with different initial peptide conformation (Helix: P^h; Coil: P^c).

Simulations successfully deconvoluted the LL-14:SDS binding event in terms of secondary structure (random coil P^c versus helix P^h) and gave atomic insight into the initial and the final LL-14:SDS complexes. Electrostatics drove the N-terminus (L1 and K2) of LL-14 (P^c or P^h) to bind the SDS surface, initiating complex formation. Faster and deeper burial into the SDS micelle was confirmed for LL-14(P^h) relative to LL-14(P^c). Increasing NaCl concentration systematically delayed LL-14:SDS binding by shielding the overall charges of the interacting partners. LL-14 binding to the SDS micelle was significantly faster relative to that of the zwitterionic DPC micelle due to obvious electrostatic reasons. The thermodynamics of LL-14 binding to simple membrane-mimetic systems and the effect of NaCl (concentrations of 0.0%, 0.5%, 1.0% w/v) on the stability of the LL-14:SDS-micelle complex has been investigated using SMD-US method. It has been shown that the increase

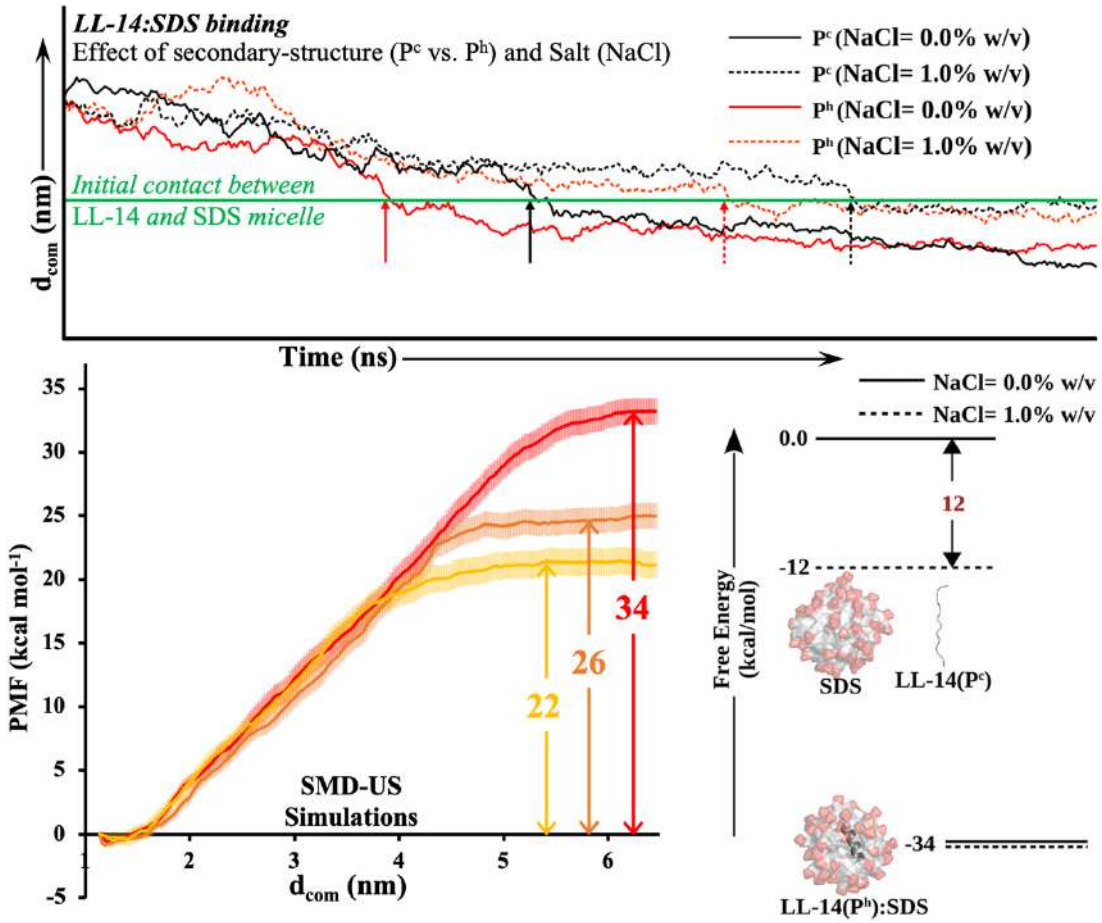

1. **Random-coil (P^c) → Helix (P^h) of the LL-14 in response to bilayer binding.**
2. **Salt (NaCl) systematically delays the peptide:membrane-mimic binding event.**
3. **Salt stabilizes the unbound state and alters the binding affinity.**

Figure S3b: Temporal averaged distance between the center of mass of a LL-14 and the center of mass of the micelle (d_{COM}) as a function of time. Peptide: micelle initial contact distance is represented as a horizontal green line (d_{COM} ~3.47 nm). An increase in salt (NaCl) concentration delays the initial binding event. Potential of mean force (PMF) as a function of peptide:micelle dissociation showed salt disfavoured binding (bootstrapping error as a vertical bar). A schematic free energy diagram of LL-14 binding to SDS micelle illustrates that selective stabilization of the free state alters the free energy difference.

in NaCl concentration systematically disfavoured the LL-14:SDS binding, primarily by stabilizing the dissociative state (i.e., free LL-14 and free micelles in water). A kinetic scheme has been proposed in which the salt-induced selective stabilization of the dissociative state increased the activation barrier for the peptide:micelle binding event resulting in reduced affinity (Figure S3b). Interactions involving the N-terminal of the LL-14 (residues 1–6) and SDS micelle were found to be crucial for the stability of the LL-14:SDS complex. Simulations of the dissociation event provided insight into the LL-14 conformational change (helix → unstructured). The observed structural features from the simulation of the LL-14:SDS-micelle dissociation pathway corroborate well with the circular dichroism (CD), and fluorescence experiments.

In **Chapter 4**, the effect of Leu/Val Mutation on the Energetics of peptide:SDS binding has been discussed. Experiments confirmed that Leucine-rich LL-14 is highly active as well as cytotoxic relative to its valine analogue (VV-14: NH_3^+-VKWVKKVVKWVKKV-$CONH_2$, Charge = +7). Thus, we attempted to understand the thermodynamics underlying this differential toxicity and antimicrobial activity of LL-14 and VV-14. We performed alchemical free energy simulations that allowed us to quantitatively estimate the strength of peptide discrimination (based on single- or multiple-site Leu/Val mutations in LL-14) by membrane mimetic micelles (SDS and DPC) and decipher the energetics underlying peptide selectivity by micelles (Figure S4). The Leu-containing peptide (LL-14) was found to be preferred for micelle (SDS and DPC) binding relative to its Val analogues (single or multiple Val mutants). The strength of the preference depended on the position of the Leu/Val mutation in the peptide. Surprisingly, the N-terminal LL-14 single mutation (Leu → Val: L1V) was found to fine-tune the electrostatic interactions, resulting in the highest peptide selectivity ($\Delta\Delta G \sim 8$ kcal/mol for both SDS and DPC). However, the mechanism of L1V peptide selectivity was distinctly different for SDS and DPC micelles. SDS ensured high selectivity by disrupting the peptide:micelle salt bridge, whereas DPC desolvated the broken-peptide-backbone hydrogen bond in the V1 peptide:micelle complex. Mutations (Leu → Val) in the middle positions of the LL-14 (4^{th}, 7^{th}, 8^{th}, and 11^{th}) were disfavoured by the micelles primarily due to the loss of peptide:micelle hydrophobic interactions. Peptides differing at the C-terminal (i.e., L14V) were recognized by SDS micelles ($\Delta\Delta G \sim$ 4 kcal/mol) by altering peptide:micelle interactions. L14V mutation, on the other hand, did not play any role in the peptide:DPC binding, as no direct interactions between the C-terminal and DPC micelle, were observed due to obvious electrostatic reasons. The strength of selectivity favouring LL-14 binding against VV-14 was found to be much higher for DPC micelles ($\Delta\Delta G \sim 25$ kcal/mol) relative to SDS micelles ($\Delta\Delta G \sim 19$ kcal/mol). The loss of the peptide:micelle hydrophobic contact in response to LL-14 → VV-14 mutation was found to be significantly larger for DPC relative to SDS micelles, resulting in higher discriminatory power for the former. Peptide:SDS salt bridges seemed to prevent the loss of peptide:micelle hydrophobic contact to some extent, leading to weaker selectivity for SDS micelles. The high selectivity of DPC micelles provided an efficient mechanism for VV-14 dissociation from DPC micelles, whereas the low selectivity of SDS micelles ensured the binding of both LL-14 and VV-14. The experimental observations

(antimicrobial activity and toxicity) between leucine-rich and valine-rich peptides have been explained by establishing a direct link between the energetics and structures.

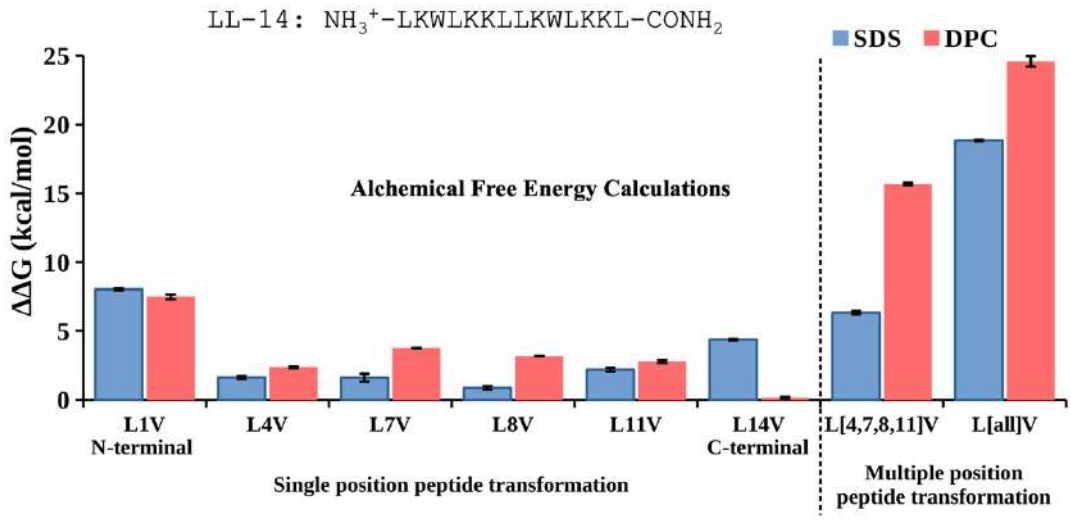

Figure S4: Estimated changes in binding free energy, $\Delta\Delta G$, for SDS (blue) and DPC (red) as a result of leucine to valine transformation (at single or multiple positions) in the LL-14 peptide. Error bars, 1 s.e.m.

In **Chapter 5**, the effect of unnatural amino-acid substitution on the stability of the LL-14:bilayer (POPE:POPG or POPC) complex has been discussed. The calculations involve computing the change in binding affinity of LL-14:bilayer upon Lys →

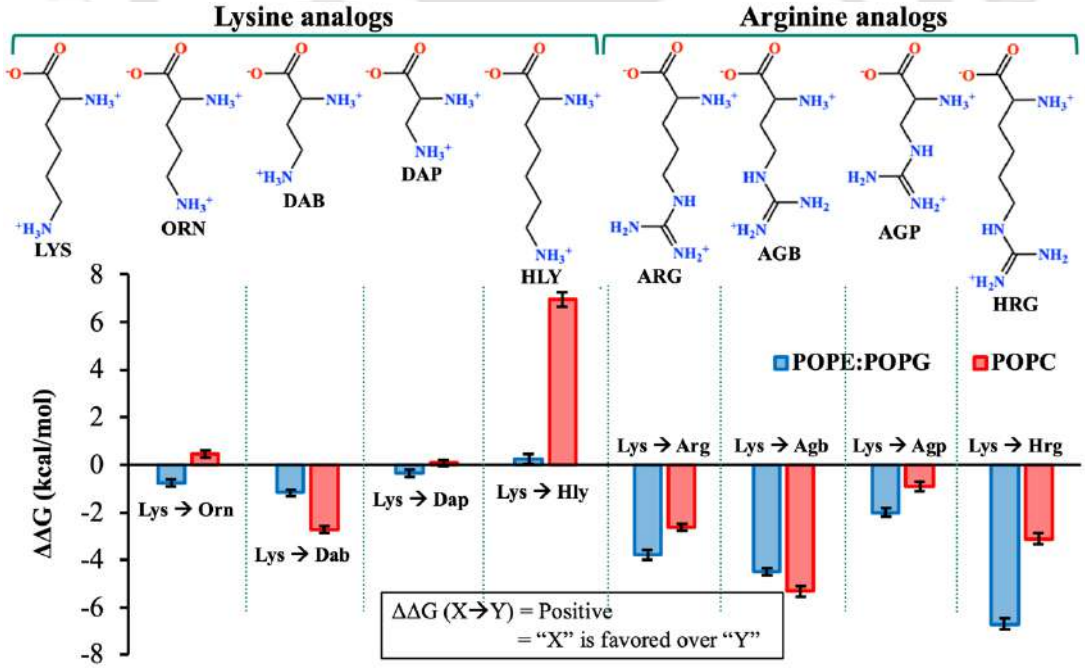

Figure S5: Lysine-rich LL-14 cationic (Charge =+7) fourteen residue long peptide. Relative binding affinities (LL-14 versus Lysine-mutant(s)) estimated from alchemical simulations for membrane-mimetic bilayers (POPE:POPG, POPC). Arg-peptide binding to lipid bilayer is favoured relatively to LL-14. Homoarginine-peptide showed the highest affinity for the bilayer. Homolysine-peptide binding to POPC bilayer is strongly disfavoured, whereas the binding affinity of Homolysine-peptide and LL-14 is comparable to the POPE:POPG bilayer. Error bars, 1 s.e.m.

(Orn/Dab/Dap/Hly/Arg/Agb/Agp/Hrg) alchemical transformation in all six lysine positions in LL-14 (Figure S5). These substitutions alter the aliphatic chain length without altering the overall charge on the peptide (Charge = +7). The arginine analogues were strongly favoured relative to the lysine analogues for bilayer binding. Based on the estimated energy, it has been hypothesized that (1) the Homoarginine analogue of LL-14 might be toxic but likely to be the most potent protease-resistant AMP among the studied peptides. (2) Homolysine analogue of LL-14 might be a non-toxic antimicrobial peptide with moderate potency (equivalent to LL-14). However, these claims can be subjected to experimental verification in the future.

The overall conclusion from this thesis work and the future scope of this current work is discussed in **Chapter 6**. We think the adopted methodology and the hypothesis that emerged from our study will be helpful for the rational design of potent antimicrobial peptides.

List of Tables

Table 1.1: Popular lipid compositions as membrane-mimetic-models. **20**

Table 2.1: MM/PBSA absolute peptide:(micelle/bilayer) binding free energy (ΔG_{bind}) and its components: ΔE_{ele} (electrostatic energy), ΔE_{vdw} (van der Waals energy), ΔG_{PB} (polar solvation) ΔG_{SA} (non-polar solvation), and $T\Delta S$ (entropy contribution). Energies are in kcal/mol and the standard error of the mean (s.e.m) is reported as error after ±. **59**

Table 2.2: Peptide:bilayer interaction area, number of interactions, and number of water molecules around the peptide for various peptide:bilayer complexes. Standard deviation is given as error. **61**

List of Figures

Figure 1.1: a) Different sources of AMPs. Physiochemical properties of AMPs b) amino acid length, c) net charge and d) hydrophobicity. **2**
Figure 1.2: a) Common AMP folds, represented by example AMPs. α-helix, β-sheet and coil structures represented in cyan, red and pink respectively. b) Structural classes of AMPs. **3**
Figure 1.3: a) Peptides isolated from various sources. Overview of AMP's mode of action b) Membranolytic c) Non membranolytic intra cellular activity. **4**
Figure 1.4: Comparison of Gram-positive bacteria, Gram-negative bacteria and mammalian cell wall. **6**
Figure 1.5: Amino acid residues that constitute the peptides modelled in this thesis. Amino acid sequence of the template model peptides: P4 and P5. **19**
Figure 1.6: Structure of the lipid molecules that are used for modelling membranes in this thesis work. **21**
Figure 1.7: Periodic boundary conditions for a 2D system. **25**
Figure 1.8: Periodic cell used in computer simulation: The cube, hexagonal prism, truncated octahedron and rhombic dodecahedron. **25**
Figure 1.9: Screening charge distribution. Point charges can be split into Direct space (original charges) and Reciprocal space (Gaussian-distributed) screening charges. **26**
Figure 1.10: Thermodynamic and free energies. **29**
Figure 1.11: Overview of steered MD. Blue (macromolecule) and green (ligand). Spring represents the harmonic potential. Pulling force applied along the direction of the arrow. **32**
Figure 2.1: The sequence of positively charged seven residues long synthetic antimicrobial peptide(P4) and its arginine (P5), histidine (P6), and leucine (P7) analogues. At neutral pH, the charge on P6 is +1. **50**
Figure 2.2: P4 dissociation from the SDS-micelle (red) and DOPE/DOPG-bilayer (blue). Potential of mean force (PMF) as a function of COM pulling coordinate "ξ". Bootstrapping errors (100 cycles) are shown as vertical transparent bars. **52**
Figure 2.3: Thermodynamic cycle for peptide:bilayer (DOPE/DOPG) binding. Horizontal legs correspond to the alchemical transformation of the peptide side-chains (e.g, Lysine's into Arginine's) either in the complex with SDS-micelle (top) or free in water (bottom); vertical legs correspond to the binding. The micelle binding free energy difference between binding lysine-peptide(P4) and histidine-peptide(P6) is $\Delta\Delta G = \Delta G^{comp} - \Delta G^{free} = \Delta G_{bind}(P6) - \Delta G_{bind}(P4)$. Alchemical free energy differences (ΔG^{comp} and ΔG^{free}) are estimated through Bennett's acceptance ratio method (BAR), and absolute binding free energies (ΔG_{bind}'s) was estimated from MM/PBSA approach. **53**
Figure 2.4: Estimated relative peptide-binding free energy (ΔΔG) to SDS-micelle (lighter shade) or DOPE/DOPG-bilayer (darker shade). BAR estimates are in grey, and MM-PBSA estimates are in red. Error bars, 1 s.e.m. **58**
Figure 2.5: Representative MD structures. (a-d) P4, P5, P6 (Charge = +1, neutral histidine), and P6* (Charge=+4, protonated histidine) are bound to the DOPE/DOPG Bilayer. Bilayer in surface representation (red and grey) and peptides in the cartoon (wheat). Key residues (sticks; red: oxygen, blue: nitrogen) and interaction networks (dashed line: green represents direct interaction, yellow represents interaction with water) are highlighted. Water in the red-sphere. Hydrogens are not shown for clarity. **60**
Figure 2.6: Representative MD structures. P4 (a) and P7 (b) are bound to the DOPE/DOPG Bilayer. Bilayer in surface representation (red and grey) and peptides in the cartoon (wheat). Key residues (sticks; red: oxygen, blue: nitrogen) and interaction networks (dashed line: green represents direct interaction, yellow represents interaction with water) are highlighted. Water in the red-sphere. Hydrogens are not shown for clarity. **61**
Figure 2.7: (a) Antimicrobial activity of P4 (blue), P5 (green), P6 (red), and P7 (grey) against *P. aeruginosa* at physiological pH 7.4. $MIC_{90\%}$ was calculated from Microbroth Dilution Assay (values given within the box). The control experiment was performed in presence of 100 μM polymixin B at pH 7.4 and other readings were normalized against the same. P5 is found to be the most potent peptide, and P6 was found to be inactive against *P. aeruginosa.* Field emission scanning electron microscopy (FESEM) images of *P. aeruginosa* (b) Control/without-peptide (c) 1 × MIC P4 (d) 1× MIC P5 (e) 200 μM P6 (f) 1× MIC P7. Active peptides (P4, P5, P7) are found to be membranolytic. Cell morphology in the control is preserved in the presence of P6. **63**

Figure 2.8: Antimicrobial activity of P4 (blue), P5 (green), P6 (red), and P7 (grey) against *E. coli* at physiological pH 7.4. $MIC_{90\%}$ (values given within the box) was calculated from Microbroth Dilution Assay. The control experiment was performed in presence of 100 μM polymixin B at pH 7.4 and other readings were normalized against the same. Antimicrobial activity against *E. coli* at pH 7.4: P5 most-potent, P6 poor-activity, P7 inactive. **64**

Figure 2.9: (a) Antimicrobial activity of P6 at various pH (7.4, 6, 5, 4, 3) against *E. coli*. $MIC_{90\%}$ (values given within the box) was calculated from Microbroth Dilution Assay. The activity enhanced upon lowering of pH. The control experiment was performed in presence of 100 μM polymixin B at various pH and other readings were normalized against the same. Field emission scanning electron microscopy (FESEM) images of *E. coli* at (b) pH 7.4 and without P6, (c) pH 3.0 and without peptide, and (d) pH 3.0 at 1× MIC P6. In the absence of P6, the cells morphology is intact at pH 7.4 and 3. P6 is a membranolytic pH-sensitive AMP, active at lower pH. **64**

Figure 3.1: Primary sequence of LL-14 peptide. The N-terminal and C-terminal were $-NH_3^+$ and $-CONH_2$, respectively. Unstructured random coil (**P^c**) and amphipathic α-helical (**P^h**) and structures of LL-14. Helical wheel representation of the α-helical LL-14 with amino acid sequence highlighting the amphipathicity. **72**

Figure 3.2: Average structural and dynamical parameters obtained from simulation. (a) Distance of heavy atoms from the centre of mass of the SDS micelle. (b) Oxygen (H_2O) to sulphur (SDS) radial distribution function. (c) Representative snapshots of free SDS, P^c bound SDS, and P^h bound SDS. Na^+ (Yellow sphere), peptide (dark grey), SDS (aliphatic: light grey, sulphate: red). Waters and hydrogens not shown for clarity. Eccentricity (*e*), radius of gyration (R_g), micelle radius (R_s), solvent accessible surface area (SASA), diffusion coefficient (*D*) of Na^+ are given. (d) Residue-wise root mean square fluctuation (RMSF) of the heavy atoms of LL-14 in the absence and presence of SDS micelle. Error bars (standard deviation) are shown either as vertical bars (a) or reported after ± (c). **78**

Figure 3.3: Temporal averaged distance between the centre of mass of a LL-14 and the centre of mass of the SDS micelle (d_{COM}) as a function of time. (a) Initial binding event. Peptide: micelle initial contact distance is represented as green line at d_{COM} ~3.47 nm. (b) Plateau of d_{COM} vs. time plot (after 10 ns) indicate structural convergence of the final peptide: micelle complex. Error bars are not shown for clarity (see Appendix II Figure A3.3 for detail). **81**

Figure 3.4: Structures from the peptide: micelle (SDS) binding event, with distinct secondary structures of the peptide (P^c or P^h) as initial condition. (a and d): peptide: SDS-micelle initial contact. Micelle surface forms direct interactions with the NH_3^+ of the N-terminal (L1) and side-chain of K2 of the LL-14 peptide both in the (a) P^c and (d) P^h conformations. (b and e) Final structure of the peptide: micelle complex. Interaction network is shown as dotted line for (b) P^c:micelle and (e) P^h:micelle complex respectively. For clarity, van der Waals radii of the micelle was reduced by 50% in (e). The local environment around W3 and W10 are explicitly shown without van der Waals reduction in the in-set (e). (c and f) Residue-wise solvent exposure (in percentage) of LL-14 in the final complex was estimated as: (SASA of amino acid residue in SDS:LL-14 complex/SASA of the amino acid residue in LL-14) × 100. Trajectory averaged percent solvent exposure (yellow) is shown in the net-plot with contours of constant percent exposure. Waters and hydrogens not shown for clarity in the structures. **82**

Figure 3.5: Electrostatic and Lennard-Jones interaction energy as a function of time during the initial stage of peptide: micelle (SDS) binding. The peptides in distinctly different conformations (P^c or P^h) were subjected to MD simulation. Long-range cut-off of 1.4 nm was used to compute the energies. **84**

Figure 3.6: (a) CD spectra of free SDS micelle (as control, broken line) and LL-14 in various conditions (presence or absence of SDS micelle and urea, solid lines). CD spectra indicate characteristic SDS induced LL-14 conformational change form random coil to helix (P^c:Solid black / P^h:Solid colours) even in the presence of urea. (b) Tryptophan Fluorescence emission spectra of free LL-14 (black), LL-14 in presence of SDS (red), and LL- 14 in presence of SDS and salt (red). Blue shift in LL-14 emission observed upon addition of SDS micelle in presence or absence of salt (NaCl). **85**

Figurer 3.7: (a) Structure of an SDS micelle. (e) LL-14(P^h):SDS complex. Centre-of-mass distance between the helical LL-14 (cartoon and sticks) and the SDS micelle (surface) is shown as "d_{COM}". For a clear visual representation of the peptide, the van der Waals radii of the SDS molecule are reduced by 50%. (b) Magnified view of the local environment of LL-14 in the SDS micelle. Direct electrostatic interactions between the peptide and micelle are represented as dashed lines. Local environments of W3 and W10 are more or less similar (buried in the hydrophobic core of the micelle). Hydrogens are not shown for clarity. **92**

Figure 3.8: (a and b) LL-14 dissociation pathways from the SDS micelle at various salt-concentrations. Red (arrow and structure) and blue (arrow and structure) correspond to two high force points, the former being the highest. Red - Blue corresponds to secondary structural transition (helix - random-coil) of the LL-14 in the presence of the SDS micelle. The yellow (arrow and structure) point is an intermediate between red and blue points. Green corresponds to the structure just before the complete dissociation of LL-14 from the SDS micelle with a single salt-bridge between the N-terminal tip (-NH_3^+) and SDS sulphate. (c) Plots of solvent accessible surface area (SASA) of the amino-acid residues of LL-14 peptide as a function of time. (d) The number of intra-peptide hydrogen bonds. Different colored lines in (c and d) corresponded to different time points of SMD. **96**

Figure 3.9: Potential of mean force (PMF) as a function of dissociation coordinate "ξ" at various salt concentrations. The errors are shown as vertical bars (computed by using 100 cycles of bootstrapping calculations). Estimated binding affinities (ΔG) and errors (right-side of). The red arrow corresponds to the reference state (ξ = 1.14 nm) of PMF calculations. **98**

Figure 3.10: (a) Thermodynamic cycle for protein:micelle binding in the absence and presence of salt. Vertical legs correspond to the peptide:micelle binding (in the absence of salt: left-side, in the presence of salt: right-side); horizontal legs correspond to the transformation of the salt environment from 0% to 1%, either in the protein:micelle complex (above) or in the dissociative/free state (below). Free energy is a state function, thus: $\Delta\Delta G = \Delta G_{complex}(0 - 1\%)$ $\Delta G_{free}(0 - 1\%) = \Delta G_{bind}(1\%)$ $\Delta G_{bind}(0\%)$. (b) Schematic free energy diagram of LL-14 binding to SDS micelles, illustrating altered free energy difference (by +12 kcal mol^{-1}) between the bound and dissociative state as a result of selective salt-stabilization of the dissociative state (i.e., free LL-14 and free SDS). **101**

Figure 4.1: Thermodynamic cycle for studying micelle:peptide binding. Vertical legs correspond to binding; horizontal legs correspond to the alchemical transformation of the peptide side chain from leucine (L) into valine (V), either in the micelle (upper) or free in water (lower). The Leu peptide(P^L)/Val peptide(P^V) binding free energy difference is $\Delta\Delta G = \Delta G^{comp} - \Delta G^{free} = \Delta G_{bind}(P^L) - \Delta G_{bind}(P^V)$. Based on our previous experiments, we confirmed that free LL-14 adopted helical conformation only after micelle binding; thus, a random coil structure was considered for leucine to valine transformation in the lower horizontal arm (ΔG^{free}). **110**

Figure 4.2: Estimated changes in binding free energy, $\Delta\Delta G$, for SDS (blue) and DPC (red) as a result of leucine to valine transformation (at single or multiple positions) in the LL-14 peptide. Error bars, 1 s.e.m. **113**

Figure 4.3: N-terminal selectivity. Recognition of leucine disfavouring valine observed from the average MD structures of peptide:micelle complexes (SDS: top and DPC: bottom), with the leucine peptide (a,c) and valine peptide (b,d). Peptides in the schematic (wheat) and micelles in surface representation (red and grey). Key residues are shown in sticks (red; oxygen and blue: nitrogen). Key interaction networks are indicated by the black dashed line. Water is indicated in in red spheres. Hydrogens are not shown for clarity. The discrimination against valine is reflected by the loss of salt-bridge interaction (K2:SDS) in (b), whereas the backbone hydrogen bond (NH(K7)···OC(W3), standard deviation as error) was disrupted and shielded from water in the DPC micelle (d). The discrimination against valine is further supported by the increase in flexibility (RMSF) and solvent accessibility (weighted solvent exposer of the side-chain: WSE) in both (b) and (d), somewhat more pronounced in the former. **115**

Figure 4.4: C-terminal selectivity. Representative molecular dynamics structures of peptide: micelle complexes (SDS: upper, DPC: lower) with the leucine-peptide (left-side: a, c) and valine-peptide (right-side: b, d) (colour coding as in Figure 3). Leucine at the C-terminal is preferred by SDS micelle ($\Delta\Delta G$ ~4 kcal/mol), as reflected by the favourable interactions with terminal $CONH_2$ with the negatively charged SDS surface (a). V-14 in the SDS micelle disrupt the $CONH_2$…SDS interaction, supported by increased flexibility and solvent exposer of the valine reside (V14). Peptide binding to DPC micelle (lower) is independent of the nature of the peptide residue at the C-terminal (Leucine or valine in the 14th position). No direct interaction between the C-terminal and DPC micelle was observed, as is also evident from the estimated energetics ($\Delta\Delta G$ ~0 kcal/mol). **116**

Figure 4.5: (a) zoomed in view of the LL-14: SDS complex highlighting the leucine residues at the middle of the peptide (4^{th}, 7^{th}, 8^{th}, and 11^{th} position) embedded in the hydrophobic core of the SDS micelle (colour coding as in Figure 3). Some part of the micelle was not shown for clear representation of the peptide. (b) Area of the hydrophobic aliphatic region of the micelle around the 0.35 nm side-chain of peptide residue leucine (area= A_L in nm^2) and valine (A_V in nm^2). Loss of hydrophobic surface area in response to Leucine ⟶ Valine transformation is given as (A_L - A_V) in presence of SDS (4^{th} column) and DPC (7^{th} column) micelle. Error bars, 1 s.e.m. **118**

Figure 4.6: Zoomed in view from the representative MD structures of (a) LL-14: SDS , (b)VV-14: SDS, (c) LL-14: DPC, and (d) VV-14: DPC complexes. The complexes are shown by keeping the peptide in the horizontal axis (above) and rotated by 90 degree around the horizontal axis (below, N-terminal towards the reader). The peptide was found to be somewhat more deeply buried (a,b: closed conformation) relative to the DPC micelle bound form (c, d; Partially-open/open). Black dashed line indicate interaction. Peptide residues and its key interacting surfactants (polar terminals) are shown as sticks. Waters interacting with the peptide (within 0.35 nm of the peptide) is explicitly shown as red spheres. **119**

Figure 4.7: Schematic free energy (in kcal/mol) diagram for peptide: DPC (left, red) and peptide: SDS (right, blue) binding relative to the unbound (*Free State,* black) state. Absolute binding affinity (ΔG_{bind}, represented by dashed double-headed lines) estimated from umbrella sampling simulation (will be published elsewhere) place LL-14: DPC, LL-14: SDS complexes downhill relative to the free state. Estimated binding free energy differences ($\Delta\Delta G$, represented by solid double-headed arrow) between LL-14 and VV-14 peptides to DPC/SDS were ~ 25/19 kcal/mol and between LL-14 and II-14 peptides to DPC/SDS were ~ 10/6 kcal/mol. The scheme illustrates that, the VV-14:DPC complex is uphill, whereas VV-14: SDS complex is downhill relative to the free state. Thermodynamically favourable dissociation of VV-14 from DPC micelle was shown as transparent red arrow. **123**

Figure 5.1: Thermodynamic cycle for studying peptide:bilayer binding. Vertical legs correspond to binding; horizontal legs correspond to the alchemical transformation of the peptide side chain from lysine (Lys) into homoarginine (Hrg), either in the bilayer (upper) or free in water (lower). The Lysine peptide(LL-14^{Lys})/Homoarginine peptide(LL-14^{Hrg}) binding free energy difference is $\Delta\Delta G = \Delta G^{comp} - \Delta G^{free} = \Delta G_{bind}$(LL-$14^{Hrg}$) - ΔG_{bind}(LL-14^{Lys}). Based on our previous experiments, we confirmed that free LL-14 adopted helical conformation only after micelle binding; thus, a random coil structure was considered for lysine to homoarginine transformation in the lower horizontal arm (ΔG^{free}). **132**

Figure 5.2: Representative MD structures. LL-14 bound to a) POPE/POPG bilayer and b) POPC bilayer within 0.35 nm. Bilayer represented as surface (Carbon light grey, Oxygen red and Phosphorus yellow color) and peptide represented as cartoon and sticks (cyan color). Peptide interacting with bilayers and waters were highlighted in blue dashed lines and red spheres. Hydrogens are not shown for clarity. **133**

Figure 5.3: LL-14 binding energy with POPE/POPG bilayer (blue) and POPC bilayer (red). a) Potential of mean force (PMF) as a function of COM (ξ). Bootstrapping errors (100 cycles) were shown as transparent area. b) binding free energy (ΔG_{bind}) and its components: ΔE_{ele} (electrostatic energy), ΔE_{vdw} (van der Waals energy), ΔG_{PB} (polar solvation) ΔG_{SA} (non-polar solvation), and $T\Delta S$ (entropy contribution) was estimated using MM/PBSA approach. **134**

Figure 5.4: Estimated changes in binding free energy, $\Delta\Delta G$, for POPE/POPG (blue) and POPC (red) as a result of Lys to Orn/Dab/Dap/Hly/Arg/Agb/Agp/Hrg transformation (at multiple positions) in the LL-14 peptide. Error bars, 1 s.e.m. Where Lys: Lysine, Orn: Ornithine, Dab: 2,4-diaminobutyric acid, Dap: 2,3-diaminopropionic acid, Hly: Homolysine, Arg: Arginine, Agb: 2-amino-4-guanidinobutyric acid, Agp: 2-amino-3-guanidinopropanoic acid, Hrg: Homoarginine. **136**

Figure 5.5: Representative MD structures. LL-14^{Arg} bound to a) POPE/POPG bilayer and b) POPC bilayer within 0.35 nm. Bilayer represented as surface (Carbon light grey, Oxygen red and Phosphorus yellow color) and peptide represented as cartoon and sticks (cyan color). Peptide interacting with bilayers and waters were highlighted in blue dashed lines and red spheres. Hydrogens are not shown for clarity. **137**

Figure 5.6: Representative MD structures. LL-14^{Hly} and LL-14^{Hrg} bound to a,c) POPE/POPG bilayer and b,d) POPC bilayer within 0.35 nm. Bilayer represented as surface (Carbon light grey, Oxygen red and Phosphorus yellow color) and peptide represented as cartoon and sticks (cyan color). Peptide interacting with bilayers and waters were highlighted in blue dashed lines and red spheres. Hydrogens are not shown for clarity. **138**

Chapter 1

Introduction, Objective, and Methodology

Conventional antibiotic treatment is used to combat infection caused by pathogenic bacteria (Fair & Tor, 2014; Mishra & Bayer, 2013). However, the antibiotic misuse in medicine, agriculture, and animal husbandry led to rapid microbial resistance and development of infectious diseases (Hiltunen et al., 2017; Hoffman, 2016). Antimicrobial resistance has emerged as a pressing issue in healthcare, with the number of antibiotic resistance infections predicted to reach 10 million per year by 2050 (Petrosillo, 2020; Sohrabi et al., 2020). According to current estimates (X. Kang et al., 2019; O'Neill, 2016), at least 500,000 people die yearly from these infections. Due to the increasing quantity of antibiotics provided to COVID-19 patients in light of the 2020 COVID-19 pandemic (Fard et al., 2021; Sohrabi et al., 2020), antibiotic-resistant concerns are further aggravated (N. Chen et al., 2020). Multidrug-resistant bacteria cannot be treated with the current antibiotic repertory. Thus, there is an urgent need to develop new classes (alternative) of antibiotics. Antimicrobial Peptides (AMP: short chain of 10 to 50 amino acid residues) are promising alternative to conventional antibiotics (Mahlapuu et al., 2020). AMPs have the advantages of acting on multiple targets on the plasma membrane and intracellular targets of pathogenic bacteria, thus inhibit the rapid antibiotic resistance. AMPs are already in use to treat inflammation, wound healing, and infections caused by pathogenic microorganisms (Costa et al., 2019; Mahlapuu et al., 2020). However, the development of therapeutic AMPs are very limited, primarily due to their instability in the serum and loss of activity in the presence of salt. Therefore, it is crucial to investigate the mechanism of AMP activity in terms of structures, thermodynamics, activity, and cytotoxicity. This thesis examines the mechanism of synthetic cationic antimicrobial peptide (seven and fourteen amino-acid residue long) binding to membrane-mimetic-systems (micelles, bilayers) using molecular dynamics simulations.

1.1 Antimicrobial Peptides

Antimicrobial peptides (AMPs) are a family of short peptides (typically 10-50 amino acid residues long) commonly found in nature and play a crucial role in innate immunity. Antimicrobial peptide data from PubMed, PDB, Google, and Swiss-Prot were carefully

collected and curated in antimicrobial peptide database (APD, Wang & Wang, 2004). The recent updated version is APD3 (third iteration) (G. Wang et al., 2009, 2016) which include 3217 peptides. AMPs are found in all the six main kingdoms of life (**Figure 1.1a**). In the APD3 database, the length of AMP varies from 2 to 183 aa residues, with an average length

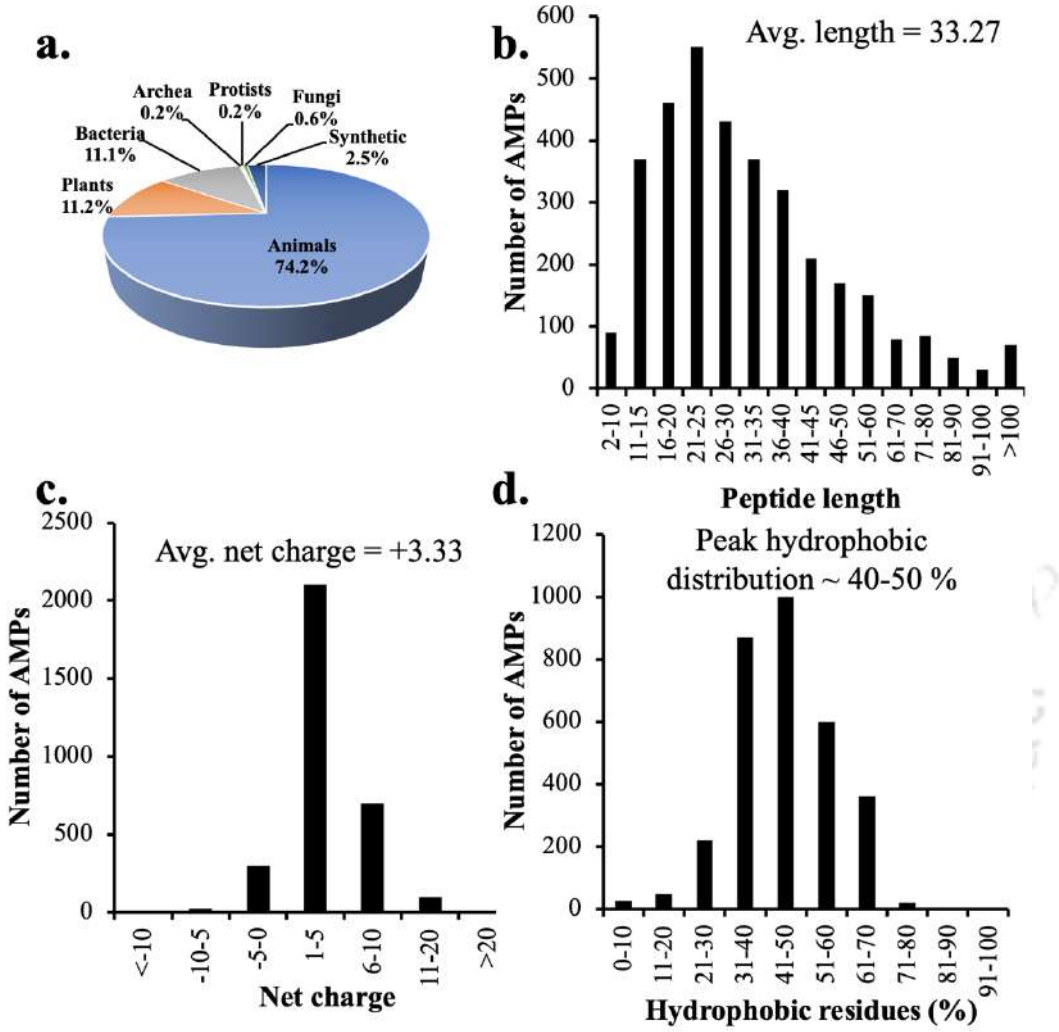

Figure 1.1: a) Different sources of AMPs. Physiochemical properties of AMPs b) amino acid length, c) net charge and d) hydrophobicity.

of 33.27 aa residues (**Figure 1.1b**). However, the highest limit is arbitrary and solely determined by the variety of peptides gathered in the database. Two residue-long peptides, viz., Gageotetrin A (sequenc: LQ) and peptide F3 (seqeunce: YL) are found to be post-translationally modified by attachment of lipid and bisphosphonate, respectively. The shortest AMPs without post-translational modification were found to be of five residues long, and many of them belong to the vermipeptide family (C. Wang et al., 2007). The majority of AMPs (88.5%) in the database are between 11 and 60 residues long (**Figure 1.1b**). ShLysG (G-type lysozyme) found in the big-belly seahorse (*Hippocampus abdominalis*) is 183 aa long AMP. The physiochemical property (viz., net charge,

hydrophobicity) on the AMP depend on its amino acid composition. APD3 reports 2834 AMPs with a positive net charge, 188 AMPs with a zero net charge, and 195 AMPs with a negative net charge at physiological pH 7.0 (**Figure 1.1c**). The range of net charges is astonishing, which include chrombacin (most anionic, net charge = -12) to fish histone-derived Oncorhyncin II and sheep cathelicidin OaBac11 (most cationic, net charge = +30). The vast majority of AMPs (96.2%) have a net charge between -5 and +10. Thus, at neutral pH, AMPs are mostly cationic in nature (average net charge = +3.33). The vast majority of AMPs (98.6%) had a hydrophobicity between 10 and 80% and a distribution peak between 40 and 50% (**Figure 1.1d**). Baceridin (sequence: WAIVLL), for instance, exhibits 100% hydrophobicity and is made entirely of hydrophobic residues. Gramicidin A (VGALAVVVWLWLWLW) and B (VGALAVVVWLFLWLW) both have a strikingly high hydrophobicity of 93%. In contrast, sheep anionic peptide doesn't include any hydrophobic residues. Based on the secondary structures, the antimicrobial peptides can be divided into four families (**Figure 1.2a**). The four families of AMPs are α, β, αβ, and non-αβ(unstructured). α-helical structures are most common (**Figure 1.2b**). Based on the targets of the antimicrobial peptides, AMPs can broadly classified into six categories, viz.,

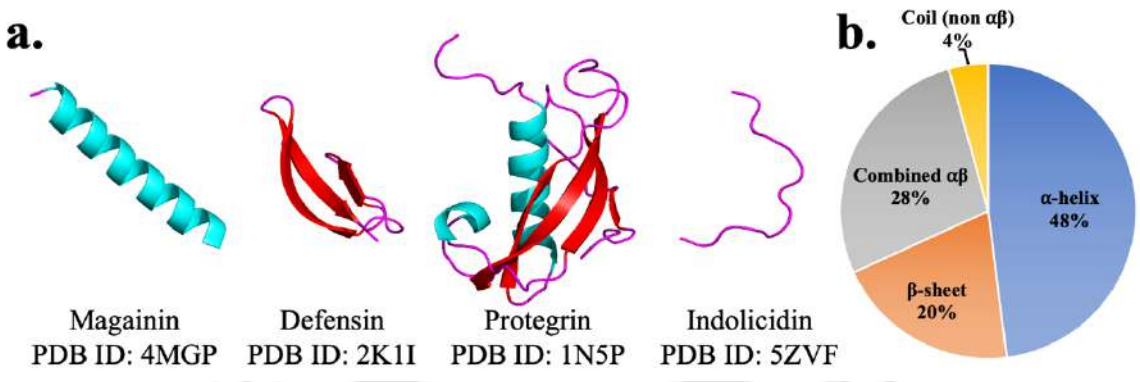

Figure 1.2: a) Common AMP folds, represented by example AMPs. α-helix, β-sheet and coil structures represented in cyan, red and pink respectively. b) Structural classes of AMPs.

antibacterial, antiparasitic, antifungal, antiviral, anti-human immunodeficiency virus (HIV), and anti-tumour peptides (**Figure 1.3a**). Thus, AMPs are diverse in terms of their length (2-100 residues), net charge (positive, negative, neutral), origin (natural or synthetic or combination of both), presence or absence of numerous post-translational modification etc.

1.1.1. Activity of Antimicrobial Peptides

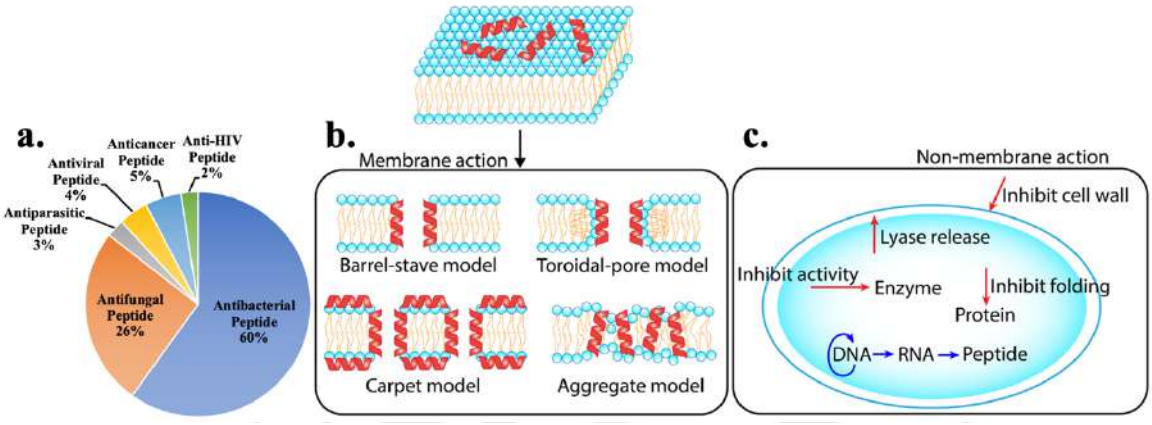

Figure 1.3: a) Peptides isolated from various sources. Overview of AMP's mode of action b) Membranolytic c) Non membranolytic intra cellular activity.

In general, AMPs kill bacteria by either destabilizing bacterial membrane (**Figure 1.3b**), or inhibiting the intracellular processes after entering inside the cells (**Figure 1.3c**). Popular models (Barrel-stave (R. B. Lipkin & Lazaridis, 2015; Lohner & Prossnigg, 2009), toroidal-pore (Matsuzaki et al., 1995, 1996); **Figure 1.3b**) explains the bacterial membrane disruption at lower concentration of the AMP. Higher order peptide aggregation at higher concentration of the AMPs also disrupt the bacterial membrane architechture (Carpet, (Oren & Shai, 1998), aggregate (Hale & Hancock, 2007) models, **Figure 1.3b**). Arginine-Tryptophan peptides are known to disrupt the bacterial membrane (Walrant et al., 2020). On the contrary, proline-rich short peptides are known to enter into the cytoplasm of the bacteria and hinder intra cellular activity by binding to intracelluar targets (Mattiuzzo et al., 2007, Seefeldt et al., 2015). Histidine-peptides are also known to permeate bacterial membranes (Lointier et al., 2020). Antimicrobial activity of glycine-rich peptides were also reported in the literature (Kwon et al., 2008; J. H. Lee et al., 2001). Translocation of AMPs into the intracellular space is facilitated by this membrane permeabilization. Buforin II binds to DNA and RNA and known to permeate lipid vesicles in vitro without altering membrane permeability (Cardoso et al., 2019). AMPs can indirectly prevent DNA replication or transcription causing DNA damage (X. Chen & Li, 2016; H. K. Kang et al., 2018; C. Wu et al., 2019). PR-39, an AMP isolated from the small intestine of pigs and rich in proline and arginine, readily penetrates the outer membrane of E. coli (Boman et al., 1993). As soon as PR-39 enters the cytoplasm, it prevents protein synthesis and leads to the breakdown of proteins needed for DNA synthesis, obstructing DNA synthesis. Usually,

the proline-enriched AMPs attach to ribosomes and obstruct protein production (Graf et al., 2017). AMPs also known to block the bacterial intracellular enzymatic activity (Bechinger & Gorr, 2016). It has been demonstrated that bacterial heat shock protein DnaK from E. coli protein lysates was selectively bound by a PrAMP pyrrhocoricin (Otvos et al., 2000). The same group showed that pyrrhocoricin prevented DnaK from acting as an ATPase in a subsequent investigation (Kragol et al., 2001). HNP1 was initially discovered to enter E. coli's outer and inner membranes and inhibit the synthesis of the bacteria's DNA, RNA, and proteins (Lehrer et al., 1989). Notably, the deadly event appears to involve inner membrane permeabilization. The short PrAMPs pyrrhocoricin, drosocin, and apidaecin interact with bacterial DnaK to elicit antibiotic actions (Kragol et al., 2001). Recent research indicates that a key antibacterial mechanism of AMP activity is the direct coaggregation of amyloidogenic peptides and amyloids (Kurpe et al., 2020). The fact that antimicrobial peptides form fibrils and that amyloidogenic proteins have antimicrobial activity suggests a potential similarity in actions, despite the low similarity between AMPs and amyloidogenic peptides in terms of sequences, secondary structures, or biological activity (M. Zhang et al., 2014). Antimicrobial peptides have also demonstrated excellent anti-fungal activity against common pathogenic fungi, including yeast, filamentous fungi (such as Aspergillus flavus), mold, and Aspergillus and Candida albicans in clinical practice (Madanchi et al., 2019). The anticancer activity includes (1) activation of immune cells, viz., dendritic cells; (2) induction of apoptosis; (3) prevention of metastasis; and (4) interruption of gene expression (R. Ma et al., 2019; D. Wu et al., 2014). Antiviral peptides are known to (1) block the virus attachment to the host cell, (2) rupture the viral envelope, and (3) prevent virus multiplication (Y. Jung et al., 2019). Anti-microbial peptides are also effective against parasite-causing diseases like leishmaniasis and malaria. (Mangoni et al., 2005; Rhaiem & Houimel, 2016) Peptides are also effective in immunomodulation, anti-inflammatory, anti-diabetic, and spermicidal activity. (Lointier et al., 2020) AMPs are also referred to as host defense peptides, that function as both antibacterial agents and immunomodulators to shield the host against infection (Emilio & Magrone, 2018; Hancock et al., 2016; H. K. Kang et al., 2019; Mack & Kim, 2016). The function of AMPs in the immune system is incredibly intricate. AMPs modulate the activities of the immune cells like dendritic cells (DCs), monocytes, macrophages, mast cells, granulocytes, and lymphocytes, as well as the section of cytokines like interleukins, tumour necrosis factors (TNFs), IFNs, and chemokines. AMPs are known to control intracellular signal pathways, including nuclear factor-B (NF-B), extracellular signal transduction, and cell surface

receptors like cytokine receptors, chemokine receptors, G-protein coupled receptors (GPCRs), including formyl peptide receptors (FPRs) and Toll-like receptors (TLRs), among others (Agier & Brzezińska-Błaszczyk, 2016; Neumann et al., 2014; Tjabringa et al., 2006)

1.1.2 Overview of Bacterial and Mammalian Membrane

The cytoplasmic membrane of the bacteria is composed of more or less equal proportions of proteins and lipids. Phospholipids are the main component of the membrane which include variation in the acyl chain length, branching pattern, saturation, head group size and charge etc. Membrane properties (viz., fluidity, charge, curvature etc.) are determined by the phospholipid variants that in turn modulate the lipid-protein interactions. Based on the staining, the bacteria can be divided into two types, gram-positive or gram-negative bacteria (**Figure 1.4**). The rigid thick cell wall of the gram-positive bacteria is composed of multiple layers of peptidoglycan. Moreover, the cell wall contains two types of teichoic acids (teichoic wall acid and lipoteichoic acid), sugars (N-acetylglucosamine: NAG and N-acetylmuramic acid: NAM) and phosphate. The cell-wall of gram-negative bacteria is made up of an outer membrane (composed of lipopolysaccharide: LPS, lipoproteins viz. porin, phospholipids viz. Lipid A) and a thinner peptidoglycan layer (relative to the gram-positive bacteria). The peptidoglycan layer in the gram-negative bacteria stays in the periplasm (between the plasma membrane and the outer membrane). Braun's lipoprotein (BLP) is an abundant protein which link the peptidoglycan and outer membrane of the gram-negative bacteria. The periplasm contains proteins and enzymes which assist in molecular transport. In general, gram-negative bacteria are more resistant to antibodies due

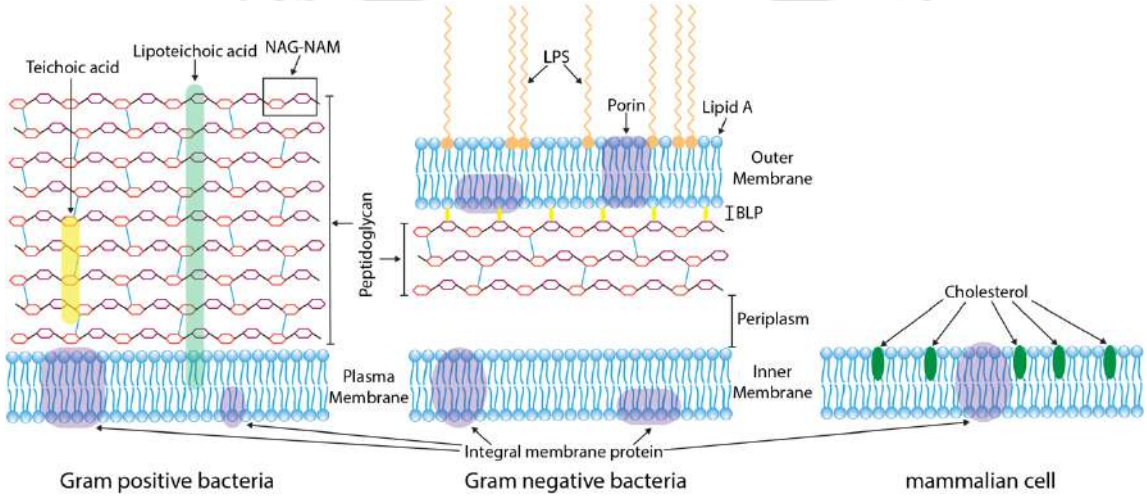

Figure 1.4: Comparison of Gram-positive bacteria, Gram-negative bacteria and mammalian cell wall.

to their impenetrable double cell membrane (outer and plasma membrane). The lipid composition and the surface charge of the bacterial and the mammalian cell membranes are distinctly different (**Figure 1.4**). Bacterial membranes are anionic where as mammalian membranes are zwitterionic. The most prevalent anionic lipids in bacteria are phosphatidylethanolamine (PE), phosphatidylglycerol (PG), and cardiolipin (CL) (Singh & Prasad, 2011). Whereas, human cell membranes mostly consists of zwitterionic phospholipids viz., phosphatidylcholine (PC), phosphatidylinositol (PI), and phosphotidylethanolamine (PE). Moreover, mammalian plasma membranes also contain cholesterol.

1.1.3 Drawbacks of Antimicrobial Peptides

Large number of natural AMPs have been identified, isolated and characterized. However, the commercial use is very limited due to several drawbacks listed below.

1. *Serum Stability*: Natural AMPs are susceptible to the protease degradation resulting a short half-life in the serum. Bacterial peptidases and proteases can catalyse site-specific peptide cleavage and inactivate the AMPs (Maria-Neto et al., 2015). Gram-positive bacteria are known to combat AMPs by secreting AMP-degrading proteases into the extracellular matrix. Proteases, however, are primarily found on the outer membrane of the gram-negative bacteria. For instance, antimicrobial activity of LL-37 against Chlamydia infection was known to be severely compromised in the presence of chlamydial protease-like activity factor (CPAF) (Tang et al., 2015).

2. *Salt-sensitivity*: The activity of many natural AMPs are known to be compromised in physiological salt concentrations. It has been widely noted that numerous AMPs, including clavanins, tachyplesin, histatins, and defensins, exhibit decreased activity in situations with high salt concentrations (Goldman et al., 1997; Hee Lee et al., 1997; Rothstein et al., 2001; Tam et al., 2000). Patients with cystic fibrosis (CF), are susceptible to opportunistic pathogens like *P. aeruginosa* and frequently experience chronic infections in the pulmonary mucus, which typically has an elevated salt concentration. Patients with cystic fibrosis were reported to contain high chloride concentrations in their trachea (Cl^- = 129 mM compared to 84 mM for healthy individuals) and airway surface liquid (ASL) (Cl^- = 170 mM compared to 85 mM for healthy individuals) (J. J. Smith et al., 1996). Interestingly, the antimicrobial activity in the ASL of the CF patients was reported to be significantly lower relative to the healthy individuals (Hiemstra, 2007; J. J. Smith et al., 1996, L. Zhang et al., 2005). MD simulations confirmed that ionic strength has a profound effect on the

peptide structure and peptide-lipid interaction (favourable in low salt concentration) (Kandasamy & Larson, 2006). Impact of salt concentrations on AMPs structure activity is of significant clinical relevance. Divalent cations (Zn^{2+}, Ca^{2+}, and Mg^{2+}) concentration has been demonstrated to affect the antibacterial action of AMPs such kappacin and DCD-1L, however, there are conflicting reports as to whether these cations are present in significantly higher concentrations in CF patients (Baconnais et al., 2012; Dashper et al., 2005; Halmerbauer et al., 2000; Paulmann et al., 2012). The examples provided here demonstrate that a variety of structural alterations in the AMP can improve the activity of AMP in presence of salt, however the available data is quite particular to each peptide and the target bacteria.

3. *pH sensitivity*: The biological activity of AMPs are known to be regulated by the pH (Malik et al., 2016). The pH at the therapeutic site might be different from the physiological pH (pH 7.4). For example, sites of inflammation often characterized by low pH due to the local increase in lactic acid and fatty acid waste products generated from bacterial metabolism (Grinstein et al., 1991; Nekoofar et al., 2009). Another location where acidity (pH 4-6) is essential for preventing bacterial growth and accelerating wound healing is the skin (Y. Liu et al., 2002; Schneider et al., 2007). The pH sensitive AMP activity is mostly studied in the pH range from 5.5 to 7.5 (Hee Lee et al., 1997; Yount et al., 2009). Enhancement of the antimicrobial activity of the histidine-peptides has been observed at lower pH, as at physiological pH (7.4) histidines are mostly neutral (pKa 6.5). Lowering the pH below 6.5 enhance the protonated histidine species and increase the overall positive charge, which in turn enhances the interaction with the negatively charged bacterial membrane (Hee Lee et al., 1997; Malik et al., 2016; Yount et al., 2009). For similar reasons, the activity of negatively charged AMPs were also reported to be enhanced upon decreasing the pH (Dashper et al., 2005; Paulmann et al., 2012). Wimley and co-workers showed that AMPs decrease their antimicrobial activity (against Gram-negative bacteria *P. aeruginosa* and *E. coli*) upon increasing pH. In contrast, the opposite trend was reported for *S. aureus* (a Gram-positive bacterium), where antimicrobial potency was increased at higher pH (Walkenhorst et al., 2013). Welsh and co-workers demonstrated that in the acidic pH, the antibacterial activity of LL-37 and β-defensin-3 was compromised against *S. aureus* and *P. aeruginosa*. However, at basic pH, where β-defensin-3 and LL-37 peptides are less positive, displayed better antibacterial activity against *S. aureus* (Alaiwa et al., 2014). Thus, pH can influence the protonation states of AMPs and the charged molecules in microbial

cell walls/membranes, which influence peptide:membrane binding and alter antimicrobial activity.

4. *Toxicity*: Many AMPs isolated from other organisms may display toxicity and high immunogenicity in humans, thus, limiting therapeutic use.

5. Commercial scale synthesis of long sequences (and or the presence of disulfide bridges, post-translation modification) are challenging and costly.

6. Delivery of the AMPs to the specific site is challenging.

7. Proper folding of synthetic AMPs (α-helical, β-sheet, etc.) might be challenging and compromise activity.

Needless to say, considerable focus has been given to overcoming the drawbacks of natural AMPs and designing new synthetic AMPs. Some of the popularly adopted approaches are:

1) Natural AMPs as a template for synthetic peptide design: Using known natural AMP as a template, the truncated sequences were selected for synthesis. The truncated peptides can be diversified by amino acid mutations resulting in overall charge, hydrophobicity, and secondary structure alteration of the designed peptides. Moreover, a fusion of multiple peptide sequences using covalent linkage, incorporation of unnatural amino acid residues, D-amino acid residues, peptidomimetic fragments, cyclization, lipidation, etc., further diversify the peptide design space (Gan et al., 2021; Sarkar et al., 2021).

2) Rigorous biophysical studies: The promising synthetic peptides are first studied in the presence and absence of simple hydrophobic membrane-mimetic environments to gain atomic insight into the structure and dynamics of the designed peptides.

Truncated sequences are easy to synthesize. Antimicrobial potency of the truncated peptides was attempted by mutation, net charge/hydrophobicity alteration, and optimize the hydrophilic/lipophilic balance in an ad hoc way. The stability of the AMPs against proteases was achieved by chemical modifications (viz., cyclization, terminal protection (Jenssen et al., 2006; Sarkar et al., 2021), D-amino acid incorporation (Y. Chen et al., 2006; H. J. Jung et al., 2007; Vunnam et al., 1998), unnatural amino acid substitution (Lu et al., 2020). Hydrogels (Borro et al., 2020) and nano-assemblies based on metal/metal oxide nanoparticles (Pal et al., 2019)) were reported recently as promising methods for AMP delivery.

The bacterial membrane is a complex structure composed of lipids, proteins, and other small molecules arranged in an intricate pattern. This complexity makes it very difficult to explore using wet-lab experiments and/or accurate computational models. To study the binding of antimicrobial peptides to the bacterial membrane, researchers often resort to

designing a simple bacterial mimic membrane, which is a simplified version of the bacterial membrane (micelle or bilayer) that can be used to capture the real peptide: membrane binding event to some extent in experiments and simulations. These membrane mimic typically includes only the essential components of the bacterial membrane, such as lipids. Simple bacterial mimic membranes are advantageous as researchers can better understand the interactions between antimicrobial peptides and the bacterial membrane, which can aid in developing new treatments for bacterial infections.

Molecular dynamics (MD) simulation is a powerful complement to experiments that allows researchers to study the dynamics of the system at an atomic scale, providing valuable insights into the interactions between the antimicrobial peptides and the bacterial membrane. MD simulations are successful in accurately capturing the mechanism of peptide binding to membranes, folding, partitioning into the lipid bilayers, spontaneous polypeptide channel formation in the bilayer, ion and other cargo conduction across membranes, all at atomic resolution (Ulmschneider & Ulmschneider, 2018). MD simulations can also be used to study the effects of different physical and chemical conditions on the interactions between the peptides and the membrane, such as temperature and pH. The advancement in computational power, efficient algorithms, and techniques (accelerated sampling schemes) made computational analysis increasingly popular and gained knowledge in spatial and temporal resolution. The MD trajectories can be used to estimate thermodynamic properties, viz., binding free energy.

The focus of this thesis is to study the structure and dynamics of membrane-active antimicrobial peptides and their binding to simple membrane mimetic model using conventional classical molecular dynamics simulations. The thermodynamics of peptide binding to membrane mimetic models were estimated using various methodologies, including steered molecular dynamics followed by umbrella sampling (SMD-US), molecular-mechanics/Poisson-Boltzmann surface area (MM/PBSA), and alchemical free energy simulations, includes free energy perturbation (FEP), thermodynamic integration (TI) and Bennett acceptance ratio (BAR).

1.2 Literature relevant to this thesis

Most AMPs kill bacteria by selectively rupturing bacterial membranes (Shai, 2002), resulting in cell leakage and death. There are additional reports of AMPs acting in various ways, such as oncocin, which targets intracellular ribosomes (Peng et al., 2018), and several

AMPs that can break down bacterial DNA inside the cell (Lan et al., 2010). We have chosen to focus on reviewing membrane activity using computational approach.

There are several underlying mechanisms speculated to be responsible for AMP activity on bacterial membranes, discussed previously. Here we try to understand and give an overview of the role of molecular dynamics (MD) simulations in developing this understanding, including methods used for studying peptide conformation, aggregation, and interactions with the membrane.

Based on their amino acid sequence and biological context, peptides fold into several conformations. As seen with melittin, which adopts random coils in an aqueous solution but forms α-helix when binding to a lipid bilayer (Appadu et al., 2015). It is known that many AMPs fold into an active conformation upon interacting with (or insertion into) the membrane. The peptide's available conformations determine the preferred method of an AMP's or its aggregates' contact with the membrane interface, followed by an insertion. X-ray crystallography is frequently used to probe the structure of AMPs in their crystallized forms (Baeriswyl et al., 2019; Hayouka et al., 2013; Lay et al., 2019), solution-state NMR to probe their aqueous forms (or active forms in solvents that mimic membranes (Benetti et al., 2019; Warschawski et al., 2011)), solid-state NMR to probe their membrane-embedded forms (Harmouche et al., 2017) and circular dichroism (CD) to probe their secondary structures, whether they are in solution or embedded in the membrane (Agadi et al., 2018; Appadu et al., 2015; Bürck et al., 2016; Woody, 1985). There are thorough discussions of the experimental methods applied to the biophysical characterization of AMPs (Avci et al., 2018). MD simulations have greatly complemented these techniques and some of the examples are covered here.

X-ray crystallography is frequently used to determine peptide and protein conformations (Baeriswyl et al., 2019; J. Li et al., 2017). However, due to desolvation and crystal packing effects, these static structures might not accurately depict the more physiologically relevant shapes the peptides adopt in the solution phase. The solution-phase behaviour of AMPs has been studied using MD, and its comparison to their X-ray structures has been made. For instance, Baeriswyl et al. discovered that the AMP SB1's helical structure in crystals is unstable in solution. To investigate the interactions and solvation effects causing this behaviour, they carried out conventional atomistic MD starting with a 4-helix bundle (representing the crystal form) and an isolated helix (representing the solution form) (Baeriswyl et al., 2019). They concluded that N-acylation plays a critical function in the

peptide's AMP activity and that aggregation and bundle formation is essential for the peptide's stabilization. The molecular explanation for the observed differences between the X-ray crystal structure and solution-phase NMR structure of the AMP human β-defensin 2 was developed using enhanced conformational sampling approaches, such as Hamiltonian replica exchange (HREMD) (J. Li et al., 2017), which are also increasingly being used to enable sufficient conformational sampling (HBD-2).

Since it is challenging to determine the behaviour of AMPs in the membrane phase through experimentation, MD simulations have significantly contributed to examining the difference in conformational propensity of AMPs in solution and within membrane models. To conduct this inquiry, peptide conformations that have been experimentally confirmed or anticipated can be positioned above or inside a membrane model. The MD simulation can then be used to track the resulting structural changes (Agadi et al., 2018; Benetti et al., 2019; Hazam et al., 2019; Manzo et al., 2019; Zhao et al., 2018). These simulations assist in identifying the impact that the membrane surroundings have on the AMP structure by allowing comparisons of differences in interactions between the AMPs and various membrane compositions. For instance, it has been demonstrated using all atom MD, that the presence of negatively charged lipids (typical of bacterial membranes) electrostatically stabilizes the α-helix of the positively charged AMP LL-37, and remained uninteracted with the zwitterionic mammalian membranes. This finding provides a mechanism for the ability of LL-37 to specifically target bacteria (Zhao et al., 2018). Similarly, using a sodium dodecyl sulfate (SDS) micelle model that mimics the target membrane, atomistic MD has been used to monitor the stability of the NMR-determined structure of maximin 3, an anti-HIV peptide. This described the interfacial contact of peptide:micelle, (a combination of hydrophobic and electrostatic interactions) results in a more ordered α-helix than solution-state NMR (Benetti et al., 2019). In this instance, using MD in conjunction with NMR yielded new knowledge regarding the peptide's structure in the membrane environment.

Additionally, attempts have been made to predict AMP structures using MD as an *ab initio* peptide folding strategy, which is helpful in the absence of experimental evidence (C. H. Chen et al., 2014; Fox et al., 2018). Traditional MD is unlikely to reach the time scales required to sample the process adequately. It is crucial to adopt methods that improve conformational sampling to achieve peptide folding from an extended structure (Bernardi et al., 2015). Melittin, an AMP produced from honey-bee venom, was sampled on the surface of a phospholipid bilayer using the enhanced sampling technique known as

HREMD. This allowed researchers to observe how the peptide's structural propensity changed as it interacted with the membrane (Fox et al., 2018). It has also been demonstrated that a simulation method known as high-temperature MD (HT-MD) can accelerate the kinetics of membrane insertion and peptide folding for some helical membrane-active peptides without changing the thermodynamic minima encountered by the peptide inside the membrane. Ulmschneider et al. demonstrated that the membranes can improve the thermostability of helices and prevent unfolding (Ulmschneider & Ulmschneider, 2018). To explore melittin's interactions with a POPC bilayer, Chen et al. used simulation temperatures of up to 120 °C. This allowed the peptide to insert into the membrane and fold into its empirically verified helical structure within 2 μs (C. H. Chen et al., 2014).

Finally, it is helpful to mention a few significant trajectory analytic techniques are applied to investigate peptide conformations. Converged reaction coordinates that characterize the desired property in order to get useful information about the structures present throughout the simulation. For instance, peptide conformation can be described according to the backbone dihedral space (ϕ and φ) (Ramachandran et al., 1963). Additionally, the radius of gyration (Vymětal & Vondrášek, 2011), root-mean-squared deviations of atomic locations (RMSD), number of intramolecular hydrogen bonds, residue contacts, helicity, and dictionary of protein secondary structure (DSSP) analysis (Kabsch & Sander, 1983) are used to characterize peptide conformations. Monitoring the values of the selected reaction coordinates throughout the simulation is crucial to ensure convergence. The reaction coordinates can be used with various clustering techniques to pin-point important simulated peptide conformations (Shao et al., 2007).

In conclusion, biology is widely known for the link between shape and function, and AMPs are no different. Understanding their behaviour and capacity to interact with membranes comes from their shape and structure. Several spectroscopic methods can be employed to get an empirically verified structure. However, they might not be enough to get an in-depth mechanistic understanding. The computational techniques that are frequently utilized in the literature to supplement experimental methods are described in this section.

Numerous AMPs' propensity to specifically damage bacterial cell membranes may be connected to their function. Despite the existence of assays that can detect the presence of membrane ruptures and AMP activity, such as cell or vesicle leakage assays (Chrom et al., 2019) the precise interactions between an AMP and its target membrane at the atomic level. Now we will discuss how modelling and simulation are increasingly utilized to investigate

these connections. Area per lipid, bilayer thickness, lipid chain order parameter, depth and orientation of the peptide in the membrane, lateral pressure, membrane curvature, clustering of charged lipids, the electrostatic surface potential of the membrane, hydrogen bonds, and electrostatic interactions between cationic residues with phosphate groups, as well as the free energy of peptide partitioning between the aqueous and membrane phases, are properties that are frequently used to measure these interactions (Buchoux, 2017; Piggot et al., 2012; Pluhackova et al., 2016).

Using advanced computational methods that change or accelerate the sampling of the energy landscape in MD simulations, such as accelerated atomistic MD, several research aims to sample entire penetration and/or pore-forming events. Because they are big and take a long time to simulate, simulation studies of membranes are computationally intensive; using Coarse-Grained (CG) helps solve these issues (Marrink & Tieleman, 2013). In order to mimic the long-timescale behaviour of melittin and its variations interacting with a phospholipid bilayer, Deng et al. used the MARTINI CG force field (Deng et al., 2019). This study witnessed numerous aggregation and pore-forming events since several simulations were run for 10 μs (far longer than the time scales available to atomistic MD of similar-sized systems). The study found that the peptides must aggregate before pores can develop. The relative pore lifetimes caused by the various melittin variations differ from experimental data and the computational aggregation studies outlined above (Deng et al., 2019). The effects of melittin on lipid vesicles have also been studied using the Dry MARTINI CG force field (where the solvent is implicitly represented) (Shi et al., 2018). Due to the higher sampling brought on by the lack of specified water particles, vesicle deformation and pore-forming events were recorded in 1 μs. In the aforementioned instances, CG simulations have enabled researchers to learn more about the mechanisms by which melittin disrupts bacterial membranes, demonstrating the importance of CG as a technique for supporting observations regarding these mechanisms.

There are other additional methods for improving membrane sampling as well. In order to determine the free energy required to transfer a peptide from bulk water onto a membrane, umbrella sampling (US) is frequently used as an example (W. F. D. Bennett et al., 2016; Liu & Karttunen, 2018; Yeasmin et al., 2018). Yeasmin et al. ran atomistic US simulations to model the penetration of human β-defensin 3 (HBD-3) into a lipid bilayer (Yeasmin et al., 2018). The authors proposed that HBD-3 functions as a dimer to induce a toroidal membrane pore by contrasting the energy surfaces produced by a monomer and a dimer as

well as factors like bilayer thickness and peptide RMSD (Yeasmin et al., 2018). Metadynamics has been utilized, similar to US, to improve the sampling of AMPs passing through phospholipid bilayers while providing information on the associated energy surface. The membrane system is characterized by numerous invisible barriers, which makes it more difficult to select the best collective variables. As a result, careful considerations must be made. Metadynamics has been combined with the MARTINI CG force field to analyze melittin in a bilayer (J. Liu et al., 2018). High-temperature MD, which was discussed in a previous section, may help hasten the sampling of AMPs in membranes by improving the system's capacity to get past kinetic barriers (Ulmschneider & Ulmschneider, 2018). Wang et al. used this method to simulate several copies of the helical peptide on a bilayer at 353–373 K in order to explore the capacity of maculatin to generate pores in different membrane models (Y. Wang et al., 2016). They found a number of potential oligomeric pore configurations and witnessed insertion and pore-forming processes throughout the simulations. Finally, electroporation, which simulates a synthetic transmembrane potential to induce stress in the bilayer, has increased the chance of membrane porosity. Using a double bilayer system to create two water baths where the charge could be adjusted by removing and adding charged peptides or ions, the technique was used to study the translocation of protegrin-1 (PG-1) across a lipid bilayer (Lai & Kaznessis, 2020; Piggot et al., 2011). The charge imbalance led to the observation of various peptide-lined pores, which allowed hypotheses about the structure of PG-1-membrane pores to be made.

Lack of integration of pKa shifts that happen when a peptide is transported from the aqueous phase to the membrane phase is one potential drawback in traditional MD simulations (e.g., the lipid tail region of the membrane). This is crucial because there is disagreement over the protonation states of amino acids in the bilayer, which significantly impact interactions with membranes. For example, arginine was demonstrated to be protonated in the bilayer center, whereas lysine is probably deprotonated there (L. Li et al., 2013; Yoo & Cui, 2008). The peptide can establish advantageous electrostatic contacts with the membrane thanks to arginine and lysine. Shifts in pKa must be considered. These problems are being addressed using developments in constant pH MD (Lousa et al., 2020; Vila-Viçosa et al., 2018), which have also been exploited in investigating AMPs. For instance, Pohl et al. found that the peptide aggregated more at higher pH when they tested the pH dependent aggregation of the AMP plectasin (Pohl et al., 2020). Similarly, Nhan et al. simulated how lactoferrin's structure changes when its pH deviates from neutral and how

these structural changes affect its antibacterial activities (Nhan et al., 2018). Lactoferrin is a protein with antimicrobial activity from which AMPs can be isolated (Bruni et al., 2016), which involves placing the lipid, peptide, and water molecules in a random configuration and watching the assembly of a peptide-embedded bilayer in order to study the preferred position and orientation of AMPs in lipid bilayers without biasing the results by selecting initial configurations (Cruz et al., 2013; Ermakova et al., 2019; Farrotti et al., 2015). This method can derive potential AMP pore architectures without overcoming the energy barriers in piercing and permeating a premade bilayer. For instance, the self-assembly of lipids in fungal cell membranes was modelled using the MARTINI CG force field with a model β-sheet AMP with sequence RMCKTPCGKFYCYKPCP, resulting in the observation of semi-toroidal pores. The differences between the protonated and unprotonated forms of LAH4 known to act as an AMP in acidic conditions but as a cell-penetrating peptide (CPP) in basic conditions, were also investigated using self-assembly. The protonated peptide was discovered to have a greater impact on bilayer stability (Farrotti et al., 2015; Reid et al., 2019).

Other model membranes, such as the outer membranes of different types of Gram-negative bacteria at both the atomistic and coarse-grained levels, as well as fungal membranes, have also received much attention in addition to bacterial cytoplasmic membranes (Jefferies et al., 2019; Jo et al., 2015; Khalid et al., 2019; Lakshminarayanan et al., 2014; P. Li et al., 2010; H. Ma et al., 2015; Pontes et al., 2012; van Oosten & Harroun, 2016). MD simulations of these membranes usefully reveal the action mechanisms of several AMPs. By simulating the fungal membrane with a four-part model membrane (POPC:POPE:POPS:erg), Li et al. discovered that a branched peptide tetramer called B4010 could bind preferentially with the anionic lipid POPS (Lakshminarayanan et al., 2014). The same team then investigated the mode of interaction of a branched AMP dimer B2088 with the lipid A membrane. It noted a sizable release of calcium from the membrane surface and a significant deformation of the membrane (Lakshminarayanan et al., 2016). The simulations of polymyxin B with the lipid A membrane also revealed similar membrane effects (Santos et al., 2017). The creation of different types of model membranes significantly improves the computational understanding of how AMPs affect these membranes when MD simulations are used, as seen in the work done by the Khalid group, which includes atomistic studies of bacterial membranes (Piggot et al., 2011), CG studies (Bond et al., 2007), and updating existing force fields to the more easily model membrane (Hsu et al., 2017).

Peptide-membrane simulations are, nevertheless, vulnerable to the issues with force field accuracy and sampling, as stated with relation to peptide folding and aggregation. While conventional atomistic MD can be used to validate experimentally derived or predicted pore structures, it is unlikely to reach the time scales required to observe spontaneous transitions between the various metastable states that may be important to the AMP mechanism. This emphasizes how crucial it is to execute numerous simulation iterations in order to boost the statistical significance of the observations. Additionally, a number of enhanced sampling techniques can be used to improve system sampling and reduce the time needed to get useful findings.

However, despite the field's recent popularity, there are still problems that need to be solved. For example, the precision of force fields and models, which need continuous adjustment, is crucial for MD simulations. Due to the computing cost involved in simulating large biological systems at the time scales required to monitor the relevant events, they also experience problems with convergence and sampling.

1.3 The objective of the thesis

Biological membranes ensure cellular integrity which include defining cell boundary, controlling selective transport across the membrane, maintaining solute gradient across the transmembrane, containing a diverse set of receptors, favouring cell-cell adhesion and recognition, intracellular and intracellular communication, and energy transduction etc. This thesis focuses on studying the mechanism of antimicrobial activity of AMPs, which display antimicrobial activity primarily by disrupting bacterial membrane. We studied seven and fourteen amino-acid residue long synthetic cationic antimicrobial peptides binding to membrane-mimetic-systems (micelles, bilayers) using various molecular dynamics simulation techniques (conventional molecular dynamics, Steered molecular dynamics, Umbrella sampling, MM/PBSA, alchemical free energy simulations). The goal is to estimate the energetics of the peptide binding to the membrane-mimetic-systems and establish a direct link between the estimated energetics with the 3D-structures. The specific objectives are:

1. Study the structure and dynamics of the synthetic cationic antimicrobial heptapeptide AMP (P4: NH_3^+-LKWLKKL-$CONH_2$ Charge +4) and its analogs (P5: Lysine's → Arginine's; P6: Lysine's → Uncharged-Histidine's; P7: Tryptophan → Leucine) in presence and absence of membrane-mimetic-systems (SDS micelle and DOPE:DOPG bilayer). Quantitative estimation of the role of peptide side-chain mutations and C-terminal charge on the peptide: membrane-mimic binding energetics.
2. Explore the effect of monovalent salt (NaCl) on the thermodynamics of 14 residue-long antimicrobial peptide (LL-14 obtained by doubling the length of peptide P4, Charge = +7) binding to the membrane-mimetic-models.
3. Experiments established that Leucine-rich LL-14 is highly active as well as cytotoxic relative to its valine analogue. Thus, we wanted to explore how fine-tuning hydrophobicity (Leu/Val Mutation) alters the energetics of peptide:SDS binding and explain the cytotoxicity in thermodynamic sense.
4. Explore the effect of unnatural amino-acid substitution on the stability of the LL-14:bilayer (POPE:POPG or POPC) complexes. The simulations involve computing the change in binding affinity of LL-14:bilayer upon Lys → (Orn/Dab/Dap/Hly/Arg/Agb/Agp/Hrg) substitution in all six lysine positions in LL-14.

1.4 Methods adopted in this thesis

The application of classical molecular dynamics (MD) simulations rely on the numerical and iterative solution of the Newton's equation of motion. The trajectories generated from the MD simulations are expected to recover statistical ensembles and to track the time evolution of a system. Simple particle-based descriptions of the system under study are constructed. The system is then propagated by deterministic (Newton's Law) rule and generate a trajectory describing its time evolution. The two popular approaches of the molecular simulation techniques are Molecular Dynamics (MD) and Monte Carlo (MC) simulations. MC approaches produce a new configuration from the existing configuration by random evolution of the system and selection of the new configuration based on probabilistic rules. MC simulation can compute structural and thermodynamic parameters but not dynamical properties. This thesis adopted classical MD simulations for studying the structure, dynamics, and thermodynamics of the peptide: membrane-mimetic-systems. The X-ray or cryo-EM structures of the peptide and the membranes studied in this thesis is unknown. Thus, we generated initial models of the systems and subjected the models to classical MD simulations.

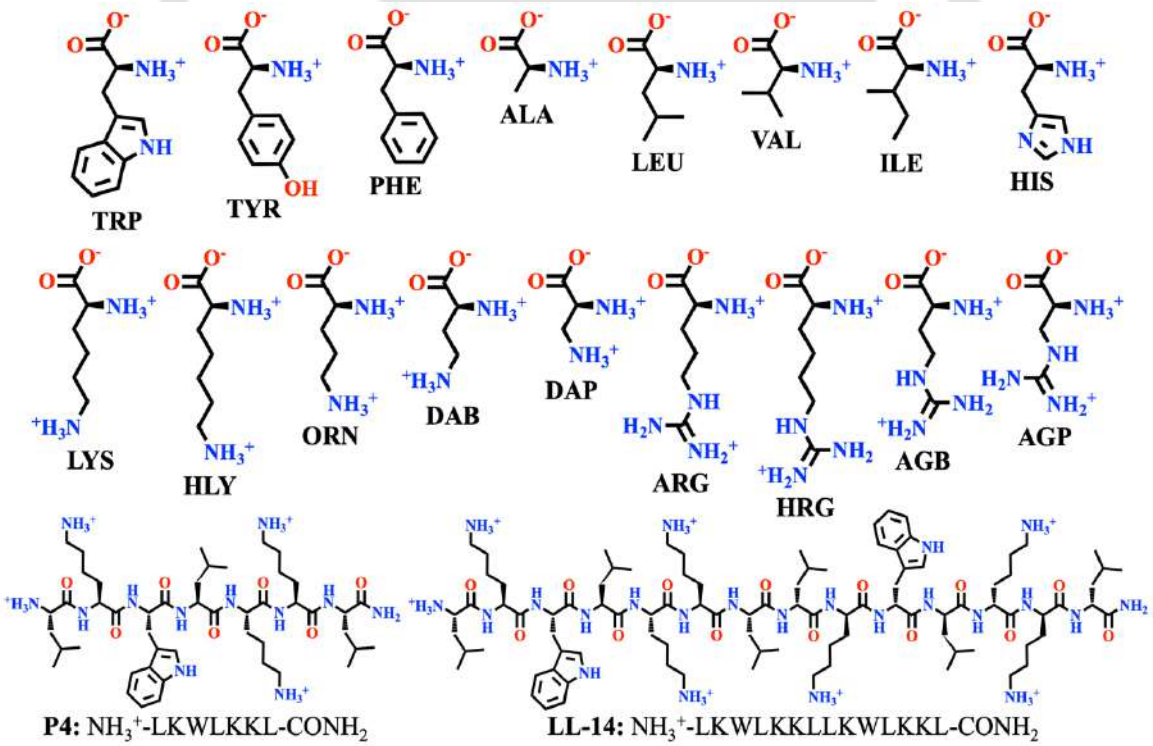

Figure 1.5: Amino acid residues that constitute the peptides modelled in this thesis. Amino acid sequence of the template model peptides: P4 and P5.

1.4.1 Peptide models

3D model of the linear peptides were generated (based on the primary sequences) using popular software such as PyMOL (Schrödinger, LLC, 2010) or VMD (Humphrey et al., 1996). In this thesis we modelled two cationic peptides (seven residue long: P4 and fourteen residue long: LL-14) and their analog (**Figure 1.5**).

1.4.2 Membrane mimetic models

Computational analysis of the real complex membrane requires simple representative models (**Table 1.1**). In this thesis, we considered two popular models micelles (SDS/DPC

Table 1.1: Popular lipid compositions as membrane-mimetic-models.

Lipid compositions (ratio)	Membrane model	references
SDS micelle	**Bacterial**	(Benetti et al., 2019; Langham et al., 2007; Sayyed-Ahmad et al., 2009)
DPC micelle	**Mammalian**	(Langham et al., 2007; Sayyed-Ahmad et al., 2009)
POPE:POPG (3:1)	**Gram-negative-IL**	(Agadi et al., 2018; Lai & Kaznessis, 2020; Manzo et al., 2019; Mukherjee et al., 2017; Zou et al., 2018)
POPC	**Mammalian-OL**	(W. F. D. Bennett et al., 2016; Mukherjee et al., 2017)
DOPE:DOPG (3:1)	**Gram-negative**	(Corin & Bowie, 2020)
POPG	Gram-positive	(Manzo et al., 2019; Zhao et al., 2018)
POPC:POPG (3.1)	Gram-positive	(Hazam et al., 2019)
POPE:POPG (7:3)	Bacterial	(R. Lipkin et al., 2017)
POPE:POPG:Chl (7:2.2:0.8)	Bacterial	(R. Lipkin et al., 2017)
POPS	Mammalian-IL	(Mukherjee et al., 2017)
POPC:POPG (7:3)	Bacterial-IL	(Mukherjee et al., 2017)
POPC:POPS (7:3)	Bacterial	(Mukherjee et al., 2017)
POPG:POPE (3:1)	Gram-positive	(Mukherjee et al., 2017)
DMPC:DMPG (1:1)	Bacterial	(B. Liu & Karttunen, 2018)
DMPC	Mammalian	(B. Liu & Karttunen, 2018)
DOPC:DOPG (7:3)	Bacterial	(Shi et al., 2018)
POPE:POPG (1:1)	Bacterial	(W. F. D. Bennett et al., 2016)

POPE: 1-palmitoyl-2-oleoyl-sn-glycerol-3-phosphoethanolamine. POPG: 1-palmitoyl-2-oleoyl-sn-glycero-3-phospho-(1′-rac-glycerol). SDS: sodium dodecyl sulfate. DPC: Dodecyl phosphocholine. POPC: 1-palmitoyl-2-oleoyl-sn- glycerol-3-phosphocholine. POPS: 1-palmitoyl-2-oleoyl-sn-glycerol-3-phospho-L-serine. DMPC: 1,2-dimyristoyl phosphatidylcholine. DMPG: 1,2- dimyristoyl-sn-glycero-3-phospho-(1′-rac-glycerol). Chl: Cholesterol. IL- Inner Leaflet. OL-Outer Leaflet.

micelle for modelling anionic-bacterial/zwitterionic-mammalian membranes) and bilayers (POPE:POPG (3:1)/DOPE:DOPG (3:1) as bacterial and POPC as mammalian membrane) (**Table 1.1**, **Figure 1.6**). Models of these micelles and bilayer were built using CHARM-GUI Membrane Builder (Jo et al., 2008; Lee et al., 2016).

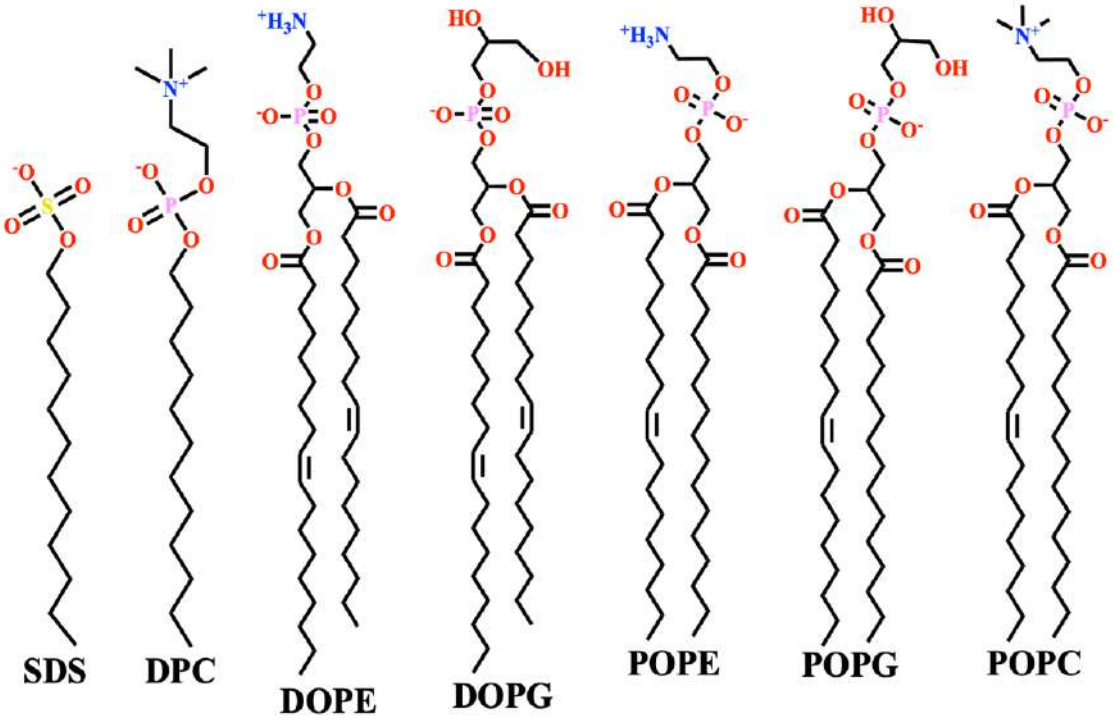

Figure 1.6: Structure of the lipid molecules that are used for modelling membranes in this thesis work.

1.4.3 Classical MD simulation

A classical system is described by a Hamiltonian, $\mathcal{H}$, which is a function of both coordinates r and momenta p. The potential energy function is independent of time and velocity for normal molecular systems. The Hamiltonian is equal to the total energy,

$$\mathcal{H} = \mathcal{H}(r,p) = K(p) + U(r) = \sum_i \frac{p_i}{2m_i} + U(r) \quad (1.1)$$

Where $K(p)$ is the kinetic energy, $U(r)$ is the potential energy, p_i is the momenta of the atom i, and m_i is the mass of the atom i. A microscopic state of the system is, therefore characterized by the set of values $\{r,p\}$, which corresponds to a point in the phase space (defined by both coordinates r and momenta p of the particles of the system).

1.4.3.1 Newtons Equation of Motion

Newton's Second Law of Motion states that

$$F_i = m_i a_i = m_i \ddot{r}_i \quad (1.2)$$

Where F_i is the force acting on the atom i, m_i is the mass of the atom i, a_i is the acceleration and $\ddot{r}_i$ is the second derivative of the atomic position r with respect of time.

The force F_i can be determined by the gradient of the potential energy function $U(r)$, which is a function of all the atomic coordinates r.

$$F_i = -\frac{\partial}{\partial r_i} U(r) \tag{1.3}$$

A more general formulation of Newton's equation of motion is given in terms of the system's Hamiltonian, $\mathcal{H}$.

$$\dot{r}_k = \frac{\partial \mathcal{H}(r,p)}{\partial p_k}; \dot{p}_k = \frac{\partial \mathcal{H}(r,p)}{\partial r_k} \tag{1.4}$$

The above two equations are used to update the positions and velocities.

1.4.3.2 Computational Algorithms

A numerical method (finite-difference approach) for integrating the differential equation is necessary to solve Newton's equation of motion. In this approach, the molecular coordinates and velocities at a time $t + \Delta t$ are obtained from the molecular coordinates and velocities at an earlier time t.

Taylor expansion of position at the time $t + \Delta t$ about time *t*

$$r(t + \Delta t) = r(t) + \dot{r}(t)\Delta t + \ddot{r}(t)\Delta t^2 + \cdots \tag{1.5}$$

This can be also written as:

$$r(t + \Delta t) = r(t) + v(t)\Delta t + \frac{1}{2} a(t)\Delta t^2 + \cdots \tag{1.6}$$

Where $v(t)$ is the velocity vector, and $a(t)$ is the acceleration at the "*t*". The above expression can be rewritten as, r_n and r_{n+1} to indicate the position at step n (at time t) and $n + 1$ (at time $t + \Delta t$), and using Eq. 1.2

$$r_{n+1} = r_n + v_n \Delta t + \frac{1}{2}\left(\frac{F_n}{m}\right)\Delta t^2 + O(t^3) \tag{1.7}$$

Where $O(t^3)$ is the terms of order Δt^n or smaller.

- **Verlet integration**

The Verlet algorithm is the integrator most frequently employed in studying biomolecules. It is based on summing the forward $(t + \Delta t)$ and backward $(t - \Delta t)$ Taylor expansions,

$$r_{n+1} = 2r_n - r_{n-1} + \frac{F_n}{m}\Delta t^2 + O(\Delta t^4) \tag{1.8}$$

This algorithm is executed in two steps:

1. Use the current position r_n to calculate the current force F_n.

2. Use the current and previous positions r_n and r_{n-1} together with the current force F_n to calculate position in the next step, r_{n+1}.

For every time step, each atom in the system involves repeating these two stages.

Subtracting the backward and forward expansion gives an algorithm for propagating the velocities,

$$v_n = \frac{r_{n+1} - r_{n-1}}{2\Delta t} + O(\Delta t^3) \tag{1.9}$$

- **Velocity Verlet integrator**

Velocity Verlet algorithm is a variation of Verlet algorithm, which achieves even better handling of the velocities. This algorithm stores positions, velocities, and accelerations at the same time t, and minimizes round-off errors. The algorithm is written as:

$$r_{n+1} = r_n + v_n \Delta t + \frac{1}{2}\left(\frac{F_n}{m}\right)\Delta t^2 \tag{1.10}$$

$$v_{n+1} = v_n + \frac{1}{2}\left[\frac{F_n}{m} + \frac{F_{n+1}}{m}\right]\Delta t \tag{1.11}$$

The Velocity Verlet algorithm consists of the following steps:

1. Calculating the position r_{n+1} at time $t + \Delta t$ from Eq. 1.10
2. Calculate the velocity at mid step $v_{n+1/2}$ using the equation

$$v_{n+1/2} = v_n + \frac{1}{2}\left(\frac{F_n}{m}\right)\Delta t \tag{1.12}$$

3. Calculating the force F_{n+1} at time $t + \Delta t$.
4. Finally compute the velocity move to v_n using

$$v_{n+1} = v_{n+1/2} + \frac{1}{2}\left(\frac{F_{n+1}}{m}\right)\Delta t \tag{1.13}$$

This velocity Verlet algorithm provides an accurate assessment of velocities and hence the kinetic energy and is numerically stable, practical, and straightforward. In this thesis, we used the "Velocity Verlet algorithm" for solving the equation of motion.

1.4.3.3 Assigning Initial velocities

Initial velocities to the atoms of the system was randomly assigned from the standard Maxwellian velocity distribution at a temperature T,

$$P(v)dv = \left(\frac{m}{2\pi k_b T}\right)^{1/2} exp\left[\frac{-mv^2}{2k_b T}\right] dv \tag{1.14}$$

Velocities are initially assigned at a low temperature, increasing gradually to the desired temperature during the equilibration phase of the simulation, allowing for dynamic

relaxation. Heating is performed by increasing atomic velocities. This heating process requires a measurable definition of the system's temperature T at time t. The temperature, $T(t)$, at any given time t is defined in terms of mean kinetic energy by

$$T(t) = \frac{1}{k_b N_{dof}} \sum_{i=1}^{N_{dof}} m_i |v_i|^2 \quad (1.15)$$

Where N_{dof} is the number of unconstrained degrees of freedom in the system ($N_{dof} = 3N - n$, where N is the number of atoms and n is the number of constraints). Scaling the velocities by a factor of $[T_0/T(t)]^{1/2}$ till result in a mean kinetic energy corresponding to a desired temperature T_0. Simulations were carried out at 310K in this thesis.

1.4.3.4 Potential Energy Function and force fields

A potential energy (U, Eq. 1.3) is a function of the 3D-structue. The total potential energy of a system $U(R)_{total}$ can be described as a sum of covalent/bonded $U(R)_{bonded}$ and noncovalent/nonbonded $U(R)_{nonbonded}$ potential energy as described in the following equations,

$$U(R)_{total} = U(R)_{bonded} + U(R)_{nonbonded} \quad (1.16)$$

$$U(R)_{bonded} = \sum_{bonds} \frac{1}{2} k_b (b - b_0)^2 + \sum_{bonds} \frac{1}{2} k_\theta (\theta - \theta_0)^2 + \sum_{dihedral} k_\omega [1 + \cos(n\omega - \gamma)] \quad (1.17)$$

$$U(R)_{nonbonded} = \sum_{\substack{nonbonded \\ atom\ pairs}} \left(4\varepsilon_{ij} \left[\left(\frac{\sigma_{ij}}{r_{ij}} \right)^{12} - \left(\frac{\sigma_{ij}}{r_{ij}} \right)^{6} \right] + \frac{q_i q_j}{4\pi\varepsilon r_{ij}} \right) \quad (1.18)$$

Where, b_0, k_b, θ_0, k_θ, n, ω, γ, k_ω, ε_{ij}, σ_{ij}, q_i, q_j, r_{ij} are the force field parameters. Some force fields also contain a Urey-Bradley term that treats 1,3 atoms (the two terminal atoms in an angle) with a harmonic bond-stretching term in order to model vibrational spectra more accurately. Current computer investigations of biological systems involve a variety of forcefields. The CHARMM (Huang et al., 2017), AMBER (Case et al., 2008), and GROMOS (Christen et al., 2005) programs are used to carry out the majority of biomolecular simulations. CHARMM added the improper and Urey-Bradley components, and there is substantial conceptual and parameter optimization even if the potential energy function forms in CHARMM and AMBER are comparable. Saturated and unsaturated lipids were incorporated in the most recent version of CHARMM. So CHARMM may also be used for protein-lipid simulations. Note that the classical force-fields described above do not allow bond breaking (harmonic springs for bonds). This thesis primarily used the CHARMM force field, and the van der Walls interaction was truncated at 1.2 nm.

1.4.3.5 Periodic Boundary Conditions

Simulation of a finite system surrounded by a vacuum is limited by the boundary effect. Periodic boundary conditions (adopted in this thesis) enable more precise modelling of the bulk behaviours in the finite simulation systems. The application of periodic boundary conditions ensures that a central two-dimensional box (cell) is surrounded by eight neighbours (in 3D, each box would have 26 neighbours) (**Figure 1.7**). A particle exits the central box during the simulation is replaced by an imaged particle that enters from the other side, keeping the number of particles of the system constant throughout the simulation. The simplest periodic system to represent and implement in software is the cubic cell (adopted in this thesis). Other popular shape of the cells adopted for simulation studies are shown in **Figure 1.8**.

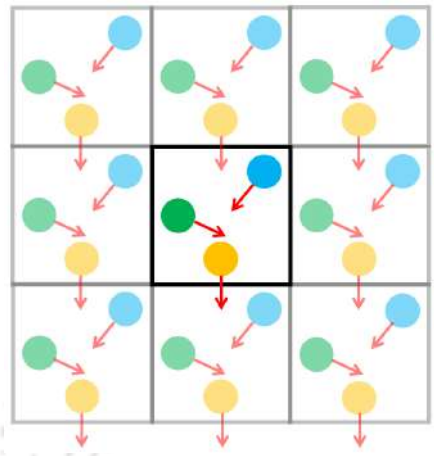

Figure 1.7: Periodic boundary conditions for a 2D system.

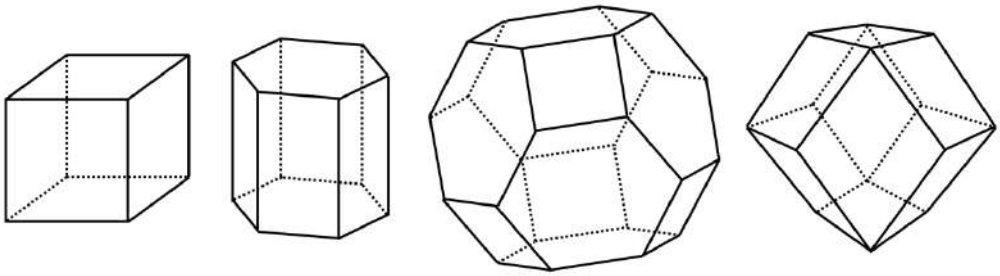

Figure 1.8: Periodic cell used in computer simulation: The cube, hexagonal prism, truncated octahedron and rhombic dodecahedron.

Other than periodic boundary condition, simulation in a like liquid droplet is also common in MD simulations (Lind et al., 2019), which is beyond the scope of this thesis.

1.4.3.6 Long-range Electrostatic interactions and Ewald Summation Method

Estimation of the electrostatic interaction is the most expensive aspect of MD simulation. The Ewald summation method efficiently estimates the long-range electrostatic interaction in the periodic systems. The charge-charge contribution to the potential energy (U_c , $Coulomb\ protential$) due to all pairs of charges in the central simulation box can be written as:

$$U_c = \frac{1}{2}\sum_{i=1}^{N}\sum_{j=1}^{N}\frac{q_i q_j}{4\pi\varepsilon_0 r_{ij}} \qquad (1.19)$$

The interaction is long-range and decays slowly with distance (~$1/r_{ij}$) and varies rapidly at small distances. A cubic lattice vector n (= (n_xL, n_yL, n_zL) with n_x, n_y, n_z being integers and L is the size of the cubic box) define the integration between the central simulation box an d its image boxes generated by the periodic boundary condition:

$$U_c = \frac{1}{2}\sum'_{|n|=0}\sum_{i=1}^{N}\sum_{j=1}^{N}\frac{q_iq_j}{4\pi\varepsilon_0|r_{ij}+n|} \quad (1.20)$$

Note, the central box (for which $|n| = 0$) does not include the self-interaction $i = j$. The $i = j$ interaction only survives between primely (central cell) and image cell interaction. The prime on the first summation that the series does not include the self-interaction(where $i = j$). The Ewald method screen the point charges are screened by overlaying a charge distribution (viz., Gaussian charge distribution of opposite sign of the point charge), which allow the treatment of long-range electrostatic interaction as a short-range one. The screening distribution is of the opposite sign to allow the screened interactions to fall off rapidly with distance, as we will see below. The overall charge distribution is divided into a short-range or "direct space" component (ρ^{sr}) involving the original point charges screened by the Gaussian-distributed charge of the same magnitude (**Figure 1.9**) but the opposite sign and a long-range component involving Gaussian-distributed charges of the original sign (ρ^{lr}). The sum of the short-range ρ^{sr} and the long-range ρ^{lr} charge distributions is still the same as the original charge distribution. Unlike the original, full potential, the direct space-screened (Figure 1.9) interaction decays rapidly. It decays even faster than Van der Waals interactions ($1/r^6$), and hence relative short cut-offs, comparable to those used for Van der Waals interactions, can also be used for handling direct-space Coulomb interactions.

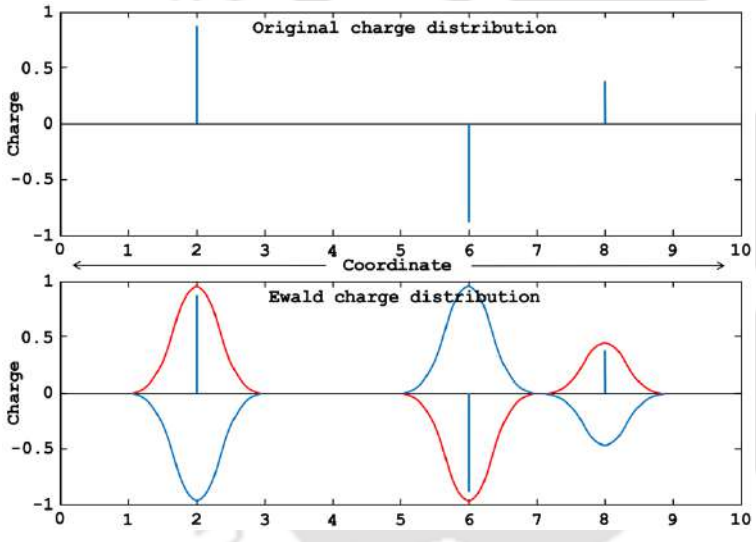

Figure 1.9: Screening charge distribution. Point charges can be split into Direct space (original charges) and Reciprocal space (Gaussian-distributed) screening charges.

In the Ewald method, the electrostatic potential can be divided into four parts (see Eq. 1.21): direct interactions involving the screed charges, direct interaction between charges in the

reciprocal space, subtraction of the interaction involving the gaussian function in the real space, and the correction term which depends on the width of the gaussian charge distribution.

$$U_c = \frac{1}{2}\sum_{i=1}^{N}\sum_{j=1}^{N}\begin{cases}\sum_{|n|=0}^{\infty}\frac{q_i q_j}{4\pi\varepsilon_0}\frac{erfc(\alpha|r_{ij}+n|)}{|r_{ij}+n|} \\ +\sum_{k\neq 0}\frac{1}{\pi L^3}\frac{q_i q_j}{4\pi\varepsilon_0}\frac{4\pi^2}{k^2}exp\left(-\frac{k^2}{4\alpha^2}\right)\cos(k\cdot r_{ij}) \\ -\frac{\alpha}{\sqrt{\pi}}\sum_{k=1}^{N}\frac{q_k^2}{4\pi\varepsilon_0}+\frac{2\pi}{3L^3}\left|\sum_{k=1}^{N}\frac{q_k}{4\pi\varepsilon_0}r_k\right|^2\end{cases} \quad (1.21)$$

The $erfc(r)$ converges rapidly. The rate of convergence depends upon the width (α) of cancelling "Gaussian distribution". The wider the gaussian, the faster the series converges. Specifically, α should be chosen so that the only terms in the series are those for which $|n| = 0$ (i.e., only pairwise interactions involving charges in the central box, or if a cut-off is used α is chosen so that only interactions with other charges within the cut-off are included). The second summation is performed in a reciprocal space. The vectors k are reciprocal vectors given by $k = 2\pi n/L$. This reciprocal sum also converges much more rapidly than the original point-charge sum. The sum of Gaussian functions in real space includes the interaction of each Gaussian with itself. So the third self-term must therefore be subtracted, and the fourth correction term is required depending upon the medium that surrounds (surrounding medium is a vacuum) the sphere of simulation boxes. The Ewald sum is the most correct way yet devised to accurately include all the effects of long-range forces in a computer simulation. A short range cut-off of 1.2 nm was used for the simulation.

1.4.3.7 Energy Minimization and Equilibration

The purpose of energy minimization is to remove the unfavourable contact (if any) and find a local minimum in the potential energy hypersurface. Two popular first-order minimization algorithms used in this thesis are the *steepest descents* (Deift & Zhou, 1993) and the *conjugate gradient* method (Hestenes & Stiefel, 1952). Post-minimized structures of the system were subjected to an equilibration (considering *NVT* followed *NPT* ensemble, where N = number of particles, V = volume, P = pressure, and Temperature = T). The production dynamics were performed with *an NPT* ensemble, where the temperature and pressure were maintained at 310K and 1 bar, respectively.

- **Temperature control**

The temperature of the simulation system is related to the average kinetic energy, as defined using the equipartition theorem:

$$\langle \sum_{i=1}^{N} \frac{1}{2} m_i v_i^2 \rangle = \frac{3}{2} N k_b T \quad (1.22)$$

Where m_i and v_i are the mass and velocity of the i^{th} particle. The simple velocity rescaling thermostat is one of the easiest thermostats to implement; however, this thermostat is also one of the most non-physical thermostats. This thermostat relies on rescaling the momenta of the particles such that the simulation's instantaneous temperature matches the target temperature.

The Berendsen thermostat (also known as the weak coupling thermostat) is similar to the simple velocity rescaling thermostat, but instead of rescaling velocities completely and abruptly to the target kinetic energy, it includes a relaxation term to allow the system to approach the target slowly. Although the Berendsen thermostat allows for temperature fluctuations, it samples neither the canonical nor the isokinetic distribution.

The Nosé-Hoover thermostat abstracts away the thermal bath from the previous thermostats and condenses it into a single additional degree of freedom. This fictitious degree of freedom has a "mass" that can be changed to interact with the particles in the system in a predictable and reproducible way while maintaining the canonical ensemble. The choice of "mass" of the fictitious particle (which in many simulation packages is instead expressed as a time-damping parameter) can be important as it affects the fluctuations that will be observed. For many reasonable choices of mass, dynamics are well-preserved. This is one of the most widely implemented and adopted in this thesis.

- **Pressure control**

As with thermostats, the pressure is controlled using barostat algorithms. The Berendsen weak coupling barostat is very similar to the Berendsen thermostat discussed earlier, which rescale the volume of the system to control the pressure. This is achieved by coupling the system to a weakly interacting pressure bath. This bath scales the volume periodically by a scaling factor, which produces more realistic fluctuations in the pressure as it slowly approaches the target pressure.

Andersen barostat first described by Andersen in 1980, the system is coupled to a fictitious pressure bath, by adding an additional degrees of freedom to the equations of motion. This behaves as if an isotropic piston is acting upon the system. This is similar to the Nosé-

Hoover thermostat, an extended system algorithm. This barostat does sample the correct ensemble.

The Parrinello-Rahman barostat is an extension to the Andersen barostat. Unlike the Andersen barostat, Parrinello-Rahman supports the anisotropic scaling of the size and shape of the simulation box. This can be quite useful in solid simulations, where phase changes can be shape changes in a crystal lattice compared to a liquid or gas, which has no well-defined shape. This barostat has essentially the same properties as the Andersen one, with additional support anisotropy.

In this thesis, 2 fs time-step was used. The temperature and pressure were controlled by using Nose-Hoover thermostat and Parrinello-Rahman barostat respectively.

1.4.4 Thermodynamic cycle and Free energy calculations

The free energy of binding of a molecule to a receptor ΔG_{BIND} can be reliably experimentally measured. Nevertheless, computational machinery able to predict the experimental values would be useful, saving time and reducing the cost of a fully experiment-based drug discovery campaign. A thermodynamic cycle (**Figure 1.10**) can efficiently compute the energetics of the system where the vertical arms correspond to the binding of two ligands, a and b. ΔG_{BIND} is the free energy change associated with the binding. These vertical arms are often realized experimentally. The horizontal arms represent the transformation of ligands a to b when it is in complex with the host or free in the water. These horizontal arms cannot be experimentally realized (follow a nonphysical path). That's why they are called alchemical transformations. Since free energy is a state function, the nonphysical nature of the path is relevant from the theoretical viewpoint.

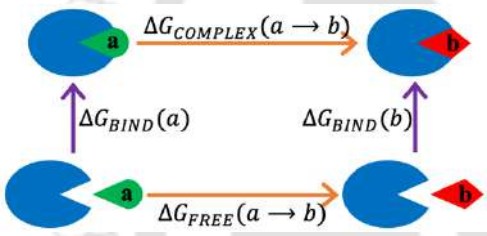

Figure 1.10: Thermodynamic and free energies.

$$\Delta\Delta G_{BIND} = \Delta G_{BIND}(b) - \Delta G_{BIND}(a)$$
$$= \Delta G_{COMPLEX}(a \rightarrow b) - \Delta G_{FREE}(a \rightarrow b) \quad (1.23)$$

In this thesis, we have estimated the absolute binding free energy (vertical arms of Figure 11) by employing two popular approaches: Molecular Mechanics Poisson-Boltzmann Surface Area (MM/PBSA) and Steered molecular dynamics followed by Umbrella Sampling. The alchemical free energy charge (horizontal arm of Figure 10) was estimated by employing free energy perturbation (FEP), thermodynamic integration (TI), and Bennett

acceptance ratio (BAR) methods. Large conformational changes might not be adequately addressed by perturbative techniques like FEP and TI. A correct convergence of this type of simulation may be hampered by the significant difference between ligands and active pockets, which could ultimately have an impact on predictions of the free energy difference. However, alchemical simulations are arguably the best methods currently available relative free energy estimation.

1.4.4.1 Molecular Mechanics Poisson-Boltzmann Surface Area (MM/PBSA)

In standard MM/PBSA, the binding free energy (ΔG_{bind}) between the biomolecule and ligand is calculated as:

$$\begin{aligned}\Delta G_{bind} &= \Delta H - T\Delta S \\ &\approx \Delta E_{MM} + \Delta G_{sol} - T\Delta S \\ &\approx \Delta E_{ele} + \Delta E_{vdw} + \Delta G_{PB} + \Delta G_{SA} - T\Delta S \end{aligned} \quad (1.24)$$

Where, ΔE_{ele} and ΔE_{vdw} are the change in electrostatic and van der Waals energy in vacuum; ΔG_{PB} and ΔG_{SA} are polar and non-polar solvation free energy, and $-T\Delta S$ is the entropy change in response to the ligand: biomolecule binding at temperature T.

Notably, ΔE_{ele} is the electrostatic energy of the complex:

$$\Delta E_{ij}^{ele} = \sum_i \sum_j \frac{q_i q_j}{4\pi\varepsilon_0 \varepsilon_{in} r_{ij}} \quad (1.25)$$

where q_i and q_j are the charges of the atom i and j, r_{ij} is the distance between atom i and j, ε_0 is the dielectric constant in vacuum and ε_{in} is the relative dielectric constant of the solute (i.e. biomolecule).

The effective electrostatic interaction is significantly altered, though, when the system has a large number of counterions nearby. According to the Debye-Huckel theory, an extra exponential damping factor is added to the Columbic term to simulate the screening effect between two charged particles/biomolecules (Debye & Zeitschrift, 1923; Levin, 2002).

$$\Delta E_{ij}^{ele} = \sum_i \sum_j \frac{q_i q_j}{4\pi\varepsilon_0 \varepsilon_{in} r_{ij}} e^{-r_{ij}/\lambda_D} \quad (1.26)$$

Where λ_D is the electrostatic screening length and has the following form when salt concentration is not very high (<1.0M)

$$\lambda_D = \sqrt{\varepsilon_0 \varepsilon_{out} k_b T \Big/ \sum_i c_i e^2 z_i^2} \quad (1.27)$$

Where ε_{out} (~80) is the relative dielectric constant of the solvent (i.e., water), k_b is the Boltzmann constant, T is the temperature, c and z are the concentration and charge of an ion, respectively, e is the electron charge, and the sum is calculated over all ionic species.

The total energy of the van der Waals term, ΔE_{vdw}, can be approximated by the Lennard-Jones expression:

$$\Delta E_{ij}^{vdw} = 4\varepsilon\left[\left(\frac{\sigma}{r_{ij}}\right)^{12} - \left(\frac{\sigma}{r_{ij}}\right)^{6}\right] \quad (1.28)$$

Where ε is the depth of the energy minimum for the interaction, σ is the separation at which the interaction energy is zero, and r_{ij} is the distance between two atoms.

To compute the polar solvation energy (ΔG_{PB}), an implicit continuum solvent is introduced to replace the explicit one. An approximate Generalized Born (GB) pairwise method or a finite-difference solution is used to determine the polar solvation term of the Poisson-Boltzmann equation (PBE) (Bashford & Karplus, 1990; Jean-Charles et al., 1991; Warwicker & Watson, 1982). This thesis adopted PBE for estimating free energy.

The PBE is based on the more fundamental Poisson equation:

$$\nabla \cdot \varepsilon(\vec{r})\nabla\phi(\vec{r}) = -4\pi\rho^{f}(\vec{r}) \quad (1.29)$$

Where $\varepsilon(\vec{r})$ is the predefined dielectric distribution function for the solvated molecular system, $\phi(\vec{r})$ is the potential distribution function, and $\rho^{f}(\vec{r})$ is the fixed atomic charge density. To simulate the electrostatic interaction brought on by the addition of salt to the aqueous solution, the electrostatic potential $\phi(\vec{r})$ can be described by the PBE as:

$$\nabla \cdot \varepsilon(\vec{r})\nabla\phi(\vec{r}) + \lambda(\vec{r})f\left(\phi(\vec{r})\right) = -4\pi\rho^{f}(\vec{r}) \quad (1.30)$$

Where, $f\left(\phi(\vec{r})\right) = 4\pi\sum_{i}^{N} z_i e c_i exp\left(-\frac{z_i e\phi(\vec{r})}{k_b T}\right)$ (1.31)

Here, $\lambda(\vec{r})$ is a predefined ion-exclusion function with a value of 0 within the Stern layer and the molecular interior and 1 outside the Stern layer. The salt-related term $f\left(\phi(\vec{r})\right)$ is a function of potential, $\phi(\vec{r})$, the valence, z_i, of ion type i, and the bulk concentration, c_i, at a given temperature T. Where both the ionic strength and electric field are weak, the PBE can be linearized for easier numerical solutions:

$$\nabla \cdot \varepsilon(\vec{r})\nabla\phi(\vec{r}) = -4\pi\rho^{f}(\vec{r}) + \varepsilon_{\nu}\kappa^{2}\phi(\vec{r}) \quad (1.32)$$

Where $\kappa^2 = \frac{8\pi e^2 I}{\varepsilon_{\nu k_b T}}$. Here ε_{ν} is the solvent dielectric constant, and I represents the ionic strength of the solution.

The non-polar (non-electrostatic) solvation-free energy contribution (ΔG_{SA}) to the solute cavity forms inside the solvent, and the solute and solvent interact around the cavity through van der Waals interactions. This causes the solvation-free energy to change (Pratt & Chandler, 2008; R. Smith & Tanford, 1973; Weeks et al., 2003). Until recent times, the

non-polar solvation-free energy has been simply estimated to be proportional to the solvent-accessible surface area (SASA) of the solute:

$$\Delta G_{SA} = \gamma \cdot SASA + b \tag{1.33}$$

This is referred to as the classical approach. The surface tension γ and the correction term b are often specified to be constant for all solute molecules.; for example, these are 0.00542 kcal/mol-Å^2 and 0.92 kcal/mol, respectively, in the AMBER package (Case et al., 2008) The configurational entropy (S) is often approximated by normal mode or quasi-harmonic analysis. The entropy can be calculated using a variety of approaches (Kassem et al., 2015), however, getting a converged value is notoriously challenging. Further approximations are frequently applied; for example, normal mode analysis typically only uses residues within a tiny sphere (radius of 8-12 Å) centered at the ligand and a small number of snapshots (100). To explore the entropy shift during binding, an interaction entropy (IE) approach was also suggested (Duan et al., 2016). The interaction entropy (IE) contribution to binding free energy was defined as:

$$-T\Delta S = k_b T \ln \langle e^{\beta E_{pl}^{int}} \rangle \tag{1.34}$$

Where ΔE_{pl}^{int} is the fluctuation of protein-ligand interaction energy for both electrostatic and van der Waals interactions, the ensemble average of $\langle e^{\beta E_{pl}^{int}} \rangle$ can be extracted from MD simulations, avoiding normal mode calculations.

1.4.4.2 Steered Molecular Dynamics and Umbrella Sampling

The timescale of protein: ligand dissociation is often inaccessible to conventional molecular dynamics simulations. Thus, the center of mass pulling (or Steered Molecular Dyanmics) biases the system and generates structures along the dissociation pathway. In the steered molecular dynamics (Izrailev et al., 1999) methodology a harmonic potential U is applied (Eq. 1.35) and the center of the parabolic potential (ξ_0) moves as a function of time and ensure adequate sampling of specific phase space region (ξ) of interest (**Figure 1.11**).

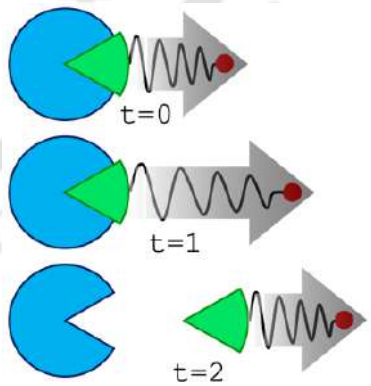

Figure 1.11: Overview of steered MD. Blue (macromolecule) and green (ligand). Spring represents the harmonic potential. Pulling force applied along the direction of the arrow.

$$\Delta U = \frac{1}{2}K\left(\xi - \xi_0(t)\right)^2 \quad (1.35)$$

Here K and ξ represent the spring constant and the reaction coordinate of the harmonic potential. The center $\xi_0(t)$ of the parabolic potential often moves at constant velocity upon pulling:

$$\xi_0(t) = \xi_0(0) + vt \quad (1.36)$$

Where v is the constant velocity, is t time. The choice of the reaction coordinate (ξ) is arbitrary. the effect of the bias potential is to connect the energetically separated regions in phase space gave. External force (pulling) disturbs the equilibrium, thus estimation of equilibrium properties, viz., free energy, is tricky from non-equilibrium SMD simulations. SMD simulations not only provide structural insight into the dissociation event along the reaction coordinate (ξ) but also estimate the force profile (Force versus ξ plot).

Two popular approaches are Jarzynski method (Jarzynski, 1997) and the weighted histogram analysis method (WHAM) (Kumar et al., 1992), respectively. Jarzynski method estimate work from multiple independent SMD trajectories and relates the average work to the free energy. In the WHAM method, equilibrium simulations were performed on the structures generated by the SMD simulation. SMD-generated structures (between bound and unbound states) were taken as starting configurations for equilibrium umbrella sampling windows (applying a harmonic/umbrella potential). We have adopted the WHAM approach in this work for estimating free energy (Potential of mean force: PMF). Umbrella sampling (Torrie & Valleau, 1977) is historically the first and one of the most popular methods used to enhance sampling in near-nonergodic conditions.

The bias potential ω_i of windows i is an additional energy term, which depends only on the reaction coordinate:

$$U^b(r) = U^u(r) + \omega_i(\xi) \quad (1.37)$$

The superscript 'b and u' denotes the biased and unbiased potential. A bias function is applied in each window to keep the system close to the reference point ξ_i^{ref} to the respective window i. Often, a simple harmonic bias of strength K is used:

$$\omega_i(\xi) = \frac{K}{2}\left(\xi - \xi_i^{ref}\right)^2 \quad (1.38)$$

The unbiased free energy $G_i(\xi)$ (for the i^{th} window) can be written in terms of biased probability distribution, harmonic biasing potential ($\omega_i(\xi)$) and a constant (F_i)

$$G_i(\xi) = -(1/\beta)\ln P_i^b(\xi) - \omega_i(\xi) + F_i \quad (1.39)$$

$$F_i = -(1/\beta)\ln\langle exp[-\beta\omega_i(\xi)]\rangle \quad (1.40)$$

Where biased probability distribution $P_i^b(\xi)$ is obtained from the equilibrium umbrella simulations (biased system), $\omega_i(\xi)$ is the applied bias potential and F_i is a constant independent to ξ. The "F_i" is computed using weighted histogram analysis method (WHAM) (Kumar et al., 1992). The choice of K, has to be made before running umbrella simulation. Overall, K has to be large enough to drive the system over the barrier. Too large K, however, will cause a very narrow distribution $P_i^b(\xi)$. Note, sufficient overlap between the probability distributions between the neighbouring windows (viz., i and $i+1$) is an absolute requirement for reliable estimation of the free energy. Thus, the choice of K and number of windows are critical. However, no standard protocol exists for the selection of K and the number of windows (i). One should try multiple combination and ensure the overlap of probability distribution between neighbouring windows. The potential of mean force (PMF or free energy) as a function of reaction coordinate was generated by employing WHAM method on the umbrella sampling simulations.

1.4.4.3 Alchemical transformation

Difference in the binding free energy of two different molecule ("a" and "b", Figure 1.10) to a biomolecule can be estimated by estimating the alchemical free energies ($\Delta G_{COMPLEX}(a \longrightarrow b), \Delta G_{FREE}(a \longrightarrow b)$, Eq. 1.23).

A hybrid energy function (U) is defined, where the coupling coordinate "λ" linearly connect the two end states ("a" and "b")

$$U(r;\lambda) = \lambda U_b(r) + (1-\lambda)U_a(r) \quad 0 \leq \lambda \leq 1 \tag{1.41}$$

Where $U_a(r)$ and $U_b(r)$ represents the end-states "a" and "b" respectively. The coupling coordinate "λ" was defined which modify the identity of the ligand. Varying λ from 0 to 1 transformed "a" to "b" by gradually altering the force-field parameters. λ values other than 0 or 1 represented the unphysical state (mixture of two endpoints: "a" and "b"), thus, justifying the term alchemical-transformation. 21(or 51) equally spaced λ values between 0 and 1 were used for the alchemical transformation in this thesis. A soft-core potential was employed for the transformation of the van der Waals interactions. 21 (or 51) MD trajectories corresponding to 21(or 51) λ windows were used to estimate the free energy difference between two end states employing the popular methods: Thermodynamic integration (TI) (Kirkwood, 2004), Free energy perturbation (FEP) (Zwanzig, 2004) and Bennett Acceptance Ratio (BAR) (C. H. Bennett, 1976).

Thermodynamic integration (TI) approach use the formula $\frac{\partial G}{\partial \lambda} = \langle \frac{\partial U}{\partial \lambda} \rangle_\lambda = \langle U(\lambda = 1) - U(\lambda = 0) \rangle_\lambda$, where the brackets "$<>_\lambda$" imply averaging over the MD trajectory for a given value of "λ". The free energy change (ΔG) is estimated by numerically integrating the derivative $\frac{\partial G}{\partial \lambda}$ versus "λ" plots.

In fee energy perturbation approach the overall free energy change (ΔG) is summed up over n steps as given below:

$$\Delta G = \sum_{i=1}^{n-1} \Delta G_i = -\beta^{-1} \sum_{i=1}^{n-1} \ln \langle exp(-\beta \Delta U \Delta \lambda_i) \rangle \quad (1.42)$$

where, $\Delta \lambda_i = \lambda_{i+1} - \lambda_i$.

The free energy difference between two neighbouring window (*i* and *i+1*) can also be obtained from the Bennett acceptance ratio method (BAR) as:

$$\Delta G_i = -\beta^{-1} \ln \frac{\langle 1 + exp - \beta(\Delta U \, \Delta \lambda_i + C_i) \rangle_{i+1}}{\langle 1 + exp - \beta(\Delta U \, \Delta \lambda_i + C_i) \rangle_i} + C_i \quad (1.43)$$

The brackets denote an ensemble average of configurations subject to two neighbouring windows "i" and "j". The constant C_i is optimized iteratively such that the two ensemble averages become equal and yield $G_i = C_i$.

1.4.5 Software used in this thesis

The thesis used GROMACS, an open-source MD tool, to perform molecular dynamics and analyze the results (Berendsen et al., 1995; Lindahl et al., 2001; van der Spoel et al., 2005). Membrane mimetic models (micelle or bilayer) have been generated by CHARMM-GUI (Brooks et al., 2009; Cheng et al., 2013; Jo et al., 2008; Lee et al., 2016; E. L. Wu et al., 2014). Modelling, visualization, trajectory movie preparation were done using PyMOL (Schrödinger, LLC, 2010), VMD (Humphrey et al., 1996), and UCSF Chimera (Pettersen et al., 2004). Data plotting was done in MS Excel (Microsoft Corporation, 2018), matplotlib (Hunter, 2007), and gnuplot (Racine, 2006). Bash (Burtch, 2004), perl (Wall, 1994), python (Rossum, 2007), AWK (Aho et al., 1979), and TCL (Ousterhout, 1989) were used to write in-house scripts to post-process the MD trajectories.

REFERENCES

Agadi, N., Vasudevan, S., & Kumar, A. (2018). Structural insight into the mechanism of action of antimicrobial peptide BMAP-28(1–18) and its analogue mutBMAP18. *Journal of Structural Biology*, *204*(3), 435–448. https://doi.org/10.1016/J.JSB.2018.10.003

Agier, J., & Brzezińska-Błaszczyk, E. (2016). Cathelicidins and defensins regulate mast cell antimicrobial activity. *Postepy Higieny i Medycyny Doswiadczalnej (Online)*, *70*(0), 618–636. https://doi.org/10.5604/17322693.1205357

Aho, A. v., Kernighan, B. W., & Weinberger, P. J. (1979). Awk — a pattern scanning and processing language. *Software: Practice and Experience*, *9*(4), 267–279. https://doi.org/10.1002/SPE.4380090403

Alaiwa, M. H. A., Reznikov, L. R., Gansemer, N. D., Sheets, K. A., Horswill, A. R., Stoltz, D. A., Zabner, J., & Welsh, M. J. (2014). pH modulates the activity and synergism of the airway surface liquid antimicrobials β-defensin-3 and LL-37. *Proceedings of the National Academy of Sciences of the United States of America*, *111*(52), 18703–18708. https://doi.org/10.1073/PNAS.1422091112/SUPPL_FILE/PNAS.201422091SI.PDF

Appadu, A., Jelokhani-Niaraki, M., & DeBruin, L. (2015). Conformational Changes and Association of Membrane-Interacting Peptides in Myelin Membrane Models: A Case of the C-Terminal Peptide of Proteolipid Protein and the Antimicrobial Peptide Melittin. *Journal of Physical Chemistry B*, *119*(47), 14821–14830. https://doi.org/10.1021/ACS.JPCB.5B07375/ASSET/IMAGES/LARGE/JP-2015-073759_0007.JPEG

Avci, F. G., Akbulut, B. S., & Ozkirimli, E. (2018). Membrane Active Peptides and Their Biophysical Characterization. *Biomolecules 2018, Vol. 8, Page 77*, *8*(3), 77. https://doi.org/10.3390/BIOM8030077

Baconnais, S., Tirouvanziam, R., Zahm, J. M., de Bentzmann, S., Péault, B., Balossier, G., & Puchelle, E. (2012). Ion Composition and Rheology of Airway Liquid from Cystic Fibrosis Fetal Tracheal Xenografts. *Https://Doi.Org/10.1165/Ajrcmb.20.4.3264*, *20*(4), 605–611. https://doi.org/10.1165/AJRCMB.20.4.3264

Baeriswyl, S., Gan, B. H., Siriwardena, T. N., Visini, R., Robadey, M., Javor, S., Stocker, A., Darbre, T., & Reymond, J. L. (2019). X-ray Crystal Structures of Short Antimicrobial Peptides as Pseudomonas aeruginosa Lectin B Complexes. *ACS Chemical Biology*, *14*(4), 758–766. https://doi.org/10.1021/ACSCHEMBIO.9B00047/ASSET/IMAGES/LARGE/CB-2019-00047M_0007.JPEG

Bashford, D., & Karplus, M. (1990). pKa's of Ionizable Groups in Proteins: Atomic Detail from a Continuum Electrostatic Model. *Biochemistry*, *29*(44), 10219–10225. https://doi.org/10.1021/BI00496A010

Bechinger, B., & Gorr, S. U. (2016). Antimicrobial Peptides: Mechanisms of Action and Resistance. *Http://Dx.Doi.Org/10.1177/0022034516679973*, *96*(3), 254–260. https://doi.org/10.1177/0022034516679973

Benetti, S., Timmons, P. B., & Hewage, C. M. (2019). NMR model structure of the antimicrobial peptide maximin 3. *European Biophysics Journal*, *48*(2), 203–212. https://doi.org/10.1007/S00249-019-01346-7/FIGURES/7

Bennett, C. H. (1976). Efficient estimation of free energy differences from Monte Carlo data. *Journal of Computational Physics*, *22*(2), 245–268. https://doi.org/10.1016/0021-9991(76)90078-4

Bennett, W. F. D., Hong, C. K., Wang, Y., & Tieleman, D. P. (2016a). Antimicrobial Peptide Simulations and the Influence of Force Field on the Free Energy for Pore Formation in Lipid Bilayers. *Journal of Chemical Theory and Computation*, *12*(9), 4524–4533. https://doi.org/10.1021/ACS.JCTC.6B00265/ASSET/IMAGES/LARGE/CT-2016-00265Y_0010.JPEG

Bennett, W. F. D., Hong, C. K., Wang, Y., & Tieleman, D. P. (2016b). Antimicrobial Peptide Simulations and the Influence of Force Field on the Free Energy for Pore Formation in Lipid Bilayers. *Journal of Chemical Theory and Computation*, *12*(9), 4524–4533. https://doi.org/10.1021/ACS.JCTC.6B00265/ASSET/IMAGES/LARGE/CT-2016-00265Y_0010.JPEG

Berendsen, H. J. C., van der Spoel, D., & van Drunen, R. (1995). GROMACS: A message-passing parallel molecular dynamics implementation. *Computer Physics Communications*, *91*(1–3), 43–56. https://doi.org/10.1016/0010-4655(95)00042-E

Bernardi, R. C., Melo, M. C. R., & Schulten, K. (2015). Enhanced sampling techniques in molecular dynamics simulations of biological systems. *Biochimica et Biophysica Acta (BBA) - General Subjects*, *1850*(5), 872–877. https://doi.org/10.1016/J.BBAGEN.2014.10.019

Boman, H. G., Agerberth, B., Boman, A., Lee, -y, Boman, A., Sun, C., Andersson, M., Jornvall, H., Mutt, V., Boman, H. G., Natl Acad Sci USA, P., Agerberth, B., Lee, J., Bergman, T., Carlquist, M., & Biochem, E. J. (1993). Mechanisms of action on Escherichia coli of cecropin P1 and PR-39, two

antibacterial peptides from pig intestine. *Infection and Immunity*, *61*(7), 2978–2984. https://doi.org/10.1128/IAI.61.7.2978-2984.1993

Bond, P. J., Holyoake, J., Ivetac, A., Khalid, S., & Sansom, M. S. P. (2007). Coarse-grained molecular dynamics simulations of membrane proteins and peptides. *Journal of Structural Biology*, *157*(3), 593–605. https://doi.org/10.1016/J.JSB.2006.10.004

Borro, B. C., Nordström, R., & Malmsten, M. (2020). Microgels and hydrogels as delivery systems for antimicrobial peptides. *Colloids and Surfaces. B, Biointerfaces*, *187*. https://doi.org/10.1016/J.COLSURFB.2020.110835

Brooks, B. R., Brooks, C. L., Mackerell, A. D., Nilsson, L., Petrella, R. J., Roux, B., Won, Y., Archontis, G., Bartels, C., Boresch, S., Caflisch, A., Caves, L., Cui, Q., Dinner, A. R., Feig, M., Fischer, S., Gao, J., Hodoscek, M., Im, W., … Karplus, M. (2009). CHARMM: The biomolecular simulation program. *Journal of Computational Chemistry*, *30*(10), 1545–1614. https://doi.org/10.1002/JCC.21287

Bruni, N., Capucchio, M. T., Biasibetti, E., Pessione, E., Cirrincione, S., Giraudo, L., Corona, A., & Dosio, F. (2016). Antimicrobial Activity of Lactoferrin-Related Peptides and Applications in Human and Veterinary Medicine. *Molecules 2016, Vol. 21, Page 752*, *21*(6), 752. https://doi.org/10.3390/MOLECULES21060752

Buchoux, S. (2017). FATSLiM: a fast and robust software to analyze MD simulations of membranes. *Bioinformatics*, *33*(1), 133–134. https://doi.org/10.1093/BIOINFORMATICS/BTW563

Bürck, J., Wadhwani, P., Fanghänel, S., & Ulrich, A. S. (2016). Oriented Circular Dichroism: A Method to Characterize Membrane-Active Peptides in Oriented Lipid Bilayers. *Accounts of Chemical Research*, *49*(2), 184–192. https://doi.org/10.1021/ACS.ACCOUNTS.5B00346/ASSET/IMAGES/LARGE/AR-2015-00346J_0007.JPEG

Burtch, K. (2004). *Linux shell scripting with Bash: A comprehensive guide and reference for Linux users and administrators*. https://repository.vnu.edu.vn/handle/VNU_123/90669

Cardoso, M. H., Meneguetti, B. T., Costa, B. O., Buccini, D. F., Oshiro, K. G. N., Preza, S. L. E., Carvalho, C. M. E., Migliolo, L., & Franco, O. L. (2019). Non-Lytic Antibacterial Peptides That Translocate Through Bacterial Membranes to Act on Intracellular Targets. *International Journal of Molecular Sciences 2019, Vol. 20, Page 4877*, *20*(19), 4877. https://doi.org/10.3390/IJMS20194877

Case, D., Darden, T., Cheatham, T., & Simmerling, C. (2008). *Amber 10*. https://infoscience.epfl.ch/record/121435/files/Amber10i.pdf

Chen, C. H., Wiedman, G., Khan, A., & Ulmschneider, M. B. (2014). Absorption and folding of melittin onto lipid bilayer membranes via unbiased atomic detail microsecond molecular dynamics simulation. *Biochimica et Biophysica Acta (BBA) - Biomembranes*, *1838*(9), 2243–2249. https://doi.org/10.1016/J.BBAMEM.2014.04.012

Chen, N., Zhou, M., Dong, X., Qu, J., Gong, F., Han, Y., Qiu, Y., Wang, J., Liu, Y., Wei, Y., Xia, J., Yu, T., Zhang, X., & Zhang, L. (2020). Epidemiological and clinical characteristics of 99 cases of 2019 novel coronavirus pneumonia in Wuhan, China: a descriptive study. *The Lancet*, *395*(10223), 507–513. https://doi.org/10.1016/S0140-6736(20)30211-7

Chen, X., & Li, L. (2016). [Non-membrane mechanisms of antimicrobial peptide P7 against Escherichia coli]. *Wei Sheng Wu Xue Bao = Acta Microbiologica Sinica*, *56*(11), 1737–1745. https://europepmc.org/article/med/29741836

Cheng, X., Jo, S., Lee, H. S., Klauda, J. B., & Im, W. (2013). CHARMM-GUI micelle builder for pure/mixed micelle and protein/micelle complex systems. *Journal of Chemical Information and Modeling*, *53*(8), 2171–2180. https://doi.org/10.1021/CI4002684/SUPPL_FILE/CI4002684_SI_001.PDF

Chrom, C. L., Renn, L. M., & Caputo, G. A. (2019). Characterization and Antimicrobial Activity of Amphiphilic Peptide AP3 and Derivative Sequences. *Antibiotics 2019, Vol. 8, Page 20*, *8*(1), 20. https://doi.org/10.3390/ANTIBIOTICS8010020

Corin, K., & Bowie, J. U. (2020). How bilayer properties influence membrane protein folding. *Protein Science : A Publication of the Protein Society*, *29*(12), 2348. https://doi.org/10.1002/PRO.3973

Costa, F., Teixeira, C., Gomes, P., & Martins, M. C. L. (2019). Clinical Application of AMPs. *Advances in Experimental Medicine and Biology*, *1117*, 281–298. https://doi.org/10.1007/978-981-13-3588-4_15

Cruz, V. L., Ramos, J., Melo, M. N., & Martinez-Salazar, J. (2013). Bacteriocin AS-48 binding to model membranes and pore formation as revealed by coarse-grained simulations. *Biochimica et Biophysica Acta (BBA) - Biomembranes*, *1828*(11), 2524–2531. https://doi.org/10.1016/J.BBAMEM.2013.05.036

Dashper, S. G., O'Brien-Simpson, N. M., Cross, K. J., Paolini, R. A., Hoffmann, B., Catmull, D. v., Malkoski, M., & Reynolds, E. C. (2005). Divalent metal cations increase the activity of the antimicrobial Peptide kappacin. *Antimicrobial Agents and Chemotherapy*, *49*(6), 2322–2328. https://doi.org/10.1128/AAC.49.6.2322-2328.2005

Debye, P., & Zeitschrift, E. (1923). De la theorie des electrolytes. I. abaissement du point de congelation et phenomenes associes. *Physikalische Zeitschrift*, *24*(9), 185–206. https://perso.uclouvain.be/ernest.matagne/SOLAIRE/SEM11/Debye.doc

Deift, P., & Zhou, X. (1993). A Steepest Descent Method for Oscillatory Riemann--Hilbert Problems. Asymptotics for the MKdV Equation. *The Annals of Mathematics*, *137*(2), 295. https://doi.org/10.2307/2946540

Deng, Z.-X., 邓智雄, Li, J.-L., 李景亮, Yuan, B., 元冰, Yang, K., & 恺杨. (2019). Residue-Specialized Membrane Poration Kinetics of Melittin and Its Variants: Insight from Mechanistic Landscapes*. *Communications in Theoretical Physics*, *71*(7), 887. https://doi.org/10.1088/0253-6102/71/7/887

Duan, L., Liu, X., & Zhang, J. Z. H. (2016). Interaction entropy: A new paradigm for highly efficient and reliable computation of protein-ligand binding free energy. *Journal of the American Chemical Society*, *138*(17), 5722–5728. https://doi.org/10.1021/JACS.6B02682/ASSET/IMAGES/JA-2016-026824_M008.GIF

Emilio, J., & Magrone, T. (2018). Editorial: Antimicrobial Peptides as Mediators of Innate Immunity. *Current Pharmaceutical Design*, *24*(10), 1041–1042. https://doi.org/10.2174/1381612824666180416113811

Ermakova, E., Kurbanov, R., & Zuev, Y. (2019). Coarse-grained molecular dynamics of membrane semitoroidal pore formation in model lipid-peptide systems. *Journal of Molecular Graphics and Modelling*, *87*, 1–10. https://doi.org/10.1016/J.JMGM.2018.11.003

Fair, R. J., & Tor, Y. (2014). Antibiotics and Bacterial Resistance in the 21st Century. *Perspectives in Medicinal Chemistry*, *6*(6), 25. https://doi.org/10.4137/PMC.S14459

Fard, M. B., Fard, S. B., Ramazi, S., Atashi, A., & Eslamifar, Z. (2021). Thrombosis in COVID-19 infection: Role of platelet activation-mediated immunity. *Thrombosis Journal 2021 19:1*, *19*(1), 1–11. https://doi.org/10.1186/S12959-021-00311-9

Farrotti, A., Bocchinfuso, G., Palleschi, A., Rosato, N., Salnikov, E. S., Voievoda, N., Bechinger, B., & Stella, L. (2015). Molecular dynamics methods to predict peptide locations in membranes: LAH4 as a stringent test case. *Biochimica et Biophysica Acta (BBA) - Biomembranes*, *1848*(2), 581–592. https://doi.org/10.1016/J.BBAMEM.2014.11.002

Fox, S. J., Lakshminarayanan, R., Beuerman, R. W., Li, J., & Verma, C. S. (2018). Conformational Transitions of Melittin between Aqueous and Lipid Phases: Comparison of Simulations with Experiments. *Journal of Physical Chemistry B*, *122*(37), 8698–8705. https://doi.org/10.1021/ACS.JPCB.8B06781/ASSET/IMAGES/LARGE/JP-2018-06781K_0006.JPEG

Gan, B. H., Gaynord, J., Rowe, S. M., Deingruber, T., & Spring, D. R. (2021). The multifaceted nature of antimicrobial peptides: current synthetic chemistry approaches and future directions. *Chemical Society Reviews*, *50*(13), 7820–7880. https://doi.org/10.1039/D0CS00729C

Goldman, M. J., Anderson, G. M., Stolzenberg, E. D., Kari, U. P., Zasloff, M., & Wilson, J. M. (1997). Human beta-defensin-1 is a salt-sensitive antibiotic in lung that is inactivated in cystic fibrosis. *Cell*, *88*(4), 553–560. https://doi.org/10.1016/S0092-8674(00)81895-4

Graf, M., Mardirossian, M., Nguyen, F., Seefeldt, A. C., Guichard, G., Scocchi, M., Innis, C. A., & Wilson, D. N. (2017). Proline-rich antimicrobial peptides targeting protein synthesis. *Natural Product Reports*, *34*(7), 702–711. https://doi.org/10.1039/C7NP00020K

Grinstein, S., Swallow, C. J., & Rotstein, O. D. (1991). Regulation of cytoplasmic pH in phagocytic cell function and dysfunction. *Clinical Biochemistry*, *24*(3), 241–247. https://doi.org/10.1016/0009-9120(91)80014-T

Hale, J. D. F., & Hancock, R. E. W. (2007). Alternative mechanisms of action of cationic antimicrobial peptides on bacteria. *Expert Review of Anti-Infective Therapy*, *5*(6), 951–959. https://doi.org/10.1586/14787210.5.6.951

Halmerbauer, G., Arri, S., Schierl, M., Strauch, E., & Koller, D. Y. (2000). The relationship of eosinophil granule proteins to ions in the sputum of patients with cystic fibrosis. *Clinical & Experimental Allergy*, *30*(12), 1771–1776. https://doi.org/10.1046/J.1365-2222.2000.00988.X

Hancock, R. E. W., Haney, E. F., & Gill, E. E. (2016). The immunology of host defence peptides: beyond antimicrobial activity. *Nature Reviews Immunology 2016 16:5*, *16*(5), 321–334. https://doi.org/10.1038/nri.2016.29

Harmouche, N., Aisenbrey, C., Porcelli, F., Xia, Y., Nelson, S. E. D., Chen, X., Raya, J., Vermeer, L., Aparicio, C., Veglia, G., Gorr, S. U., & Bechinger, B. (2017). Solution and Solid-State Nuclear Magnetic Resonance Structural Investigations of the Antimicrobial Designer Peptide GL13K in Membranes. *Biochemistry*, *56*(32), 4269–4278. https://doi.org/10.1021/ACS.BIOCHEM.7B00526/ASSET/IMAGES/LARGE/BI-2017-00526T_0006.JPEG

Hayouka, Z., Mortenson, D. E., Kreitler, D. F., Weisblum, B., Forest, K. T., & Gellman, S. H. (2013). Evidence for phenylalanine zipper-mediated dimerization in the X-ray crystal structure of a magainin 2 analogue. *Journal of the American Chemical Society*, *135*(42), 15738–15741. https://doi.org/10.1021/JA409082W/SUPPL_FILE/JA409082W_SI_001.PDF

Hazam, P. K., Akhil, R., Jerath, G., Saikia, J., & Ramakrishnan, V. (2019). Topological effects on the designability and bactericidal potency of antimicrobial peptides. *Biophysical Chemistry*, *248*, 1–8. https://doi.org/10.1016/J.BPC.2019.02.005

Hee Lee, I. N., Cho, Y., & Lehrer, R. I. (1997). Effects of pH and salinity on the antimicrobial properties of clavanins. *Infection and Immunity*, *65*(7), 2898–2903. https://doi.org/10.1128/IAI.65.7.2898-2903.1997

Hestenes, M. R., & Stiefel, E. (1952). Methods of conjugate gradients for solving linear systems. *Journal of Research of the National Bureau of Standards*, *49*(6), 409–435. https://cir.nii.ac.jp/crid/1573105975360024576

Hiemstra, P. S. (2007). Antimicrobial peptides in the real world: implications for cystic fibrosis. *The European Respiratory Journal*, *29*(4), 617–618. https://doi.org/10.1183/09031936.00017007

Hiltunen, T., Virta, M., & Anna-Liisa, L. (2017). Antibiotic resistance in the wild: an eco-evolutionary perspective. *Philosophical Transactions of the Royal Society of London. Series B, Biological Sciences*, *372*(1712). https://doi.org/10.1098/RSTB.2016.0039

Hoffman, S. B. (2016). Mechanisms of Antibiotic Resistance. *Microbiology Spectrum*, *4*(2), 464–472. https://doi.org/10.1128/MICROBIOLSPEC.VMBF-0016-2015

Hsu, P. C., Bruininks, B. M. H., Jefferies, D., Cesar Telles de Souza, P., Lee, J., Patel, D. S., Marrink, S. J., Qi, Y., Khalid, S., & Im, W. (2017). CHARMM-GUI Martini Maker for modeling and simulation of complex bacterial membranes with lipopolysaccharides. *Journal of Computational Chemistry*, *38*(27), 2354–2363. https://doi.org/10.1002/JCC.24895

Humphrey, W., Dalke, A., & Schulten, K. (1996). VMD: Visual molecular dynamics. *Journal of Molecular Graphics*, *14*(1), 33–38. https://doi.org/10.1016/0263-7855(96)00018-5

Hunter, J. D. (2007). Matplotlib: A 2D Graphics Environment. *Computing in Science & Engineering*, *9*(03), 90–95. https://doi.org/10.1109/MCSE.2007.55

Izrailev, S., Stepaniants, S., Isralewitz, B., Kosztin, D., Lu, H., Molnar, F., Wriggers, W., & Schulten, K. (1999). *Steered Molecular Dynamics*. Springer, Berlin, Heidelberg. https://doi.org/10.1007/978-3-642-58360-5_2

Jarzynski, C. (1997). Nonequilibrium equality for free energy differences. *Physical Review Letters*, *78*(14), 2690–2693. https://doi.org/10.1103/PhysRevLett.78.2690

Jean-Charles, A., Nicholls, A., Sharp, K., Honig, B., Tempczyk, A., Hendrickson, T. F., & Still, W. C. (1991). Electrostatic Contributions to Solvation Energies: Comparison of Free Energy Perturbation and Continuum Calculations. *Journal of the American Chemical Society*, *113*(4), 1454–1455. https://doi.org/10.1021/JA00004A079/SUPPL_FILE/JA00004A079_SI_001.PDF

Jefferies, D., Shearer, J., & Khalid, S. (2019). Role of O-Antigen in Response to Mechanical Stress of the E. coli Outer Membrane: Insights from Coarse-Grained MD Simulations. *Journal of Physical Chemistry B*, *123*(17), 3567–3575. https://doi.org/10.1021/ACS.JPCB.8B12168/ASSET/IMAGES/LARGE/JP-2018-12168D_0005.JPEG

Jenssen, H., Hamill, P., & Hancock, R. E. W. (2006). Peptide antimicrobial agents. *Clinical Microbiology Reviews*, *19*(3), 491–511. https://doi.org/10.1128/CMR.00056-05/ASSET/885405EA-2BFA-4A39-AF5E-1A0445AEA662/ASSETS/GRAPHIC/ZCM0030621790002.JPEG

Jo, S., Kim, T., Iyer, V. G., & Im, W. (2008). CHARMM-GUI: a web-based graphical user interface for CHARMM. *Journal of Computational Chemistry*, *29*(11), 1859–1865. https://doi.org/10.1002/jcc.20945

Jo, S., Wu, E. L., Stuhlsatz, D., Klauda, J. B., Mackerell, A. D., Widmalm, G., & Im, W. (2015). Lipopolysaccharide membrane building and simulation. *Methods in Molecular Biology*, *1273*, 391–406. https://doi.org/10.1007/978-1-4939-2343-4_24/FIGURES/6

Jung, Y., Kong, B., Moon, S., Yu, S. H., Chung, J., Ban, C., Chung, W. J., Kim, S. G., & Kweon, D. H. (2019). Envelope-deforming antiviral peptide derived from influenza virus M2 protein. *Biochemical and Biophysical Research Communications*, *517*(3), 507–512. https://doi.org/10.1016/J.BBRC.2019.07.088

Kabsch, W., & Sander, C. (1983). Dictionary of protein secondary structure: Pattern recognition of hydrogen-bonded and geometrical features. *Biopolymers*, *22*(12), 2577–2637. https://doi.org/10.1002/BIP.360221211

Kandasamy, S. K., & Larson, R. G. (2006). Effect of salt on the interactions of antimicrobial peptides with zwitterionic lipid bilayers. *Biochimica et Biophysica Acta*, *1758*(9), 1274–1284. https://doi.org/10.1016/J.BBAMEM.2006.02.030

Kang, H. K., Lee, H. H., Seo, C. H., & Park, Y. (2019). Antimicrobial and Immunomodulatory Properties and Applications of Marine-Derived Proteins and Peptides. *Marine Drugs 2019, Vol. 17, Page 350*, *17*(6), 350. https://doi.org/10.3390/MD17060350

Kang, H. K., Seo, C. H., Luchian, T., & Park, Y. (2018). Pse-T2, an antimicrobial peptide with high-level, broad-spectrum antimicrobial potency and skin biocompatibility against multidrug-resistant pseudomonas aeruginosa infection. *Antimicrobial Agents and Chemotherapy*, *62*(12). https://doi.org/10.1128/AAC.01493-18/SUPPL_FILE/ZAC012187685S1.PDF

Kang, X., Dong, F., Shi, C., Liu, S., Sun, J., Chen, J., Li, H., Xu, H., Lao, X., & Zheng, H. (2019). DRAMP 2.0, an updated data repository of antimicrobial peptides. *Scientific Data 2019 6:1*, *6*(1), 1–10. https://doi.org/10.1038/s41597-019-0154-y

Kassem, S., Ahmed, M., El-Sheikh, S., & Barakat, K. H. (2015). Entropy in bimolecular simulations: A comprehensive review of atomic fluctuations-based methods. *Journal of Molecular Graphics and Modelling*, *62*, 105–117. https://doi.org/10.1016/J.JMGM.2015.09.010

Khalid, S., Piggot, T. J., & Samsudin, F. (2019). Atomistic and Coarse Grain Simulations of the Cell Envelope of Gram-Negative Bacteria: What Have We Learned? *Accounts of Chemical Research*, *52*(1), 180–188. https://doi.org/10.1021/ACS.ACCOUNTS.8B00377/ASSET/IMAGES/LARGE/AR-2018-00377Z_0006.JPEG

Kirkwood, J. G. (2004). Statistical Mechanics of Fluid Mixtures. *The Journal of Chemical Physics*, *3*(5), 300. https://doi.org/10.1063/1.1749657

Kragol, G., Lovas, S., Varadi, G., Condie, B. A., Hoffmann, R., & Otvos, L. (2001). The antibacterial peptide pyrrhocoricin inhibits the ATPase actions of DnaK and prevents chaperone-assisted protein folding. *Biochemistry*, *40*(10), 3016–3026. https://doi.org/10.1021/BI002656A/ASSET/IMAGES/LARGE/BI002656AF00006.JPEG

Kumar, S., Rosenberg, J. M., Bouzida, D., Swendsen, R. H., & Kollman, P. A. (1992). The weighted histogram analysis method for free-energy calculations on biomolecules. I. *Journal of Computational Chemistry*, *13*(8), 1011–1021. https://doi.org/10.1002/JCC.540130812

Kurpe, S. R., Grishin, S. Y., Surin, A. K., Panfilov, A. v., Slizen, M. v., Chowdhury, S. D., & Galzitskaya, O. v. (2020). Antimicrobial and Amyloidogenic Activity of Peptides. Can Antimicrobial Peptides Be Used against SARS-CoV-2? *International Journal of Molecular Sciences 2020, Vol. 21, Page 9552*, *21*(24), 9552. https://doi.org/10.3390/IJMS21249552

Lai, P. K., & Kaznessis, Y. N. (2020). Insights into membrane translocation of protegrin antimicrobial peptides by multistep molecular dynamics simulations. *AIChE Annual Meeting, Conference Proceedings*, *2020-November*, 6056–6065. https://doi.org/10.1021/ACSOMEGA.8B00483/ASSET/IMAGES/LARGE/AO-2018-004837_0004.JPEG

Lakshminarayanan, R., Liu, S., Li, J., Nandhakumar, M., Aung, T. T., Goh, E., Chang, J. Y. T., Saraswathi, P., Tang, C., Safie, S. R. B., Lin, L. Y., Riezman, H., Lei, Z., Verma, C. S., & Beuerman, R. W. (2014). Synthetic Multivalent Antifungal Peptides Effective against Fungi. *PLOS ONE*, *9*(2), e87730. https://doi.org/10.1371/JOURNAL.PONE.0087730

Lakshminarayanan, R., Tan, W. X., Aung, T. T., Goh, E. T. L., Murugananthan, N., Li, J., Chang, J. Y. T., Dikshit, N., Saraswathi, P., Lim, R. R., Kang, T. S., Balamuralidhar, V., Sukumaran, B., Verma, C. S., Sivaraman, J., Chaurasia, S. S., Liu, S., & Beuerman, R. W. (2016). Branched Peptide, B2088, Disrupts the Supramolecular Organization of Lipopolysaccharides and Sensitizes the Gram-negative Bacteria. *Scientific Reports 2016 6:1*, *6*(1), 1–17. https://doi.org/10.1038/srep25905

Lan, Y., Ye, Y., Kozlowska, J., Lam, J. K. W., Drake, A. F., & Mason, A. J. (2010). Structural contributions to the intracellular targeting strategies of antimicrobial peptides. *Biochimica et Biophysica Acta (BBA) - Biomembranes*, *1798*(10), 1934–1943. https://doi.org/10.1016/J.BBAMEM.2010.07.003

Langham, A. A., Waring, A. J., & Kaznessis, Y. N. (2007). Comparison of interactions between beta-hairpin decapeptides and SDS/DPC micelles from experimental and simulation data. *BMC Biochemistry*, *8*(1), 1–13. https://doi.org/10.1186/1471-2091-8-11/TABLES/3

Lay, F. T., Ryan, G. F., Caria, S., Phan, T. K., Veneer, P. K., White, J. A., Kvansakul, M., & Hulett, M. D. (2019). Structural and functional characterization of the membrane-permeabilizing activity of Nicotiana occidentalis defensin NoD173 and protein engineering to enhance oncolysis. *The FASEB Journal*, *33*(5), 6470–6482. https://doi.org/10.1096/FJ.201802540R

Lee, J., Cheng, X., Swails, J. M., Yeom, M. S., Eastman, P. K., Lemkul, J. A., Wei, S., Buckner, J., Jeong, J. C., Qi, Y., Jo, S., Pande, V. S., Case, D. A., Brooks, C. L., MacKerell, A. D., Klauda, J. B., & Im, W. (2016). CHARMM-GUI Input Generator for NAMD, GROMACS, AMBER, OpenMM, and CHARMM/OpenMM Simulations Using the CHARMM36 Additive Force Field. *Journal of Chemical Theory and Computation*, *12*(1), 405–413. https://doi.org/10.1021/acs.jctc.5b00935

Lehrer, R. I., Barton, A., Daher, K. A., Harwig, S. S. L., Ganz, T., & Selsted, M. E. (1989). Interaction of human defensins with Escherichia coli. Mechanism of bactericidal activity. *The Journal of Clinical Investigation*, *84*(2), 553–561. https://doi.org/10.1172/JCI114198

Levin, Y. (2002). Electrostatic correlations: from plasma to biology. *Reports on Progress in Physics*, *65*(11), 1577. https://doi.org/10.1088/0034-4885/65/11/201

Li, J., Hu, Z., Beuerman, R., & Verma, C. (2017). Molecular Environment Modulates Conformational Differences between Crystal and Solution States of Human β-Defensin 2. *Journal of Physical Chemistry B*, *121*(13), 2739–2747. https://doi.org/10.1021/ACS.JPCB.7B00083/ASSET/IMAGES/LARGE/JP-2017-00083W_0006.JPEG

Li, L., Vorobyov, I., & Allen, T. W. (2013). The different interactions of lysine and arginine side chains with lipid membranes. *Journal of Physical Chemistry B*, *117*(40), 11906–11920. https://doi.org/10.1021/JP405418Y/SUPPL_FILE/JP405418Y_SI_001.PDF

Li, P., Poon, Y. F., Li, W., Zhu, H. Y., Yeap, S. H., Cao, Y., Qi, X., Zhou, C., Lamrani, M., Beuerman, R. W., Kang, E. T., Mu, Y., Li, C. M., Chang, M. W., Jan Leong, S. S., & Chan-Park, M. B. (2010). A polycationic antimicrobial and biocompatible hydrogel with microbe membrane suctioning ability. *Nature Materials 2010 10:2*, *10*(2), 149–156. https://doi.org/10.1038/nmat2915

Lind, C., Esguerra, M., Jespers, W., Satpati, P., Gutierrez-de-Terán, H., & Åqvist, J. (2019). Free energy calculations of RNA interactions. *Methods*, *162–163*, 85–95. https://doi.org/10.1016/J.YMETH.2019.02.014

Lindahl, E., Hess, B., & van der Spoel, D. (2001). GROMACS 3.0: a package for molecular simulation and trajectory analysis. *Journal of Molecular Modeling*, *7*(8), 306–317. https://doi.org/10.1007/s008940100045

Lipkin, R. B., & Lazaridis, T. (2015). Implicit Membrane Investigation of the Stability of Antimicrobial Peptide β-Barrels and Arcs. *The Journal of Membrane Biology*, *248*(3), 469–486. https://doi.org/10.1007/S00232-014-9759-4

Lipkin, R., Pino-Angeles, A., & Lazaridis, T. (2017). Transmembrane Pore Structures of β-Hairpin Antimicrobial Peptides by All-Atom Simulations. *Journal of Physical Chemistry B*, *121*(39), 9126–9140. https://doi.org/10.1021/ACS.JPCB.7B06591/SUPPL_FILE/JP7B06591_SI_002.XLSX

Liu, B., & Karttunen, M. (2018). Lipopeptide daptomycin: Interactions with bacterial and phospholipid membranes, stability of membrane aggregates and micellation in solution. *Biochimica et Biophysica Acta (BBA) - Biomembranes*, *1860*(9), 1949–1954. https://doi.org/10.1016/J.BBAMEM.2018.03.028

Liu, J., Xiao, S., Li, J., Yuan, B., Yang, K., & Ma, Y. (2018). Molecular details on the intermediate states of melittin action on a cell membrane. *Biochimica et Biophysica Acta (BBA) - Biomembranes*, *1860*(11), 2234–2241. https://doi.org/10.1016/J.BBAMEM.2018.09.007

Liu, Y., Kalén, A., Risto, O., & Wahlström, O. (2002). Fibroblast proliferation due to exposure to a platelet concentrate in vitro is pH dependent. *Wound Repair and Regeneration*, *10*(5), 336–340. https://doi.org/10.1046/J.1524-475X.2002.10510.X

Lohner, K., & Prossnigg, F. (2009). Biological activity and structural aspects of PGLa interaction with membrane mimetic systems. *Biochimica et Biophysica Acta*, *1788*(8), 1656–1666. https://doi.org/10.1016/J.BBAMEM.2009.05.012

Lointier, M., Aisenbrey, C., Marquette, A., Tan, J. H., Kichler, A., & Bechinger, B. (2020). Membrane pore-formation correlates with the hydrophilic angle of histidine-rich amphipathic peptides with multiple biological activities. *Biochimica et Biophysica Acta. Biomembranes*, *1862*(8). https://doi.org/10.1016/J.BBAMEM.2020.183212

Lousa, D., Pinto, A. R. T., Campos, S. R. R., Baptista, A. M., Veiga, A. S., Castanho, M. A. R. B., & Soares, C. M. (2020). Effect of pH on the influenza fusion peptide properties unveiled by constant-pH molecular dynamics simulations combined with experiment. *Scientific Reports 2020 10:1*, *10*(1), 1–18. https://doi.org/10.1038/s41598-020-77040-y

Lu, J., Xu, H., Xia, J., Ma, J., Xu, J., Li, Y., & Feng, J. (2020). D- and Unnatural Amino Acid Substituted Antimicrobial Peptides With Improved Proteolytic Resistance and Their Proteolytic Degradation Characteristics. *Frontiers in Microbiology*, *11*. https://doi.org/10.3389/FMICB.2020.563030

Ma, H., Irudayanathan, F. J., Jiang, W., & Nangia, S. (2015). Simulating Gram-Negative Bacterial Outer Membrane: A Coarse Grain Model. *Journal of Physical Chemistry B*, *119*(46), 14668–14682. https://doi.org/10.1021/ACS.JPCB.5B07122/ASSET/IMAGES/LARGE/JP-2015-07122R_0002.JPEG

Ma, R., Wong, S. W., Ge, L., Shaw, C., Siu, S. W. I., & Kwok, H. F. (2019). In Vitro and MD Simulation Study to Explore Physicochemical Parameters for Antibacterial Peptide to Become Potent Anticancer Peptide. *Molecular Therapy Oncolytics*, *16*, 7–19. https://doi.org/10.1016/J.OMTO.2019.12.001

Mack, M. R., & Kim, B. S. (2016). Superficial Immunity: Antimicrobial Responses Are More Than Skin Deep. *Immunity*, *45*(1), 6–8. https://doi.org/10.1016/J.IMMUNI.2016.07.001

Madanchi, H., Shoushtari, M., Kashani, H. H., & Sardari, S. (2019). Antimicrobial peptides of the vaginal innate immunity and their role in the fight against sexually transmitted diseases. *New Microbes and New Infections*, *34*. https://doi.org/10.1016/J.NMNI.2019.100627

Mahlapuu, M., Björn, C., & Ekblom, J. (2020). Antimicrobial peptides as therapeutic agents: opportunities and challenges. *Critical Reviews in Biotechnology*, *40*(7), 978–992. https://doi.org/10.1080/07388551.2020.1796576

Malik, E., Dennison, S. R., Harris, F., & Phoenix, D. A. (2016). pH Dependent Antimicrobial Peptides and Proteins, Their Mechanisms of Action and Potential as Therapeutic Agents. *Pharmaceuticals (Basel, Switzerland)*, *9*(4). https://doi.org/10.3390/PH9040067

Mangoni, M. L., Saugar, J. M., Dellisanti, M., Barra, D., Simmaco, M., & Rivas, L. (2005). Temporins, small antimicrobial peptides with leishmanicidal activity. *The Journal of Biological Chemistry*, *280*(2), 984–990. https://doi.org/10.1074/JBC.M410795200

Manzo, G., Ferguson, P. M., Gustilo, V. B., Hind, C. K., Clifford, M., Bui, T. T., Drake, A. F., Atkinson, R. A., Sutton, J. M., Batoni, G., Lorenz, C. D., Phoenix, D. A., & James Mason, A. (2019). Minor sequence modifications in temporin B cause drastic changes in antibacterial potency and selectivity by fundamentally altering membrane activity. *Scientific Reports 2019 9:1*, *9*(1), 1–16. https://doi.org/10.1038/s41598-018-37630-3

Maria-Neto, S., de Almeida, K. C., Macedo, M. L. R., & Franco, O. L. (2015). Understanding bacterial resistance to antimicrobial peptides: From the surface to deep inside. *Biochimica et Biophysica Acta (BBA) - Biomembranes*, *1848*(11), 3078–3088. https://doi.org/10.1016/J.BBAMEM.2015.02.017

Marrink, S. J., & Tieleman, D. P. (2013). Perspective on the Martini model. *Chemical Society Reviews*, *42*(16), 6801–6822. https://doi.org/10.1039/C3CS60093A

Matsuzaki, K., Murase, O., Fujii, N., & Miyajima, K. (1995). Translocation of a channel-forming antimicrobial peptide, magainin 2, across lipid bilayers by forming a pore. *Biochemistry*, *34*(19), 6521–6526. https://doi.org/10.1021/BI00019A033

Matsuzaki, K., Murase, O., Fujii, N., & Miyajima, K. (1996). An antimicrobial peptide, magainin 2, induced rapid flip-flop of phospholipids coupled with pore formation and peptide translocation. *Biochemistry*, *35*(35), 11361–11368. https://doi.org/10.1021/BI960016V

Microsoft Corporation. (2018). *Microsoft Excel*. Https://Office.Microsoft.Com/Excel.

Mishra, N. N., & Bayer, A. S. (2013). Correlation of Cell Membrane Lipid Profiles with Daptomycin Resistance in Methicillin-Resistant Staphylococcus aureus. *Antimicrobial Agents and Chemotherapy*, *57*(2), 1082. https://doi.org/10.1128/AAC.02182-12

Mukherjee, S., Kar, R. K., Nanga, R. P. R., Mroue, K. H., Ramamoorthy, A., & Bhunia, A. (2017). Accelerated molecular dynamics simulation analysis of MSI-594 in a lipid bilayer. *Physical Chemistry Chemical Physics*, *19*(29), 19289–19299. https://doi.org/10.1039/C7CP01941F

Nekoofar, M. H., Namazikhah, M. S., Sheykhrezae, M. S., Mohammadi, M. M., Kazemi, A., Aseeley, Z., & Dummer, P. M. H. (2009). pH of pus collected from periapical abscesses. *International Endodontic Journal*, *42*(6), 534–538. https://doi.org/10.1111/J.1365-2591.2009.01550.X

Neumann, A., Völlger, L., Berends, E. T. M., Molhoek, E. M., Stapels, D. A. C., Midon, M., Friães, A., Pingoud, A., Rooijakkers, S. H. M., Gallo, R. L., Mörgelin, M., Nizet, V., Naim, H. Y., & von Köckritz-Blickwede, M. (2014). Novel role of the antimicrobial peptide LL-37 in the protection of neutrophil extracellular traps against degradation by bacterial nucleases. *Journal of Innate Immunity*, *6*(6), 860–868. https://doi.org/10.1159/000363699

Nhan, C., Small, D. M., May, B. K., & Hung, A. (2018). pH-induced structural changes of apo-lactoferrin and implications for its function: a molecular dynamics simulation study. *Https://Doi.Org/10.1080/08927022.2018.1535178*, *45*(2), 87–103. https://doi.org/10.1080/08927022.2018.1535178

O'Neill, J. (2016). *Tackling drug-resistant infections globally: final report and recommendations*.

Oren, Z., & Shai, Y. (1998). Mode of Action of Linear Amphipathic-Helical Antimicrobial Peptides. *Biopoly*, *47*, 451–463. https://doi.org/10.1002/(SICI)1097-0282(1998)47:6

Otvos, L., Insug, O., Rogers, M. E., Consolvo, P. J., Condie, B. A., Lovas, S., Bulet, P., & Blaszczyk-Thurin, M. (2000). Interaction between heat shock proteins and antimicrobial peptides. *Biochemistry*, *39*(46), 14150–14159. https://doi.org/10.1021/BI0012843/ASSET/IMAGES/LARGE/BI0012843F00007.JPEG

Ousterhout, J. K. (1989). *Tcl: An embeddable command language*. https://citeseerx.ist.psu.edu/document?repid=rep1&type=pdf&doi=5902593c97ea063025bb4f2f06d5e9158cc33316

Pal, I., Bhattacharyya, D., Kar, R. K., Zarena, D., Bhunia, A., & Atreya, H. S. (2019). A Peptide-Nanoparticle System with Improved Efficacy against Multidrug Resistant Bacteria. *Scientific Reports*, *9*(1). https://doi.org/10.1038/S41598-019-41005-7

Paulmann, M., Arnold, T., Linke, D., Özdirekcan, S., Kopp, A., Gutsmann, T., Kalbacher, H., Wanke, I., Schuenemann, V. J., Habeck, M., Bürck, J., Ulrich, A. S., & Schittek, B. (2012). Structure-Activity Analysis of the Dermcidin-derived Peptide DCD-1L, an Anionic Antimicrobial Peptide Present in Human Sweat. *Journal of Biological Chemistry*, *287*(11), 8434–8443. https://doi.org/10.1074/JBC.M111.332270

Peng, S., Yang, M., Sun, R. N., Liu, Y., Wang, W., Xi, Q., Gong, H., & Chen, C. (2018). Mechanism of actions of Oncocin, a proline-rich antimicrobial peptide, in early elongation revealed by single-molecule FRET. *Protein and Cell*, *9*(10), 890–895. https://doi.org/10.1007/S13238-017-0495-2/FIGURES/2

Petrosillo, N. (2020). Infections: The Emergency of the New Millennium. *Nuclear Medicine in Infectious Diseases*, 1. https://doi.org/10.1007/978-3-030-25494-0_1

Pettersen, E. F., Goddard, T. D., Huang, C. C., Couch, G. S., Greenblatt, D. M., Meng, E. C., & Ferrin, T. E. (2004). UCSF Chimera—A visualization system for exploratory research and analysis. *Journal of Computational Chemistry*, *25*(13), 1605–1612. https://doi.org/10.1002/JCC.20084

Piggot, T. J., Holdbrook, D. A., & Khalid, S. (2011). Electroporation of the E. coli and S. aureus membranes: Molecular dynamics simulations of complex bacterial membranes. *Journal of Physical Chemistry B*, *115*(45), 13381–13388. https://doi.org/10.1021/JP207013V/SUPPL_FILE/JP207013V_SI_001.PDF

Piggot, T. J., Piñeiro, Á., & Khalid, S. (2012). Molecular dynamics simulations of phosphatidylcholine membranes: A comparative force field study. *Journal of Chemical Theory and Computation*, *8*(11), 4593–4609. https://doi.org/10.1021/CT3003157/SUPPL_FILE/CT3003157_SI_001.PDF

Pluhackova, K., Kirsch, S. A., Han, J., Sun, L., Jiang, Z., Unruh, T., & Böckmann, R. A. (2016). A Critical Comparison of Biomembrane Force Fields: Structure and Dynamics of Model DMPC, POPC, and POPE Bilayers. *Journal of Physical Chemistry B*, *120*(16), 3888–3903. https://doi.org/10.1021/ACS.JPCB.6B01870/ASSET/IMAGES/LARGE/JP-2016-01870N_0010.JPEG

Pohl, C., Zalar, M., Bialy, I. el, Indrakumar, S., Peters, G. H. J., Friess, W., Golovanov, A. P., Streicher, W. W., Noergaard, A., Harris, P., Noergaard, A., & Harris, P. (2020). The Effect of Point Mutations on the Biophysical Properties of an Antimicrobial Peptide: Development of a Screening Protocol for Peptide Stability Screening. *Molecular Pharmaceutics*, *17*(9), 3298–3313. https://doi.org/10.1021/ACS.MOLPHARMACEUT.0C00406/ASSET/IMAGES/LARGE/MP0C00406_0012.JPEG

Pontes, F. J. S., Rusu, V. H., Soares, T. A., & Lins, R. D. (2012). The effect of temperature, cations, and number of Acyl chains on the lamellar to non-lamellar transition in Lipid-A membranes: A microscopic view. *Journal of Chemical Theory and Computation*, *8*(10), 3830–3838. https://doi.org/10.1021/CT300084V/ASSET/IMAGES/LARGE/CT-2012-00084V_0001.JPEG

Pratt, L. R., & Chandler, D. (2008). Theory of the hydrophobic effect. *The Journal of Chemical Physics*, *67*(8), 3683. https://doi.org/10.1063/1.435308

Racine, J. (2006). gnuplot 4.0: a portable interactive plotting utility. *Journal of Applied Econometrics*, *21*(1), 133–141. https://doi.org/10.1002/JAE.885

Ramachandran, G. N., Ramakrishnan, C., & Sasisekharan, V. (1963). Stereochemistry of polypeptide chain configurations. *Journal of Molecular Biology*, *7*(1), 95–99. https://doi.org/10.1016/S0022-2836(63)80023-6

Reid, L. M., Verma, C. S., & Essex, J. W. (2019). The role of molecular simulations in understanding the mechanisms of cell-penetrating peptides. *Drug Discovery Today*, *24*(9), 1821–1835. https://doi.org/10.1016/J.DRUDIS.2019.06.013

Rhaiem, R. ben, & Houimel, M. (2016). Targeting Leishmania major parasite with peptides derived from a combinatorial phage display library. *Acta Tropica*, *159*, 11–19. https://doi.org/10.1016/J.ACTATROPICA.2016.03.018

Rossum, G. van. (2007). Python Programming Language. *In USENIX Annual Technical Conference*, *41*(1), 1–36. https://ir.cwi.nl/pub/18204/18204A.pdf

Rothstein, D. M., Spacciapoli, P., Tran, L. T., Xu, T., Roberts, F. D., Dalla Serra, M., Buxton, D. K., Oppenheim, F. G., & Friden, P. (2001). Anticandida activity is retained in P-113, a 12-amino-acid fragment of histatin 5. *Antimicrobial Agents and Chemotherapy*, *45*(5), 1367–1373. https://doi.org/10.1128/AAC.45.5.1367-1373.2001

Santos, D. E. S., Pol-Fachin, L., Lins, R. D., & Soares, T. A. (2017). Polymyxin Binding to the Bacterial Outer Membrane Reveals Cation Displacement and Increasing Membrane Curvature in Susceptible but Not in Resistant Lipopolysaccharide Chemotypes. *Journal of Chemical Information and Modeling*,

57(9), 2181–2193. https://doi.org/10.1021/ACS.JCIM.7B00271/ASSET/IMAGES/LARGE/CI-2017-002713_0010.JPEG
Sarkar, T., Chetia, M., & Chatterjee, S. (2021). Antimicrobial Peptides and Proteins: From Nature's Reservoir to the Laboratory and Beyond. *Frontiers in Chemistry*, *9*, 432. https://doi.org/10.3389/FCHEM.2021.691532/BIBTEX
Sayyed-Ahmad, A., Khandelia, H., & Kaznessis, Y. N. (2009). Relative free energy of binding between antimicrobial peptides and SDS or DPC micelles. *Https://Doi.Org/10.1080/08927020902902742*, *35*(10–11), 986–997. https://doi.org/10.1080/08927020902902742
Schneider, L. A., Korber, A., Grabbe, S., & Dissemond, J. (2007). Influence of pH on wound-healing: A new perspective for wound-therapy? *Archives of Dermatological Research*, *298*(9), 413–420. https://doi.org/10.1007/S00403-006-0713-X/FIGURES/2
Schrödinger, LLC. (2010). *The PyMOL Molecular Graphics System, Version 2.4.0*. https://pymol.org/2/
Shai, Y. (2002). Mode of action of membrane active antimicrobial peptides. *Peptide Science*, *66*(4), 236–248. https://doi.org/10.1002/BIP.10260
Shao, J., Tanner, S. W., Thompson, N., & Cheatham, T. E. (2007). Clustering molecular dynamics trajectories: 1. Characterizing the performance of different clustering algorithms. *Journal of Chemical Theory and Computation*, *3*(6), 2312–2334. https://doi.org/10.1021/CT700119M/SUPPL_FILE/CT700119M-FILE002.PDF
Shi, Y., Wan, M., Fu, L., Zhang, S., Wang, S., Gao, L., & Fang, W. (2018). Peptide-Lipid Interaction Sites Affect Vesicles' Responses to Antimicrobial Peptides. *Biophysical Journal*, *115*(8), 1518–1529. https://doi.org/10.1016/J.BPJ.2018.08.040
Singh, A., & Prasad, R. (2011). Comparative lipidomics of azole sensitive and resistant clinical isolates of Candida albicans reveals unexpected diversity in molecular lipid imprints. *PloS One*, *6*(4). https://doi.org/10.1371/JOURNAL.PONE.0019266
Smith, J. J., Travis, S. M., Greenberg, E. P., & Welsh, M. J. (1996). Cystic fibrosis airway epithelia fail to kill bacteria because of abnormal airway surface fluid. *Cell*, *85*(2), 229–236. https://doi.org/10.1016/S0092-8674(00)81099-5
Smith, R., & Tanford, C. (1973). Hydrophobicity of Long Chain n-Alkyl Carboxylic Acids, as Measured by Their Distribution Between Heptane and Aqueous Solutions. *Proceedings of the National Academy of Sciences*, *70*(2), 289–293. https://doi.org/10.1073/PNAS.70.2.289
Sohrabi, C., Alsafi, Z., O'Neill, N., Khan, M., Kerwan, A., Al-Jabir, A., Iosifidis, C., & Agha, R. (2020). World Health Organization declares global emergency: A review of the 2019 novel coronavirus (COVID-19). *International Journal of Surgery (London, England)*, *76*, 71–76. https://doi.org/10.1016/J.IJSU.2020.02.034
Tam, J. P., Lu, Y. A., & Yang, J. L. (2000). Design of salt-insensitive glycine-rich antimicrobial peptides with cyclic tricystine structures. *Biochemistry*, *39*(24), 7159–7169. https://doi.org/10.1021/BI0003487
Tang, L., Chen, J., Zhou, Z., Yu, P., Yang, Z., & Zhong, G. (2015). Chlamydia-secreted protease CPAF degrades host antimicrobial peptides. *Microbes and Infection*, *17*(6), 402–408. https://doi.org/10.1016/J.MICINF.2015.02.005
Tjabringa, G. S., Ninaber, D. K., Drijfhout, J. W., Rabe, K. F., & Hiemstra, P. S. (2006). Human cathelicidin LL-37 is a chemoattractant for eosinophils and neutrophils that acts via formyl-peptide receptors. *International Archives of Allergy and Immunology*, *140*(2), 103–112. https://doi.org/10.1159/000092305
Torrie, G. M., & Valleau, J. P. (1977). Nonphysical Sampling Distributions in Monte Carlo Free-Energy Estimation: Umbrella Sampling. *JCoPh*, *23*(2), 187–199. https://doi.org/10.1016/0021-9991(77)90121-8
Ulmschneider, J. P., & Ulmschneider, M. B. (2018). Molecular Dynamics Simulations Are Redefining Our View of Peptides Interacting with Biological Membranes. *Accounts of Chemical Research*, *51*(5), 1106–1116. https://doi.org/10.1021/ACS.ACCOUNTS.7B00613/ASSET/IMAGES/LARGE/AR-2017-00613W_0006.JPEG
van der Spoel, D., Lindahl, E., Hess, B., Groenhof, G., Mark, A. E., & Berendsen, H. J. C. (2005). GROMACS: Fast, flexible, and free. *Journal of Computational Chemistry*, *26*(16), 1701–1718. https://doi.org/10.1002/jcc.20291
van Oosten, B., & Harroun, T. A. (2016). A MARTINI extension for Pseudomonas aeruginosa PAO1 lipopolysaccharide. *Journal of Molecular Graphics and Modelling*, *63*, 125–133. https://doi.org/10.1016/J.JMGM.2015.12.002
Vila-Viçosa, D., Silva, T. F. D., Slaybaugh, G., Reshetnyak, Y. K., Andreev, O. A., & Machuqueiro, M. (2018). Membrane-Induced p Ka Shifts in wt-pHLIP and Its L16H Variant. *Journal of Chemical Theory and Computation*, *14*(6), 3289–3297.

https://doi.org/10.1021/ACS.JCTC.8B00102/ASSET/IMAGES/LARGE/CT-2018-001023_0006.JPEG
Vunnam, S., Juvvadi, P., Rotondi, K. S., & Merrifield, R. B. (1998). Synthesis and study of normal, enantio, retro, and retroenantio isomers of cecropin A-melittin hybrids, their end group effects and selective enzyme inactivation. *The Journal of Peptide Research : Official Journal of the American Peptide Society*, *51*(1), 38–44. https://doi.org/10.1111/J.1399-3011.1998.TB00414.X
Vymětal, J., & Vondrášek, J. (2011). Gyration- and inertia-tensor-based collective coordinates for metadynamics. Application on the conformational behavior of polyalanine peptides and Trp-cage folding. *Journal of Physical Chemistry A*, *115*(41), 11455–11465. https://doi.org/10.1021/JP2065612/ASSET/IMAGES/JP-2011-065612_M018.GIF
Walkenhorst, W. F., Klein, J. W., Vo, P., & Wimley, W. C. (2013). PH dependence of microbe sterilization by cationic antimicrobial peptides. *Antimicrobial Agents and Chemotherapy*, *57*(7), 3312–3320. https://doi.org/10.1128/AAC.00063-13/ASSET/0740D634-DC8E-4898-A0E3-007F2393EFBC/ASSETS/GRAPHIC/ZAC9991019680007.JPEG
Wall, L. (1994). *The Perl programming language*. http://www.fxjyzy.com:8080/ebook/%E5%B9%BF%E4%BF%A1%E4%B9%A6%E5%BA%93/1211/gjfd/ts005085.pdf
Wang, C., Sun, Z., Liu, Y., Zhang, X., & Xu, G. (2007). A novel antimicrobial vermipeptide family from earthworm Eisenia fetida. *European Journal of Soil Biology*, *43*(SUPPL. 1), S127–S134. https://doi.org/10.1016/J.EJSOBI.2007.08.048
Wang, G., Li, X., & Wang, Z. (2009). APD2: the updated antimicrobial peptide database and its application in peptide design. *Nucleic Acids Research*, *37*(suppl_1), D933–D937. https://doi.org/10.1093/NAR/GKN823
Wang, G., Li, X., & Wang, Z. (2016). APD3: the antimicrobial peptide database as a tool for research and education. *Nucleic Acids Research*, *44*(D1), D1087–D1093. https://doi.org/10.1093/NAR/GKV1278
Wang, Y., Chen, C. H., Hu, D., Ulmschneider, M. B., & Ulmschneider, J. P. (2016). Spontaneous formation of structurally diverse membrane channel architectures from a single antimicrobial peptide. *Nature Communications 2016 7:1*, *7*(1), 1–9. https://doi.org/10.1038/ncomms13535
Wang, Z., & Wang, G. (2004). APD: the Antimicrobial Peptide Database. *Nucleic Acids Research*, *32*(suppl_1), D590–D592. https://doi.org/10.1093/NAR/GKH025
Warschawski, D. E., Arnold, A. A., Beaugrand, M., Gravel, A., Chartrand, É., & Marcotte, I. (2011). Choosing membrane mimetics for NMR structural studies of transmembrane proteins. *Biochimica et Biophysica Acta (BBA) - Biomembranes*, *1808*(8), 1957–1974. https://doi.org/10.1016/J.BBAMEM.2011.03.016
Warwicker, J., & Watson, H. C. (1982). Calculation of the electric potential in the active site cleft due to α-helix dipoles. *Journal of Molecular Biology*, *157*(4), 671–679. https://doi.org/10.1016/0022-2836(82)90505-8
Weeks, J. D., Chandler, D., & Andersen, H. C. (2003). Role of Repulsive Forces in Determining the Equilibrium Structure of Simple Liquids. *The Journal of Chemical Physics*, *54*(12), 5237. https://doi.org/10.1063/1.1674820
Woody, R. W. (1985). Circular Dichroism of Peptides. *Conformation in Biology and Drug Design*, 15–114. https://doi.org/10.1016/B978-0-12-304207-1.50008-4
Wu, C., Biswas, S., Garcia De Gonzalo, C. v., & van der Donk, W. A. (2019). Investigations into the Mechanism of Action of Sublancin. *ACS Infectious Diseases*, *5*(3), 454–459. https://doi.org/10.1021/ACSINFECDIS.8B00320/ASSET/IMAGES/LARGE/ID-2018-003206_0003.JPEG
Wu, D., Gao, Y., Qi, Y., Chen, L., Ma, Y., & Li, Y. (2014). Peptide-based cancer therapy: opportunity and challenge. *Cancer Letters*, *351*(1), 13–22. https://doi.org/10.1016/J.CANLET.2014.05.002
Wu, E. L., Cheng, X., Jo, S., Rui, H., Song, K. C., Dávila-Contreras, E. M., Qi, Y., Lee, J., Monje-Galvan, V., Venable, R. M., Klauda, J. B., & Im, W. (2014). CHARMM-GUI Membrane Builder toward realistic biological membrane simulations. *Journal of Computational Chemistry*, *35*(27), 1997–2004. https://doi.org/10.1002/JCC.23702
Yeasmin, R., Buck, M., Weinberg, A., & Zhang, L. (2018). Translocation of Human β Defensin Type 3 through a Neutrally Charged Lipid Membrane: A Free Energy Study. *Journal of Physical Chemistry B*, *122*(50), 11883–11894. https://doi.org/10.1021/ACS.JPCB.8B08285/ASSET/IMAGES/LARGE/JP-2018-08285B_0002.JPEG
Yoo, J., & Cui, Q. (2008). Does Arginine Remain Protonated in the Lipid Membrane? Insights from Microscopic pKa Calculations. *Biophysical Journal*, *94*(8), L61–L63. https://doi.org/10.1529/BIOPHYSJ.107.122945

Yount, N. Y., Kupferwasser, D., Spisni, A., Dutz, S. M., Ramjan, Z. H., Sharma, S., Waring, A. J., & Yeaman, M. R. (2009). Selective reciprocity in antimicrobial activity versus cytotoxicity of hBD-2 and crotamine. *Proceedings of the National Academy of Sciences of the United States of America*, *106*(35), 14972–14977. https://doi.org/10.1073/PNAS.0904465106/SUPPL_FILE/0904465106SI.PDF

Zhang, L., Parente, J., Harris, S. M., Woods, D. E., Hancock, R. E. W., & Falla, T. J. (2005). Antimicrobial peptide therapeutics for cystic fibrosis. *Antimicrobial Agents and Chemotherapy*, *49*(7), 2921–2927. https://doi.org/10.1128/AAC.49.7.2921-2927.2005

Zhang, M., Zhao, J., & Zheng, J. (2014). Molecular understanding of a potential functional link between antimicrobial and amyloid peptides. *Soft Matter*, *10*(38), 7425–7451. https://doi.org/10.1039/C4SM00907J

Zhao, L., Cao, Z., Bian, Y., Hu, G., Wang, J., & Zhou, Y. (2018). Molecular Dynamics Simulations of Human Antimicrobial Peptide LL-37 in Model POPC and POPG Lipid Bilayers. *International Journal of Molecular Sciences 2018, Vol. 19, Page 1186*, *19*(4), 1186. https://doi.org/10.3390/IJMS19041186

Zou, R., Zhu, X., Tu, Y., Wu, J., & Landry, M. P. (2018). Activity of Antimicrobial Peptide Aggregates Decreases with Increased Cell Membrane Embedding Free Energy Cost. *Biochemistry*, *57*(18), 2606–2610. https://doi.org/10.1021/ACS.BIOCHEM.8B00052/ASSET/IMAGES/LARGE/BI-2018-000527_0004.JPEG

Zwanzig, R. W. (2004). High-Temperature Equation of State by a Perturbation Method. I. Nonpolar Gases. *The Journal of Chemical Physics*, *22*(8), 1420. https://doi.org/10.1063/1.1740409

Chapter 2

Thermodynamics, Activity and pH Sensitivity of Cationic Hepta-Peptides

Understanding the thermodynamics of peptide:membrane binding and the factors that alter the stability is the key to designing potent and selective small antimicrobial peptides. Here, we report the thermodynamics, antimicrobial activity, and mechanism of de novo designed seven residues long cationic antimicrobial peptide (P4: NH_3^+-LKWLKKL-$CONH_2$, Charge +4) and its analogue (P5: Lysine's → Arginine's; P6: Lysine's → Uncharged-Histidine's; P7: Tryptophan → Leucine) by combining computation and experiments. Energetics of peptide binding to bacterial-membrane-mimetic models (SDS-micelle and DOPE/DOPG-bilayer) was estimated from classical MD simulations (Sampling ~ 47.5 μs; employing three approaches: Umbrella Sampling, MM/PBSA, Alchemical Free Energy simulations). We showed that the absolute peptide binding affinity (ΔG) strongly depends on the model of the bacterial-membrane-mimic (micelle or bilayer). However, the relative peptide-binding affinities (ΔΔG: P5/P6/P7 binding relative to P4, +ve sign indicates favourable P4 binding) are independent of the membrane model. The calculated order of decreasing peptide binding affinity to the micelle/bilayer was P5 (ΔΔG ~ -2 kcal/mol) > P4 (ΔΔG ~ 0 kcal/mol) > P7 (ΔΔG ~ +2 kcal/mol) >> P6 (ΔΔG ~ +10 kcal/mol). Substitution of the uncharged-histidine (P6) by charged-histidine (P6*) significantly favoured micelle/bilayer binding; P6*(ΔΔG ~ +0.5 kcal/mol). Thus, computational analysis suggests that among the peptides (P4, P5, P6, and P7), (1) P5 is the strongest binder to the bacterial-membrane-mimetic models, and (2) P6 might be an effective antimicrobial peptide at low pH. Minimal inhibitory concentration (MIC) assays confirmed that the antimicrobial activity against *P. aeruginosa* at physiological pH 7.4 was correlated [$MIC_{90\%}$: P5(30 μM) > P4(20 μM) >> P7(200 μM) >> P6 (inactive up to 200 μM)] with the estimated ΔΔG values. The strength of the antimicrobial activity of the peptides against *E. coli* at pH 7.4 [MIC: P5(50 μM) > P4(20 μM) > P6(150 μM) >> P7(inactive up to 200 μM)] also confirmed P5 as the most potent peptide whereas P6 showed very poor activity. P7 was found to be inactive against *E. coli*. Noticeable improvement of the antimicrobial activity of the histidine-peptide P6 against *E. coli* (an acid-resistant bacteria which can survive in the low pH gastric

environment) upon lowering of pH was demonstrated ($MIC_{90\%}$= 150 μM, 120 μM, 75 μM, 25 μM at pH = 7.4, 6.0, 4.0, and 3.0 respectively). Field emission scanning electron microscopy (FESEM) experiments showed that the peptides were membranolytic in nature. Histidine-peptide (P6) was shown to be active against acid-resistant bacteria, thus, a promising membranolytic pH-sensitive AMP. The correlation between the calculated energetics (ΔΔG) and the experimental activity has been highlighted. The results may be relevant for related cationic antimicrobial peptides in general and important for rational design of more potential therapeutic AMPs.

2.1 Background

We demonstrated potent antimicrobial and antifungal activity of de novo designed seven-residue long leucine-lysine/arginine peptides (NH_3^+-LKWLKKL-$CONH_2$: P4; NH_3^+-LRWLRRL-$CONH_2$: P5) (Pandit et al., 2018). Short AMPs (less than 20 amino acid residues) are known to be less immunogenic and less likely to trigger allergies (Hans et al., 2012; Rahnamaeian & Vilcinskas, 2015). Moreover, short AMPs can be easily synthesized and modified (for improving stability, toxicity, and specificity). Thus, the seven-residue long peptides (P4, P5, P6, and P7) are worth attention. leucine-arginine peptide (P5) was reported to be relatively more potent than the leucine-lysine peptide (P4). The leucine-histidine analogue (NH_3^+-LHWLHHL-$CONH_2$: P6) was reported to be inactive, whereas partial loss of activity was observed upon tryptophan substitution with leucine (NH_3^+-LKLLKKL-$CONH_2$: P7). The peptides were unstructured in the presence or absence of membrane mimicking environment and proposed to be membranolytic. The observed differential antimicrobial activity can be speculated to have a direct link with the differential ability of the peptides to bind to the microbial membrane. However, the energetics of membrane binding associated with these peptides is unknown. Understanding the mechanism in terms of structures and its link to the energetics is the key to designing AMPs with therapeutic potential. Computational study of peptide binding to simple membrane mimetic systems (viz., micelles and bilayer) has been successful to fill up the gap to some extent (Aronica et al., 2021; Bals et al., 1998; Croonen et al., 1983; Ghosh et al., 2022; Lebecque et al., 2017; MacKerell, 1995; Pandit et al., 2018, 2020, 2021; Rakitin & Pack, 2004; Ulmschneider, 2017) and providing critical insights into the somewhat complicated peptide:microbe interactions.

In this chapter, we have reported a combined computational (classical MD) and experimental (Minimal inhibitory concentration assays, Field emission scanning electron microscopy) study focused to estimate the energetics of peptide: membrane-mimetic-systems binding and establishing a link between estimated energetics, atomic structures, and antimicrobial activity. The wet-lab experiments were performed by our experimental collaborators.

MD simulations revealed that the peptides were unstructured in the presence and absence of micelle (SDS and DPC). The peptides: SDS binding was found to be fast (within 1.5 ns) and sequential : first, the positively charged residues of peptides interacted with the negatively charged sulphates of micelles; Second, placement of the hydrophobic side-chain of the peptides into the hydrophobic core of SDS micelle resulting in a local deformation on the SDS surface. The backbone of the peptides was found to be more or less parallel to the micelle surface. MD simulations further revealed that the peptides with the negatively charged C-terminal end (COO^-) could not bind efficiently to the SDS micelle due to electrostatic repulsion (indicated by the loss of peptide: micelle interaction area upon $CONH_2 \rightarrow COO^-$ substitution at the C-terminal). The peptides exhibited no binding to the DPC micelle within 50 ns of MD.

MD simulations also revealed that the peptides caused significant deformation of the SDS micelles upon binding. Membrane perturbation experiments, demonstrated that both of the peptides significantly permeabilized the liposomes and helped in establishing the membranolytic mode of action of the designed peptides.

Free energy calculations demonstrated that the peptide (P4, P5, P6, and P7) binding energetics on the membrane-mimetic-systems (viz., micelle and bilayer) varies dramatically in response to side-chain mutations and the estimated differential binding free energies corroborates with the antimicrobial activity against *Pseudomonas aeruginosa* and *Escherichia coli*. P5 was the strongest binder to the micelle/bilayer and displayed the highest activity against the microbes (*P. aeruginosa* and *E.coli*). Histidine peptide (P6) has been demonstrated as a promising membranolytic pH-sensitive AMP, active against acid-resistant pathogenic bacteria (viz. *E. coli*).

2.2 Materials and Methods

2.2.1 Computational Modelling of the Synthesized Peptides

Peptides (**Figure 2.1**) with extended conformation were modelled using PyMOL software (Schrödinger, LLC, 2010), where N- and C-terminals were capped with $-NH_3^+$ and -

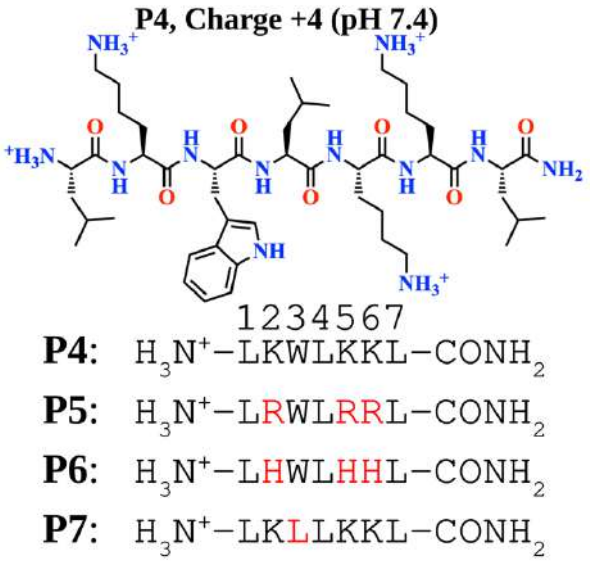

Figure 2.1: The sequence of positively charged seven residues long synthetic antimicrobial peptide(P4) and its arginine (P5), histidine (P6), and leucine (P7) analogues. At neutral pH, the charge on P6 is +1.

$CONH_2$, respectively. The extended model peptide model was then placed in a box of water (dimension = 5 × 5 × 5 nm^3) and subjected to MD simulations (Simulation details given in **Appendix I Table A2.1** and **Figure A2.1**). Negatively charged counter ions (chloride ions) were added to neutralize the simulation box. P6* was modelled by considering protonated side-chain of the histidine residues. All the free peptides in water were found to be unstructured (**Appendix I Figure A2.2**), in line with our previous CD experiments (Pandit et al., 2018). The flexibility of the peptides was more or less similar (**Appendix I Figure A2.3**).

2.2.2 Micelle/Bilayer Modelling and Peptide Binding

We have considered two simple models for mimicking the cell membranes of the bacteria: (1) SDS micelle and (2) DOPE/DOPG bilayer. SDS micelles and DOPE/DOPG bilayer models were built using CHARM-GUI Membrane Builder (Jo et al., 2008; Lee et al., 2016). Micelle model consists of 60 SDS (Sodium dodecyl sulphate, **Appendix I Figure A2.1**) molecules, close to the experimental aggregation number of SDS (Croonen et al., 1983), and a popular choice for computer simulations (Lebecque et al., 2017; MacKerell, 1995; Rakitin & Pack, 2004; Wang et al., 2010). The SDS micelle was placed at the center of a water box (7 × 7 × 7 nm^3) containing 60 Na^+ counter-ions. The bilayer model considered zwitterionic (DOPE) and negatively charged (DOPG) lipids of ratio DOPE:DOPG = 3:1 (consisting of 60/20 of DOPE:DOPG molecules, **Appendix I Figure A2.1**), which is a popular choice for computational modelling of the inner membrane of gram-negative bacteria.(Corin & Bowie, 2020; Hirano et al., 2021; Saigo et al., 2019) A 3.5 nm thick water layer has been placed on either side of the DOPE/DOPG bilayer. The solvated, charge-neutralized simulation system of the micelle/bilayer was subjected to MD simulations. The final analysed (**Appendix I Figure A2.4**) structures of the solvated micelle/bilayer from the post-equilibrated production dynamics were selected for studying

peptide:(micelle/bilayer) binding. The peptide was placed ~2 nm away from the micelle/bilayer surface (**Appendix I Figure A2.1**) and subjected to MD simulation. The peptides were found to be in the unstructured random coil conformation (final MD snapshot) in complex with micelle/bilayer as suggested by our previous experimental study (Pandit et al., 2018). Thus, the secondary structure seems to have no prominent role in membrane binding for these small seven-residue long peptides (P4, P5, P6, P7). Peptide:micelle/bilayer interaction area was estimated as the difference of solvent accessible surface area (SASA) of the peptide in the presence and absence of micelles/bilayer [(SASA of peptide + SASA of the micelle/bilayer in the absence of peptide – SASA of the peptide:micelle/bilayer complex) / 2]. Multiple independent simulations (varying the initial velocities: Trials) were performed from a minimum of 50 ns to a maximum of 500 ns (**Appendix I Table A2.1**). The final structures from the production dynamics of P4:micelle/bilayer standard molecular dynamics simulations (**Appendix I Figure A2.5**) were finally subjected to SMD-US and alchemical free energy simulations.

2.2.3 MD Simulation Parameters

Simulations were performed using GROMACS software (Abraham et al., 2015; Lindahl et al., 2001; van der Spoel et al., 2005). Standard CHARMM36 (Best et al., 2012; Huang & Mackerell, 2013; Klauda et al., 2012) force field was used to model the peptide, surfactants, and ions. CHARMM modified TIP3P (Bussi et al., 2007; Jorgensen et al., 1998) water model was used for describing the water molecules. Hydrogen atoms connected to heavy atoms were restrained using the LINCS algorithm. (Hess, 2008; Hess et al., 1997) The steepest descent algorithm minimized the simulation system (step size ~0.01 nm, steps ~50000). Post-minimized structure of the system was subjected to an equilibration (considering NVT followed NPT ensemble). The production dynamics were performed with an NPT ensemble, where the temperature and pressure were maintained at 310K and 1 bar, respectively. The temperature was maintained using Nose-Hoover (Hoover, 1985; Nosé, 1998) thermostat with a coupling constant of 1 ps. The pressure was maintained isotropically (for the SDS micelle setup) and semi-isotropically (for the DOPE/DOPG bilayer setup) using the Parrinello-Rahman (Parrinello & Rahman, 1982) barostat with a time constant of 5 ps. We used 2 fs timestep, and Particle Mesh Ewald (Darden et al., 1993) summation was used to treat the long-range electrostatics with a short-range cut-off of 1.2 nm. The van der Waals interactions were truncated at 1.2 nm. The overview of the simulation strategy is schematically given in **Appendix I Figure A2.1**.

2.2.4 Steered Molecular Dynamics and Umbrella Sampling Simulations: Absolute Binding Affinity (ΔG)

The converged final MD structure of the P4:micelle/bilayer complex (Center-of-mass distance between the peptide and micelle/bilayer is ~1.13/1.14 nm) from the conventional classical MD simulation was selected and subjected to the center of mass pulling (applying external force) or steered molecular dynamics (SMD) simulations. The timescale of peptide:micelle/bilayer dissociation is inaccessible to conventional molecular dynamics simulations. Thus, the center of mass pulling (SMD) biases the system and generates structures along the dissociation pathway. SMD is a popular method for studying protein-protein, protein-ligand, and protein-membrane dissociation pathways (Decherchi & Cavalli, 2020; Ghosh et al., 2022; Izrailev et al., 1999; Lemkul & Bevan, 2010; Patel et al., 2014) P4 was pulled away from the micelle/membrane along the z-axis using a harmonic spring (spring constant of 1000 kJ mol^{-1} nm^{-2}) at three different pulling rates (0.002, 0.001, and 0.0005 nm/ps), respectively. The final peptide and micelle/bilayer COM distance of ~5 nm was achieved for the SMD simulations of various pulling rates. The trajectories and the force profile were more or less independent of the pulling rate (**Appendix I Figure A2.6**). External force disturbs the equilibrium. Thus, estimation of equilibrium properties, viz., free energy, is tricky from non-equilibrium SMD simulations. Two popular approaches are the Jarzynski method (Jarzynski, 1997) and the weighted histogram analysis method (WHAM) (Kumar et al., 1992), respectively. Jarzynski's method estimate work from multiple independent SMD trajectory trajectories and relates the average work to the free energy. In the WHAM method, equilibrium simulations were performed on the structures generated by the SMD simulation. SMD-generated structures (between bound and unbound states) were taken as starting configurations for equilibrium umbrella sampling windows (applying a harmonic/umbrella potential of spring constant of 42 kJ mol^{-1} nm^{-2}).

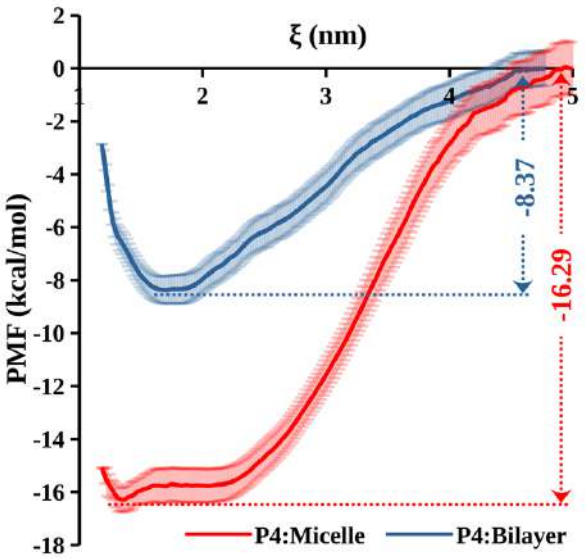

Figure 2.2: P4 dissociation from the SDS-micelle (red) and DOPE/DOPG-bilayer (blue). Potential of mean force (PMF) as a function of COM pulling coordinate "ξ". Bootstrapping errors (100 cycles) are shown as vertical transparent bars.

We have adopted the WHAM approach in this work for estimating free energy (Potential of mean force: PMF). The slow pull SMD trajectory (0.0005 nm/ps) was considered for umbrella sampling free energy estimation. PMF profile from ~30 μs umbrella sampling simulation (**Figure 2.2**) showed that the peptide binding is more favored for micelle (ΔG ~ -16 kcal/mol) relative to bilayer (ΔG ~-8 kcal/mol) bacterial mimic. Higher peptide:micelle binding affinity can be attributed to higher electrostatic interaction due to a higher surface charge on the micelle.

2.2.5 Thermodynamic Cycle, Alchemical Free Energy Simulation, and Relative Binding Affinity (ΔΔG)

An appropriate thermodynamic cycle (**Figure 2.3**) was used to estimate the relative binding free energies. Final MD structures from the standard molecular dynamics simulations (**Table A2.1**) of the free peptide(P4) and the P4:micelle/bilayer complexes were subjected to alchemical transformation (horizontal arms of **Figure 2.3**), in which the side-chain(s) of

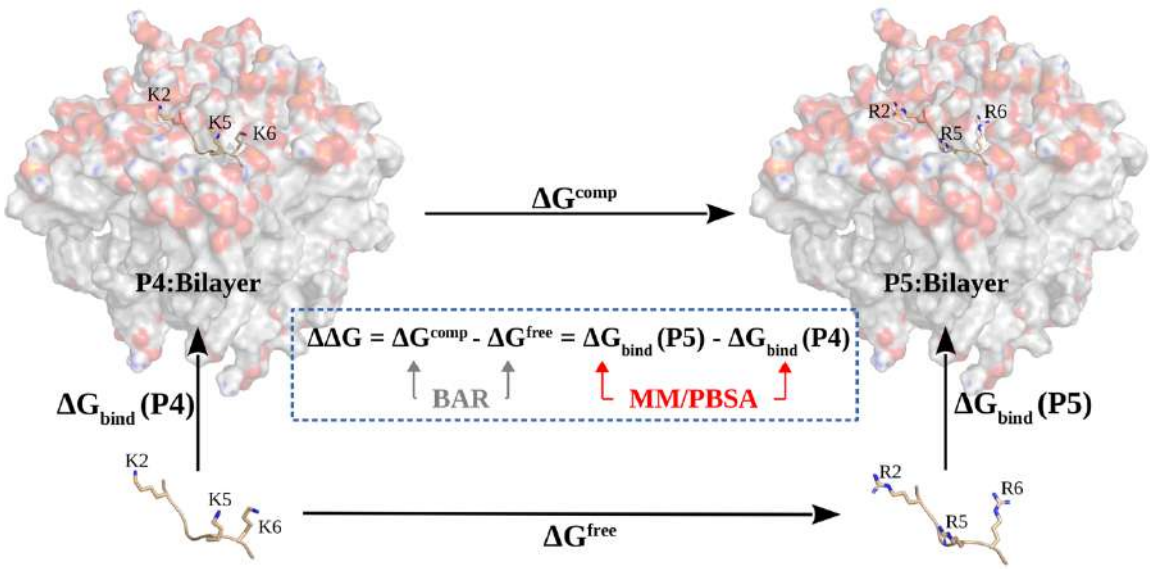

Figure 2.3: Thermodynamic cycle for peptide:bilayer (DOPE/DOPG) binding. Horizontal legs correspond to the alchemical transformation of the peptide side-chains (e.g, Lysine's into Arginine's) either in the complex with SDS-micelle (top) or free in water (bottom); vertical legs correspond to the binding. The micelle binding free energy difference between binding lysine-peptide(P4) and histidine-peptide(P6) is $\Delta\Delta G = \Delta G^{comp} - \Delta G^{free} = \Delta G_{bind}(P6) - \Delta G_{bind}(P4)$. Alchemical free energy differences (ΔG^{comp} and ΔG^{free}) are estimated through Bennett's acceptance ratio method (BAR), and absolute binding free energies (ΔG_{bind}'s) was estimated from MM/PBSA approach.

the P4 was slowly transformed and alter the identity of the peptide [Lys(P4) → Arg(P5), Lys(P4) → His^0(P6), Lys(P4) → His^+(P6*), Trp(P4) → Leu(P7)]. The free energy charge associated with the alchemical transformations (ΔG^{comp} and ΔG^{free}) was estimated using the Bennett acceptance-ratio (BAR) (Bennett, 1976) method implemented in GROMACS software. The difference between the estimated ΔG^{comp} and ΔG^{free} provides the relative

peptide binding affinity to the micelle/peptide (ΔΔG, **Figure 2.3**). For alchemical transformation, hybrid structure and topology files for the amino acids were generated using the PMX package. A coupling coordinate "λ" was defined, which modifies the identity of the amino-acid residues by altering the Hamiltonian. Varying λ from 0 to 1 transforms lysine(P4) to arginine(P5) by gradually changing the force-field parameters (simultaneously modifying the electrostatic, van der Waals, and bonded terms). λ values other than 0 or 1 represent the unphysical state (mixture of two end-states: Lysine and Arginine), thus, justifying the term alchemical-transformation. Thus, λ is a coupling coordinate that modifies the hybrid energy function (U) (where $U = \lambda U(Arg) + (1-\lambda)U(Lys)$) and connects the two end states as λ varies from 0 → 1. Twenty-one equally spaced λ values between 0 and 1 (0.00 0.05 0.10 0.15 0.20 0.25 0.30 0.35 0.40 0.45 0.50 0.55 0.60 0.65 0.70 0.75 0.80 0.85 0.90 0.95 1.00) with a soft-core potential were used for smooth alchemical transformation. MD trajectories were generated for every 21 λ windows. The estimated ΔG's from various independent trials were averaged and reported as ΔG^{comp} and ΔG^{free} (**Appendix I Table A2.3**). The first 1 ns of MD trajectory at every λ window was considered as equilibration and not considered for free energy estimation. In the case of the P4 → P6 mutation, three Cl^- ions were simultaneously mutated to a ghost particle (with or without applying harmonic restraint in the aqueous environment) to maintain charge neutrality throughout the alchemical pathway. The estimated free energy was independent of the presence or absence of restraint on Cl^- ions (**Appendix I Table A2.4**). Positive ΔΔG indicated that P4 binding to micelle/membrane was favorable relative to its analogues, except P5 (**Appendix I Table A2.4**).

2.2.6 MM/PBSA Calculation and Absolute Binding Affinity (ΔG_{bind})

In this work, we fine-tuned the dielectric constant of peptide: micelle/bilayer such that the estimated MM/PBSA binding affinity agrees with the SMD-US data (**Figure 2.2**). The adopted dielectric constant for the micelle and bilayer were ε(micelle) = 18.9 and ε(bilayer) = 18.4, respectively. Spectroscopic measurements(Chaudhuri et al., 2009) on the SDS micelle (16 mM concentration) at various salt concentrations reported a range of dielectric constants between 22 to 32. Thus, the adopted dielectric constant of ε(micelle) = 18.9 was weakly underestimated compared to the experimental apparent dielectric constant ε(micelle) = 22-32. The absolute binding affinities were estimated from the MD trajectories of the end-states of alchemical free energy simulations.

2.2.7 Sampling and Convergence of the Free Energy Simulation

Steered molecular dynamics and Umbrella Sampling: A total of 25 windows separated by spacing 0.15 nm (in COM distance) were subjected to umbrella sampling. Each window was subjected to 500 ps equilibration followed by 200 ns production dynamics at the *NPT* ensemble. A total of ~5 μs production MD trajectory was used to estimate the free energy profile (PMF). Furthermore, to ensure reliability and convergence, we triplicate the umbrella sampling simulation with different initial velocities, which makes a total of ~15 μs production umbrella sampling for every system ("P4 bound to micelle" and "P4 bound to bilayer"). A total of ~30 μs umbrella sampling simulations have been performed (**Appendix I Table A2.2**).

Alchemical simulations: Adequate sampling is the key to good quality alchemical free energy estimates (ΔG^{comp}, ΔG^{free}). Multiple independent alchemical simulations were performed that differed not only in their initial structures (final structures taken from various standard MD trials, **Appendix I Table A2.1**, **Figure A2.2 and A2.5**) but also in the sampling strategies (run-length at every λ = 5 ns or 15 ns) (**Appendix I Table A2.3**). The first 1 ns at every λ window has been removed from the free energy estimates, which was considered equilibration to adjust to the new Hamiltonian (Pohorille et al., 2010). Thus, each alchemical free energy simulation (comprised of 21 λ windows) ensured sampling of a minimum of 105 ns to 315 ns of MD. Estimated free energies from various independent alchemical trials are in excellent agreement (differ by less than 1.5 kcal/mol, **Appendix I Table A2.3**), which indicates convergence. The averaged free energy from two to three independent alchemical trials was reported as ΔG^{comp} or ΔG^{free} (**Appendix I Table A2.3**) and used for estimating relative binding affinities ($\Delta\Delta G$). A total of ~13 μs of alchemical simulations (MDFE) was performed to achieve good convergence and reasonable statistical error (<1 kcal/mol, **Appendix I Table A2.4**).

MM/PBSA simulations: 2000 frames from the last 4 ns (2 ps interval) of the MD simulation of the end states (λ = 0 and λ = 1 of alchemical transformation) were subjected to MM/PBSA binding free energy calculations. Every λ window was sampled from a minimum of 5 ns to a maximum of 15 ns (**Appendix I Table A2.3**). We have adopted a single trajectory approach for MM/PBSA free energy estimates from multiple independent simulations.

2.2.8 Material used for peptide synthesis and antimicrobial assay

Rink amide-MBHA resin, Fmoc-Leu-OH, Fmoc-Lys(Boc)-OH, Fmoc-Arg(Pbf)-OH, Fmoc-Trp(Boc)-OH, Fmoc-His(Trt)-OH, HBTU (2-(1*H*-benzotriazol-1-yl)-1,1,3,3-tetramethyluronium hexafluorophosphate, Hexafluorophosphate Benzotriazole Tetramethyl Uronium) and HOBt (Hydroxybenzotriazole) were purchased from GL Biochem Ltd., Shanghai, China. N,N-diisopropylethylamine (DIPEA) was purchased from Spectrochem Pvt. Ltd. Mumbai, India. N,N-dimethyl formamide (DMF), Trifluoroacetic acid (TFA), were purchased from Merck Life Science Pvt. Ltd., Mumbai, India. Dichloromethane (DCM) and HPLC grade acetonitrile were purchased from Finar Limited, Ahmedabad, India. Monosodium phosphate (NaH_2PO_4), Disodium phosphate (Na_2HPO_4), Nutrient broth were purchased from Himedia Laboratories Pvt. Ltd., Mumbai, India. *Pseudomonas aeruginosa* (MTCC 2488) and *Escherichia coli* (MTCC 433) were purchased from Microbial Type Culture Collection and Gene Bank (MTCC), Chandigarh, India.

2.2.9 Synthesis and characteristic of peptides

All peptides were synthesized by standard Fmoc-based solid-phase peptide synthesis (SPPS) strategy using MBHA-Rink amide resin with loading capacity of 0.7 mmol/g. For each amino-acid attachment, 3.0 equiv. of Fmoc amino acids, 3.0 equiv. of coupling reagent (PyBOP), 3.0 equiv of HOBt, and 3.3 equiv. of base (DIPEA) were used. To avoid deletion peptide formation, capping with 7:2:1 DMF, acetic anhydride, and pyridine was done post amino acid attachment. Fmoc deprotection was performed with 20% piperidine in DMF. The final peptide was cleaved from the resin using a cleavage cocktail (96% TFA, 2.5% TIS, and 1.5% H_2O) for 2h. The crude peptide was precipitated by cold diethyl ether followed by centrifugation to get the crude solid peptide.

Crude peptides were purified by reverse-phase high-performance liquid chromatography (Thermo Scientific Dionex Ultimate 3000) on a semi preparative C-18 column (Luna, 250 X 21.2 mm, 5 µm, C-18, 100 Å) using binary {CH_3CN-H_2O (5−100%)} solvent system at a flow rate of 5 mL/min using dual UV detection at 214 and 280 nm. Purity of the peptides were confirmed using a Thermo Scientific Dionex Ultimate 3000 analytical HPLC system Agilent 1260 Infinity II and a Thermo Scientific BioBasic 18 analytical column (**Appendix I Figures A2.7-2.10**). A flow rate of 1 ml/min and a linear gradient of 10 to100% CH_3CN-H_2O was used. The purified peptides were characterized by MALDI mass spectrometry on MALDI TOF instrument (Bruker Autoflex Speed) (**Appendix I Figures A2.11-2.14**).

The purified peptides were further characterized by ^{1}H-NMR spectroscopy on a Bruker Ascend Aeon 600 MHz spectrometer at 298 K in D_2O solvent (**Appendix I Figures A2.15-A2.18**). Peptide stock solution was prepared either in water, in sodium phosphate buffer (pH 7.4), or both and filter-sterilized unless stated otherwise.

2.2.10 Minimum Inhibitory Concentration (MIC) assay

Minimum inhibitory concentration (MIC90%) is defined as the concentration of an antimicrobial agent that can inhibit the growth of a microorganism by 90%. *Escherichia coli and Pseudomonas aeruginosa* were both grown in nutrient broth (NB) media. After two consecutive subcultures, 1 ml of the cells grown till mid-log phase were centrifuged at 6000 rpm for 5 minutes. The pelleted cells were then washed thrice using phosphate buffer of strength 10 mM and pH 7.4, and finally resuspended in the same buffer. The optical density of the suspended cells was measured and CFU/ml value of the cells were calculated from the optical density (OD) values. Finally, the cell suspensions were diluted to 10^5 CFU/ml. 50 µL of these cell suspensions were then added to 50 µL of the peptides at various concentrations diluted in the same phosphate buffer from a peptide stock solution of 1 mM strength in a 96-well microtiter plate. Only cells (untreated) in the buffer solution were considered as the negative control, while cells incubated with 10 µM Polymixin-B was taken to be a positive control. The cell-peptide mixtures were then incubated for 4 hours at a steady temperature of 37 °C and maintained a constant orbital shaking speed of 150 rpm. After 4 hours of incubation, 100 µL of nutrient broth media was added to each of the wells containing the cell-peptide mixture. After addition of the media, the microtiter plate was kept incubated overnight under the same conditions of temperature and rpm as described above. Finally, the OD values of the cells were measured at 600 nm and the percentage killing of the cells at various concentrations were determined in reference to the OD values of the positive and negative controls.

For P6, the process for determining the MIC90% values of the peptides at various pH values was the same as that determined at pH 7.4. For determination of the MIC90% value at any particular pH, all the processes where buffers were utilized, starting from the washing of the cells, suspensions of cells, dilution of the cells, and the preparation of the peptide stock solutions, used buffers of corresponding pH.

2.2.11 FESEM imaging

Escherichia coli and *Pseudomonas aeruginosa* grew till the mid-log phase were pelleted down and washed in a phosphate buffer solution. Cells were resuspended in the same buffer after three consecutive washes. The cells were then diluted to 105 CFU/ml and incubated with the peptides at their respective MIC values for two hours. Untreated cells were considered to be the negative control for the experiment. Post incubation, cells treated with peptides and untreated cells (negative control) were fixed with a solution of 2.5 % glutaraldehyde for one hour. Subsequently, glutaraldehyde fixed cells were centrifuged and washed with the same buffer solution twice before resuspended. 3 µL of the cells were then cast on the silicon wafers and allowed to dry overnight in the laminar hood. The dried samples were washed serially in an aqueous solution containing 30%, 50%, 70% and 90% of ethanol, respectively. Post-washing, the prepared samples were allowed to dry again. The samples were gold-coated and the FESEM images were captured using a FESEM instrument (Zeiss, Model: Gemini 300).

2.3 Results

2.3.1 Energetics of peptide selectivity

To estimate the energetics of peptide selectivity by the negatively charged bacterial membrane and elucidate the effect of peptide side-chain (Lysine verses Arginine, Lysine versus His^0(Neutral)/His^+(Charged), Tryptophan versus Leucine) in the membrane binding affinities, we performed molecular dynamics free energy (MDFE) simulations of peptide-micelle/bilayer complexes by differing the side-chain of the 7 residues long antimicrobial peptide. These calculations include computing the change in peptide binding affinity (ΔΔG) for micelle/bilayer upon peptide mutation (viz., Lys → Arg, Lys → His^0, Lys → His^+, Trp → Leu), employing an appropriate thermodynamic cycle (Estimating ΔG^{comp}, ΔG^{free}; horizontal arms of **Figure 2.3**). Moreover, absolute binding affinity (ΔG_{bind}, Vertical arms

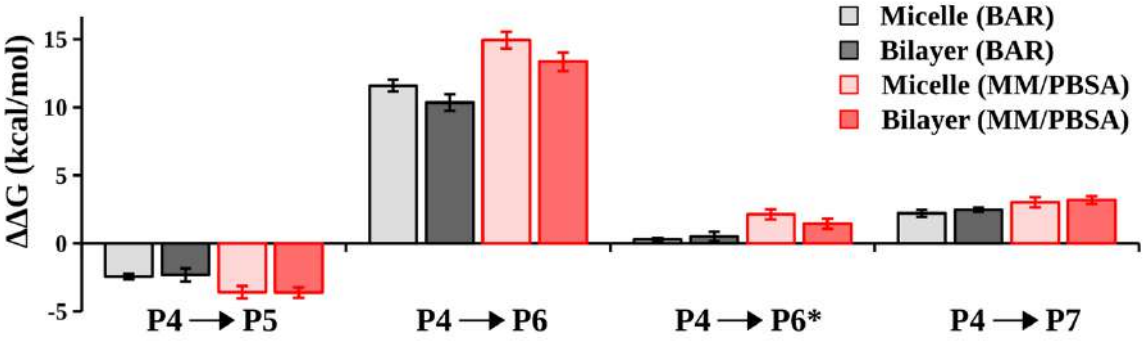

Figure 2.4: Estimated relative peptide-binding free energy (ΔΔG) to SDS-micelle (lighter shade) or DOPE/DOPG-bilayer (darker shade). BAR estimates are in grey, and MM-PBSA estimates are in red. Error bars, 1 s.e.m.

of **Figure 2.3**) has been estimated using MM/PBSA calculations and compared with the alchemical free energy estimates (grey and red bars of **Figure 2.4**).

The results (**Figure 2.4**, **Appendix I Table A2.4**) reveal that: (i) Lys → Arg mutation in the peptide increases the binding affinity for the micelle/bilayer by ~2.3 kcal/mol. (ii) Negatively charged micelle/bilayer prefers Lys-peptide relative to its His-peptide analogue. But the strength of preference strongly depends on the protonation state of the Histidine side-chain. Lys → His^0 substitution in the peptide reduces the overall positive charge on the peptide (P4 = +4 → P6 =+1), which is strongly disfavored by the micelle/bilayer, boosting the peptide discrimination by ΔΔG ~10.35 kcal/mol. On the other hand, Lys → His^+ substitution was weakly disfavored (ΔΔG ~1 kcal/mol) by the micelle/membrane. Thus, micelle/bilayer strongly discriminate peptides of different charges, which would otherwise be significantly less selective. The results indicate that the histidine-peptide (P6) might demonstrate the pH-dependent antimicrobial activity by favorable membrane-binding at acidic pH. (iii) Stability of the peptide: micelle complex is compromised upon Tryptophan(P4)→ Leucine(P7) substitution by ~2.5 kcal/mol, implying the importance of tryptophan for micelle binding. (iv) The micelle/bilayer binding affinity order of peptides

Table 2.1: MM/PBSA absolute peptide:(micelle/bilayer) binding free energy (ΔG_{bind}) and its components: ΔE_{ele} (electrostatic energy), ΔE_{vdw} (van der Waals energy), ΔG_{PB} (polar solvation) ΔG_{SA} (non-polar solvation), and $T\Delta S$ (entropy contribution). Energies are in kcal/mol and the standard error of the mean (s.e.m) is reported as error after ±.

	P4	P5	P6	P6*	P7
Peptide:Micelle binding					
ΔE_{ele}	-174.39 ± 0.40	-182.71 ± 0.42	-38.83 ± 0.29	-177.95 ± 0.47	-170.14 ± 0.49
ΔE_{vdw}	-61.75 ± 0.17	-77.03 ± 0.28	-57.05 ± 0.25	-67.58 ± 0.18	-52.17 ± 0.21
ΔG_{PB}	220.73 ± 0.42	244.22 ± 0.45	97.01 ± 0.36	232.43 ± 0.49	211.48 ± 0.53
ΔG_{SA}	-9.46 ± 0.05	-11.95 ± 0.08	-8.77 ± 0.07	-10.93 ± 0.08	-10.62 ± 0.09
$-T\Delta S$	8.56 ± 0.10	7.65 ± 0.11	6.29 ± 0.09	9.32 ± 0.09	8.11 ± 0.12
ΔG_{bind}	**-16.31± 0.09**	**-19.82 ± 0.08**	**-1.35 ± 0.12**	**-14.71 ± 0.10**	**-13.34 ± 0.08**
Peptide:Bilayer binding					
ΔE_{ele}	-72.84 ± 0.27	-90.78 ± 0.32	-8.22 ± 0.21	-83.54 ± 0.28	-68.87 ± 0.26
ΔE_{vdw}	-65.01 ± 0.11	-84.11 ± 0.13	-59.25 ± 0.16	-72.47 ± 0.15	-59.46 ± 0.18
ΔG_{PB}	133.91 ± 0.31	171.74 ± 0.39	77.59 ± 0.24	153.42 ± 0.30	127.27 ± 0.37
ΔG_{SA}	-10.59 ± 0.04	-13.43 ± 0.08	-9.21 ± 0.05	-11.38 ± 0.07	-11.03 ± 0.08
$-T\Delta S$	6.12 ± 0.09	4.89 ± 0.08	4.81 ± 0.08	7.01 ± 0.09	6.87 ± 0.08
ΔG_{bind}	**-8.41 ± 0.07**	**-11.69 ± 0.08**	**5.72 ± 0.09**	**-6.96 ± 0.07**	**-5.22 ± 0.09**

were found to be P5 > P4 > P6* > P7 >> P6. (v) Estimated energetics of peptide selectivity are identical for micelle and bilayer models (light-grey and dark-grey bars of **Figure 2.4**). However, as expected, the latter is computationally more expensive and requires larger sampling for convergence (see Methods). The estimated strength of peptide discrimination by micelle/bilayer (ΔΔG, grey bars of **Figure 2.4**) is a robust feature of these calculations. The results are almost insensitive to the initial structural model (peptide: micelle or peptide-bilayer complexes), the choice of method for free energy estimation (alchemical free-energy simulation or MM/PBSA), and multiple independent replicas of various sampling strategies (**Appendix I Table A2.1** and **Figure A2.5**).

Peptide binding to the bilayer is penalized primarily by desolvation ($\Delta G_{pb,}$ polar term) as well as entropy ($T\Delta S$), but offsets by the favorable peptide:bilayer interaction (ΔE_{ele} and ΔE_{vdw}; former being the major component) (**Table 2.1**). Favorable non-polar free energy component associated with the desolvation (ΔG_{SA}) of the peptide:bilayer binding is small (between -6 kcal/mol to -9 kcal/mol) and similar for various peptides (P4, P5, P6, P6*, P7). MD simulation confirmed that the peptides adopted a random coil structure in the presence or absence of micelle/bilayer as observed in our previous CD experiments.(Pandit et al., 2018) MD structures of the equilibrated peptide:bilayer complexes (**Figure 2.5a-d**) showed

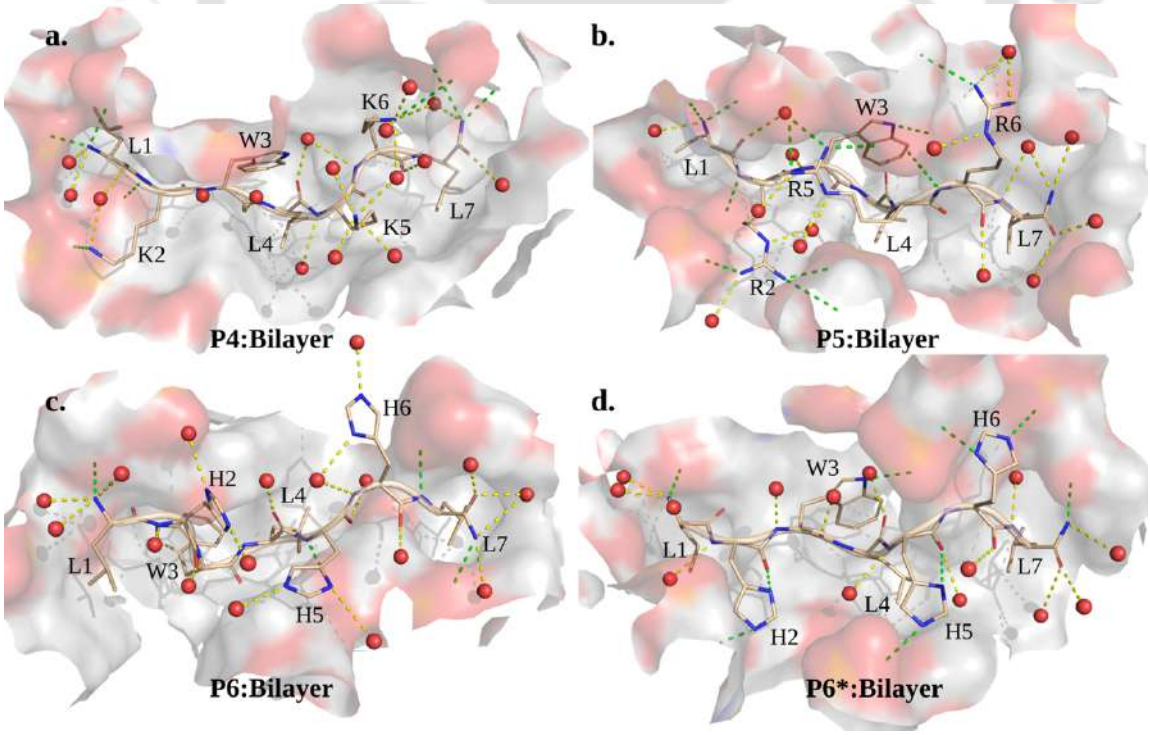

Figure 2.5: Representative MD structures. (a-d) P4, P5, P6 (Charge = +1, neutral histidine), and P6* (Charge=+4, protonated histidine) are bound to the DOPE/DOPG Bilayer. Bilayer in surface representation (red and grey) and peptides in the cartoon (wheat). Key residues (sticks; red: oxygen, blue: nitrogen) and interaction networks (dashed line: green represents direct interaction, yellow represents interaction with water) are highlighted. Water in the red-sphere. Hydrogens are not shown for clarity.

Table 2.2: Peptide:bilayer interaction area, number of interactions, and number of water molecules around the peptide for various peptide:bilayer complexes. Standard deviation is given as error.

	P4	P5	P6	P6*	P7
Interaction Area (Å^2)	762 ± 53	825 ± 46	706 ± 54	792 ± 49	749 ± 49
Number of Peptide (NH)…DOPE/DOPG(O) interaction (<3.5 Å)	7.2 ± 1.6	13.3 ± 1.8	4.1 ± 1.1	6.3 ± 1.3	5.9 ± 1.2
Water molecules within 3.5 Å of the peptide	15.7 ± 1.4	13.8 ± 2.1	17.9 ± 3.6	14.4 ±1.7	19.1 ± 2.1

that the complexes were stabilized by (a) direct and water-mediated interactions involving the positively charged tips of the peptide and the negatively charged surface of the bilayer and (b) placing the hydrophobic side-chains into the hydrophobic core of the micelle. Arginine peptide (P5) in complex with bilayer interacted with the highest number of phosphates and attracted the lowest number of water molecules (**Figure 2.5b, Table 2.2**). Extensive H-bonding interactions between the cationic guanidinium moiety (five H-bond donors) of arginine (of P5) and phosphate of SDS offset the unfavorable desolvation and entropic term, thereby facilitating P5 binding with the highest affinity (**Figure 2.5**, **Table 2.1**).

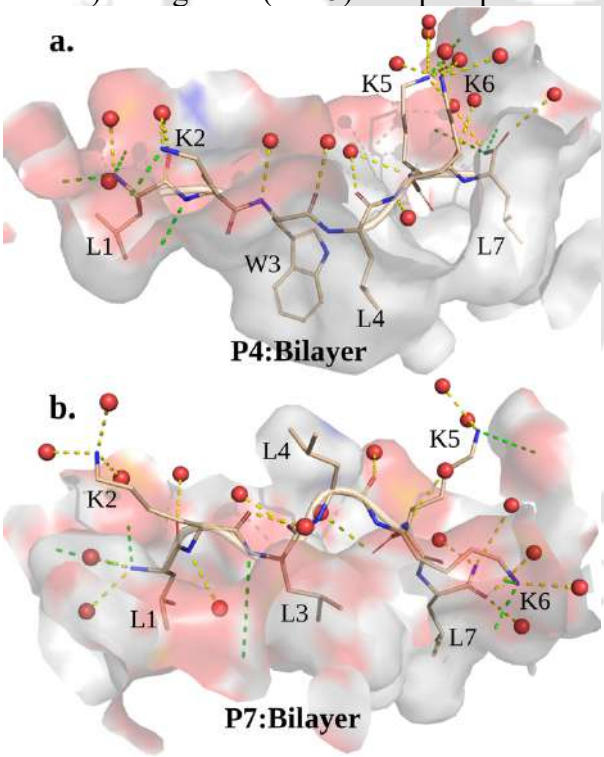

Figure 2.6: Representative MD structures. P4 (a) and P7 (b) are bound to the DOPE/DOPG Bilayer. Bilayer in surface representation (red and grey) and peptides in the cartoon (wheat). Key residues (sticks; red: oxygen, blue: nitrogen) and interaction networks (dashed line: green represents direct interaction, yellow represents interaction with water) are highlighted. Water in the red-sphere. Hydrogens are not shown for clarity.

Binding affinity is compromised in the case of P4 relative to P5 because the charge in the lysine is more localized, and the number of H-bond donors is reduced to two. Peptide containing neutral histidine (P6, Charge =+1) was severely disfavored for micelle binding relative to the charged histidine-analog (P6*, Charge =+4), highlighting the importance of peptide charge for binding (**Figure 2.5c**) as suggested previously for similar peptides (Ghosh et al., 2021; Pandit et al., 2020, 2021). Thus, the reduction of positive charge on the peptide amplifies the

discriminatory strength of the bilayer. MD simulations further reveal that the side-chains of tryptophan and leucine (W3, L4 of the peptides P4, P5, P6, P6*) are on the same side and embedded in the hydrophobic interior of the bilayer (**Figure 2.6, 2.5a-d**). Still, the relative orientation of the third and fourth residues (L3, L4 of peptide P7) was altered by exposing L4 to water upon W3/L3 substitution (**Figure 2.6b**). The same observation was also confirmed from peptide:micelle complexes (**Appendix I Figure A2.19**). A noticeable compromise of the van der Waals interaction was also evident for P7 (**Table 2.1**). Thus, the compromise of the hydrophobic interaction upon W3/L3 substitution is likely the key factor for disfavoring Leu-peptide (P7) binding to the micelle relative to its tryptophan-analogue (P4).

2.3.2 Antimicrobial activity of P4, P5, P6, and P7 at pH 7.4

Out of four peptides, three peptides P4, P5, and P7 showed activity against *P. aeruginosa* (**Figure 2.7a**) at pH 7.4 with a $MIC_{90\%}$ value of 30 μM, 20 μM, and 200 μM respectively. Thus, the strength of antimicrobial activity (**Figure 2.7**) follows the order P5 > P4 > P7, which corroborates with the calculated relative binding free energies (ΔΔG of **Figure 2.4**). P6 did not show activity at pH 7.4 against *P. aeruginosa*. Membranolytic mode of action of the active peptides (P5, P4, P7) against *P. aeruginosa* was confirmed from FESEM study (**Figures 2.7b-f**). The size, shape, and surface morphology of the *P. aeruginosa* cells were found to be similar between the control (**Figure 2.7b**) and in the presence of P6 peptide (**Figure 2.7e**), thus, corroborating the observed inactivity of the P6 peptide (**Figure 2.7a**). Computed energetics suggested that the micelle/bilayer binding affinity is significantly favored for the protonated-histidine-analogue (P6*) relative to its neutral-histidine-peptide (P6). Thus, the peptide (P6*) might be a promising AMP against acid-resistance (AR) pathogenic bacteria. *Escherichia coli* is known to withstand a strongly acidic environment of pH 2.5 or less.(Castanie-Cornet et al., 1999) Antimicrobial assays at pH 7.4 against *E. coli* confirmed the highest activity for P5 (MIC 20 μM), the very-weak activity of P6 (MIC 150 μM), and no activity for P7 (**Figure 2.8**).

2.3.3 The pH-sensitivity of histidine-containing peptide P6 against *Escherichia coli*

The net charge of P6 seems to correlate with its antimicrobial activity. The net charge (Z) on the peptides at various pH was estimated by the following equation

$$Z = \sum_i N_i \frac{10^{pKa_i}}{10^{pH}+10^{pKa_i}} - \sum_j N_j \frac{10^{pH}}{10^{pH}+10^{pKa_j}} \quad (2.1)$$

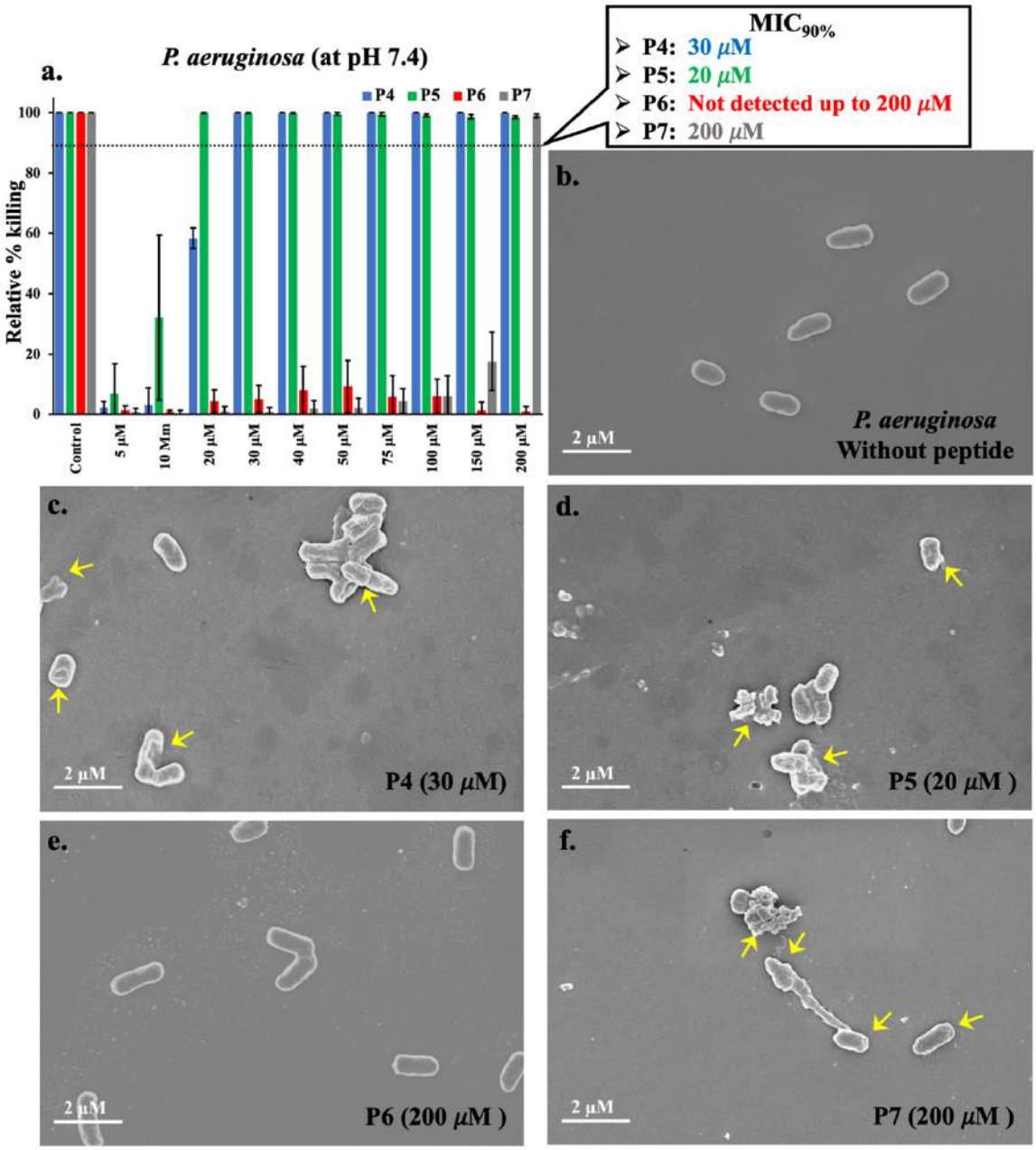

Figure 2.7: (a) Antimicrobial activity of P4 (blue), P5 (green), P6 (red), and P7 (grey) against *P. aeruginosa* at physiological pH 7.4. $MIC_{90\%}$ was calculated from Microbroth Dilution Assay (values given within the box). The control experiment was performed in presence of 100 μM polymixin B at pH 7.4 and other readings were normalized against the same. P5 is found to be the most potent peptide, and P6 was found to be inactive against *P. aeruginosa.* Field emission scanning electron microscopy (FESEM) images of *P. aeruginosa* (b) Control/without-peptide (c) 1 × MIC P4 (d) 1× MIC P5 (e) 200 μM P6 (f) 1× MIC P7. Active peptides (P4, P5, P7) are found to be membranolytic. Cell morphology in the control is preserved in the presence of P6.

Where $N_{(ij)}$, $pK_{a_{(i,j)}}$ are the numbers and pK_a of the (basic, acidic) amino acid residues present in the peptide. The titratable residues under investigation (**Figure 2.1**) were the amine group (NH_3^+) at the N-terminal of leucine (pK_a 9.60), the side chains of lysine (pK_a 10.53)/ arginine (pK_a 12.48)/ histidine (pK_a 6.0) and tyrosine (pK_a 10.07) (Lehninger et al., 1993) (**Appendix I Figure A2.20**). The result indicated that the overall charge on the

peptide P6 is ~ +1 at pH 7.4 and attains +4 charge only at acidic pH 4.0 and below. P6 displayed poor antimicrobial activity against *E. Coli* at pH 7.4 (MIC = 150 μM, **Figure**

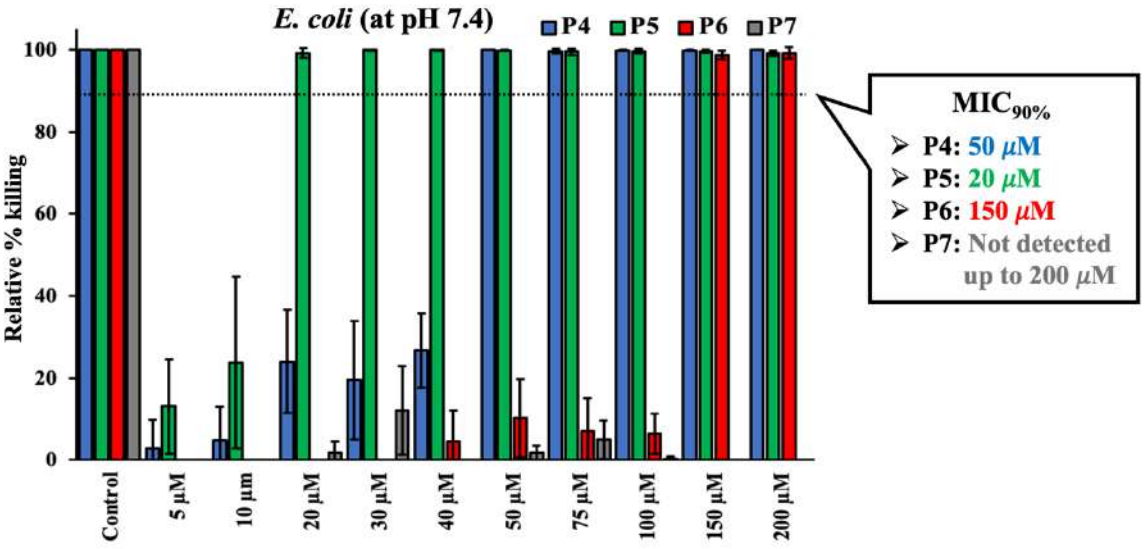

Figure 2.8: Antimicrobial activity of P4 (blue), P5 (green), P6 (red), and P7 (grey) against *E. coli* at physiological pH 7.4. $MIC_{90\%}$ (values given within the box) was calculated from Microbroth Dilution Assay. The control experiment was performed in presence of 100 µM polymixin B at pH 7.4 and other readings were normalized against the same. Antimicrobial activity against *E. coli* at pH 7.4: P5 most-potent, P6 poor-activity, P7 inactive.

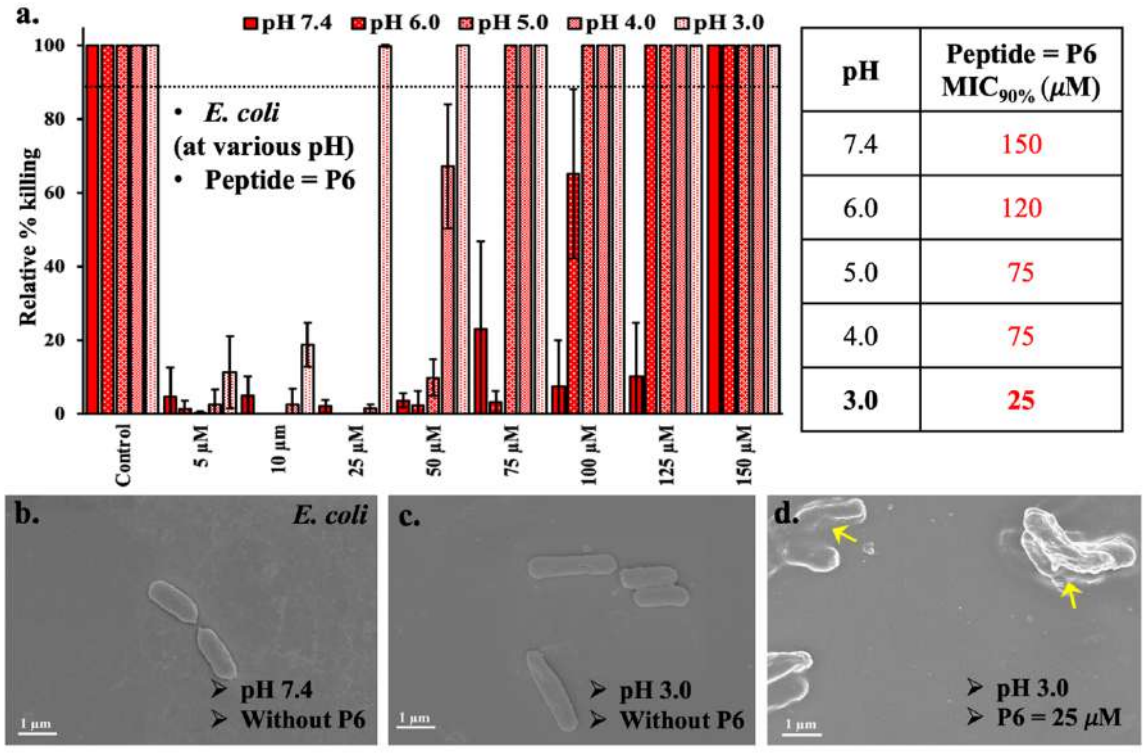

pH	Peptide = P6 $MIC_{90\%}$ (μM)
7.4	150
6.0	120
5.0	75
4.0	75
3.0	25

Figure 2.9: (a) Antimicrobial activity of P6 at various pH (7.4, 6, 5, 4, 3) against *E. coli*. $MIC_{90\%}$ (values given within the box) was calculated from Microbroth Dilution Assay. The activity enhanced upon lowering of pH. The control experiment was performed in presence of 100 µM polymixin B at various pH and other readings were normalized against the same. Field emission scanning electron microscopy (FESEM) images of *E. coli* at (b) pH 7.4 and without P6, (c) pH 3.0 and without peptide, and (d) pH 3.0 at 1× MIC P6. In the absence of P6, the cells morphology is intact at pH 7.4 and 3. P6 is a membranolytic pH-sensitive AMP, active at lower pH.

2.8). However, the antimicrobial activity of P6 was found to be improved upon lowering the pH, notable at pH 3.0 (MIC = 25 μM, **Figure 2.9**). Thus, a gain in the net positive charge on P6 correlated well with the favorable binding affinities (**Figure 2.4**) as well as with the increase in the antimicrobial activity (**Figure 2.9**). The optical density value of the *E. coli* cells of the control experiments (**Figure 2.9a**) was more or less insensitive to the pH (OD range: 0.44 - 0.50 in the pH range: 7.4-3.0), suggesting that the growth of *E. Coli* was independent of pH. Moreover, in the absence of peptides, the morphology of the *E. coli* cells at pH 7.4 (**Figure 2.9b**) and pH 3.0 (**Figure 2.9c**) were similar, corroborating the pH insensitivity of *E. coli* cell growth. P6 was found to possess a membranolytic mode of action against *E. Coli* at pH 3.0 (**Figure 2.9b-d**).

2.4 Discussion

Free energy simulations showed that the estimated absolute peptide binding affinity on the membrane-mimetic-system strongly depends on the model of the membrane, i.e., micelle or bilayer (**Figure 2.2** and **Table 2.1**). However, the relative peptide binding free energies are more or less independent of the nature of the membrane-mimic (**Figure 2.4**). The results (**Figure 2.4**) quantitatively showed that Lys(P4) → Arg(P5) side-chain mutations favor micelle/bilayer binding by increasing peptide:micelle contact (**Figures 2.5a,b** and **Tables 2.1, 2.2**). Poly-Arg entry to the cells was much more efficient than its Lys, ornithine, or histidine analogue.(Mitchell et al., 2000) Moreover, cell-penetrating peptides (CPP, e.g., penetratin19)(Åmand et al., 2008) containing Arg showed higher translocation efficiency relative to its Lys analogue.(Bitler & Schroeder, 2010; Chandra et al., 2011; Ezzat et al., 2010; Frigyes et al., 2001; Kneeland et al., 1993; Li et al., 2013; Mandell et al., 2007; Sakai et al., 2005; Sakai & Matile, 2003; Vondrášek et al., 2009) A diverse family of antimicrobial mammalian peptides (α-defensin) contains high Arg:Lys (9:1) mole-ratio, which are essential for immunity against bacteria.(Llenado et al., 2009; Zou et al., 2007) Thus, the higher estimated binding affinity of Arg-peptide (P5) relative to Lys-peptide (P4) justifies the higher potency of the former and the need for higher arginine content in the α-defensins, even though Arg is relatively less abundant than Lys in various kingdom of life (Archaea, bacteria, and eukaryotes.(Gilis et al., 2001) Substitution of Lys (P4, Charge = +4) with neutral-histidine (P6, Charge = +1) severely compromises the electrostatic interactions (**Table 2.1**), thus, strongly disfavored P6 binding to membrane-mimic (**Figure 2.4**). Antimicrobial assays (**Figures 2.7a, 2.8**) at physiological pH 7.4 confirmed that P4 and P5 are active (the latter being the most potent). In contrast, activity P6 is severely

compromised, corroborating the hypothesis from estimated binding affinities. Moreover, protonated-histidine-analogue (P6*) was very weakly (ΔΔG ~1 kcal/mol) discriminated by the membrane-mimic relative to P4, suggesting favorable binding for P6*. The increased intermolecular interaction network observed in the MD structures of the P6*:bilayer complex (**Figure 2.7d**) relative to P6:bilayer complex (**Figure 2.7c**) could explain the favourable bilayer binding for the P6*. Thus, P6 might show antimicrobial activity in a highly acidic environment. Investigation of the pH-dependent antimicrobial activity of P6 against *E. coli* indeed demonstrated striking improvement in the activity at lower pH values (**Figure 2.9a**). At pH 3.0, MIC90% was found to be 25 μM, comparable to the activity of the most potent P5 peptide at pH 7.4 (MIC90% = 20 μM). Previous studies reported pH sensitivity for larger histidine-rich peptides(Kacprzyk et al., 2007; Mason et al., 2006; Vogt & Bechinger, 1999) and short (5-11 residues long) Trp-Arg-rich peptides (synthetic or based on bovine and murine lactoferricin) (Bacalum et al., 2017; Huan et al., 2020; Strøm et al., 2002) as potent antibacterial agents. A short seven-residue histidine-peptide (P6) seems to be a promising antimicrobial pH-sensitive membranolytic (**Figure 2.9d**) antimicrobial agent. Single tryptophan (P4) substitution by leucine (P7) disfavored micelle/bilayer binding (**Figure 2.4**), which was in line with the observed reduced activity of P7 peptides in the assays (**Figures 2.7** and **2.8**).

Our study showed that short Arginine-peptide (P5) is the most potent AMP, whereas its histidine-analogue (P6) is pH sensitive, only active at the strong acidic environment. Thus, the Arginine-Histidine class of AMPs might be a promising potent antimicrobial agent against acid-resistant bacteria and provoke experimental verification. Moreover, the estimated energetics of the peptide binding to the simple membrane-mimic models was shown to have a direct correlation with the activity of the peptides.

2.5 Conclusion

We report seven residue-long arginine-peptides P5 as the most potent peptide (among P4, P5, P6, P7) at physiological pH 7.4 (MIC90% = 20 μM) against Gram-negative bacteria *P. aeruginosa* and *E. Coli* respectively. The histidine-peptide P6 manifested pH-sensitive activity against *E. Coli* (active in the acidic environment, $MIC_{90\%}$ at pH 3.0 = 25 μM). The peptides displayed a membranolytic mode of action. We established a direct link between the calculated energetics (peptide binding to simple membrane mimic models), atomic structure, and antimicrobial activity. The study illustrated how side-chain substitution

(Lys→Arg, Lys → Leu, Lys → His) and pH alter the hydrophobic-hydrophilic balance of the peptide: membrane complex and fine-tune the activity. P6 peptide is a promising template for designing future antimicrobial agents against acid-resistant bacteria.

2.6 Supporting Information

This chapter contains Supporting Information given in **Appendix I**.

REFERENCES

Abraham, M. J., Murtola, T., Schulz, R., Páll, S., Smith, J. C., Hess, B., & Lindah, E. (2015). Gromacs: High performance molecular simulations through multi-level parallelism from laptops to supercomputers. *SoftwareX*, *1–2*, 19–25. https://doi.org/10.1016/j.softx.2015.06.001

Åmand, H. L., Fant, K., Nordén, B., & Esbjörner, E. K. (2008). Stimulated endocytosis in penetratin uptake: effect of arginine and lysine. *Biochemical and Biophysical Research Communications*, *371*(4), 621–625. https://doi.org/10.1016/J.BBRC.2008.04.039

Aronica, P. G. A., Reid, L. M., Desai, N., Li, J., Fox, S. J., Yadahalli, S., Essex, J. W., & Verma, C. S. (2021). Computational Methods and Tools in Antimicrobial Peptide Research. *Journal of Chemical Information and Modeling*, *61*(7), 3172–3196. https://doi.org/10.1021/ACS.JCIM.1C00175/ASSET/IMAGES/LARGE/CI1C00175_0005.JPEG

Bacalum, M., Janosi, L., Zorila, F., Tepes, A. M., Ionescu, C., Bogdan, E., Hadade, N., Craciun, L., Grosu, I., Turcu, I., & Radu, M. (2017). Modulating short tryptophan- and arginine-rich peptides activity by substitution with histidine. *Biochimica et Biophysica Acta. General Subjects*, *1861*(7), 1844–1854. https://doi.org/10.1016/J.BBAGEN.2017.03.024

Bals, R., Wang, X., Wu, Z., Freeman, T., Bafna, V., Zasloff, M., & Wilson, J. M. (1998). Human β-defensin 2 is a salt-sensitive peptide antibiotic expressed in human lung. *Journal of Clinical Investigation*, *102*(5), 874–880. https://doi.org/10.1172/JCI2410

Bennett, C. H. (1976). Efficient estimation of free energy differences from Monte Carlo data. *Journal of Computational Physics*, *22*(2), 245–268. https://doi.org/10.1016/0021-9991(76)90078-4

Best, R. B., Zhu, X., Shim, J., Lopes, P. E. M., Mittal, J., Feig, M., & MacKerell, A. D. (2012). Optimization of the additive CHARMM all-atom protein force field targeting improved sampling of the backbone φ, ψ and side-chain χ1 and χ2 Dihedral Angles. *Journal of Chemical Theory and Computation*, *8*(9), 3257–3273. https://doi.org/10.1021/CT300400X/SUPPL_FILE/CT300400X_SI_001.PDF

Bitler, B., & Schroeder, J. (2010). Anti-cancer therapies that utilize cell penetrating peptides. *Recent Patents on Anti-Cancer Drug Discovery*, *5*(2), 99–108. https://doi.org/10.2174/157489210790936252

Bussi, G., Donadio, D., & Parrinello, M. (2007). Canonical sampling through velocity rescaling. *The Journal of Chemical Physics*, *126*(1), 014101. https://doi.org/10.1063/1.2408420

Castanie-Cornet, M. P., Penfound, T. A., Smith, D., Elliott, J. F., & Foster, J. W. (1999). Control of acid resistance in Escherichia coli. *Journal of Bacteriology*, *181*(11), 3525–3535. https://doi.org/10.1128/JB.181.11.3525-3535.1999

Chandra, S., Barola, N., & Bahadur, D. (2011). Impedimetric biosensor for early detection of cervical cancer. *Chemical Communications*, *47*(40), 11258–11260. https://doi.org/10.1039/C1CC14547A

Chaudhuri, A., Haldar, S., & Chattopadhyay, A. (2009). Organization and dynamics in micellar structural transition monitored by pyrene fluorescence. *Biochemical and Biophysical Research Communications*, *390*(3), 728–732. https://doi.org/10.1016/J.BBRC.2009.10.037

Corin, K., & Bowie, J. U. (2020). How bilayer properties influence membrane protein folding. *Protein Science*, *29*(12), 2348–2362. https://doi.org/10.1002/PRO.3973

Croonen, Y., Geladé, E., van der Zegel, M., van der Auweraer, M., Vandendriessche, H., de Schryver, F. C., & Kuleuven, M. A. (1983). Influence of Salt, Detergent Concentration, and Temperature on the Fluorescence Quenching of 1-Methylpyrene In Sodium Dodecyl Sulfate with m-Dlcyanobenzene. *J. Phys. Chem*, *87*, 1426–1431.

Darden, T., York, D., & Pedersen, L. (1993). Particle mesh Ewald: An N·log(N) method for Ewald sums in large systems. *The Journal of Chemical Physics*, *98*(12), 10089–10092. https://doi.org/10.1063/1.464397

Decherchi, S., & Cavalli, A. (2020). Thermodynamics and Kinetics of Drug-Target Binding by Molecular Simulation. *Chemical Reviews*, *120*(23), 12788–12833. https://doi.org/10.1021/ACS.CHEMREV.0C00534/ASSET/IMAGES/LARGE/CR0C00534_0020.JPEG

Ezzat, K., Andaloussi, S., Abdo, R., & Langel, U. (2010). Peptide-based matrices as drug delivery vehicles. *Current Pharmaceutical Design*, *16*(9), 1167–1178. https://doi.org/10.2174/138161210790963832

Frigyes, D., Alber, F., Pongor, S., & Carloni, P. (2001). Arginine-phosphate salt bridges in protein-DNA complexes: A Car-Parrinello study. *Journal of Molecular Structure: THEOCHEM*, *574*(1–3), 39–45. https://doi.org/10.1016/S0166-1280(01)00368-2

Ghosh, S., Chatterjee, S., & Satpati, P. (2022). Effect of Monovalent Salt on the Energetics of Antimicrobial-Peptide: Micelle Dissociation. *Physical Chemistry Chemical Physics*. https://doi.org/10.1039/D2CP02735F

Ghosh, S., Pandit, G., Debnath, S., Chatterjee, S., & Satpati, P. (2021). Effect of monovalent salt concentration and peptide secondary structure in peptide-micelle binding. *RSC Advances*, *11*(58), 36836–36849. https://doi.org/10.1039/d1ra06772a

Gilis, D., Massar, S., Cerf, N. J., & Rooman, M. (2001). Optimality of the genetic code with respect to protein stability and amino-acid frequencies. *Genome Biology 2001 2:11*, *2*(11), 1–12. https://doi.org/10.1186/GB-2001-2-11-RESEARCH0049

Hans, D., Young, P., & Fairlie, D. (2012). Current Status Of Short Synthetic Peptides As Vaccines. *Medicinal Chemistry*, *2*(6), 627–646. https://doi.org/10.2174/1573406410602060627

Hess, B. (2008). P-LINCS: A parallel linear constraint solver for molecular simulation. *Journal of Chemical Theory and Computation*, *4*(1), 116–122. https://doi.org/10.1021/ct700200b

Hess, B., Bekker, H., Berendsen, H. J. C., & Fraaije, J. G. E. M. (1997). LINCS: A linear constraint solver for molecular simulations. *Journal of Computational Chemistry*. https://doi.org/10.1002/(SICI)1096-987X(199709)18:12<1463::AID-JCC4>3.0.CO;2-H

Hirano, M., Saito, C., Yokoo, H., Goto, C., Kawano, R., Misawa, T., & Demizu, Y. (2021). Development of Antimicrobial Stapled Peptides Based on Magainin 2 Sequence. *Molecules 2021, Vol. 26, Page 444*, *26*(2), 444. https://doi.org/10.3390/MOLECULES26020444

Hoover, W. G. (1985). Canonical dynamics: Equilibrium phase-space distributions. *Physical Review A*, *31*(3), 1695. https://doi.org/10.1103/PhysRevA.31.1695

Huan, Y., Kong, Q., Mou, H., & Yi, H. (2020). Antimicrobial Peptides: Classification, Design, Application and Research Progress in Multiple Fields. *Frontiers in Microbiology*, *11*, 2559. https://doi.org/10.3389/FMICB.2020.582779/BIBTEX

Huang, J., & Mackerell, A. D. (2013). CHARMM36 all-atom additive protein force field: Validation based on comparison to NMR data. *Journal of Computational Chemistry*. https://doi.org/10.1002/jcc.23354

Izrailev, S., Stepaniants, S., Isralewitz, B., Kosztin, D., Lu, H., Molnar, F., Wriggers, W., & Schulten, K. (1999). *Steered Molecular Dynamics*. Springer, Berlin, Heidelberg. https://doi.org/10.1007/978-3-642-58360-5_2

Jarzynski, C. (1997). Nonequilibrium equality for free energy differences. *Physical Review Letters*, *78*(14), 2690–2693. https://doi.org/10.1103/PhysRevLett.78.2690

Jo, S., Kim, T., Iyer, V. G., & Im, W. (2008). CHARMM-GUI: a web-based graphical user interface for CHARMM. *Journal of Computational Chemistry*, *29*(11), 1859–1865. https://doi.org/10.1002/jcc.20945

Jorgensen, W. L., Chandrasekhar, J., Madura, J. D., Impey, R. W., & Klein, M. L. (1998). Comparison of simple potential functions for simulating liquid water. *The Journal of Chemical Physics*, *79*(2), 926. https://doi.org/10.1063/1.445869

Kacprzyk, L., Rydengård, V., Mörgelin, M., Davoudi, M., Pasupuleti, M., Malmsten, M., & Schmidtchen, A. (2007). Antimicrobial activity of histidine-rich peptides is dependent on acidic conditions. *Biochimica et Biophysica Acta*, *1768*(11), 2667–2680. https://doi.org/10.1016/J.BBAMEM.2007.06.020

Klauda, J. B., Monje, V., Kim, T., & Im, W. (2012). Improving the CHARMM Force Field for Polyunsaturated Fatty Acid Chains. *The Journal of Physical Chemistry B*, *116*(31), 9424–9431. https://doi.org/10.1021/jp304056p

Kneeland, D. M., Ariga, K., Lynch, V. M., Huang, C. Y., & Anslyn, E. v. (1993). Bis(alkylguanidinium) Receptors for Phosphodiesters: Effect of Counterions, Solvent Mixtures, and Cavity Flexibility on Complexation. *Journal of the American Chemical Society*, *115*(22), 10042–10055. https://doi.org/10.1021/JA00075A021/SUPPL_FILE/JA10042B.PDF

Kumar, S., Rosenberg, J. M., Bouzida, D., Swendsen, R. H., & Kollman, P. A. (1992). The weighted histogram analysis method for free-energy calculations on biomolecules. I. *Journal of Computational Chemistry*, *13*(8), 1011–1021. https://doi.org/10.1002/JCC.540130812

Lebecque, S., Crowet, J. M., Nasir, M. N., Deleu, M., & Lins, L. (2017). Molecular dynamics study of micelles properties according to their size. *Journal of Molecular Graphics and Modelling*, *72*, 6–15. https://doi.org/10.1016/j.jmgm.2016.12.007

Lee, J., Cheng, X., Swails, J. M., Yeom, M. S., Eastman, P. K., Lemkul, J. A., Wei, S., Buckner, J., Jeong, J. C., Qi, Y., Jo, S., Pande, V. S., Case, D. A., Brooks, C. L., MacKerell, A. D., Klauda, J. B., & Im, W. (2016). CHARMM-GUI Input Generator for NAMD, GROMACS, AMBER, OpenMM, and CHARMM/OpenMM Simulations Using the CHARMM36 Additive Force Field. *Journal of Chemical Theory and Computation*, *12*(1), 405–413. https://doi.org/10.1021/acs.jctc.5b00935

Lehninger, A. L., Nelson, D. L., & Cox, M. M. (1993). Principles of biochemistry 2nd ed. (Lehninger, Albert L.; Nelson, David L.; Cox, Michael M.). *Journal of Chemical Education*, *70*(8), A223. https://doi.org/10.1021/ED070PA223.1

Lemkul, J. A., & Bevan, D. R. (2010). Assessing the stability of Alzheimer's amyloid protofibrils using molecular dynamics. *The Journal of Physical Chemistry. B*, *114*(4), 1652–1660. https://doi.org/10.1021/JP9110794

Li, L., Vorobyov, I., & Allen, T. W. (2013). The different interactions of lysine and arginine side chains with lipid membranes. *Journal of Physical Chemistry B*, *117*(40), 11906–11920. https://doi.org/10.1021/JP405418Y/SUPPL_FILE/JP405418Y_SI_001.PDF

Lindahl, E., Hess, B., & van der Spoel, D. (2001). GROMACS 3.0: a package for molecular simulation and trajectory analysis. *Journal of Molecular Modeling*, *7*(8), 306–317. https://doi.org/10.1007/s008940100045

Llenado, R. A., Weeks, C. S., Cocco, M. J., & Ouellette, A. J. (2009). Electropositive charge in α-defensin bactericidal activity: Functional effects of Lys-for-Arg substitutions vary with the peptide primary structure. *Infection and Immunity*, *77*(11), 5035–5043. https://doi.org/10.1128/IAI.00695-09/SUPPL_FILE/SUPP_IAI_00695_09_082009.PDF

MacKerell, A. D. (1995). Molecular dynamics simulation analysis of a sodium dodecyl sulfate micelle in aqueous solution: Decreased fluidity of the micelle hydrocarbon interior. *Journal of Physical Chemistry*, *99*(7), 1846–1855. https://doi.org/10.1021/j100007a011

Mandell, D. J., Chorny, I., Groban, E. S., Wong, S. E., Levine, E., Rapp, C. S., & Jacobson, M. P. (2007). Strengths of hydrogen bonds involving phosphorylated amino acid side chains. *Journal of the American Chemical Society*, *129*(4), 820–827. https://doi.org/10.1021/JA063019W/SUPPL_FILE/JA063019WSI20061124_081951.PDF

Mason, A. J., Gasnier, C., Kichler, A., Prévost, G., Aunis, D., Metz-Boutigue, M. H., & Bechinger, B. (2006). Enhanced membrane disruption and antibiotic action against pathogenic bacteria by designed histidine-rich peptides at acidic pH. *Antimicrobial Agents and Chemotherapy*, *50*(10), 3305–3311. https://doi.org/10.1128/AAC.00490-06/ASSET/2C40FC6A-F2D8-4D9D-B37F-9901C43510D0/ASSETS/GRAPHIC/ZAC0100660470003.JPEG

Mitchell, D. J., Steinman, L., Kim, D. T., Fathman, C. G., & Rothbard, J. B. (2000). Polyarginine enters cells more efficiently than other polycationic homopolymers. *The Journal of Peptide Research : Official Journal of the American Peptide Society*, *56*(5), 318–325. https://doi.org/10.1034/J.1399-3011.2000.00723.X

Nosé, S. (1998). A unified formulation of the constant temperature molecular dynamics methods. *The Journal of Chemical Physics*, *81*(1), 511. https://doi.org/10.1063/1.447334

Pandit, G., Biswas, K., Ghosh, S., Debnath, S., Bidkar, A. P., Satpati, P., Bhunia, A., & Chatterjee, S. (2020). Rationally designed antimicrobial peptides: Insight into the mechanism of eleven residue peptides against microbial infections. *Biochimica et Biophysica Acta - Biomembranes*, *1862*(4), 183177. https://doi.org/10.1016/j.bbamem.2020.183177

Pandit, G., Chowdhury, N., Abdul Mohid, S., Bidkar, A. P., Bhunia, A., & Chatterjee, S. (2021). Effect of Secondary Structure and Side Chain Length of Hydrophobic Amino Acid Residues on the Antimicrobial Activity and Toxicity of 14-Residue-Long de novo AMPs. *ChemMedChem*, *16*(2), 355–367. https://doi.org/10.1002/cmdc.202000550

Pandit, G., Ilyas, H., Ghosh, S., Bidkar, A. P., Mohid, S. A., Bhunia, A., Satpati, P., & Chatterjee, S. (2018). Insights into the Mechanism of Antimicrobial Activity of Seven-Residue Peptides. *Journal of Medicinal Chemistry*, *61*(17), 7614–7629. https://doi.org/10.1021/ACS.JMEDCHEM.8B00353/SUPPL_FILE/JM8B00353_SI_001.CSV

Parrinello, M., & Rahman, A. (1982). Strain fluctuations and elastic constants. *The Journal of Chemical Physics*, *76*(5), 2662–2666. https://doi.org/10.1063/1.443248

Patel, J. S., Berteotti, A., Ronsisvalle, S., Rocchia, W., & Cavalli, A. (2014). Steered molecular dynamics simulations for studying protein-ligand interaction in cyclin-dependent kinase 5. *Journal of Chemical Information and Modeling*, *54*(2), 470–480. https://doi.org/10.1021/CI4003574/SUPPL_FILE/CI4003574_SI_001.PDF

Pohorille, A., Jarzynski, C., & Chipot, C. (2010). Good practices in free-energy calculations. *Journal of Physical Chemistry B*, *114*(32), 10235–10253. https://doi.org/10.1021/JP102971X/SUPPL_FILE/JP102971X_SI_001.PDF

Rahnamaeian, M., & Vilcinskas, A. (2015). Short antimicrobial peptides as cosmetic ingredients to deter dermatological pathogens. *Applied Microbiology and Biotechnology*, *99*(21), 8847–8855. https://doi.org/10.1007/S00253-015-6926-1/FIGURES/1

Rakitin, A. R., & Pack, G. R. (2004). Molecular dynamics simulations of ionic interactions with dodecyl sulfate micelles. *Journal of Physical Chemistry B*, *108*(8), 2712–2716. https://doi.org/10.1021/jp030914i

Saigo, N., Izumi, K., & Kawano, R. (2019). Electrophysiological Analysis of Antimicrobial Peptides in Diverse Species. *ACS Omega*, *4*(8), 13124–13130. https://doi.org/10.1021/ACSOMEGA.9B01033

Sakai, N., & Matile, S. (2003). Anion-Mediated Transfer of Polyarginine across Liquid and Bilayer Membranes. *Journal of the American Chemical Society*, *125*(47), 14348–14356. https://doi.org/10.1021/JA037601L/ASSET/IMAGES/MEDIUM/JA037601LE00002.GIF

Sakai, N., Takeuchi, T., Futaki, S., & Matile, S. (2005). Direct Observation of Anion-Mediated Translocation of Fluorescent Oligoarginine Carriers into and across Bulk Liquid and Anionic Bilayer Membranes. *ChemBioChem*, *6*(1), 114–122. https://doi.org/10.1002/CBIC.200400256

Schrödinger, LLC. (2010). *The PyMOL Molecular Graphics System, Version 2.4.0*. https://pymol.org/2/

Strøm, M. B., Rekdal, Ø., & Svendsen, J. S. (2002). Antimicrobial activity of short arginine- and tryptophan-rich peptides. *Journal of Peptide Science : An Official Publication of the European Peptide Society*, *8*(8), 431–437. https://doi.org/10.1002/PSC.398

Ulmschneider, J. P. (2017). Charged Antimicrobial Peptides Can Translocate across Membranes without Forming Channel-like Pores. *Biophysical Journal*, *113*(1), 73–81. https://doi.org/10.1016/j.bpj.2017.04.056

van der Spoel, D., Lindahl, E., Hess, B., Groenhof, G., Mark, A. E., & Berendsen, H. J. C. (2005). GROMACS: Fast, flexible, and free. *Journal of Computational Chemistry*, *26*(16), 1701–1718. https://doi.org/10.1002/jcc.20291

Vogt, T. C. B., & Bechinger, B. (1999). The Interactions of Histidine-containing Amphipathic Helical Peptide Antibiotics with Lipid Bilayers: THE EFFECTS OF CHARGES AND pH *. *Journal of Biological Chemistry*, *274*(41), 29115–29121. https://doi.org/10.1074/JBC.274.41.29115

Vondrášek, J., Mason, P. E., Heyda, J., Collins, K. D., & Jungwirth, P. (2009). The molecular origin of like-charge arginine-arginine pairing in water. *The Journal of Physical Chemistry. B*, *113*(27), 9041–9045. https://doi.org/10.1021/JP902377Q

Wang, Q., Hong, G., Johnson, G. R., Pachter, R., & Cheung, M. S. (2010). Biophysical properties of membrane-active peptides based on micelle modeling: A case study of cell-penetrating and antimicrobial peptides. *Journal of Physical Chemistry B*, *114*(43), 13726–13735. https://doi.org/10.1021/jp1069362

Zou, G., de Leeuw, E., Li, C., Pazgier, M., Li, C., Zeng, P., Lu, W. Y., Lubkowski, J., & Lu, W. (2007). Toward understanding the cationicity of defensins. Arg and Lys versus their noncoded analogs. *The Journal of Biological Chemistry*, *282*(27), 19653–19665. https://doi.org/10.1074/JBC.M611003200

Chapter 3

Salt-Sensitivity of the fourteen residue long cationic anti-microbial peptide

Our experimental collaborators reported a cationic 14 residue peptide LL-14 (LKWLKKLLKWLKKL) with salt-sensitive broad-spectrum antimicrobial potency. However, the mechanism of its salt (NaCl) sensitivity remained unclear. This chapter was divided into two parts (A and B). Part A describes the conventional molecular dynamics simulations of LL-14 in the presence and absence of micelle at various monovalent (NaCl) salt concentrations. In Part B, the thermodynamics of peptide: micelle binding has been estimated using enhanced sampling methods. In Part A, we have reported computational (~14.2 μs of MD) and experimental (CD, fluorescence) investigations to examine the salt-sensitivity and the role of peptide secondary structure on LL-14 binding to simple membrane mimetic (SDS, DPC) systems. LL-14 was shown to adopt random coil (P^c) conformation in water and α-helical conformation (P^h) in peptide: SDS micelle complex, accompanied by tryptophan burial, using both simulations and experiments. Simulations successfully deconvoluted the LL-14: micelle binding event regarding secondary structure (random coil P^c versus helix P^h) and gave atomic insight into the initial and final LL-14:SDS complexes. Electrostatics drove the N-terminus (L1 and K2) of LL-14 (P^c or P^h) to bind the SDS micellar surface, initiating complex formation. LL-14 in amphipathic P^h conformation bound faster and buried deeper into the SDS micelle relative to P^c. Increasing NaCl concentration incrementally delayed LL-14: micelle binding by shielding the overall charges of the interacting partners. LL-14 binding to SDS micelle was significantly faster relative to zwitterionic DPC micelle due to electrostatic reasons. Cationic α-helical amphipathic peptides (with positively charged N-terminus) in low salt-ion concentration seemed to be ideal for faster SDS binding.

In Part B, we reported the thermodynamics of LL-14 binding to SDS micelle (simplest bacterial membrane mimic) at various NaCl concentrations (0.0%, 0.5%, 1.0% w/v). The thermodynamics of LL-14 dissociation from the SDS micelle was estimated by employing standard classical molecular dynamics (MD) simulation in addition to center-of-mass pulling followed by umbrella sampling. Results indicated that the increase in NaCl

concentration systematically disfavoured the LL-14:SDS binding, primarily by stabilizing the dissociative state (i.e., free LL-14 and free micelle in water). We proposed a kinetic scheme in which the salt-induced selective stabilization of the dissociative state increased the activation barrier for the peptide:micelle binding event resulting in reduced affinity. Center-of-mass pulling indicated that the interactions involving the N-terminal of the LL-14 (residue 1-6) and SDS micelle were crucial for the stability of LL-14:SDS complex, and LL-14 underwent conformational change (helix → unstructured) before dissociating from the SDS micelle. The observed features from the peptide: micelle dissociation pathway corroborates our previous simulations as well as circular dichroism (CD), and fluorescence experiments.

3.1 Background

Salt sensitivity and short serum stability are key factors, limiting the clinical use of AMPs. No systematic investigation has been done to understand the salt sensitivity of the AMPs. Though some salt-tolerant AMPs are reported in the literature, they are mostly the results of serendipitous discovery rather than rational design. Most AMPs lose their activity in the presence of physiological salt concentrations, which severely limits the commercialization of AMPs. For example, various peptides, viz., β-defensins (except for β-defensin III) present in humans, are prone to salt-induced inactivation (Bals et al., 1998; García et al., 2001; Goldman et al., 1997). In this chapter, we have tried to understand the reason for the salt sensitivity of a synthetic AMP, LL-14, earlier reported by our group (Pandit et al., 2021). Cationic fourteen residues long membranolytic LL-14 (**Figure 3.1**) was shown to have high activity (MIC99% ~1-10 μM) against several ESKAPE pathogens and fungal strains (Pandit et al., 2021). However, the activity of LL-14 was salt-sensitive against

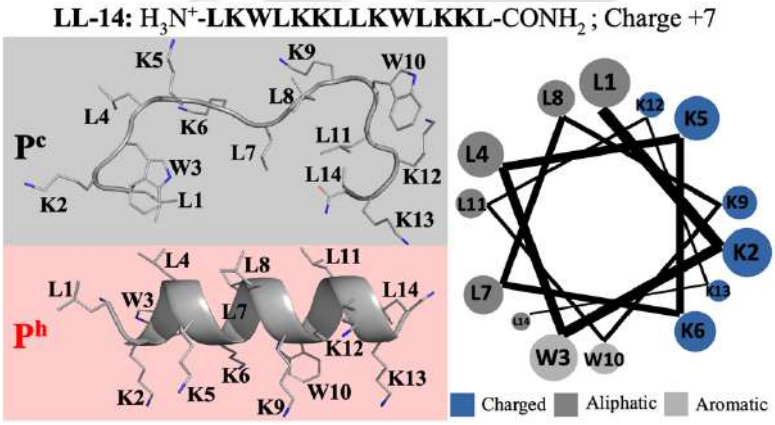

Figure 3.1: Primary sequence of LL-14 peptide. The N-terminal and C-terminal were -NH_3^+ and -$CONH_2$, respectively. Unstructured random coil (**P^c**) and amphipathic α-helical (**P^h**) and structures of LL-14. Helical wheel representation of the α-helical LL-14 with amino acid sequence highlighting the amphipathicity.

several microbes (*P. aeruginosa*, *S. aureus, C. neoformans*), leading to a partial loss of activity at physiological NaCl concentrations.

MD simulations helps to understand the thermodynamic and kinetic aspects of peptide binding to membrane mimetic systems (Berglund et al., 2015; Khandelia et al., 2006; Pandit et al., 2018, 2020; Ulmschneider, 2017; Wang et al., 2010). Electrostatics is shown to be a crucial factor in the cationic AMP binding to microbial membranes (Pandit et al., 2018, 2020). MD simulations are an excellent complement to popular experimental investigations (viz. isothermal calorimetry (ITC), circular dichroism (CD), nuclear magnetic resonance (NMR), fluorescence spectroscopy, microscopy (FESEM, CLSM, etc.), and biochemical assays (Bals et al., 1998; Pandit et al., 2018, 2020, 2021).

Combining molecular simulations and experimental studies, we have attempted to understand the salt sensitivity and the role of peptide secondary structural features on the antimicrobial potency of LL-14 using simple membrane mimetic micelles.

Part A: Molecular Dynamics simulations of LL-14 in presence and absence of micelle

Fluorescence and CD experiments confirmed that the free peptide was unstructured in water and attained α-helical (**P^h**) conformation only after micelle binding. All-atom classical MD simulations were performed with LL-14 peptide (in two different conformations: (A) random coil or unstructured:P^c, and (B) amphipathic α-helical:P^h) in the presence and absence of membrane mimetic system (SDS micelles: mimicking negatively charged prokaryotic membranes) in water with varying monovalent salt (NaCl) concentrations (NaCl = 0%, 0.5%, and 1.0% w/v). MD simulations suggested that free LL-14 in water preferred random coil (P^c) conformation in lines with fluorescence and CD experiments. Simulations provided atomic insight into the initial binding complex LL-14(P^c):SDS micelles. However, peptide conformational change in response to micelle binding (LL- 14(P^c):SDS / LL-14(P^h):SDS) was not observed within the timescale of our MD simulations. To gain insight into the LL- 14(P^h):SDS complex, simulations were performed to study α-helical (P^h) peptide binding to SDS, and the resulting LL-14(P^h):SDS complex agreed with our conclusions from the fluorescence experiment. Although free LL-14 in the α-helical (P^h) peptide was not experimentally characterized and unrealistic, the study of P^h binding to SDS was significant for two reasons: (1) structural information about final LL-14(P^h):SDS complex was obtained, and (2) comparison of the initial binding events in terms of the peptide secondary structure (P^c binding to SDS versus P^h binding to

SDS) was possible. The results indicated that salt (NaCl) systematically delayed the initial SDS binding event, and secondary structure was crucial for initial binding (P^h binds faster than P^c).

3.2 Materials and Methods

3.2.1 Modelling the peptides (extended:P^c and α-helical:P^h)

Experimentally verified anti-microbial peptide LL-14 (Fourteen residues, sequence LKWLKKLLKWLKKL, **Figure 3.1**) was selected and modelled using PyMOL (Schrödinger, LLC, 2010). The N- and C-termini of the peptide were $-NH_3^+$ and $-CONH_2$, respectively. Two initial peptide models were prepared, a linear-chain (P^c) and α-helical (P^h) conformation. N-terminal and the side-chain of lysine residues were positively charged, resulting in an overall +7 charge of the peptide (**Figure 3.1**). The MD setup of free peptide in water included overlaid water-box (dimension ~10 × 10 × 10 nm^3) and counter-ions. The MD model included more than 98000 atoms, consisting of ~32665 water molecules and 7 chloride ions (**Appendix II Table A3.1**).

3.2.2 Modelling of membrane-mimetic systems (SDS and DPC micelles)

Micelles were modelled using CHARM-GUI Membrane Builder (Cheng et al., 2013; Jo et al., 2008). A total of 60 molecules of SDS were used to model the micelles. The experimental value of aggregation number (Croonen et al., 1983) was close to 60 and was adopted previously (Lebecque et al., 2017; MacKerell, 1995; Rakitin & Pack, 2004; Wang et al., 2010) for computer simulations of SDS micelle. Solvation was done by overlaying a water box of dimension ~14 × 14 × 14 nm^3. A total of 60 Na^+ ions were added to neutralize the simulation box. Additional 138 and 278 ions (Na^+ and Cl^- each) were added to model 0.5% and 1.0% w/v salt environment, respectively. A total of ~260000 atoms were considered for MD simulations of SDS in water. The final snap of the post-equilibrated production dynamics was selected for the peptide-micelle binding study. DPC micelle was modelled in the same way as SDS.

3.2.3 Peptide:SDS/DPC micelle setup

The final snapshot of the free micelle in water was selected, and the center of mass of the peptide (P^c or P^h) was placed more than 50 Å away from the center of mass of the micelle (**Appendix II Figure A3.1a**). The waters overlapping with the peptide were deleted, and

counter-ions (Cl^-) were added to ensure charge neutralization. Simulations were carried out for different monovalent salt (NaCl, at 0.0% w/v, 0.5% w/v (85.5 mmol/l) and 1.0% w/v (171 mmol/l)) concentrations with various peptide-micelle relative orientations (see "Sampling and convergence of MD simulations" section below for detail). Simulations were performed in the cubic water box of dimension 14 × 14 × 14 nm^3 centered at the micelle. More than 260000 atoms were considered for MD simulations (**Appendix II Table A3.1**).

3.2.4 Simulation specification

GROMACS software (Lindahl et al., 2001) was used to perform MD simulations. Peptide, micelle, water, and ions were simulated using a standard CHARMM36m force field (Huang & Mackerell, 2013). TIP3P water model (Durell et al., 1994; Jorgensen et al., 1983) was used to describe water. Covalent bonds involving hydrogen atoms were constrained using the LINCS algorithm (Hess, 2008; Hess et al., 1997). Neutral simulation box (including peptide, micelle, ions, and waters) was first energy minimized (step size of 0.01 nm and ~50000 steps) by the steepest descent algorithm. After minimization, the resulting structure was subjected to 200 ps equilibration (that included molecular dynamics with 100 ps *NVT* followed by 100 ps *NPT* ensemble). Initial velocities were assigned from a Maxwell velocity distribution at 300 K. After attaining equilibration, MD was performed using *NPT* ensemble. During equilibration, the temperature was controlled using a modified Berendsen thermostat (V-rescale (Bussi et al., 2007), coupling with a time constant of 0.1 ps at 300 K). Simulations were done with 2 fs time-step, 300 K temperature and 1 bar pressure. Modified Berendsen thermostat (Berendsen et al., 1984; Bussi et al., 2007) and Parrinello-Rahman algorithm(Parrinello & Rahman, 1981) (for pressure coupling with the compressibility of 4.5 × 10^5 bar^{-1} and a time constant of 2 ps) were used to maintain the temperature and pressure of the simulation system. Periodic boundary conditions were used in all simulations. Long-range electrostatic interactions were treated using the particle-mesh Ewald algorithm (Darden et al., 1993). Short-range van der Waals interactions were truncated at 1.2 nm. Structures were collected for analysis at an interval of every 10 ps.

3.2.5 Samling and convergence of MD simulations

A key objective of MD simulations of a single peptide binding to a membrane mimetic system was to capture the essence of AMP:membrane binding by identifying the (1) initial and final peptide:micelle complex at atomic resolution, (2) time-scale of the binding event,

and (3) binding induced change in the dynamics and structure. The convergence of the reported data must be supported by various independent MD replicas differing in the initial distance and orientations of the peptide relative to the micelle and their initial velocities. However, this approach was limited by convergence issues (Kandasamy & Larson, 2004; Khandelia et al., 2006; Khandelia & Kaznessis, 2005; Shepherd et al., 2003). Magainin peptides in POPC bilayer simulations were reported not to be converged up to 20 ns MD (Kandasamy & Larson, 2004). Simulations of the helical (ovispirin) and β-sheet (protegrin-1) AMPs in the presence of lipid micelles showed that the final state of the complex depended upon the starting orientation of the peptide relative to the micelle (Khandelia & Kaznessis, 2005, 2006; Langham et al., 2006). On the contrary, cell-penetrating peptide penetratin in POPC and POPG bilayers was successful in achieving convergence, i.e., converged final state from different replicas with varying starting conformations (Lensink et al., 2005).

MD simulations were performed with the peptides (P^c, P^h) in the aqueous phase, initially placed away from the micelle surface in three different orientations relative to the micelle surface (**Appendix II Figure A3.1a**). Each simulation model (Setup A, Setup B, and Setup C, **Appendix II Figure A3.1a**) was subjected to multiple independent MD simulations, using randomized initial velocities (rep1, rep2, **Appendix II Table A3.2**) at various salt (NaCl) concentrations (**Appendix II Table A3.2**). Five independent replicas were considered for the calculation of temporal averages. The first direct contact between the LL-14 and SDS micelle was defined as the distance between the positively charged nitrogen of LL-14 and the oxygen head group of the SDS and fixed to ~0.35 nm (cut-off distance for hydrogen bonds in proteins) (Kajander et al., 2000). Analysing multiple independent MD trajectories, we estimated the distance (d_{COM}) between the centre of mass of LL-14 (P^c or P^h) and the center of mass of SDS micelle as ~3.47 ± 0.01 nm, which represented the first contact (Fig. A3.1b) distance between them. It should be noted that the choice of center-of-mass cut-off distance as 3.47 nm for describing the first LL-14:SDS contact was the best estimate with a standard deviation of 0.01 nm. Simulations of free peptides (P^c, P^h) and the free micelles (SDS, DPC) in the water were performed. Each replica was subjected to post-equilibrated MD simulations for 10 ns to a maximum of 6 μs (**Appendix II Table A3.2**). A total ~14.2 μs simulation was considered for analysis, confirming our reported data's convergence.

3.2.6 Circular dichroism (CD) experiments

CD spectroscopy was performed to gain insight into the secondary structural content of LL-14 in the presence and absence of SDS micelle. Curious about looking into the stability of the LL-14:micelle complex, we performed a CD experiment of the system in the presence of a chaotropic reagent Urea. CD spectra were recorded on a Jasco J-815 spectropolarimeter (Tokyo, Japan) calibrated with (±)10-camphorsulfonic acid for optical rotation. The spectra were recorded from 250 nm to 190 nm using a 1 mm path length in a Suprasil quartz cuvette at a scan rate of 100 nm min1, an interval of 0.5 nm. A time constant of 1 s and taking an accumulation of three scans at 298 K. Observed ellipticity value (θ in mdeg) was plotted against the wavelength (in nm). In all the cases, peptide, SDS, and urea concentrations were 50 μM, 30 mM, and 8 M, respectively, in the final solution. Baselines were corrected by using respective solvent systems.

3.2.7 Fluorescence experiments

The intrinsic Trp fluorescence property of the LL-14 peptide was used to analyse the interaction of LL- 14 with SDS micelles in the absence and presence of salt (150 mM NaCl, physiological concentration). Tryptophan side-chains of LL-14 were excited at 280 nm, and emission was recorded from 295–540 nm in an aqueous solution of SDS micelles with or without 150 mM NaCl using Hitachi F-7000 FL spectrometer at 25 °C. The experiments were performed at 50 μM LL-14 concentration and 30 mM SDS, well above the critical micelle concentration of SDS (CMC = 8.5 mM).

3.3 Results

3.3.1 Structural and dynamical properties of LL-14 and SDS micelle

MD simulations of the free peptide (P^c or P^h) and micelle in water provided clues about their size, shape, and dynamics. Simulations of free peptide in water starting with two different conformations (i.e., extended:P^c or α-helical:P^h) showed that (1) P^c remained as a random coil all along the MD trajectory (up to 1 μs), (2) P^h (helix) conformation started melting after 800 ns. The results showed that free peptide preferred random coil conformation in water (**Figure 3.1**). Distance of selected atoms to the center of mass (COM) of the SDS micelle (**Figure 3.2a**) indicated that counter-ion (Na^+) distribution was severely affected upon peptide binding. The average distance between Na^+ and the COM of SDS-micelle increased upon peptide binding. It was substantial in the case of P^c binding

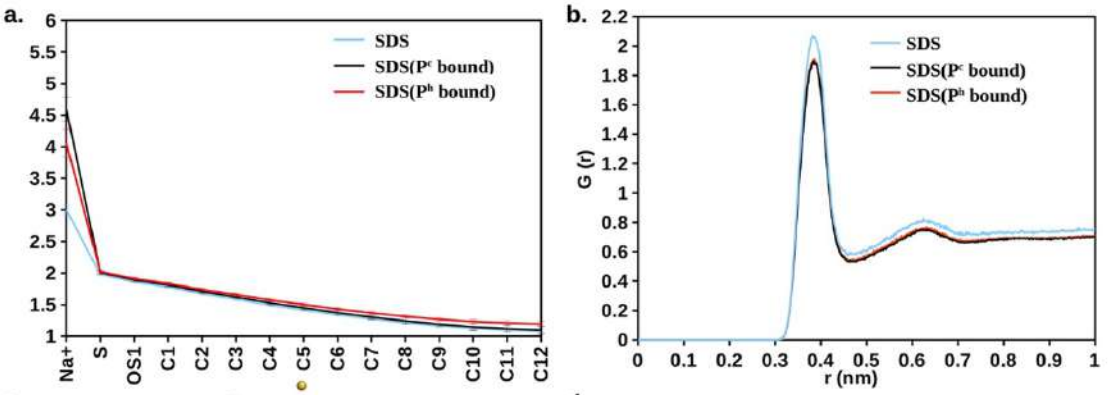

	SDS	P^c_SDS	P^h_SDS
e	0.14 ±0.05	0.15 ±0.04	0.17 ±0.06
R_g (nm)	1.65 ±0.02	1.68 ±0.03	1.73 ±0.04
R_s (nm)	2.12 ±0.03	2.17 ±0.03	2.23 ±0.05
SASA (nm²)	104.52 ±2.83	109.47 ±3.09	114.19 ±3.16
D of Na^+ (cm^2/s)	1.14 ±0.25 X 10^{-5}	1.37 ±0.06 X 10^{-5}	1.28 ±0.10 X 10^{-5}

Figure 3.2: Average structural and dynamical parameters obtained from simulation. (a) Distance of heavy atoms from the centre of mass of the SDS micelle. (b) Oxygen (H_2O) to sulphur (SDS) radial distribution function. (c) Representative snapshots of free SDS, P^c bound SDS, and P^h bound SDS. Na^+ (Yellow sphere), peptide (dark grey), SDS (aliphatic: light grey, sulphate: red). Waters and hydrogens not shown for clarity. Eccentricity (e), radius of gyration (R_g), micelle radius (R_s), solvent accessible surface area (SASA), diffusion coefficient (D) of Na^+ are given. (d) Residue-wise root mean square fluctuation (RMSF) of the heavy atoms of LL-14 in the absence and presence of SDS micelle. Error bars (standard deviation) are shown either as vertical bars (a) or reported after ± (c).

relative to P^h. The results suggested deeper binding of P^h into the SDS micelle core, leading to a closer approach of the counter-ions relative to P^c binding.

The radial distribution functions (RDF: oxygen atom of water molecules around the sulphur atoms of the SDS micelle) calculated from MD simulation indicated that the first coordination sphere of water was located 0.38 nm away from the sulphur atom of the micelle (**Figure 3.2b**). Beyond the first coordination shell, the water distribution was unstructured and relatively less dense than the bulk. Peptide binding displaced water from the first coordination sphere, resulting in a dip of the RDF peak (**Figure 3.2b**). The effective radius (Bogusz et al., 2000; Bruce et al., 2002; Itri & Amaral, 1991) or size (R_s) of the micelle can be defined as the average of two distances, (a) the center of mass of the micelle to the sulphur atoms of the head group (1.98 nm, **Figure 3.2a,b**) head group sulphur to the first peak of water oxygen radial distribution function (0.38 nm, **Figure 3.2b**) minus the radius of water (0.14 nm). Our estimated effective radius of the micelle was 2.22 nm, which

was in excellent agreement with the X-ray scattering experiment (Itri & Amaral, 1991) (2.23 nm). Micelle radius (Bogusz et al., 2000; Bruce et al., 2002) is also defined as:

$$R_s = \sqrt{\frac{5}{3}} R_g \tag{3.1}$$

where R_g is the trajectory average radius of gyration of the micelle, computed with the gromacs tool *gmx gyrate*. The MD averaged radius of gyration, R_g, of the free SDS micelle was 1.65 nm, which was very close to the previous reports (1.54–1.62 nm) (Bendedouch et al., 1983; Bruce et al., 2002; MacKerell, 1995). The shape of the micelle can be characterized by the eccentricity defined as:

$$e = 1 - \frac{I_{min}}{I_{avg}} \tag{3.2}$$

where I_{min} is the smallest moment of inertia among *x*, *y*, or *z* axis and I_{avg} is the average of moments of inertia along the *x*, *y*, and *z* axes. A perfect sphere is characterized by $e = 0$. Therefore, the deviation from a spherical shape can be quantified by estimating the eccentricity; lower the value, the more spherical the micelle. The SDS micelle's eccentricity as a time function suggested that the micelle was not spherical (eccentricity of a sphere = 0), but the shape was stable during MD simulations (**Appendix II Figure A3.2**). The MD averaged (last 20 ns of 50 ns MD) value of eccentricity and I_{min} (of free SDS I_{avg} micelle in water, Figure 3.2c) were 0.14 ± 0.05 and 1.31 ± 0.12 respectively (close to previous studies: I_{min} ranging between I_{avg} 1.02–1.13) (Bruce et al., 2002; MacKerell, 1995; Shelley et al., 1990). The eccentricity of the micelle was found to be independent of the salt concentration (**Appendix II Table A3.3**).

Quantifying solvent-accessible surface area (SASA) (Lee & Richards, 1971) also gave insight into the structural properties of the micelle. The ions, water, and peptides were first removed from each MD snapshot. Then a spherical probe molecule with a radius of 0.14 nm (mimicking water) was rolled over the surface of the micelle. The area formed by the center of the probe quantified the total accessible surface area (SASA). The average value of the solvent-accessible surface area (SASA) of the peptide-free micelle was 104.5 nm^2 (**Figure 3.2c**), which differed significantly relative to a perfect sphere of radius 2.22 nm having a SASA of 61.9 nm^2. The surface roughness of the SDS micelle and its non-spherical nature resulted in nearly double the SDS surface area relative to that of a perfect sphere. SASA of the SDS increased significantly (**Figure 3.2c**) in response to interaction with helical peptide (P^h), indicating severe structural distortion and solvent exposure. MD simulations with helical (P^h) and coiled (P^c) peptides in the SDS micelle revealed that the

former penetrated the SDS micelles. In contrast, the latter lay on the SDS surface (Figure 3.2c). Peptide binding displaced the counter ions from the micelle surface to the bulk and increased the average distance between the counter-ions (Na^+) and COM of the SDS micelle (**Figure 3.2a**). P^c acted as a barrier (by lying over the SDS surface, **Figure 3.2c**) between the counter ions (Na^+) and SDS surface, increasing the bulk Na^+ concentration and resulting in the largest average distance between the SDS and Na^+ ions (**Figure 3.2a**). Penetration of the peptide (P^h) into SDS micelle resulted in a lower average distance between Na^+ and COM of SDS (**Figure 3.2c,a**). The flexibility of the peptide chain was estimated by calculating the root mean square fluctuation (RMSF) of the heavy atoms of the amino acid residues in the absence and presence of micelle (**Figure 3.2d**). RMSF plots revealed the following features: (1) α-helical peptide P^h had smaller RMSF relative to its random-coil-like P^c analogue. Fluctuations of the amino acid residues were expected to be more pronounced in the random-coil-like conformations and less in the structurally rigid α-helical conformations. (2) A noticeable reduction in the flexibility (particularly in the -N and -C terminal of LL-14) was observed in the case of P^h peptide binding to SDS. Micelle-induced loss of LL-14 flexibility was less pronounced for P^c than P^h analogue. Thus, the peptide's secondary structure turned out to play a key role in the structure and dynamics of LL-14:SDS complexes. The secondary structural content of the peptide was estimated (**Appendix II Figure A3.2**) using the GROMACS analysis tool (*gmx do_dssp*) that uses DSSP software (Kabsch & Sander, 1983). No significant change in the peptide conformation was observed in response to SDS binding. Peptide (P^h/P^c) more or less retains its conformation (helical/coil) after SDS micelle binding during our simulations.

3.3.2 Salt effect in peptide-micelle (SDS) binding

The distance between the center of mass of the peptide and the center of mass of the micelle (d_{COM}) was plotted as a function of time (**Figure 3.3**). Distance d_{COM} ~3.47 nm indicated first direct contact (see Method) between peptide and micelle. The results revealed several remarkable features (**Figure 3.3**). Firstly, the temporal decay of d_{COM} was much faster for α-helical (P^h) LL-14 relative to its unstructured random-coil-like (P^c) conformation. This highlighted the importance of secondary structure in peptide-micelle binding kinetics. Secondly, the presence of monovalent salt drastically delayed the peptide-micelle interaction. The salt-induced time delay was independent of the structure of the peptide (helical, P^h or random-coil P^c), indicating a general feature of the salt effect in peptide-micelle

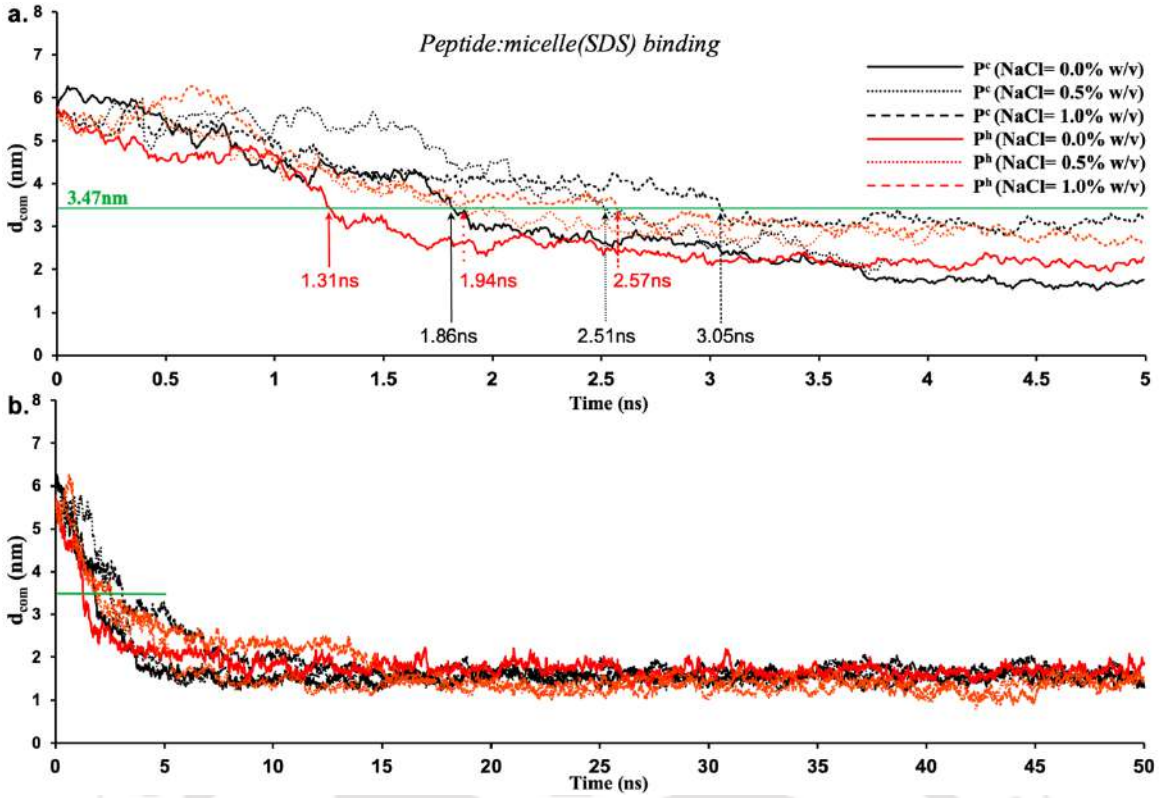

Figure 3.3: Temporal averaged distance between the centre of mass of a LL-14 and the centre of mass of the SDS micelle (d_{COM}) as a function of time. (a) Initial binding event. Peptide: micelle initial contact distance is represented as green line at d_{COM} ~3.47 nm. (b) Plateau of d_{COM} vs. time plot (after 10 ns) indicate structural convergence of the final peptide: micelle complex. Error bars are not shown for clarity (see Appendix II Figure A3.3 for detail).

binding. Increased salt concentration (0.0/0.5/1.0% w/v) systematically delayed the peptide-micelle binding. Thirdly, LL-14 bound to SDS micelle in a rapid (initial contact within 4 ns of MD) and irreversible manner. Fourthly, the distance between the centre of mass of the peptide and micelle was more or less constant after 10 ns, indicating structural convergence of the peptide-micelle complex. The robustness of the above features was confirmed by multiple trajectories (**Appendix II Table A3.2**), that differed in their initial velocities and relative positions. It should be noted that a single peptide in an explicit cubic water box of dimension ~14 nm referred to a concentration of ~605 mM in the MD simulation model. Thus, the peptide concentration in MD was much larger than in the MIC against several ESKAPE pathogens (1–10 M) and in CD experiments (100 μM) (Pandit et al., 2021). High concentration of peptide resulted in faster binding of the peptide to micelle (within 5 ns for various MD models). Using a larger water-box could be an alternative for lowering the peptide concentration, but would incur huge computational cost, rendering it impractical. The systematic salt-induced delay in the interaction time was a robust feature observed from several MD studies (confirmed from multiple simulations of various MD

models, see method). Thus it can be claimed that the general principle of salt-induced delay was captured by our simulation setup with moderate computational cost.

3.3.3 Structural insight into the sequential peptide-micelle binding event from MD simulations

Several prominent structural features were observed from MD simulations. Firstly, initial LL-14:SDS contact was formed by involving the positively charged N-terminal of the peptide and the negatively charged micelle surface (**Figure 3.4a,d**). We considered initial contact when the distance between the peptide's positively charged nitrogen and the micelle's oxygen head group was 0.35 nm. Secondly, in the finally converged LL-14:SDS complex, the helical peptide (P^h) was engulfed by the micelle (except at the terminals). In contrast, the random-coil-like peptide (P^c) lay over the surface of the micelle (**Figure 3.4b,e**). We found that the peptide-micelle binding followed a sequential order. First, electrostatic interaction between the negatively charged SDS surface with the positive

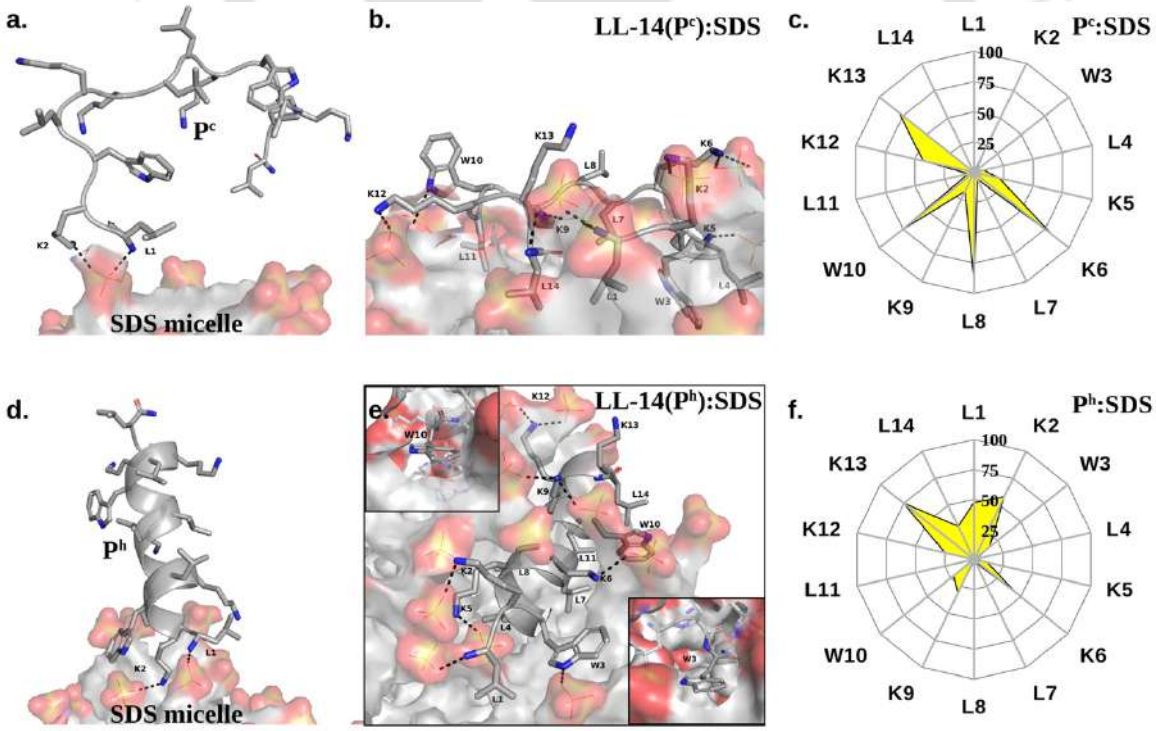

Figure 3.4: Structures from the peptide: micelle (SDS) binding event, with distinct secondary structures of the peptide (P^c or P^h) as initial condition. (a and d): peptide: SDS-micelle initial contact. Micelle surface forms direct interactions with the NH_3^+ of the N-terminal (L1) and side-chain of K2 of the LL-14 peptide both in the (a) P^c and (d) P^h conformations. (b and e) Final structure of the peptide: micelle complex. Interaction network is shown as dotted line for (b) P^c:micelle and (e) P^h:micelle complex respectively. For clarity, van der Waals radii of the micelle was reduced by 50% in (e). The local environment around W3 and W10 are explicitly shown without van der Waals reduction in the in-set (e). (c and f) Residue-wise solvent exposure (in percentage) of LL-14 in the final complex was estimated as: (SASA of amino acid residue in LL-14:SDS complex/SASA of the amino acid residue in LL-14) × 100. Trajectory averaged percent solvent exposure (yellow) is shown in the net-plot with contours of constant percent exposure. Waters and hydrogens not shown for clarity in the structures.

charge of the peptide brought them close together. Distance plot between positively charged nitrogen's of the peptide and the center of mass of SDS (**Appendix II Figure A3.4**) during the MD trajectories, including visual examination of MD snaps confirmed that the N-terminal, and the side-chains of K2 of LL-14 played a key role in establishing the initial contact (**Figure 3.4a,d**). Next, additional favourable electrostatic interactions (involving other positively charged lysine's and phosphate head group of SDS) and hydrophobic interactions (involving aliphatic/aromatic side chains of the peptide and aliphatic chain of micelle) led to a stable peptide:SDS complex (**Figure 3.4b,e**).

The peptide backbone of P^c satisfied its hydrogen bonding requirement by forming an H-bond with waters or sulphates of the SDS micelle or both (**Appendix II Figure A3.5**). Out of the two tryptophan's (W3 and W10), only one tryptophan (W3) of P^c was buried in the hydrophobic aliphatic pocket of SDS (**Figure 3.4b,c**). Side-chain of four residues (K6, L8, W10, and K13) of P^c showed more than 50% solvent exposure (**Figure 3.4b,c**) while being complexed with micelle. In P^h, the backbone was involved in secondary structure formation (i.e., helix), thus, unavailable for interaction with water or SDS. P^h was mostly buried inside the micelle, except for residues K2, K13 (**Figure 3.4e,f**). Note, both the tryptophans (W3, W10) were buried into the hydrophobic core of the SDS micelle in the P^h:SDS complex (**Figure 3.4e,f**). Solvent exposure of P^c in P^c:micelle complex was much larger relative to P^h in P^h:micelle complex (**Figure 3.4c,f**). We estimated the hydration of the hydrophobic part of the SDS micelle in P^c:micelle and P^h:micelle complexes. Hydration of the hydrophobic parts (P^c:micelle = 87.1 ± 8.6, P^h:micelle = 98.6 ± 8.7) was estimated by averaging the number of water molecules (from the last 20 ns of 50 ns of MD trajectory) within the commonly used cut-off of 0.35 nm (MacKerell, 1995) of the non-polar moiety (C1–C12) of each SDS molecule. The higher water exposure of the lipid portion of the micelle in the P^h:micelle relative to P^c:micelle complex, indicated higher hydrophobic destabilization of the micelle in the former.

Notably, irrespective of the secondary structural nature of the peptide (P^c or P^h), electrostatic interaction between the positively charged N-terminal of the peptide and the negatively charged anionic head group of the micelle lipid was the driving force for the initial binding (**Figure 3.4a,d**). Structural convergence in terms of the observed atomic interaction network in the final complex (**Figure 3.4b,e**) was confirmed from multiple independent MD simulations (**Appendix II Figure A3.1a** and **Table A3.2**). Simulations with various peptide (P^h or P^c) orientation relative to the micelle surface were found to be

converged to the same final structure of the peptide:micelle complex (**Appendix II Figure 3.4b,e**) and independent of the salt concentration (**Appendix II Figure A3.6**). Reasonable sampling (>14 μs of MD) and converged structure of the final peptide:micelle complex indicated that the reported MD structures of the peptide:micelle complex represented the true minima on the free energy hypersurface.

MD simulation with a neutral DPC micelle (zwitterionic lipid that mimics mammalian membrane) showed that P^c was able to bind DPC micelle surface after 870 ns of dynamics, the delay being attributed to the obvious electrostatic reasons. The results highlighted the importance of favourable electrostatic interactions in facilitating peptide:micelle interaction as reported in earlier studies (Pandit et al., 2018). Though LL-14 peptide was found to be cytotoxic (Pandit et al., 2021), MD studies suggested that the interaction of LL-14 with the mammalian membranes was much slower compared to that with the microbial membranes. A detailed structural analysis of the peptide:DPC binding is outside the scope of this chapter.

The driving force for the initial LL-14:SDS binding event was investigated by plotting the electrostatic (Coulomb) and Lennard-Jones (van der Waals is the attractive term) energy as

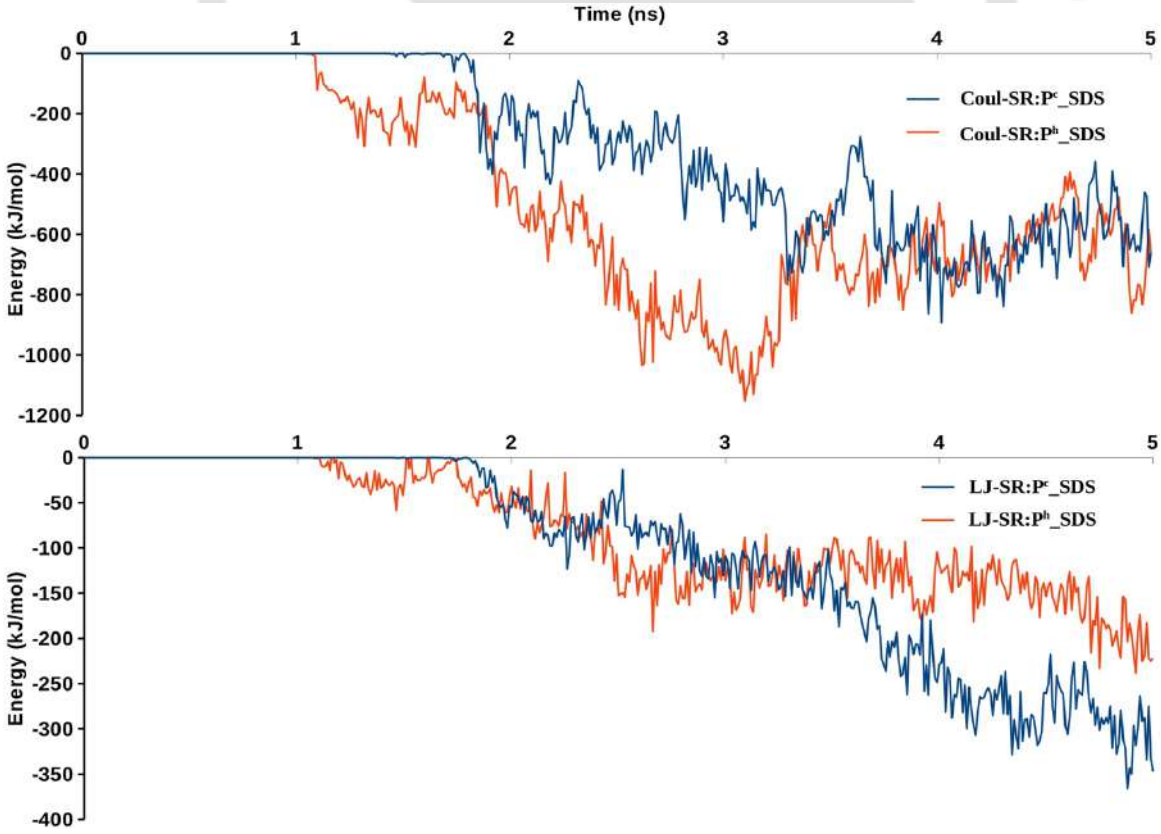

Figure 3.5: Electrostatic and Lennard-Jones interaction energy as a function of time during the initial stage of peptide: micelle (SDS) binding. The peptides in distinctly different conformations (P^c or P^h) were subjected to MD simulation. Long-range cut-off of 1.4 nm was used to compute the energies.

a function of time (**Figure 3.5**). The results showed that electrostatic energy profile, decayed faster for P^h relative to P^c, whereas there was a little difference in the decay of Lennard-Jones energy for P^h and P^c during the initial binding event (i.e., within 2 ns of MD, see **Figure 3.2a**), highlighting the electrostatic origin for the faster binding of P^h relative to P^c as observed in **Figure 3.3**. Though both the "electrostatic" and "van der Waals" energies were favourable (negative sign, **Figure 3.5**), the former was the primary contributor to the overall interaction potential energy. The favourable electrostatic term was attributed to the interactions between the positively charged side-chains of peptide and negatively charged SDS surface whereas, the favourable Lennard-Jones potential energy indicated favourable van der Waals interactions involving placement of hydrophobic residues of the peptide (Trp, Leu, aliphatic chain of Lys) into the aliphatic core of SDS micelle.

3.3.4 Secondary structural insight from CD experiments

CD experiments (**Figure 3.6a**) confirmed that free LL-14 in water adopted a random coil

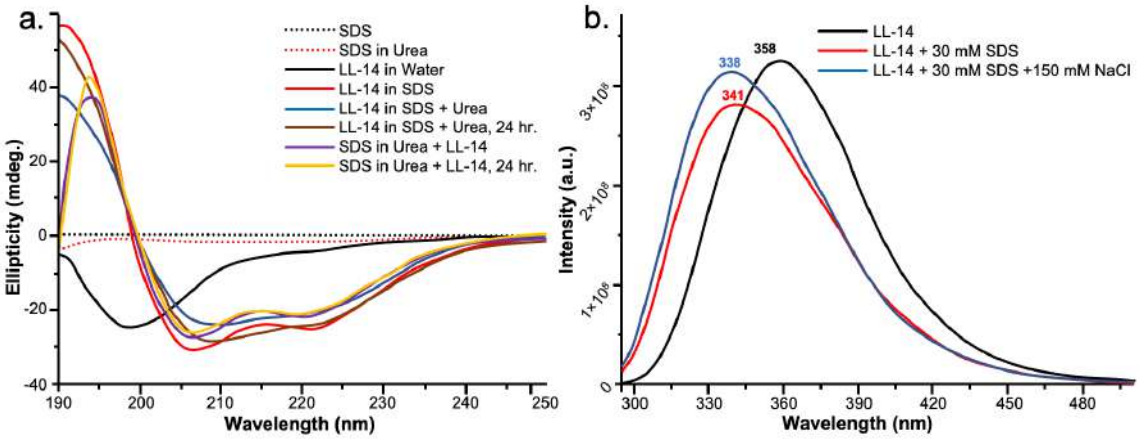

Figure 3.6: (a) CD spectra of free SDS micelle (as control, broken line) and LL-14 in various conditions (presence or absence of SDS micelle and urea, solid lines). CD spectra indicate characteristic SDS induced LL-14 conformational change form random coil to helix (P^c:Solid black / P^h:Solid colours) even in the presence of urea. (b) Tryptophan Fluorescence emission spectra of free LL-14 (black), LL-14 in presence of SDS (red), and LL- 14 in presence of SDS and salt (red). Blue shift in LL-14 emission observed upon addition of SDS micelle in presence or absence of salt (NaCl).

like (P^c) conformation with a negative peak at 200 nm. The result directly corroborated with the helix melting of free LL-14 observed in the MD simulation. However, in the presence of SDS micelles, a positive peak at 195 nm and two negative peaks at 208 nm and 222 nm were observed (characteristic features of significant helical content), which indicated helical conformation of LL-14 in the SDS micelle bound state. Thus, CD experiments suggested SDS micelle induced conformational change of LL-14 peptide (P^c free in water / P^h bound to SDS). Furthermore, the stability of the LL-14:SDS complex was investigated by CD experiments in the presence of chaotropic reagent urea. Experiments

were performed either by adding urea into the LL-14:SDS complex, or by adding LL-14 into the solution of urea and SDS micelle. Results confirmed that LL-14 in complex with SDS retained its helical conformation (P^h bound to SDS) even in the presence of urea and was independent of the order of addition of urea in the experiments.

3.3.5 Fluorescence studies and tryptophan burial in the final peptide:micelle complex

LL-14 binding to SDS micelle was investigated by monitoring the intrinsic fluorescence emission maxima of the tryptophan residues of LL14 in the presence and absence of SDS micelle (**Figure 3.6b**). The free LL-14 peptide in water, upon being excited at $\lambda_{max_{ex}}$ = 280 nm showed an excitation-emission with $\lambda_{max_{em}}$ at 358 nm. Upon addition of 30 mM of SDS micellar solution (above CMC = 8.5mM) to the peptide, $\lambda_{max_{em}}$ of LL-14 shifted to 341 nm. This large blue shift of $\lambda_{max_{em}}$ of about 17 nm in the SDS micellar system indicated the change in the microenvironment of tryptophan residues. In other words, the blue shift in the presence of SDS micelles suggested the peptide-micelle binding with the insertion of the tryptophan side chains into the hydrophobic core of the micelle. A blue shift (20 nm, $\lambda_{max_{em}}$ at 338 nm) was also observed in the presence of 150 mM NaCl, thus indicating a salt-independent feature of LL-14 binding to SDS micelle. The more or less similar value of the blue shift (20 nm/17 nm in the presence/absence of NaCl) indicated that tryptophan burial into the SDS hydrophobic core was independent of salt. The presence of a single peak at the shifted position (338 nm / 341 nm in the presence/absence of NaCl) indicated that both the tryptophan residues (W3 and W10) of LL-14 were in a similar environment in the micelle-bound state. MD structures of the converged LL-14(P^h):SDS micellar complex also showed the burial of both the tryptophan residues (W3 and W10) in the SDS micelles, thus corroborating the experimental observations. Thus, the fluorescence data indirectly proved that the structure of the final peptide:micelle complex was salt-independent and similar to the LL-14(P^h):SDS micellar complex observed from MD simulations.

3.4 Discussion

The mechanism of membrane-active AMP-induced cell death is a multi-step process that entails AMP binding to membrane, membrane-induced secondary structure formation of the peptide (coil / helix is most common), local peptide aggregation at the membrane and subsequent membrane destabilization leading to cell lysis (Shai, 1999). Unfortunately, due

to inherent complexity and large time-scale associated with the event, peptide aggregation and cell lysis are still non-tractable by current computational power. However, all-atom classical MD simulations help investigate the AMP binding to simple membrane mimetic systems. They can shed light on the general aspects (viz., structure, dynamics, and kinetics of peptide:micelle binding) of AMP-induced cell death. This information would be useful in designing peptide antimicrobials with improved activity and selectivity against pathogenic microbes.

Broad-spectrum cationic antimicrobial peptide LL-14 (**Figure 3.1**) (Pandit et al., 2021) was selected, and its binding to membrane mimetic systems was investigated in atomic details using MD simulations and experiments (CD, fluorescence). Simulations of free LL-14 in water showed that the helix (P^h) conformation melted after ~800 ns of MD, and LL-14 preferred random-coil (P^c) conformation. CD experiments also revealed that free LL-14 adopted a random coil (P^c) structure in water. Fast LL-14:SDS binding (within 4 ns of MD) (**Figure 3.3**) relative to slow helix melting (~800 ns) allowed us to study LL-14:SDS binding event considering the secondary structure of the peptide (i.e., P^c versus P^h binding to SDS, even though P^h was not the preferred conformation of the free peptide in water). The results suggested that the secondary structure of the peptide played a crucial role in SDS micelle binding kinetics (**Figure 3.3**) and insertion (**Figure 3.4**). Helical (P^h) LL-14 established faster initial contact with SDS. It was deeply inserted into the micelle in the final stage of binding relative to its coil analogue (P^c). Thus, the secondary structure of peptide was crucial for fine-tuning the speed of the initial peptide:micelle binding event. Electrostatic interaction between the negatively charged head-group of SDS and positively charged nitrogen of peptide (particularly N- terminal and side-chain of K2) was the key factor for interaction. This was followed by further hydrophobic stabilization (placement of the amino acids' aliphatic/aromatic side chains into the aliphatic interior of the micelle) and additional electrostatic interactions. The settled peptide (P^h) was found to be under the micelle surface ("hot-dog" like geometry), while P^c was found to be lying on the micelle surface. MD structure of the final converged LL-14:SDS complex showed the burial of both the tryptophan residues (W3, W10) of LL-14 into the hydrophobic core of the SDS micelles in the case of the P^h-SDS complex (**Figure 3.4e**), contrary to that of the P^c-SDS complex, where only one of the tryptophan side chains was buried (**Figure 3.4b**).

CD experiments suggested SDS-induced helical conformation of the peptide in the final LL-14:SDS complex (**Figure 3.6**). The peptide retained its helical conformation (P^h) in the LL-14:SDS complex even after 24 hours of urea exposure, suggesting the stability of the

complex. Furthermore, LL-14 addition to urea containing SDS micellar solution also supported P^h conformation of LL-14. Thus, SDS-induced LL-14 conformational change (P^c / P^h) was a consistent and robust feature. We observed a blue shift in the emission maxima of the tryptophan fluorescence (**Figure 3.6**), in the presence of the SDS micellar system, suggesting the burial of the side chains of tryptophan in the hydrophobic inner core of the micelles. The observation of a distinct single peak indicated a similar environment around the Tryptophan's (W3 and W10) of LL-14 upon micelle binding. Thus, fluorescence experiments corroborated with the observed final MD structures of LL-14(P^h):SDS complex (**Figure 3.4e**).

We did not observe P^c/P^h conformational change in response to micelle binding during our finite simulation time scale (even extending the simulation upto 6 μs). Thus, the micelle-induced LL-14 folding was not computationally tractable and was certainly limited by the time scale and simplified system description. Nonetheless, MD simulation of P^c binding to SDS provided atomic insight into the thermodynamically hidden (experimentally unresolved) high energy state, i.e., LL- 14(P^c):SDS complex. Moreover, MD simulation of P^h binding to SDS was successful in providing an atomic model (i.e., LL- 14(P^h):SDS complex, **Figure 3.4e**) for the experimentally characterized state (**Figure 3.6**). A large activation barrier between the high energy (LL-14(P^c):SDS complex) and low energy (i.e., LL- 14(P^h):SDS complex) state might hinder the observation of micelle-induced LL-14 conformational change (P^c / P^h) during the course of MD simulations. Interestingly, MD simulations not only provided atomic insight into the various stages (viz., initial (**Figure 3.4b**), final (**Figure 3.4e**) complex) of peptide binding and/ insertion process but were also useful in understanding the kinetic aspects (**Figure 3.3**). An increase in salt (NaCl) concentration shielded the charges of the SDS micelle and peptide, resulting in a delayed binding process (**Figure 3.3**). The final structure of the peptide-micelle complex was well converged and independent of the salt concentration. Thus, although the salt delayed the forward rate (k_{on}) of the LL-14:SDS initial binding event, the atomic interaction network observed in the final peptide-micelle complex was independent of the salt concentration. Fluorescence experiments showed a similar amount of blue shift in the λ_{max} of the Trp fluorescence emission in the presence of SDS both in the absence and presence of salt, suggesting similar amount of Trp side chain burial in the LL-14:SDS complex. This was completely in alignment with the findings from the simulation (**Figure 3.4e**). Though, the difference in the interaction timescale of the peptide with the SDS micelles was small (~1

ns), it should be remembered that the simulations were performed at a much higher concentration (~6x MIC) due to the constraint in the computational expenditure. Despite the absolute value of the delay time, our results definitely showed the trend of the effect of salt ions. It may be hypothesized that slowing down the initial peptide-micelle binding process might facilitate microbial progeny growth, leading to the impaired activity of LL-14 in the presence of salt. It should be noted that our argument did not underestimate the crucial effect of hydrophobic stabilization in peptide-micelle/ membrane interactions. It was an essential component of the antimicrobial effect, but came into play only after the initial peptide-micelle binding event. The present results also emphasized the importance of terminals of the peptide in rendering the activity of the AMPs, consistent with the previous experimental study (Pandit et al., 2018). We had demonstrated earlier that converting the free C-terminal to the amidated analogue in a small synthetic AMP P4 improved the antimicrobial potency many folds. Thus, α-helical conformation of any cationic peptide and lower salt (NaCl) concentration would be ideal conditions for fast peptide-micelle (SDS) binding.

MD studies based on simple micelle models certainly have limitations in addressing issues like the effect of various other salts (monovalent, divalent, etc.), importance of peptide-lipid ratios, role of proteins embedded in the bacterial membrane, inadequate representation of microbial lipids, etc. Nevertheless, systematic MD simulations emphasized the importance of (1) the secondary structure and the N-terminal of LL-14 for establishing fast initial contact with SDS, and (2) salt in delaying the peptide-micelle association.

Thus the above discussions indicated that: (i) peptide-SDS micelle binding was sequential, and electrostatics drove the initial binding followed by van der Waals stabilization. (ii) Presence of salt (NaCl) delayed the initial peptide:micelle contact by shielding the overall charge of the interacting partners. (iii) Peptide in a-helical conformation (P^h) bound faster to the SDS micelle than its random-coil analogue (P^c). Thus, peptide:micelle binding kinetics depended on both the salt concentration and the nature of the peptide (P^c or P^h). (iv) The converged MD structure of the final LL-14(P^h):SDS complex (**Figure 3.4e**) corroborated with the fluorescence experiments. The computational analysis complemented our experimental studies by providing structural and dynamical insight into the experimentally unresolved/unrealized high-energy states, like, free P^h in water and final P^c:SDS complex (**Figure 3.4b**). LL-14 binding to DPC micelle (zwitterionic eukaryotic membrane mimic) was observed to be much slower relative to SDS micelle binding.

The CD and fluorescence experiments were performed in the SDS micellar environment (above CMC concentration) at pH = 7. SDS is highly acidic with a pKa = -1.5 (D. Ristroph & K. Prud'homme, 2019). Thus, it is unlikely to alter the protonation state of the SDS molecule (negatively charged) around pH = 7. Thus, MD simulations were performed for charged SDS micelle at the same pH. However, the critical micelle concentration (CMC) of the SDS depends on the pH (Rahman & Brown, 1983) and the salt concentration (Abe et al., 1989). Self-assembly behaviour (micelle-bilayer) of lauric acid (fatty acid) was investigated extensively by Morrow et al., employing continuous constant pH molecular dynamics (CpHMD) simulations (Morrow et al., 2012, 2013). It was shown that lauric acid self-assembly was pH dependent (low pH favoured bilayer and high pH favoured micelle). Although, lauric acid is different from SDS as the former contain –COOH group whereas the later contain -SO_4 group, the results were of general importance to the surfactant assembly. Vila Viçosa et al. investigated (Vila-Viçosa et al., 2015) the titration curve of oleic acid (carboxylic acid with 18 carbons) bilayer using extended CpHMD method (CpHMD-L). The computed titration curves were in good agreement with the experimental data. The adopted methodology (CpHMD-L) is very promising for studying more realistic pH-sensitive lipid bilayers. Similar to SDS, the 14-mer AMP (LKWLKKLLKWLKKL) considered in this study contained titratable lysine side-chains and amino N-terminal. The pKa of the side-chain of lysine (amino acid) and N-terminal of Leucine (amino acid) are 10.53 and 9.6 respectively (Lide, 1991). At neutral pH = 7 the titratable residues (of the free peptide) were expected to be positively charged. Thus, simulations were performed with +7 charged 14-mer peptide. However, large shifts in pKa values (~5 units) of lysine residues buried inside a protein interior were reported by Isom et al (Isom et al., 2011). Titration events were shown to alter the AMP:micelle binding event (Alvares et al., 2021; Carvalheda et al., 2013, 2015; Magalhães et al., 2015; Teixeira et al., 2016; Vila-Viçosa et al., 2018). In the present study however, salt-bridge interaction was reported to be formed involving negatively charged SDS surface and NH_3^+ tips of peptide. The ion-pair (SO_4^-:NH_3^+) might alter the charge state to form (SO_4H:NH_2) in the anhydrous hydrophobic core, investigating which is beyond the scope of the present study. Thus, continuous constant pH molecular dynamics simulations might be helpful in understanding the role of pH in the mechanism of peptide:micelle binding.

3.5 Conclusion

In this part we have successfully established the link between the salt concentration (as well as the secondary-structure of peptide) and the speed of peptide:micelle binding and achieved structural convergence of the final peptide:micelle complex that was complemented by experimental observations. Salt (NaCl) induced slowing down of the kinetics of the peptide micelle interaction might be one of the possible reasons for the salt sensitivity of the AMPs in general. A detailed thermodynamic analysis (binding affinities at various salt concentrations) of peptide:micelle interaction will be reported in a separate study. We expect that the observations reported here will be relevant for other cationic peptides and micelle mimetic systems in general.

Part B: Thermodynamics of peptide:micelle binding

Using the converged MD structures of the LL-14(P^h):SDS complex (Ghosh et al., 2021) as a template, we estimated the peptide:micelle binding affinity by employing center-of-mass pulling (COM) and umbrella sampling simulations in explicit water at various salt concentration (NaCl = 0%, 0.5%, 1.0% w/v). Molecular dynamics simulations suggest that (1) peptide:micelle binding was compromised by monovalent salt (NaCl), primarily by stabilizing the dissociative state (i.e., free peptide and micelle in water), and (2) the interaction between the N-terminal of LL-14 (residues 1-6) and the SDS micelles was crucial for stability. The observations may be relevant for related cationic peptide binding to membrane mimetic systems in general and a plausible explanation for the salt sensitivity of cationic peptides.

3.6 Materials and Methods

3.6.1 Structure of the LL-14(P^h):SDS complex from Part A MD study

In our previous work (Part A), we reported the atomic structure of the LL-14(P^h):SDS micelle complex from MD simulations and showed that the proposed structure was converged (multiple independent runs differing in their initial velocity, relative orientation, and distance, and salt-concentration), which complemented our CD and fluorescence experiments (Ghosh et al., 2021). Thus, the MD structure of the LL-14(P^h):SDS complex was used as a starting configuration for COM pulling (simulation size and simulation parameters are given in **Appendix II Table A3.4**).

3.6.2 Steered molecular dynamics and umbrella sampling

Understanding the dissociation of two molecules using standard classical MD simulation was time-consuming as classical force fields are known to over-stabilize the salt bridges (Ahmed et al., 2018). Steered molecular dynamics (SMD) simulation (Izrailev et al., 1999; Lemkul & Bevan, 2010) apply an external force and accelerate the dissociation event, and thus is a method of choice for this work. The LL-14:SDS complex was re-oriented, and the d_{COM} (**Figure 3.7a**) was placed along the z-axis. The large size of the simulation box

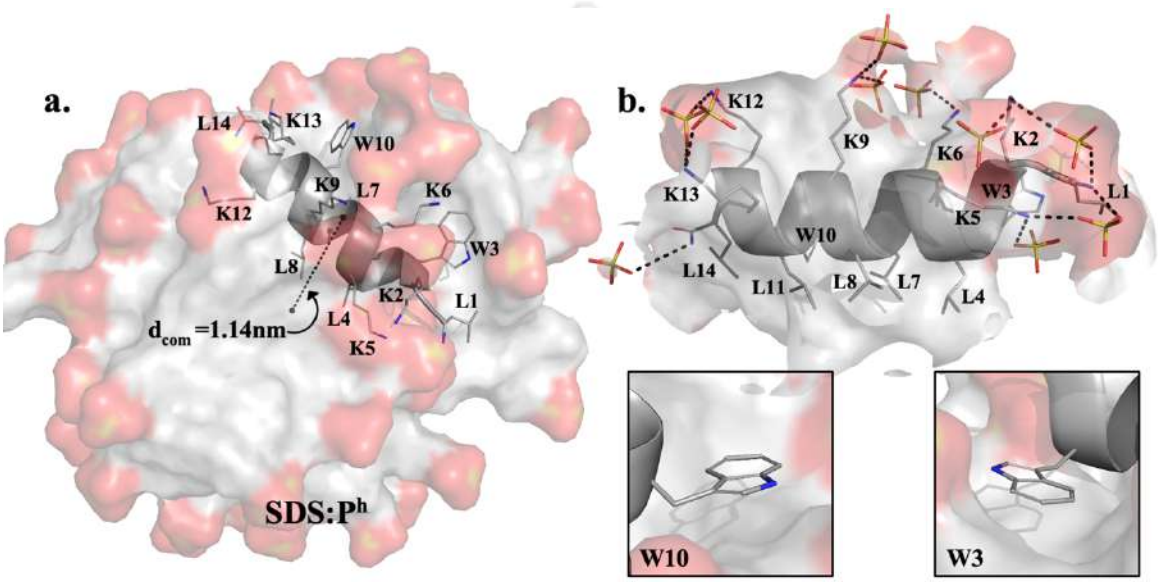

Figurer 3.7: (a) LL-14(P^h):SDS complex. Centre-of-mass distance between the helical LL-14 (cartoon and sticks) and the SDS micelle (surface) is shown as "d_{COM}". For a clear visual representation of the peptide, the van der Waals radii of the SDS molecule are reduced by 50%. (b) Magnified view of the local environment of LL-14 in the SDS micelle. Direct electrostatic interactions between the peptide and micelle are represented as dashed lines. Local environments of W3 and W10 are more or less similar (buried in the hydrophobic core of the micelle). Hydrogens are not shown for clarity.

(dimension 14 × 14 × 14 nm^3) not only minimized the image convention but also provided enough space for pulling simulation (along the z-axis). Before the pulling simulation, the LL-14:SDS complex was harmonically retrained (force constant = 1000 kJ mol^{-1} nm^{-2}) relative to the starting structure and equilibrated again for 100 ps in the NVT ensemble followed by 100 ps in the NPT ensemble at 300 K. After the equilibration, the COM pulling simulation was performed using the NPT ensemble at 300 K. The LL-14 peptide was pulled away from the SDS micelles (along z = d_{COM}, **Figure 3.7a**) over 500 ps, using a spring constant of 1000 kJ mol^{-1} nm^{-2} at three independent pull rates (0.01, 0.005, and 0.001 nm ps^{-1}). Despite distinctly different pulling rates, visual examination confirmed that the resulting trajectories were more or less identical with very similar force vs. time curves (**Appendix II Figure A3.7**). Thus, the trajectory corresponding to the fastest pulling rate

(0.01 nm ps^{-1}) was used for umbrella sampling in order to expedite data collection without compromising the reliability of the data. A final center-of-mass (COM) distance between LL-14 and the SDS micelle of ~ 6.6 nm was achieved from SMD simulation (**Appendix II Figure A3.8**). Equally spaced snapshots (spacing 0.1 nm, d_{COM} ranges from 1.14 nm to 5.45 nm) from the trajectories of pulling simulations were selected as starting configurations for the umbrella sampling simulations (total 43 windows, **Appendix II Table A3.5**). The spring constant for umbrella sampling was first estimated from the previous unrest- rained MD trajectory (50 ns) of the LL-14(P^h):SDS complex. The variance of the ''d_{COM}'' value was estimated from the last 10 ns of the 50 ns trajectory, and the spring constant (k) was estimated as:

$$k = \frac{k_b T \cdot N_A}{variance} \tag{3.3}$$

where N_A is the Avogadro's number, T = temperature (300 K), and k_b is the Boltzmann constant.

The estimated spring constant was 288.4 kJ mol^{-1} nm^{-2}. We used a slightly larger force constant (k = 300 kJ mol^{-1} nm^{-2}) to ensure adequate sampling around the biased potential. Free energies were estimated from different independent trials that differed in sampling (minimum of 50 ns per window to a maximum of 250 ns per window) for ensuring convergence (**Appendix II Table A3.5**). Snapshots at 10 ps intervals were selected from the production MD at every window and subjected to PMF profile estimation. The first 1 ns of the MD trajectory at every window has been considered as equilibration, and thus not considered for PMF estimation. PMF was estimated using the weighted histogram analysis method (WHAM) (Kumar et al., 1992). The statistical error associated with the PMF calculation was carried out using bootstrap analysis (Efron, 1992; Hub et al., 2010).

3.6.3 Sampling and convergence

The objective of COM pulling and umbrella sampling was to mimic the dissociation path (using reaction coordinate, ξ, which could be distance, angle, dihedral or any other abstract variable) and estimate the free energy from the PMF profile. In this work, the reaction coordinate (ξ) was defined as the distance between the center-of-mass of LL-14 and the SDS micelle. First, configurations along ξ were generated from the COM pulling simulations resulting in force vs time plots.

Next, configurations were selected from regular intervals and subjected to equilibrium MD simulations by applying harmonic restraint to the corresponding reaction coordinate

(windows or strata). The biased harmonic restraint allowed sampling within each window (umbrella sampling). The potential of mean force (PMF) was estimated from the umbrella sampling windows, resulting in a PMF vs. reaction coordinate (ξ) plot. Free energies (ΔG) were estimated from the PMF profile. The reliable estimation of ΔG required (I) adequate sampling at every window and (II) overlap between two neighbouring sampling windows. The choice of the strength of harmonic restraint and the number of windows (stratification) is crucial for a reliable estimate of free energies. Moreover, the COM pulling depended on the path (reaction coordinate, ξ); thus, the number of generated conformations for the umbrella simulation relied on the pulling rate. No standard procedure exists for choosing pulling rate, harmonic restraint, and stratification to ensure the best free energy estimate. Thus, the convergence of the reported data must be verified from various independent MD replicas differing in the pulling rate, harmonic potential, MD run length, etc. The positions of the high and low force points in the time axis were expected to differ (due to different pulling rates). Still, the nature of the force profiles was shown to be independent of the pulling rates (**Appendix II Figure A3.7**), and the observed structural features of the dissociation pathway were very similar between various pulling rate paths. Excellent conformational overlap between the neighbouring windows was evident from the umbrella sampling simulations (**Appendix II Figure A3.9**). The probability distribution overlap between the neighbouring windows (**Appendix II Figure A3.9**) confirmed that the estimated free energies were reasonably accurate. Small statistical uncertainty associated with the estimated free energy of 1.5 kcal mol^{-1} ensured good convergence. Note that the free energy estimates from various sampling strategies (minimum of 50 ns per window to a maximum of 250 ns per window) differ by 1 kcal mol^{-1}, implying convergence of the estimated energetics. A total of ~33.87 μs simulation was performed to ensure adequate sampling and reasonable convergence of the estimated free energies.

3.7 Results

3.7.1 MD simulations of center-of-mass (COM) pulling

Steered molecular dynamics (SMD) or center-of-mass pulling simulations were used to mimic the LL-14:SDS dissociation pathway inaccessible on the standard MD time scale. SMD simulations are a popular and successful approach for studying various biological processes, including protein–ligand interactions, protein–protein interactions, lipid extraction from membranes, etc (Izrailev et al., 1999; Lemkul & Bevan, 2010). During

SMD simulation, the applied external pulling force between the center-of-mass of the peptide and the micelle certainly disturbs the equilibrium, limiting the direct estimation of thermodynamic quantities, but allowing easy estimation of the non- equilibrium work. Two popular approaches for extracting the equilibrium property (viz., free energy ΔG) from SMD trajectories are Jarzynski's method (Jarzynski, 1997) and the weighted histogram analysis method (WHAM) by Kumar et al (Hub et al., 2010; Kumar et al., 1992). The former approach requires running multiple independent SMD simulations. In the WHAM procedure, equilibrium simulations are performed on the SMD generated configurations (applying harmonic biasing potential), and the free energy was estimated from those equilibrium simulations. We adopted the WHAM approach in this work.

The main features observed in the force profile from the pulling simulations (**Figure 3.8**) were: (I) two high force points (at, 263 ps and 351 ps, NaCl = 0.0% w/v) connected by a minima-like point (at, 284 ps, NaCl = 0.0% w/v). The highest force-point always appeared early (i.e., 263 ps). (II) The structures corresponding to the two high-force points (i.e., 263 ps and 351 ps) preserved the interactions between the N-terminal of the LL-14 (L1, K2, W3, L4, K5, and K6) and the SDS micelle. However, they differed in the secondary structural content of LL-14 (helix/P^h at 263 ps $\rightarrow$ unstructured/P^c in 351 ps). The structure corresponding to the intermediate force-point (i.e., 284 ps) implied the mid-point of helix melting of LL-14 (mostly unstructured except for the helical middle portion) on the SDS micelle. (III) A change in the LL-14 secondary structure ($P^h \rightarrow P^c$, helix melting) was observed before the complete dissociation of LL-14 from the micelle.

COM pulling built up forces until a breaking point was reached, resulting in the disruption of critical interactions, allowing the peptide to dissociate from the micelle. As the interactions involving the N-terminal (residues 1-6) of LL-14 and the SDS micelle were observed in the high-force points (force vs. time plot), they might be critical for the stability of the complex. Pulling induced LL-14 dissociation from the SDS micelle was found to be sequential. First, the LL-14(P^h):SDS complex reached the maximum force at 263 ps (red arrow in **Figure 3.8a**, red structure in **Figure 3.8b**). After that, within only 21 ps, secondary structure melting was observed at the C-terminal end of LL-14 (residues 7-14) along with disruption of several peptide:micelle interactions (solvent exposure of the hydro- phobic

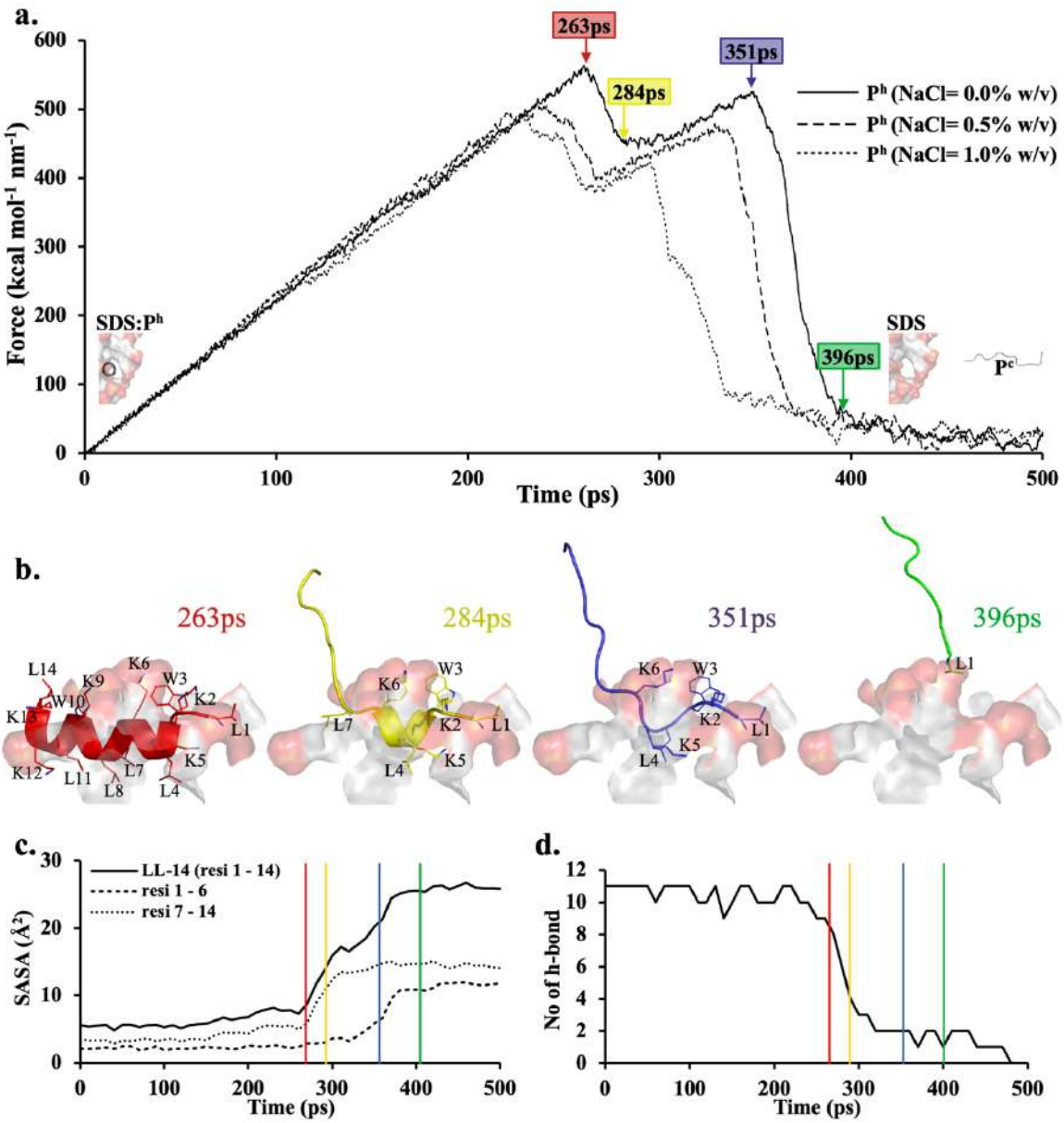

Figure 3.8: (a and b) LL-14 dissociation pathways from the SDS micelle at various salt-concentrations. Red (arrow and structure) and blue (arrow and structure) correspond to two high force points, the former being the highest. Red - Blue corresponds to secondary structural transition (helix - random-coil) of the LL-14 in the presence of the SDS micelle. The yellow (arrow and structure) point is an intermediate between red and blue points. Green corresponds to the structure just before the complete dissociation of LL-14 from the SDS micelle with a single salt-bridge between the N-terminal tip (-NH_3^+) and SDS sulphate. (c) Plots of solvent accessible surface area (SASA) of the amino-acid residues of LL-14 peptide as a function of time. (d) The number of intra-peptide hydrogen bonds. Different colored lines in (c and d) corresponded to different time points of SMD.

amino acids, disruption of salt-bridge), resulting in the decrease of force (284 ps, yellow arrow in **Figure 3.8a**, yellow structure in **Figure 3.8b**). Further pulling increased the force up to 351 ps, at which the complete loss of secondary structure (middle part melting) of LL-14 was observed (blue arrow in **Figure 3.8a**, blue structure in **Figure 3.8b**). Interestingly, the interaction involving the N-terminal of LL-14 (L1, K2, W3, L4, K5, and K6) and the SDS micelle was preserved until 351 ps. Next, a steady decrease in the force

was observed, corresponding to the disruption of the interaction between the peptide N-terminal and SDS micelle. Within 44 ps, the peptide was mostly exposed to water (396 ps), where only a single salt-bridge interaction involving the N-terminal tip of unstructured LL-14 ($NH3^+$ back-bone of L1) and the SDS surface was present (**Figure 3.8b**). Early solvent exposure of the C-terminal region of LL-14 was also evident from the SASA plot (Figure 3.8c). Thus, the interactions involved the N-terminal (LL-14; residues 1-6), and the SDS micelle seemed crucial for the stability of the complex. Loss of intra peptide backbone-hydrogen bonds supported the helix melting during the pulling simulation (**Figure 3.8d**) and it was evident from the Ramachandran Plot (Ramachandran et al., 1963) (**Appendix II Figure A3.10**).

An increase in salt concentration (0.0% - 0.5% - 1.0% w/v NaCl) systematically reduced the magnitude of the force points (263 ps, 284 ps, 351 ps) and shifted the force profile to the left in the time axis, indicating easy and early LL-14 dissociation. The above features observed in the in silico pulling experiments were insensitive to the initial structural model, and the pulling rate (confirmed from multiple independent MD replicas, see Method). Force versus time plots (**Figure 3.8**) obtained from COM pulling depended on the reaction coordinate "ξ" which was path-dependent. Thus determination of the free energy profile of the real dissociation pathway was likely to be limited by the convergence issues. However, the maximum force, the shape of the force-curve, and the derived PMF profiles (**Figure 3.8 and 3.9**) obtained from various independent pulling simulations (differing by initial position, velocity, and pulling rate) were comparable. Thus, it may be claimed that the feature which emerged from the pulling induced dissociation pathway was more or less independent of the simulation protocol. Additionally, the observed helix melting corroborated with the previous CD experiments (Ghosh et al., 2021).

3.7.2 Umbrella sampling simulations and energetics of LL-14 dissociation from the SDS micelle

Free energy (ΔG) change associated with the peptide-micelle binding was estimated using umbrella sampling simulations along with the reaction coordinate "ξ". Along the ξ coordinate, 43 windows were sampled to estimate the potential of mean force (PMF) at various salt concentrations (**Figure 3.9**). The binding free energy (ΔG) was calculated from the difference between the minimum and plateau of the PMF profile. The increase in the PMF as a function of ξ suggested that LL-14:SDS binding was thermodynamically

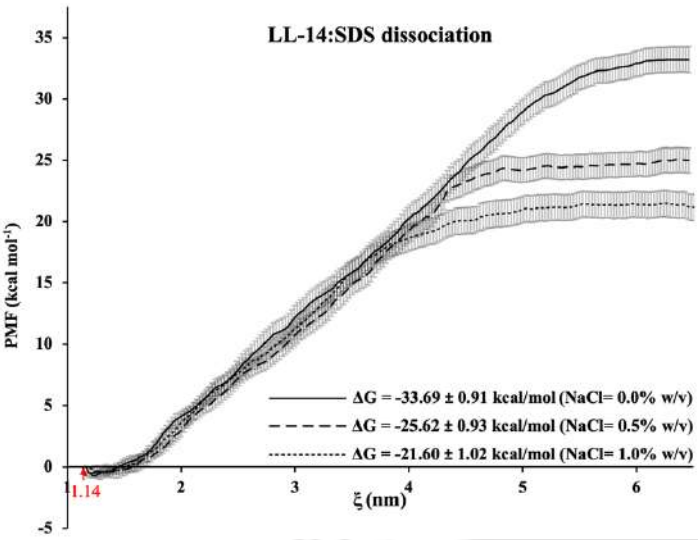

Figure 3.9: Potential of mean force (PMF) as a function of dissociation coordinate "ξ" at various salt concentrations. The errors are shown as vertical bars (computed by using 100 cycles of bootstrapping calculations). Estimated binding affinities (ΔG) and errors (right-side of). The red arrow corresponds to the reference state (ξ = 1.14 nm) of PMF calculations.

favourable. The binding free energy (ΔG) was systematically compromised (-34 kcal mol^{-1} → -26 kcal mol^{-1} → -22 kcal mol^{-1}) with an increase in salt concentration (0.0% → 0.5% → 1.0% w/v NaCl). Clearly, electrostatics played a crucial role in the energetics of LL-14 binding to the SDS micelle, and salt disfavoured LL-14:SDS binding. The location and the magnitude of the energy minimum (PMF profile, Figure 3.9) that corresponded to the LL-14(P^h):SDS complex appeared to be more or less independent of the salt-concentration, whereas the high energy dissociative state (Plateau in the PMF profile) appeared to be significantly stabilized with the increase of the salt-concentration (**Figure 3.9**). However, it is worth mentioning that the absolute free energy of the LL-14(P^h):SDS complex, as well as the dissociative state (i.e., free LL-14 and free SDS micelle), was not known. Thus, the results only indicated that salt altered the free energy difference (ΔG) between the complex and the unbound state. Salt induced selective stabilization of the dissociative state (i.e., free LL-14 water and peptide-free SDS micelle) was a plausible explanation for ΔG alteration. However, it cannot be directly inferred from the PMF plots (**Figure 3.9**) due to the inherent arbitrariness in the absolute free energy of the complex and the unbound state.

We performed additional MD simulations (**Appendix II Table A3.6 and Figure A3.11**) to estimate LL-14 binding towards neutral DPC micelles in the absence of salt (zwitterionic lipid that mimics mammalian membrane). LL-14 binding to the neutral DPC micelle (ΔG ~ -12 kcal mol^{-1}, **Appendix II Figure A3.11b**) was found to be considerably weaker than negatively charged SDS micelle binding (ΔG = -34 kcal mol^{-1}, **Figure 3.9**), due to obvious electrostatic reasons. The PMF profile of the LL-14:DPC system was found to be shifted to the left with a decrease in the magnitude of the absolute force (**Appendix II Figure A3.11b**) relative to the LL-14:SDS system (**Figure 3.9**), indicating fast and easy

dissociation in the former. Although LL-14 strongly discriminated between SDS and DPC micelles, favouring the former, the negative sign of the estimated binding affinity towards DPC micelles indicated possible cause of cytotoxicity. Previous experimental study (Pandit et al., 2021) indeed confirmed the cytotoxicity of LL-14, in line with the computational prediction.

3.8 Discussion

Recently, we have synthesised and reported salt-sensitive LL-14 as a broad-spectrum antimicrobial agent (Pandit et al., 2021). Previous MD simulations on LL-14 binding to simple membrane mimetic systems (SDS and DPC) showed that the time required for establishing initial contact (related to the forward rate) between LL-14 and SDS micelles systematically increased with the increase in salt concentration. Several experimental studies (Bals et al., 1998; García et al., 2001; Goldman et al., 1997) including our previous work (Ghosh et al., 2021; Pandit et al., 2021) have reported the salt-induced loss of antimicrobial activity of AMP's. However, a detailed thermodynamic analysis associated with the activity loss is grossly lacking in the literature.

In this work, we attempted to elucidate the effects of salt-concentration on the stability of the peptide:micelle complex and capture the general aspect of peptide:membrane interaction to some extent. The energetics of LL-14 (broad-spectrum anti-microbial peptide) binding to SDS micelles was investigated using MD simulations. Based on the CD experiments and computer simulations, LL-14 was previously reported to adopt a random coil (P^c) structure in water and attain a helical (P^h) conformation in response to SDS micelle binding (Ghosh et al., 2021; Pandit et al., 2021). Once LL-14 reached the SDS micelle surface, the peptide initially interacted with the negatively charged sulphate head groups, and then the amphipathic helical conformation was induced that allowed insertion of the hydrophobic face into the bilayer. In our earlier MD study (Ghosh et al., 2021), we proposed the atomic structure of the LL-14(P^h):SDS complex and showed that the MD structure was in excellent agreement with the tryptophan fluorescence and CD experiments. In the LL-14(P^h):SDS complex, non-polar amino acids were buried in the phospholipid core of the micelle, whereas positively charged tips of the amino-acids formed salt-bridges and/or were solvated by water molecules (**Figure 3.7**). The previously proposed structure of the LL-14(P^h):SDS complex was subjected to COM pulling simulation in this work. The pulling process resulted in the secondary structure melting of LL-14 before dissociating from the micelle, in line with our previous CD experiments (Ghosh et al., 2021; Pandit et

al., 2021). The visual examination of the structures corresponding to the high force points in the force profile (**Figure 3.8**) indicated that the interactions between the N-terminal of LL-14 (residues 1-6) and SDS micelle were pre- served. Thus, they are crucial for stability. The salt bridge between the SDS surface and N-terminal tip (NH_3^+) of unstructured LL-14 was the final interaction that needed to be disrupted for complete dissociation. Interestingly, out of the total +7 charge of LL-14, +4 charge was contributed by residues 1-6 (N-terminal tip is NH_3^+, charge = + 1). Hence, the higher positive charge density of the N terminus played a dominant role in stabilizing the complex due to strong electrostatic interactions. Interactions between the C-terminal of LL-14 (residues 7-14) and the SDS micelle were relatively weaker (note, C-terminal is neutral -$CONH_2$) than those for the N-terminal part, which resulted in the early disruption during the pulling simulations. The hydrophobic interactions certainly contributed to the overall stability of the complex, but the hydrophobic content was identical between the N-terminal (residues 1-7) and C-terminal (residues 8-14) region of LL-14. It appeared that the LL-14:SDS complex became substantially unstable if the N-terminal (residues 1-6):SDS interactions were perturbed and underwent facile dissociation after disrupting the final L1-SDS salt-bridge (**Figure 3.8**), as hypothesized earlier (Ghosh et al., 2021). The sequence of events and interaction network observed in the high-force points during the pulling process were independent of salt concentration. The visual examination of the COM pulling trajectories confirmed that the dissociation paths were independent of the simulation setup parameters (pulling velocity, sampling, etc.). The reduction of the height of the force profile suggested that it was easier to pull LL-14 from the SDS micelle with the increase in the salt concentration (**Figure 3.8**). The LL-14:SDS binding free energy was estimated from the PMF profile (**Figure 3.9**). The PMF profiles unambiguously indicated that the LL-14 binding to the SDS micelle was most favourable in the absence of salt (ΔG = -34 kcal mol^{-1}), while the affinity diminished in the presence of salt (ΔG = -26 kcal mol^{-1} and -22 kcal mol^{-1} in the presence of 0.5% w/v and 1.0% w/v NaCl, respectively). The overall shape of the PMFs was preserved among the various independent replicas differing in initial conditions (see Method section) and independent of the salt-concentration, thus implying the convergence of the umbrella sampling simulations (**Figure 3.9**).

The effect of salt on the dissociative state and the complex could be assessed using the appropriate thermodynamic cycle (TC) described in **Figure 3.10a**. The peptide:micelle

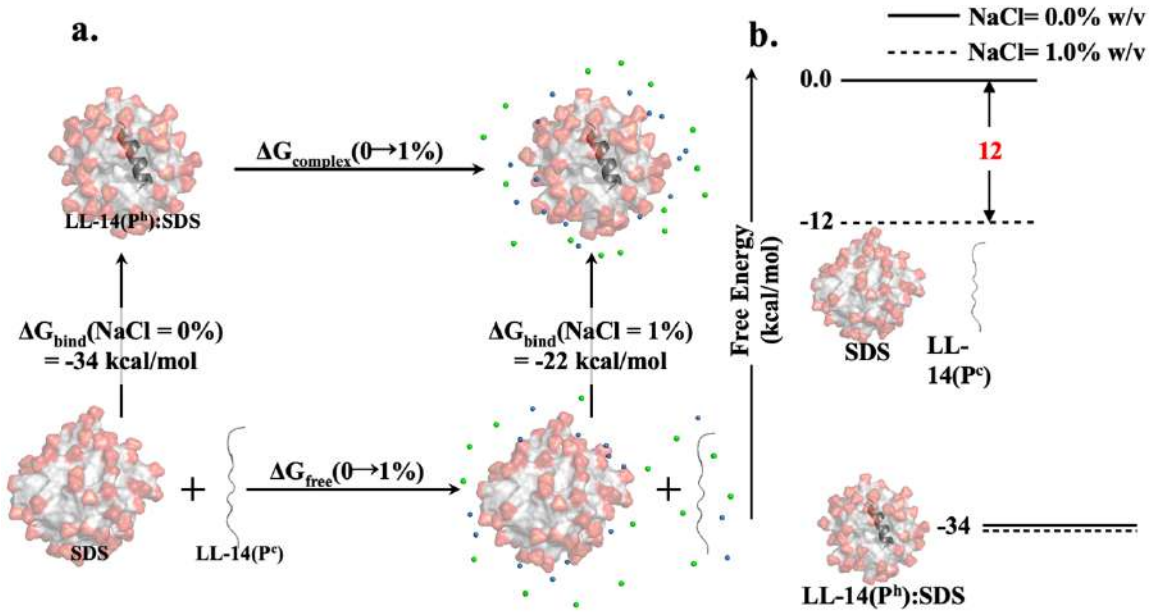

Figure 3.10: (a) Thermodynamic cycle for protein:micelle binding in the absence and presence of salt. Vertical legs correspond to the peptide:micelle binding (in the absence of salt: left-side, in the presence of salt: right-side); horizontal legs correspond to the transformation of the salt environment from 0% to 1%, either in the protein:micelle complex (above) or in the dissociative/free state (below). Free energy is a state function, thus: $\Delta\Delta G = \Delta G_{complex}(0 - 1\%)\ \Delta G_{free}(0 - 1\%) = \Delta G_{bind}(1\%)\ \Delta G_{bind}(0\%)$. (b) Schematic free energy diagram of LL-14 binding to SDS micelles, illustrating altered free energy difference (by +12 kcal mol^{-1}) between the bound and dissociative state as a result of selective salt-stabilization of the dissociative state (i.e., free LL-14 and free SDS).

binding free energy was estimated using umbrella sampling in the absence (left vertical leg of TC, $\Delta G_{bind}(0\%)$ = -34 kcal mol^{-1}) and presence (right vertical leg of TC, $\Delta G_{bind}(1\%)$ = -22 kcal mol^{-1}) of salt. We could compare the effect of salt on the complex (upper horizontal arm of TC, $\Delta G_{complex}(0 - 1\%)$ and the dissociative state (lower horizontal arm of TC, $\Delta G_{free}(0 - 1\%)$), by subtracting the estimated free energies of the vertical legs of the thermodynamic cycle. Thus, the double free energy difference was estimated as: $\Delta\Delta G = \Delta G_{complex}(0 - 1\%)\ \Delta G_{free}(0 - 1\%) = \Delta G_{bind}(1\%)\ \Delta G_{bind}(0\%)$ = +12 kcal mol^{-1}. As both the complex and dissociative states were charged, increase in salt concentration (0 - 1%) would stabilize both the complex and the dissociative state by charge shielding. Thus, the sign of the horizontal arms ($\Delta G_{complex}(0 - 1\%)$, $\Delta G_{free}(0 - 1\%)$) was expected to be negative. Large positive $\Delta\Delta G$ = +12 kcal mol^{-1} unambiguously suggested that the change in the ionic environment (0 - 1% NaCl) was energetically more favourable for the dissociative state relative to the peptide:micelle complex. Thus, salt-induced stabilization of the dissociative state was way more prominent relative to the peptide:micelle complex. Charge separation

in the dissociative state (i.e., free LL-14 and free SDS micelle) was stabilized by the salt-counterions. The addition of NaCl was shown to decrease the zeta-potential of the SDS micelles significantly (implying a reduction in the surface charge) and improve the generation and stability of SDS bubbles (Abdulelah et al., 2020; Sammalkorpi et al., 2009; Xu et al., 2009). Moreover, salt not only altered the micelle parameters but also modified the rate of exchange between the SDS micelles and solute (Rharbi & Winnik, 2002). The salt- induced loss of antimicrobial activity of related peptides (Bals et al., 1998; García et al., 2001; Goldman et al., 1997) including LL-14 (Pandit et al., 2021) and the salt-induced stability of the SDS micelles (Abdulelah et al., 2020; Naskar et al., 2013; Rharbi & Winnik, 2002; Sammalkorpi et al., 2009; Xu et al., 2009) was in line with the proposed selective stability of the dissociative state. Salt increases the viscosity of the medium and screens the overall charges of the reactants, and slows down the diffusion. Previously, we studied LL-14(P^c) binding to SDS micelles and reported that the time (t) required for establishing the initial contact between LL-14(P^c) and the SDS micelles systematically increased with the increase of NaCl concentration (Ghosh et al., 2021). The observed time delay was a robust feature of the simulations, which indicated slow diffusion for the peptide:micelle binding in the presence of salt. Thus, we proposed an energetic scheme (**Figure 3.10b**), which suggested that salt primarily stabilized the dissociative state, increased the activation barrier (of diffusion origin) for the binding event, reduced the forward rate, and altered the equilibrium constant (alteration of backward rate is unnecessary). However, it did not exclude the possibility of fine-tuning the backward rate (dissociation event, slower in the presence of salt).

In summary, salt facilitated LL-14:SDS dissociation by selectively stabilizing the dissociative state. Classical MD simulations of LL-14 binding to SDS micelles are limited by oversimplified bacterial membrane mimics, the ignored effect of various salts other than NaCl, the absence of explicit polarizability (force-filed accuracy), sampling issues, etc. Nevertheless, the computational investigations on simple model systems (SDS, DPC) could emphasize the effect of salt in altering the thermodynamics of peptide binding and provide a plausible explanation for the salt-induced loss of antimicrobial activity of cationic peptides in general.

3.9 Conclusion

The thermodynamics of a cationic 14 residue long antimicrobial peptide (LL-14) binding to SDS micelles at various salt concentrations were investigated using MD simulations. We

found that interactions between the N-terminal region of LL-14 (residues 1-6) and the SDS micelle were critical to the stability of the peptide:micelle complex. The peptide:micelle binding was disfavoured in the presence of salt. Our results conclusively showed that salt primarily stabilized the dissociative state, which might significantly increase the activation barrier for the binding event leading to weak binding affinity. In this paper, we attempted to provide a plausible explanation for the salt-induced loss of antimicrobial activity of LL-14, which might be relevant for other cationic peptides and micelle mimetic systems in general.

3.10 Supporting Information

This chapter contains supporting data given in **Appendix II**.

REFERENCES

Abdulelah, H., Negash, B. M., Yekeen, N., Al-Hajri, S., Padmanabhan, E., & Al-Yaseri, A. (2020). Synergetic Effect of Surfactant Concentration, Salinity, and Pressure on Adsorbed Methane in Shale at Low Pressure: An Experimental and Modeling Study. *ACS Omega*, *5*(32), 20107–20121. https://doi.org/10.1021/ACSOMEGA.0C01738

Abe, M., Kato, K., & Ogino, K. (1989). Effects of inorganic electrolytes and of pH on micelle formation of amphoteric-anionic mixed surfactant systems. *Journal of Colloid and Interface Science*, *127*(2), 328–335. https://doi.org/10.1016/0021-9797(89)90038-6

Ahmed, M. C., Papaleo, E., & Lindorff-Larsen, K. (2018). How well do force fields capture the strength of salt bridges in proteins? *PeerJ*, *2018*(6). https://doi.org/10.7717/peerj.4967

Alvares, D. dos S., Martins, I. B. S., Viegas, T. G., Palma, M. S., Araujo, A. S. de, Carvalho, S. J. de, & Neto, J. R. (2021). Modulatory Effects of Acidic pH and Membrane Potential on the Adsorption of pH-Sensitive Peptides to Anionic Lipid Membrane. *Membranes 2021, Vol. 11, Page 307*, *11*(5), 307. https://doi.org/10.3390/MEMBRANES11050307

Bals, R., Wang, X., Wu, Z., Freeman, T., Bafna, V., Zasloff, M., & Wilson, J. M. (1998). Human beta-defensin 2 is a salt-sensitive peptide antibiotic expressed in human lung. *The Journal of Clinical Investigation*, *102*(5), 874–880. https://doi.org/10.1172/JCI2410

Bendedouch, D., Chen, S. H., & Koehler, W. C. (1983). Structure of ionic micelles from small angle neutron scattering. *J. Phys. Chem.; (United States)*, *87:1*(1), 153–159. https://doi.org/10.1021/J100224A033

Berendsen, H. J. C., Postma, J. P. M., van Gunsteren, W. F., Dinola, A., & Haak, J. R. (1984). Molecular dynamics with coupling to an external bath. *The Journal of Chemical Physics*, *81*(8), 3684–3690. https://doi.org/10.1063/1.448118

Berglund, N. A., Piggot, T. J., Jefferies, D., Sessions, R. B., Bond, P. J., & Khalid, S. (2015). Interaction of the Antimicrobial Peptide Polymyxin B1 with Both Membranes of E. coli: A Molecular Dynamics Study. *PLOS Computational Biology*, *11*(4), e1004180. https://doi.org/10.1371/JOURNAL.PCBI.1004180

Bogusz, S., Venable, R. M., & Pastor, R. W. (2000). Molecular dynamics simulations of octyl glucoside micelles: Structural properties. *Journal of Physical Chemistry B*, *104*(23), 5462–5470. https://doi.org/10.1021/jp000159y

Bruce, C. D., Berkowitz, M. L., Perera, L., & Forbes, M. D. E. (2002). Molecular dynamics simulation of sodium dodecyl sulfate micelle in water: Micellar structural characteristics and counterion distribution. *Journal of Physical Chemistry B*, *106*(15), 3788–3793. https://doi.org/10.1021/jp013616z

Bussi, G., Donadio, D., & Parrinello, M. (2007). Canonical sampling through velocity rescaling. *The Journal of Chemical Physics*, *126*(1), 014101. https://doi.org/10.1063/1.2408420

Carvalheda, C. A., Campos, S. R. R., & Baptista, A. M. (2015). The Effect of Membrane Environment on Surfactant Protein C Stability Studied by Constant-pH Molecular Dynamics. *Journal of Chemical Information and Modeling*, *55*(10), 2206–2217. https://doi.org/10.1021/ACS.JCIM.5B00076

Carvalheda, C. A., Campos, S. R. R., Machuqueiro, M., & Baptista, A. M. (2013). Structural Effects of pH and Deacylation on Surfactant Protein C in an Organic Solvent Mixture: A Constant-pH MD Study. *Journal of Chemical Information and Modeling*, *53*(11), 2979–2989. https://doi.org/10.1021/CI400479C

Cheng, X., Jo, S., Lee, H. S., Klauda, J. B., & Im, W. (2013). CHARMM-GUI micelle builder for pure/mixed micelle and protein/micelle complex systems. *Journal of Chemical Information and Modeling*, *53*(8), 2171–2180. https://doi.org/10.1021/CI4002684/SUPPL_FILE/CI4002684_SI_001.PDF

Croonen, Y., Geladé, E., van der Zegel, M., van der Auweraer, M., Vandendriessche, H., de Schryver, F. C., & Almgren, M. (1983). Influence of salt, detergent concentration, and temperature on the fluorescence quenching of 1-methylpyrene in sodium dodecyl-sulfate with meta-dicyanobenzene. *Journal of Physical Chemistry* , *87*(8), 1426–1431. https://doi.org/10.1021/J100231A029

Darden, T., York, D., & Pedersen, L. (1993). Particle mesh Ewald: An N·log(N) method for Ewald sums in large systems. *The Journal of Chemical Physics*, *98*(12), 10089–10092. https://doi.org/10.1063/1.464397

D. Ristroph, K., & K. Prud'homme, R. (2019). Hydrophobic ion pairing: encapsulating small molecules, peptides, and proteins into nanocarriers. *Nanoscale Advances*, *1*(11), 4207–4237. https://doi.org/10.1039/C9NA00308H

Durell, S. R., Brooks, B. R., & Ben-Naim, A. (1994). Solvent-induced forces between two hydrophilic groups. *Journal of Physical Chemistry*, *98*(8), 2198–2202. https://doi.org/10.1021/J100059A038/ASSET/J100059A038.FP.PNG_V03

Efron, B. (1992). *Bootstrap Methods: Another Look at the Jackknife* (pp. 569–593). Springer, New York, NY. https://doi.org/10.1007/978-1-4612-4380-9_41

García, J.-R. C., Krause, A., Schulz, S., Rodríguez-Jiménez, F.-J., Klüver, E., Adermann, K., Forssmann, U., Frimpong-Boateng, A., Bals, R., & Forssmann, W.-G. (2001). Human β-defensin 4: a novel inducible peptide with a specific salt-sensitive spectrum of antimicrobial activity. *The FASEB Journal*, *15*(10), 1819–1821. https://doi.org/10.1096/FJ.00-0865FJE

Ghosh, S., Pandit, G., Debnath, S., Chatterjee, S., & Satpati, P. (2021). Effect of monovalent salt concentration and peptide secondary structure in peptide-micelle binding. *RSC Advances*, *11*(58), 36836–36849. https://doi.org/10.1039/D1RA06772A

Goldman, M. J., Anderson, G. M., Stolzenberg, E. D., Kari, U. P., Zasloff, M., & Wilson, J. M. (1997). Human beta-defensin-1 is a salt-sensitive antibiotic in lung that is inactivated in cystic fibrosis. *Cell*, *88*(4), 553–560. https://doi.org/10.1016/S0092-8674(00)81895-4

Hess, B. (2008). P-LINCS: A parallel linear constraint solver for molecular simulation. *Journal of Chemical Theory and Computation*, *4*(1), 116–122. https://doi.org/10.1021/ct700200b

Hess, B., Bekker, H., Berendsen, H. J. C., & Fraaije, J. G. E. M. (1997). LINCS: A linear constraint solver for molecular simulations. *Journal of Computational Chemistry*. https://doi.org/10.1002/(SICI)1096-987X(199709)18:12<1463::AID-JCC4>3.0.CO;2-H

Huang, J., & Mackerell, A. D. (2013). CHARMM36 all-atom additive protein force field: Validation based on comparison to NMR data. *Journal of Computational Chemistry*. https://doi.org/10.1002/jcc.23354

Hub, J. S., de Groot, B. L., & van der Spoel, D. (2010). g_wham—A Free Weighted Histogram Analysis Implementation Including Robust Error and Autocorrelation Estimates. *Journal of Chemical Theory and Computation*, *6*(12), 3713–3720. https://doi.org/10.1021/CT100494Z

Isom, D. G., Castañeda, C. A., Cannon, B. R., & E., B. G.-M. (2011). Large shifts in pKa values of lysine residues buried inside a protein. *Proceedings of the National Academy of Sciences*, *108*(13), 5260–5265. https://doi.org/10.1073/PNAS.1010750108

Itri, R., & Amaral, L. Q. (1991). Distance distribution function of sodium dodecyl sulfate micelles by X-ray scattering. *Journal of Physical Chemistry*, *95*(1), 423–427. https://doi.org/10.1021/j100154a074

Izrailev, S., Stepaniants, S., Isralewitz, B., Kosztin, D., Lu, H., Molnar, F., Wriggers, W., & Schulten, K. (1999). *Steered Molecular Dynamics*. Springer, Berlin, Heidelberg. https://doi.org/10.1007/978-3-642-58360-5_2

Jarzynski, C. (1997). Nonequilibrium equality for free energy differences. *Physical Review Letters*, *78*(14), 2690–2693. https://doi.org/10.1103/PhysRevLett.78.2690

Jo, S., Kim, T., Iyer, V. G., & Im, W. (2008). CHARMM-GUI: a web-based graphical user interface for CHARMM. *Journal of Computational Chemistry*, *29*(11), 1859–1865. https://doi.org/10.1002/jcc.20945

Jorgensen, W. L., Chandrasekhar, J., Madura, J. D., Impey, R. W., & Klein, M. L. (1983). Comparison of simple potential functions for simulating liquid water. *The Journal of Chemical Physics*, *79*(2), 926–935. https://doi.org/10.1063/1.445869

Kabsch, W., & Sander, C. (1983). Dictionary of protein secondary structure: Pattern recognition of hydrogen-bonded and geometrical features. *Biopolymers*, *22*(12), 2577–2637. https://doi.org/10.1002/BIP.360221211

Kajander, T., Kahn, P. C., Passila, S. H., Cohen, D. C., Lehtiö, L., Adolfsen, W., Warwicker, J., Schell, U., & Goldman, A. (2000). Buried charged surface in proteins. *Structure*, *8*(11), 1203–1214. https://doi.org/10.1016/S0969-2126(00)00520-7

Kandasamy, S. K., & Larson, R. G. (2004). Binding and insertion of alpha-helical anti-microbial peptides in POPC bilayers studied by molecular dynamics simulations. *Chemistry and Physics of Lipids*, *132*(1), 113–132. https://doi.org/10.1016/J.CHEMPHYSLIP.2004.09.011

Khandelia, H., & Kaznessis, Y. N. (2005). Molecular dynamics simulations of helical antimicrobial peptides in SDS micelles: What do point mutations achieve? *Peptides*, *26*(11), 2037–2049. https://doi.org/10.1016/j.peptides.2005.03.058

Khandelia, H., & Kaznessis, Y. N. (2006). Molecular dynamics investigation of the influence of anionic and zwitterionic interfaces on antimicrobial peptides' structure: Implications for peptide toxicity and activity. *Peptides*, *27*(6), 1192–1200. https://doi.org/10.1016/j.peptides.2005.10.022

Khandelia, H., Langham, A. A., & Kaznessis, Y. N. (2006). Driving engineering of novel antimicrobial peptides from simulations of peptide–micelle interactions. *Biochimica et Biophysica Acta (BBA) - Biomembranes*, *1758*(9), 1224–1234. https://doi.org/10.1016/J.BBAMEM.2006.03.010

Kumar, S., Rosenberg, J. M., Bouzida, D., Swendsen, R. H., & Kollman, P. A. (1992). The weighted histogram analysis method for free-energy calculations on biomolecules. I. *Journal of Computational Chemistry*, *13*(8), 1011–1021. https://doi.org/10.1002/JCC.540130812

Langham, A. A., Khandelia, H., & Kaznessis, Y. N. (2006). How can a β-sheet peptide be both a potent antimicrobial and harmfully toxic? Molecular dynamics simulations of protegrin-1 in micelles. *Biopolymers - Peptide Science Section*, *84*(2), 219–231. https://doi.org/10.1002/bip.20397

Lebecque, S., Crowet, J. M., Nasir, M. N., Deleu, M., & Lins, L. (2017). Molecular dynamics study of micelles properties according to their size. *Journal of Molecular Graphics and Modelling*, *72*, 6–15. https://doi.org/10.1016/j.jmgm.2016.12.007

Lee, B., & Richards, F. M. (1971). The interpretation of protein structures: Estimation of static accessibility. *Journal of Molecular Biology*, *55*(3). https://doi.org/10.1016/0022-2836(71)90324-X

Lemkul, J. A., & Bevan, D. R. (2010). Assessing the stability of Alzheimer's amyloid protofibrils using molecular dynamics. *The Journal of Physical Chemistry. B*, *114*(4), 1652–1660. https://doi.org/10.1021/JP9110794

Lensink, M. F., Christiaens, B., Vandekerckhove, J., Prochiantz, A., & Rosseneu, M. (2005). Penetratin-membrane association: W48/R52/W56 shield the peptide from the aqueous phase. *Biophysical Journal*, *88*(2), 939–952. https://doi.org/10.1529/biophysj.104.052787

Lide, D. R. (1991). *CRC handbook of chemistry and physics : a ready-reference book of chemical and phyical data*.

Lindahl, E., Hess, B., & van der Spoel, D. (2001). GROMACS 3.0: A package for molecular simulation and trajectory analysis. In *Journal of Molecular Modeling* (Vol. 7, Issue 8, pp. 306–317). https://doi.org/10.1007/S008940100045

MacKerell, A. D. (1995). Molecular dynamics simulation analysis of a sodium dodecyl sulfate micelle in aqueous solution: Decreased fluidity of the micelle hydrocarbon interior. *Journal of Physical Chemistry*, *99*(7), 1846–1855. https://doi.org/10.1021/j100007a011

Magalhães, P. R., Machuqueiro, M., & Baptista, A. M. (2015). Constant-pH Molecular Dynamics Study of Kyotorphin in an Explicit Bilayer. *Biophysical Journal*, *108*(9), 2282–2290. https://doi.org/10.1016/J.BPJ.2015.03.052

Morrow, B. H., Koenig, P. H., & Shen, J. K. (2012). Atomistic simulations of pH-dependent self-assembly of micelle and bilayer from fatty acids. *The Journal of Chemical Physics*, *137*(19), 194902. https://doi.org/10.1063/1.4766313

Morrow, B. H., Koenig, P. H., & Shen, J. K. (2013). Self-Assembly and Bilayer–Micelle Transition of Fatty Acids Studied by Replica-Exchange Constant pH Molecular Dynamics. *Langmuir*, *29*(48), 14823–14830. https://doi.org/10.1021/LA403398N

Naskar, B., Dey, A., & Moulik, S. P. (2013). Counter-ion Effect on Micellization of Ionic Surfactants: A Comprehensive Understanding with Two Representatives, Sodium Dodecyl Sulfate (SDS) and Dodecyltrimethylammonium Bromide (DTAB). *Journal of Surfactants and Detergents*, *16*(5), 785–794. https://doi.org/10.1007/S11743-013-1449-1

Pandit, G., Biswas, K., Ghosh, S., Debnath, S., Bidkar, A. P., Satpati, P., Bhunia, A., & Chatterjee, S. (2020). Rationally designed antimicrobial peptides: Insight into the mechanism of eleven residue peptides against microbial infections. *Biochimica et Biophysica Acta. Biomembranes*, *1862*(4). https://doi.org/10.1016/J.BBAMEM.2020.183177

Pandit, G., Chowdhury, N., Abdul Mohid, S., Bidkar, A. P., Bhunia, A., & Chatterjee, S. (2021). Effect of Secondary Structure and Side Chain Length of Hydrophobic Amino Acid Residues on the Antimicrobial Activity and Toxicity of 14-Residue-Long de novo AMPs. *ChemMedChem*, *16*(2), 355–367. https://doi.org/10.1002/CMDC.202000550

Pandit, G., Ilyas, H., Ghosh, S., Bidkar, A. P., Mohid, S. A., Bhunia, A., Satpati, P., & Chatterjee, S. (2018). Insights into the Mechanism of Antimicrobial Activity of Seven-Residue Peptides. *Journal of Medicinal Chemistry*, *61*(17), 7614–7629. https://doi.org/10.1021/ACS.JMEDCHEM.8B00353/SUPPL_FILE/JM8B00353_SI_001.CSV

Parrinello, M., & Rahman, A. (1981). Polymorphic transitions in single crystals: A new molecular dynamics method. *Journal of Applied Physics*, *52*(12), 7182–7190. https://doi.org/10.1063/1.328693

Rahman, A., & Brown, C. W. (1983). Effect of pH on the critical micelle concentration of sodium dodecyl sulphate. *Journal of Applied Polymer Science*, *28*(4), 1331–1334. https://doi.org/10.1002/APP.1983.070280407

Rakitin, A. R., & Pack, G. R. (2004). Molecular dynamics simulations of ionic interactions with dodecyl sulfate micelles. *Journal of Physical Chemistry B*, *108*(8), 2712–2716. https://doi.org/10.1021/JP030914I/ASSET/IMAGES/LARGE/JP030914IF00006.JPEG

Ramachandran, G. N., Ramakrishnan, C., & Sasisekharan, V. (1963). Stereochemistry of polypeptide chain configurations. *Journal of Molecular Biology*, *7*(1), 95–99. https://doi.org/10.1016/S0022-2836(63)80023-6

Rharbi, Y., & Winnik, M. A. (2002). Salt effects on solute exchange in sodium dodecyl sulfate micelles. *Journal of the American Chemical Society*, *124*(10), 2082–2083. https://doi.org/10.1021/JA0123397/ASSET/IMAGES/LARGE/JA0123397F00002.JPEG

Sammalkorpi, M., Karttunen, M., & Haataja, M. (2009). Ionic surfactant aggregates in saline solutions: sodium dodecyl sulfate (SDS) in the presence of excess sodium chloride (NaCl) or calcium chloride (CaCl(2)). *The Journal of Physical Chemistry. B*, *113*(17), 5863–5870. https://doi.org/10.1021/JP901228V

Schrödinger, LLC. (2010). *The PyMOL Molecular Graphics System, Version 2.4.0*. https://pymol.org/2/

Shai, Y. (1999). Mechanism of the binding, insertion and destabilization of phospholipid bilayer membranes by alpha-helical antimicrobial and cell non-selective membrane-lytic peptides. *Biochimica et Biophysica Acta*, *1462*(1–2), 55–70. https://doi.org/10.1016/S0005-2736(99)00200-X

Shelley, J., Watanabe, K., & Klein, M. L. (1990). Simulation of a sodium dodecylsulfate micelle in aqueous solution. *International Journal of Quantum Chemistry*, *38*(17 S), 103–117. https://doi.org/10.1002/qua.560381713

Shepherd, C. M., Vogel, H. J., & Tieleman, D. P. (2003). Interactions of the designed antimicrobial peptide MB21 and truncated dermaseptin S3 with lipid bilayers: molecular-dynamics simulations. *Biochemical Journal*, *370*(Pt 1), 233. https://doi.org/10.1042/BJ20021255

Teixeira, V. H., Vila-Viçosa, D., Reis, P. B. P. S., & Machuqueiro, M. (2016). pKa Values of Titrable Amino Acids at the Water/Membrane Interface. *Journal of Chemical Theory and Computation*, *12*(3), 930–934. https://doi.org/10.1021/ACS.JCTC.5B01114

Ulmschneider, J. P. (2017). Charged Antimicrobial Peptides Can Translocate across Membranes without Forming Channel-like Pores. *Biophysical Journal*, *113*(1), 73–81. https://doi.org/10.1016/J.BPJ.2017.04.056

Vila-Viçosa, D., Silva, T. F. D., Slaybaugh, G., Reshetnyak, Y. K., Andreev, O. A., & Machuqueiro, M. (2018). Membrane-Induced p Ka Shifts in wt-pHLIP and Its L16H Variant. *Journal of Chemical Theory and Computation*, *14*(6), 3289–3297. https://doi.org/10.1021/ACS.JCTC.8B00102/ASSET/IMAGES/LARGE/CT-2018-001023_0006.JPEG

Vila-Viçosa, D., Teixeira, V. H., Baptista, A. M., & Machuqueiro, M. (2015). Constant-pH MD Simulations of an Oleic Acid Bilayer. *Journal of Chemical Theory and Computation*, *11*(5), 2367–2376. https://doi.org/10.1021/ACS.JCTC.5B00095

Wang, Q., Hong, G., Johnson, G. R., Pachter, R., & Cheung, M. S. (2010). Biophysical properties of membrane-active peptides based on micelle modeling: a case study of cell-penetrating and antimicrobial peptides. *The Journal of Physical Chemistry. B*, *114*(43), 13726–13735. https://doi.org/10.1021/JP1069362

Xu, Q., Nakajima, M., Ichikawa, S., Nakamura, N., Roy, P., Okadome, H., & Shiina, T. (2009). Effects of surfactant and electrolyte concentrations on bubble formation and stabilization. *Journal of Colloid and Interface Science*, *332*(1), 208–214. https://doi.org/10.1016/J.JCIS.2008.12.044

Chapter 4

Stability of AMP:micelle system upon Leu/Val mutation

In our previous chapter we had reported a synthetic positively charged leucine-rich 14 residue long anti-microbial peptide (LL-14: NH_3^+-LKWLKKLLKWLKKL-$CONH_2$), which was highly active as well as cytotoxic relative to its valine analogue (VV-14). However, the thermodynamics underlying this differential toxicity and antimicrobial activity was unclear. Understanding the energetics of peptide binding to micelles (simplest membrane mimic, viz. SDS as bacterial membrane, DPC as eukaryotic membrane) and the effect of Leu → Val peptide mutations on the stability of the peptide:micelle complexes are of great academic and industrial interest and relevant for the rational design of potent and selective anti-microbial peptides for therapeutic use. Here, we have reported the molecular dynamics free energy simulations that allowed us to quantitatively estimate the strength of peptide discrimination (based on single or multiple-site Leu/Val mutations in LL-14) by membrane mimetic micelles (SDS and DPC) and decipher the energetics underlying peptide selectivity by micelles. Leu-containing peptide (LL-14) was found to be preferred for micelle (SDS, DPC) binding relative to its Val-analogues (single or multiple Val-mutants). The strength of the preference depends on the position of the Leu/Val mutation in the peptide. Surprisingly, the N-terminal LL-14 single mutation (Leu → Val: L1V) was found to fine-tune the electrostatic interactions resulting in the highest peptide selectivity (ΔΔG ~8 kcal/mol for both SDS and DPC). However, the mechanism of L1V peptide selectivity was distinctly different for SDS and DPC micelles. SDS ensured high selectivity by disrupting peptide:micelle salt-bridge, whereas DPC desolvated the broken-peptide-backbone-hydrogen bond in V1-peptide:micelle complex. Mutations (Leu → Val) in the middle positions of the LL-14 (4^{th}, 7^{th}, 8^{th}, and 11^{th}) were disfavored by the micelles primarily due to the loss of peptide:micelle hydrophobic interactions. Peptides differing at the C-terminal (i.e., L14V) were recognized by SDS micelle (ΔΔG ~4 kcal/mol) by altering peptide:micelle interactions. L14V mutation on the other hand did not play any role in the peptide:DPC binding, as no direct interactions between the C-terminal and DPC micelle were observed due to obvious electrostatic reasons. The strength of selectivity favoring LL-14 binding against VV-14 was found to be much higher for DPC micelle (ΔΔG ~25 kcal/mol) relative to SDS micelle (ΔΔG ~19 kcal/mol). Loss of the peptide:micelle

hydrophobic contact in response to LL-14 → VV-14 mutation was found to be significantly larger for DPC relative to SDS micelles, resulting in higher discriminatory power for the former. Peptide:SDS salt-bridges seemed to prevent the loss of peptide:micelle hydrophobic contact to some extent leading to weaker selectivity for SDS micelle. High-selectivity of DPC micelle provided an efficient mechanism for VV-14 dissociation from DPC micelle, whereas, low-selectivity of SDS micelle ensured binding of both LL-14 and VV-14. To the best of our knowledge, this is the first study in which the experimental observations (antimicrobial activity, toxicity) between leucine-rich and valine-rich peptides have been explained by establishing a direct link between the energetics and structures.

4.1 Background

Antimicrobial activity, hemolytic activity, and cytotoxicity of AMPs depend on the leucine (Béven et al., 2003; Ezugwu et al., 2020; Ma et al., 2011; Pandit et al., 2018, 2021; Park et al., 2003, 2006) or valine (Deslouches et al., 2005; Ezugwu et al., 2020; Pandit et al., 2021) content and have been widely explored. Distinctly high antimicrobial activities for the leucine peptides compared to their valine analogs have been reported. However, the direct correlation between the differential biological activities observed for Leu/Val-containing peptides and the peptide:- membrane interaction is unknown. Previously, we demonstrated that a 14-residue-long leucine-rich AMP (LL-14: LKWLKKLLKWLKKL) displayed stronger antimicrobial activity relative to its valine analogue (VV-14) (Pandit et al., 2021). Moreover, LL-14 was found to be cytotoxic in contrast to VV-14 (Pandit et al., 2021). A decrease in the peptide's hydrophobicity (Chen et al., 2002; FAUCHERE, 1983; Ma et al., 2011) in response to Leu → Val mutation was certainly linked to the observed differential antimicrobial activity, but the mechanism and its link to the atomic structure of peptide:micelle complexes were not understood. Understanding the mechanism of peptide interactions with simple membrane mimetic systems (micelles, bilayer) using molecular dynamics (MD) simulations could partially fill the gap (Berglund et al., 2015; Ghosh et al., 2021; Kandasamy & Larson, 2004; Khandelia et al., 2006; la Rocca et al., 1999; Langham et al., 2007; Pandit et al., 2020; Shai, 1999; Shepherd et al., 2001; Ulmschneider, 2017; Wang et al., 2010; Wymore & Wong, 2000) and delineate the underlying principle of the relatively complicated event of peptide: microbe interactions. In this chapter we have reported a detailed thermodynamic analysis underlying the stability of peptide:micelle complexes and their link to leucine → valine mutations. We estimated the relative binding free energy (ΔΔG) of leucine- and valine-containing peptides (LL-14 and their analogues)

to most simple membrane mimetic model systems (SDS, DPC micelle) using MD free energy (MDFE) calculations. Moreover, a direct link between the estimated energetics of peptide selectivity (ΔΔG) and the atomic structure of Leu/Val peptide:micelle complexes has been established. A qualitative correlation between the computational and previous experimental studies has been demonstrated in this study.

4.2 Materials and Methods

4.2.1 System preparation

A free peptide (LL-14 or VV-14) in water was shown to adopt the unstructured random coil conformation, which attained helical conformation (P^h) in response to SDS binding (Pandit et al., 2021). The structure of the peptide:micelle complex was proposed previously from MD simulation that could explain the experimental (CD, fluorescence) observations. LL-14 was initially placed away from the micelle, and the resulting structure was subjected to MD simulation (minimum of 10 ns to a maximum of 6 μs production MD). The MD structures of the peptide:micelle complexes obtained from the production dynamics were confirmed to be robust and independent of the simulation setup (varying the initial peptide:micelle distance, the orientation of the peptide relative to micelles, and initial velocities) (Ghosh et al., 2021). Thus, previously proposed MD structures of the LL-14(P^h):micelle complex were used as a template for estimating binding affinity differences, where the free peptide in water was modelled as the random coil. The free peptide or the peptide:micelle complex was kept at the center of a solvated water box of dimension 8 × 8 × 8 nm^3. The LL-14 peptide consisted of six leucine amino acids (L1, L4, L7, L8, L11, and L14). In this study, we performed single or multiple alchemical transformations (leucine to valine) of the peptide in complex with micelles or free in the water. All simulations were performed using the GROMACS (van der Spoel et al., 2005) v2019.6 package with the CHARMM36 forcefield (Best et al., 2012; Klauda et al., 2010) and TIP3P water model (Durell et al., 1994; Jorgensen et al., 1998) at the *NPT* ensemble (temp = 300 K and pressure = 1 bar), as described previously (Ghosh et al., 2021). The simulation parameters adopted for this work are given in **Appendix III Table A4.1**.

4.2.2 Free Energy Simulation

Binding free energy differences of peptide mutation (L → V) in the peptide:micelle complex were calculated employing the Bennett acceptance-ratio (BAR) method (Bennett, 1976) as implemented in GROMACS (van der Spoel et al., 2005). L to V mutations were

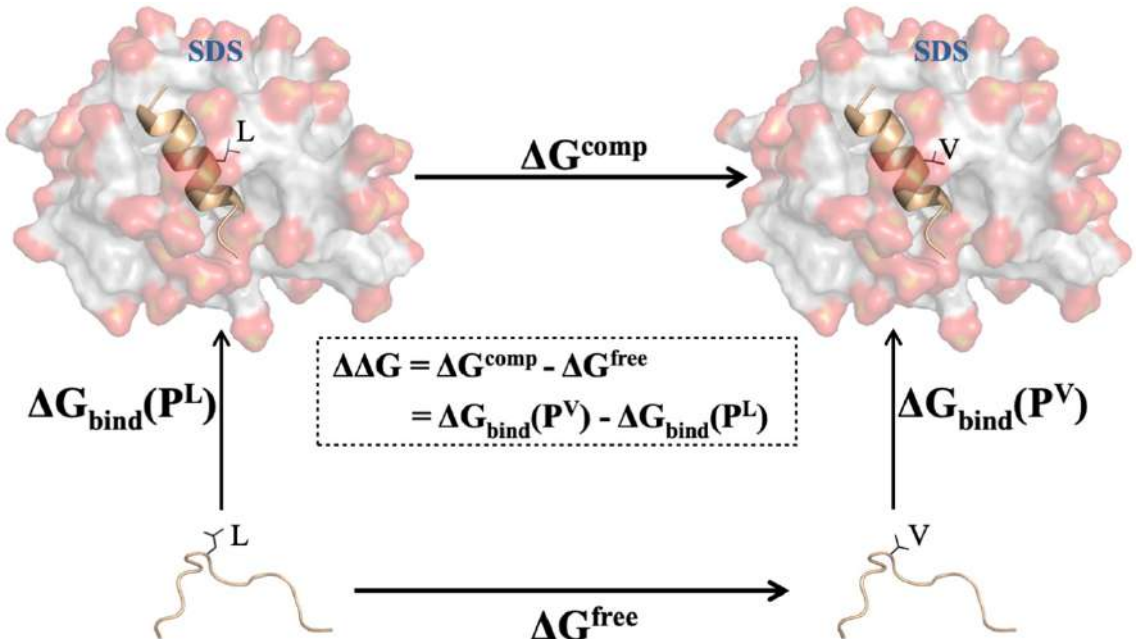

Figure 4.1: Thermodynamic cycle for studying micelle:peptide binding. Vertical legs correspond to binding; horizontal legs correspond to the alchemical transformation of the peptide side chain from leucine (L) into valine (V), either in the micelle (upper) or free in water (lower). The Leu peptide(P^L)/Val peptide(P^V) binding free energy difference is $\Delta\Delta G = \Delta G^{comp} - \Delta G^{free} = \Delta G_{bind}(P^L) - \Delta G_{bind}(P^V)$. Based on our previous experiments, we confirmed that free LL-14 adopted helical conformation only after micelle binding; thus, a random coil structure was considered for leucine to valine transformation in the lower horizontal arm (ΔG^{free}).

introduced at all six positions (L1, L4, L7, L8, L11, and L14) for the LL-14(α-helical):SDS/DPC complexes (upper-arm, **Figure 4.1**). The corresponding simulations were also performed for the free unstructured peptide (LL-14) in water for estimating $\Delta\Delta G$ through the appropriate thermodynamic cycle (**Figure 4.1**). $\Delta\Delta G$ was estimated for single and multiple mutations. Multiple mutations allowed us to investigate the effect of the multiple peptide modifications on the relative binding affinity compared to the cumulative effect of a single mutation. For simulations, initial coordinates were selected from the previous MD study (Ghosh et al., 2021). The hybrid structure and topology files for amino acids were generated using the PMX package (Gapsys et al., 2016). A coupling coordinate "λ" was defined, which modified the identity of the amino-acid residues. Varying λ from 0 to 1 transformed leucine to valine by gradually changing the force-field parameters (simultaneously modifying the electrostatic, van der Waals, and bonded terms). λ values other than 0 or 1 represented the unphysical state (mixture of two endpoints: leucine and valine), thus justifying the term alchemical transformation. A total of 21 equally spaced λ values between 0 and 1 (0.00, 0.05, 0.10, 0.15, 0.20, 0.25, 0.30, 0.35, 0.40, 0.45, 0.50, 0.55, 0.60, 0.65, 0.70, 0.75, 0.80, 0.85, 0.90, 0.95, and 1.00) were used for the alchemical transformation. A soft-core potential was employed to transform the van der

Waals interactions (Beutler et al., 1994). The 21 MD trajectories corresponding to 21 λ windows were used to estimate the free energy difference between two end states employing the popular BAR (Bennett, 1976) method implemented in the GROMACS program as *gmx bar*.

4.2.3 Sampling and convergence

The reliable free energy (ΔG) estimation demands (1) adequate sampling at every λ window and (2) microscopic reversibility between neighbouring windows (estimated free energies from forward and backward alchemical transformation should be more or less identical Figure A4.1). To ensure adequate sampling, three independent simulations were performed that differed in sampling (run length at every λ = 2 ns/5 ns/10 ns) (**Appendix III Table A4.2**). The initial 1 ns MD run from every window was considered equilibration (Hamiltonian lag) (Pohorille et al., 2010), and thus not considered for free energy estimate. Free energies estimated from the three runs confirmed that the simulation with λ = 5 ns was converged and more or less unchanged upon increasing sampling (i.e., λ = 10 ns) (**Appendix III Table A4.2**). Thus, we optimized the computational cost by selecting the λ = 5 ns simulation strategy for estimating free energies. The robustness of the simulations was further examined by repeating the calculations in the reverse direction (λ = 1 → 0) (**Appendix III Table A4.2**). Excellent agreement between the forward and backward free energy estimates confirmed that the estimated free energies were reasonably accurate (**Appendix III Table A4.2**). The estimated free energies were reasonably accurate and independent of the initial MD structure or initial velocity distribution (**Appendix III Table A4.2**). Largest alchemical transformation, namely, L[all]V, might require larger stratification (more than 21 λ windows, adequate sampling) for statistical precision. To verify the convergence of L[all]V alchemical transformation, simulations with 41 λ windows were performed, and the mutation-free energy was summarized in **Appendix III Table A4.2**. Estimated mutation-free energy associated with L[all]V transformation on SDS micelles was found to be more or less independent of the stratification strategy (ΔG[21 λ] = 131.87 kcal/mol and ΔG[41 λ] = 131.41 kcal/mol, differing by only ~0.4 kcal/mol) (**Appendix III Table A4.2**). Thus, our adopted simulation strategy (21 λ windows and 5 ns per window sampling) was robust and precise, well within the statistical uncertainty. The free energies estimated from multiple independent trials (varying velocities and structure) were averaged, and the resulting averaged ΔG^{comp} and ΔG^{free} were used for estimating $\Delta\Delta G$. A total of 7.425 μs of MDFE simulations was performed to obtain good

convergence and a reasonable statistical error (<0.5 kcal/mol; **Appendix III Table A4.2 and A4.3**). The alchemical transformation was preceded by equilibration (5.2 ns per system, total ~14.2 ns equilibration). Positive ΔΔG referred to favourable leucine peptide binding relative to their valine analogue (**Appendix III Table A4.3**). The standard errors of the mean (s.e.m) associated with the estimated free energies from different trials were generally less than 0.5 kcal/mol (**Appendix III Table A4.2**). Small s.e.m indicates good convergence. The estimated free energies from multiple independent trajectories differed only by <1 kcal/mol and further supported good convergence.

The last 4 ns of the 5 ns of every MD trajectory of the end states (i.e., $\lambda = 0$ and $\lambda = 1$) was used for estimating trajectory averaged properties, namely, root mean square fluctuation (RMSF), weighted solvent exposer (WSE) of amino acids, and hydrophobic surface area (A_L or A_V) around the peptide residues (leucine or valine). RMSF is a measure of flexibility. Weighted solvent exposure (WSE) was estimated as the ratio of averaged solvent accessible surface area of the amino acid in the presence and absence of micelles [(side-chain SASA in the presence of micelles)/(side-chain SASA in the absence of micelles) × 100]. The hydrophobic surface area (A_L or A_V) around the peptide side chain (within 0.35 nm) was estimated by calculating the trajectory averaged area of the aliphatic portion of the micelle.

4.3 Results

4.3.1 Energetics of Leucine/Valine-Containing 14-Residue Peptides to Micelle Surrogates

We have addressed the principle of peptide selectivity (between "Leu-" and "Val-" containing 14-residue peptides) by negatively charged (sodium dodecyl sulfate: SDS) or zwitterionic (dodecylphosphocholine: DPC) micelles, by carrying out MDFE simulations. Previously reported MD structures of the micelle-bound peptide complexes (LL-14(P^h):SDS/DPC) were supported by the CD and fluorescence experiments (Ghosh et al., 2021; Pandit et al., 2021). Using the MD structure of the LL-14(P^h):SDS/DPC complex as a template, we estimated the energetics associated with Leu → Val mutations in the LL-14 peptide (single mutation at residue positions: 1, 4, 7, 8, 11, and 14; multiple mutations: middle positions: L[4,7,8,11]V; and complete mutations: L[all]V: LL-14 vs VV-14) bound to the micelle. An appropriate thermodynamic cycle (Figure 4.1) was used to estimate the relative peptide binding affinities, and the results are summarized in **Figure 4.2**. The results indicated that both SDS and DPC micelles favoured "Leu peptide" binding relative to "Val peptide". Previous experimental studies (Pandit et al., 2020, 2021) established that

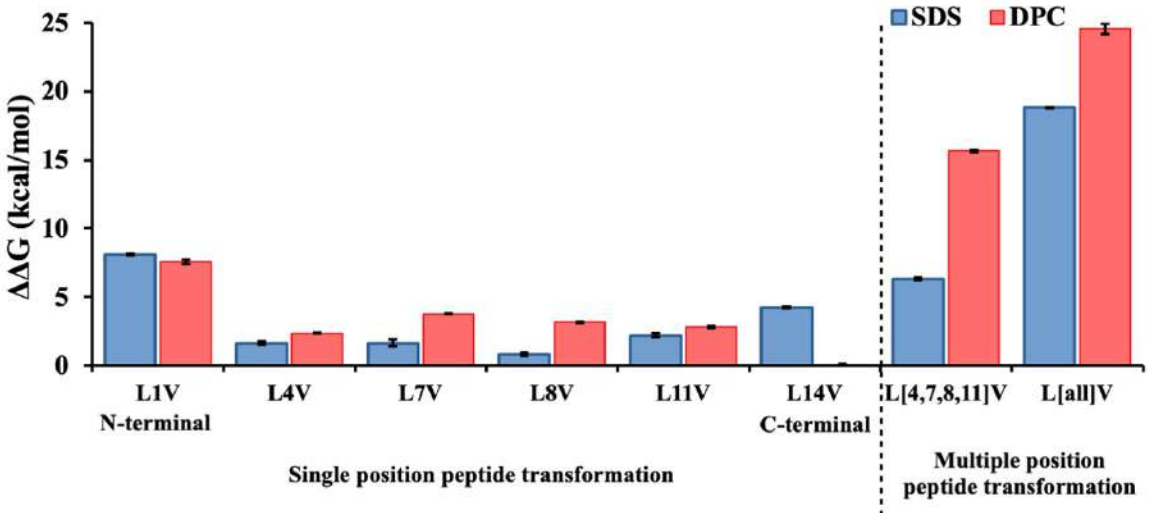

Figure 4.2: Estimated changes in binding free energy, ΔΔG, for SDS (blue) and DPC (red) as a result of leucine to valine transformation (at single or multiple positions) in the LL-14 peptide. Error bars, 1 s.e.m.

antimicrobial activity, as well as the toxicity of the leucine-rich peptide LL-14, was considerably higher than its valine analogue VV-14, thus in line with our results (**Figure 4.2**). Micelles showed the strongest discrimination in the first position (-N terminal) of the peptide favouring L1 against V1 (strength of discrimination: ΔΔG ~8 kcal/mol). Notably, -C terminal mutation (L14V) was recognized by SDS micelles (ΔΔG ~4 kcal/mol) but not by DPC micelles. Thus, L14V mutation had no significant effect on the binding affinity of the peptide to the DPC micelle. L → V mutation at the middle positions (residues: 4^{th}, 7^{th}, 8^{th}, and 11^{th}) were discriminated significantly by DPC relative to SDS micelles. To compare the effect of multiple mutations in the middle positions of the peptide toward micelle binding, L → V mutations were introduced simultaneously in all the middle positions (4^{th}, 7^{th}, 8^{th}, and 11^{th}) of the peptide and the binding free energy difference (L[4,8,7,11]V of **Figure 4.2**) was estimated. We assumed that the effect of multiple mutations in the micelle binding (i.e., ΔΔG of L[4,7,8,11]V) would approximately be equal to the sum of single mutations (i.e., ΔΔG of L4V + L7V + L8V + L11V) (**Figure 4.2**). The same assumption is referred to as the "additivity assumption". The results unambiguously showed that the "additivity assumption" was true only for SDS (**Table A4.3**). On the other hand, the cumulative sum of the strength of peptide discrimination by DPC micelles due to single mutations (i.e., ΔΔG of L4V + L7V + L8V + L11V ~12 kcal/mol) was ~4 kcal/mol less than the discriminatory strength toward multiple mutations (i.e., ΔΔG of L[4,7,8,11]V = 16 kcal/mol). Unambiguously, the discriminatory power of DPC micelles was much higher if the peptides differed by multiple mutations (L's or V's) at the middle of the peptide (**Figure 4.2**, L[4,7,8,11]V) relative to the sum of the discriminatory powers of

single-mutant peptides (**Table A4.3**). Thus, it is evident that the "cooperative" effect of multiple substitutions boosted the discriminatory power of DPC micelles and led to "nonadditivity".

It seems that the loss of the peptide–micelle hydrophobic interactions (due to L → V peptide mutations) was more severe in the case of DPC relative to SDS micelles. Thus, hydrophobic interaction seems to be the key for peptide binding to DPC micelles (eukaryotic membrane surrogate), which might be a plausible cause for reduced cytotoxicity in VV-14, as hypothesized earlier (Pandit et al., 2021). Clearly, in comparison to an SDS micelle, a DPC micelle imposes a much higher free energy penalty for VV-14 (all valine peptide) binding relative to LL-14 (all leucine peptide) binding (**Figure 4.2**, L[all]V). A DPC micelle is ~6 kcal/mol more selective relative to an SDS micelle in favor of all-leucine peptide (LL-14) binding relative to its valine analogue (VV-14). These results are in line with the experimentally observed toxicity of LL-14 relative to VV-14. (Pandit et al., 2021) Moreover, CD, fluorescence, and NMR experiments (Ghosh et al., 2021; Pandit et al., 2020, 2021) showed distinct LL-14 binding to DPC micelles (mammalian membrane mimic) but not to VV-14.

4.3.2 The link between Calculated Energetics and Structure

4.3.2.1 Discrimination of Peptides Differing at the N-Terminal (1st Position: L1 or V1)

Strikingly large discrimination of the SDS micelles toward the binding of two different 14-residue peptides differing (L/V) at the first position ($\Delta\Delta G \sim 8$ kcal/mol, **Figure 4.2**) was primarily due to a salt-bridge (K2-SDS) disruption in response to leucine → valine transformation (**Figure 4.3a,b**). A decrease in the hydrophobicity at the first position due to Leu → Val mutation in the SDS micelle disrupted the electrostatic interaction and significantly increased the energy penalty. Alchemical transformation in the reverse direction (Val → Leu) resulted in salt-bridge formation at the endpoint (**Appendix III Figure A4.2**). Moreover, leucine at the first position was found to be less flexible (RMSF = 0.07 nm) and less solvent-exposed (WSE = 67%) relative to valine (RMSF = 0.11 nm and WSE = 81%), indicating stronger L1 peptide:micelle interaction (**Figures 4.3a,b** and **Appendix III Figure A4.3a,b**). Tryptophan (W3) was found to be buried in the hydrophobic core (completely solvent-excluded) of the SDS micelle (in line with previous fluorescence experiments (Ghosh et al., 2021)). A stable W3-SDS hydrogen bond was observed in the peptide:SDS complex, only if "Leu" was present at the first position

(**Figure 4.3a,b**). Zwitterionic DPC micelles ensured high peptide selectivity, favouring L1 over V1 peptides by the complete exclusion of solvents around a broken-backbone hydrogen bond (hydrogen bond distance: 0.31 nm → 0.39 nm in response to L1 → V1 mutation) (**Figures 4.3c,d** and **Appendix III Figure A4.3c,d**). The penalty of the broken hydrogen bond in a dry hydrophobic pocket was significantly high as no water molecules could compensate for the missing hydrogen bond in the peptide(V1):SDS complex (Figure 4.3d). An increase in the solvent exposure (WSE values) in response to L1 → V1 mutation in both SDS and DPC micelles indicated the loss of peptide:micelle van der Waals interactions (**Figure 4.3** and **Appendix III Figure A4.3**) that additionally contributed to the binding free energy difference favouring L1.

However, the strong discriminatory power of SDS and DPC micelles toward peptides differing at the N-terminal (containing L1 or V1) seemed primarily of electrostatic origin.

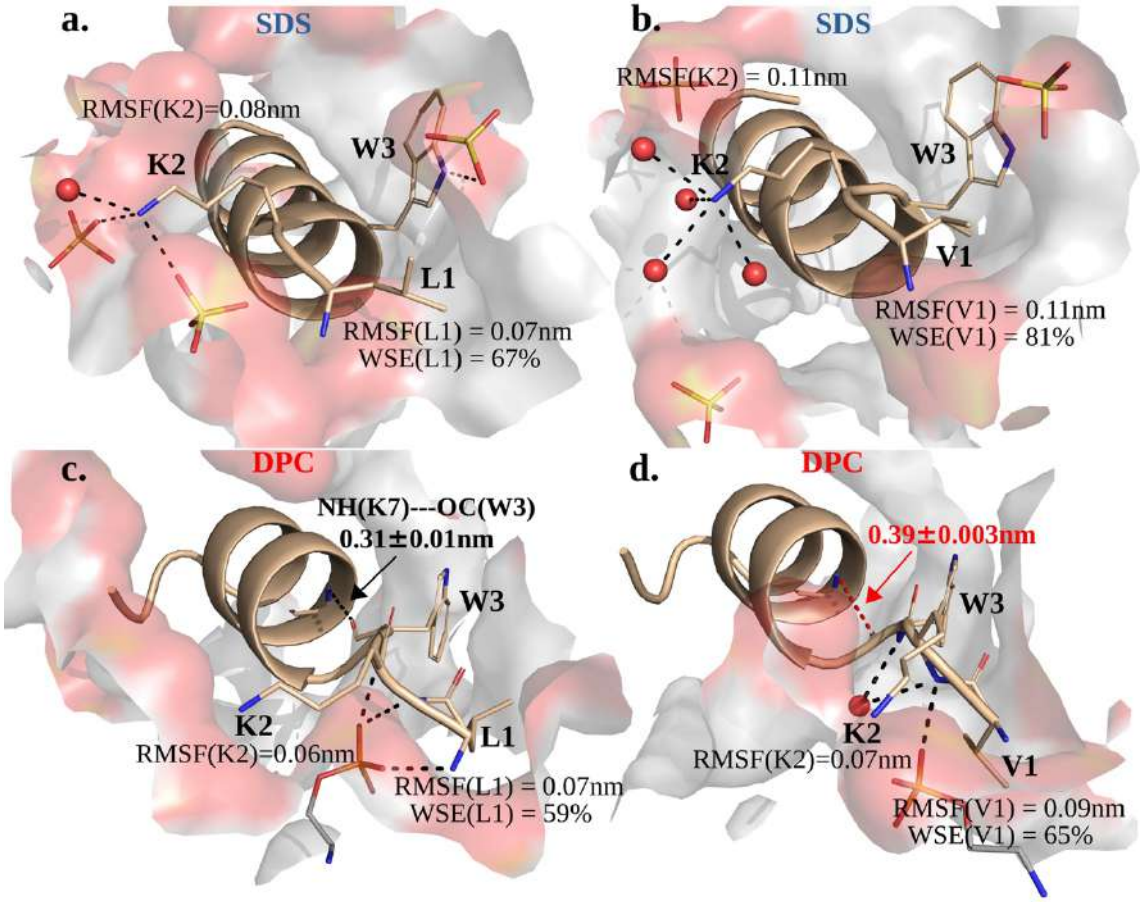

Figure 4.3: N-terminal selectivity. Recognition of leucine disfavouring valine observed from the average MD structures of peptide:micelle complexes (SDS: top and DPC: bottom), with the leucine peptide (a,c) and valine peptide (b,d). Peptides in the schematic (wheat) and micelles in surface representation (red and grey). Key residues are shown in sticks (red; oxygen and blue: nitrogen). Key interaction networks are indicated by the black dashed line. Water is indicated in in red spheres. Hydrogens are not shown for clarity. The discrimination against valine is reflected by the loss of salt-bridge interaction (K2:SDS) in (b), whereas the backbone hydrogen bond (NH(K7)···OC(W3), standard deviation as error) was disrupted and shielded from water in the DPC micelle (d). The discrimination against valine is further supported by the increase in flexibility (RMSF) and solvent accessibility (weighted solvent exposer of the side-chain: WSE) in both (b) and (d), somewhat more pronounced in the former.

Disruption of the salt bridge (K2...SDS) in the case of SDS micelles occurred. In contrast, in the case of DPC micelles, a broken-backbone hydrogen bond in the dry hydrophobic core was primarily responsible for the high free energy penalty, ensuring strong discrimination (ΔΔG ~8 kcal/mol) between leucine and valine at the first position of the 14-residue peptide.

4.3.2.2 Discriminating of Peptide Differing at the C-Terminal (14th Position: L14 or V14)

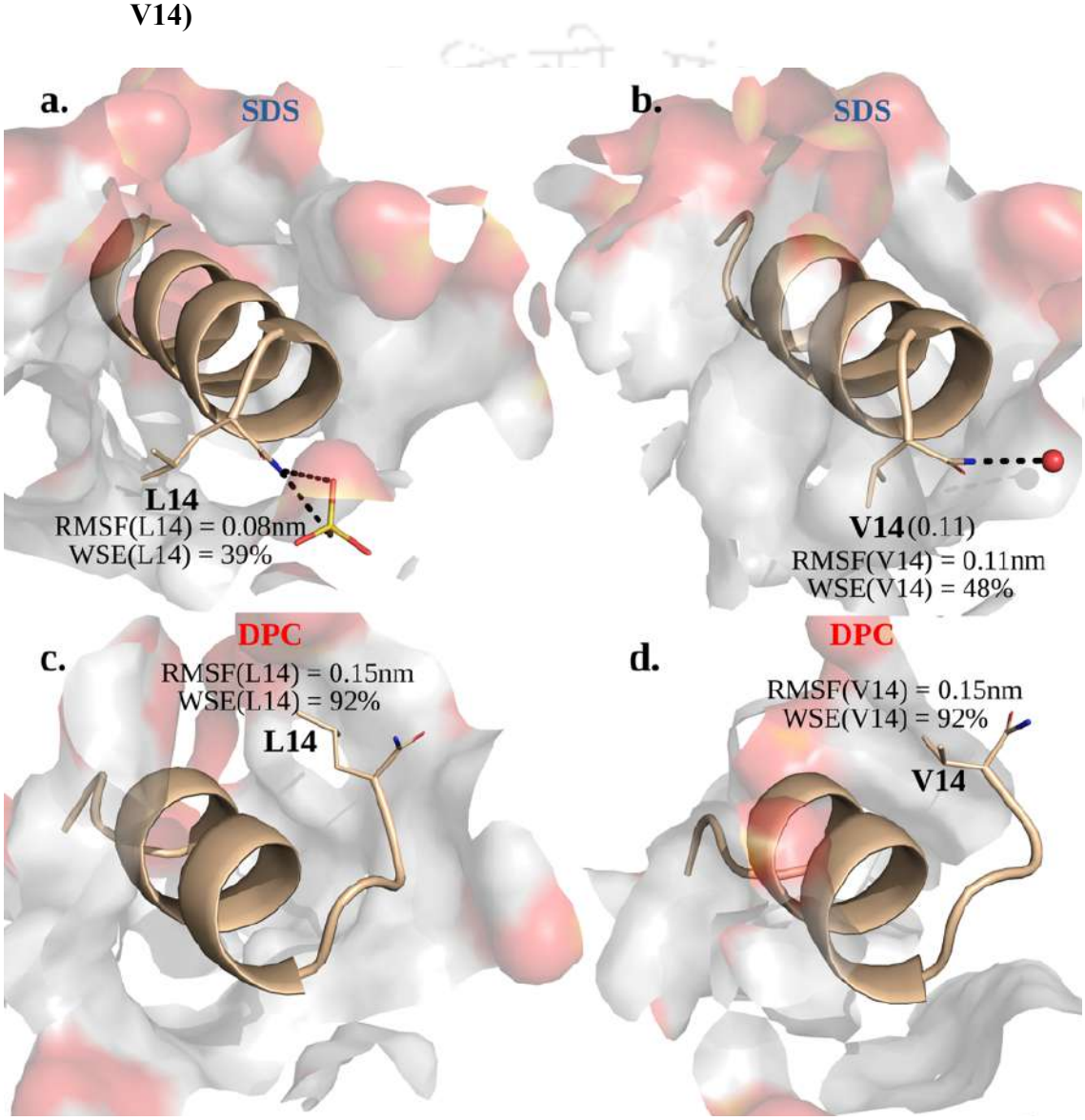

Figure 4.4: C-terminal selectivity. Representative molecular dynamics structures of peptide: micelle complexes (SDS: upper, DPC: lower) with the leucine-peptide (left-side: a, c) and valine-peptide (right-side: b, d) (colour coding as in Figure 3). Leucine at the C-terminal is preferred by SDS micelle (ΔΔG ~4 kcal/mol), as reflected by the favourable interactions with terminal $CONH_2$ with the negatively charged SDS surface (a). V-14 in the SDS micelle disrupt the $CONH_2$…SDS interaction, supported by increased flexibility and solvent exposer of the valine reside (V14). Peptide binding to DPC micelle (lower) is independent of the nature of the peptide residue at the C-terminal (Leucine or valine in the 14th position). No direct interaction between the C-terminal and DPC micelle was observed, as is also evident from the estimated energetics (ΔΔG ~0 kcal/mol).

The amide amine at the C-terminal (capped with $-CONH_2$) of the leucine-containing peptide (LL-14) formed a hydrogen bond with the negatively charged sulfate of SDS (**Figure 4.4a** and **Appendix III Figure A4.4**). This hydrogen bond was found to be broken if the peptide was mutated with valine (V14) (**Figure 4.4b**). Thus, L14 → V14 mutation in the SDS-bound complex not only diminished the van der Waals interactions due to decreasing hydrophobic content in the peptide but also disrupted the hydrogen bond. The increase in the flexibility (RMSF = 0.11 nm) and solvent exposure (WSE = 48%) of the V14-containing peptide indicated weaker peptide:SDS interaction relative to its leucine analogue (RMSF = 0.08 nm and WSE = 39%).

No direct interaction between the C-terminal (L14 or V14) of the peptide and the zwitterionic DPC micelle was observed in the MD trajectories due to electrostatic reasons (both $-CONH_2$ and surface of DPC micelles were electrically neutral) (**Figures 4.4c,d** and **Appendix III Figure A4.4**). Considerable flexibility and solvent exposure of the C-terminal residues (leucine or valine) indicated that the environment around the residues was similar (mostly solvent-exposed) in the DPC micelle. Thus, peptide mutation (L14 → V14) did not alter the binding affinity (L14V of **Figure 4.2**).

4.3.2.3 Discrimination of Peptides Differing at the Middle Positions (4th, 7th, 8th, and 11th position: Single- and Multiple-Site Mutations)

Single (L4V, L7V, L8V, and L11V) or multiple (L[4,7,8,11]V) peptide mutations (L → V) at the middle portion of the peptide were disfavoured by both DPC and SDS micelles, the former being more selective (**Figure 4.2**). The middle portion of the peptide was found to be buried in the hydrophobic core of the SDS micelle (**Figure 4.5**). L → V mutation at the middle position (Leu → Val) primarily reduced the hydrophobic surface area around the mutation site (**Figure 4.5b**) without altering the peptide:micelle electrostatic contacts. Thus, the hydrophobic interactions involving the side chain of the peptide and the micelle core were compromised due to L → V mutation. Peptide selectivity of micelles (SDS/DPC) based on the (L/V) mutation at the middle portion of the peptide was primarily due to fine-tuning of the van der Waal interactions. Thus, the strength of discrimination (L4V, L7V, L8V, and L11V) was much weaker than the L1V mutation, where electrostatics played a crucial role (**Figure 4.2**).

Notably, the hydrophobic surface area decrease due to L → V mutation was always larger when bound to DPC relative to SDS micelles (fourth and seventh column of **Figure 4.5b**). This observation perfectly correlated with the higher estimated selectivity for the DPC (i.e.,

the height of the blue bar is smaller relative to the red bar: L4V/L7V/L8V/L11V/ L[4,7,8,11]V of **Figure 4.2b**).

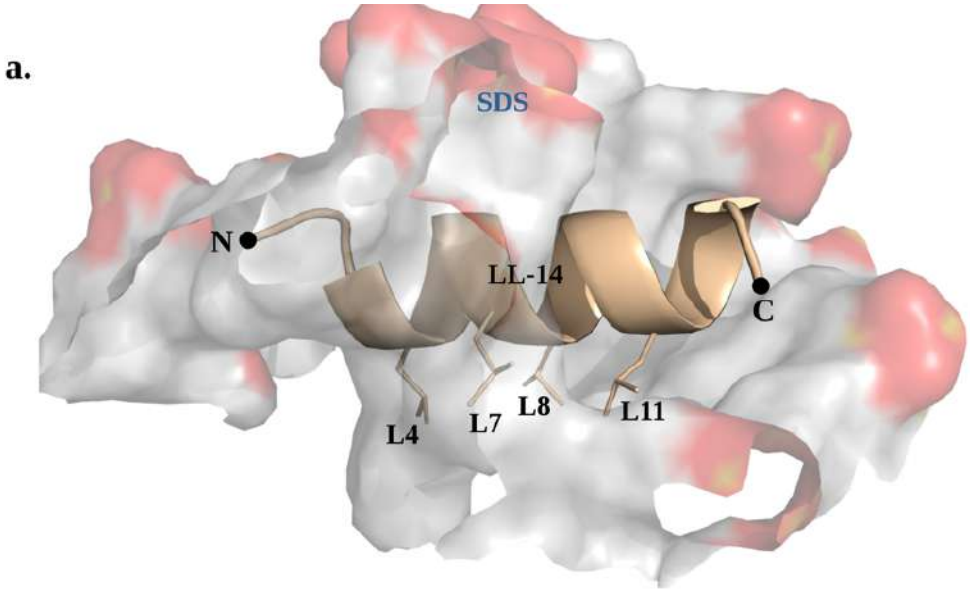

b.

	SDS			DPC		
	A_L (nm²)	A_V (nm²)	A_L -A_V (nm²)	A_L (nm²)	A_V (nm²)	A_L -A_V (nm²)
L4V	1.36 ± 0.006	1.25 ± 0.007	**0.11 ± 0.007**	1.12 ± 0.008	0.96 ± 0.009	**0.16 ± 0.007**
L7V	1.08 ± 0.005	0.99 ± 0.008	**0.11 ± 0.007**	1.13 ± 0.006	0.83 ± 0.007	**0.31 ± 0.007**
L8V	1.18 ± 0.007	1.16 ± 0.006	**0.03 ± 0.006**	0.99 ± 0.007	0.69 ± 0.008	**0.30 ± 0.008**
L11V	1.20 ± 0.007	1.08 ± 0.007	**0.12 ± 0.007**	1.09 ± 0.007	0.94 ± 0.005	**0.16 ± 0.006**
L[4,7,8,11]V	4.79 ± 0.015	4.41 ± 0.014	**0.38 ± 0.017**	4.35 ± 0.011	2.89 ± 0.013	**1.46 ± 0.012**

Figure 4.5: (a) zoomed in view of the LL-14: SDS complex highlighting the leucine residues at the middle of the peptide (4th, 7th, 8th, and 11th position) embedded in the hydrophobic core of the SDS micelle (colour coding as in Figure 3). Some part of the micelle was not shown for clear representation of the peptide. (b) Area of the hydrophobic aliphatic region of the micelle around the 0.35 nm side-chain of peptide residue leucine (area= A_L in nm²) and valine (A_V in nm²). Loss of hydrophobic surface area in response to Leucine → Valine transformation is given as (A_L - A_V) in presence of SDS (4th column) and DPC (7th column) micelle. Error bars, 1 s.e.m.

Interestingly, for the SDS-bound peptide, the cumulative sum of the loss of hydrophobic area due to single mutations (fourth column of **Figure 4.5b**) was 0.37 nm², which was very similar to the estimated loss of the hydrophobic area for multiple mutations (0.38 nm²), thus in line with the observed additivity of the discriminatory power (**Figure 4.2**). On the other hand, for DPC-bound peptides, the cumulative sum of the loss of the hydrophobic area due to single mutations (seventh column of **Figure 4.5b**) was 0.93 nm², which is much smaller than the loss of the hydrophobic area in the case of multiple mutations (1.46 nm²). Strong electrostatic interactions in the peptide:SDS micelle complex kept the peptide in place and offset the loss of the hydrophobic area (upon L[all]Valine mutation) to some

extent, unlike the case of peptide:DPC micelles, where favourable electrostatic interactions were absent.

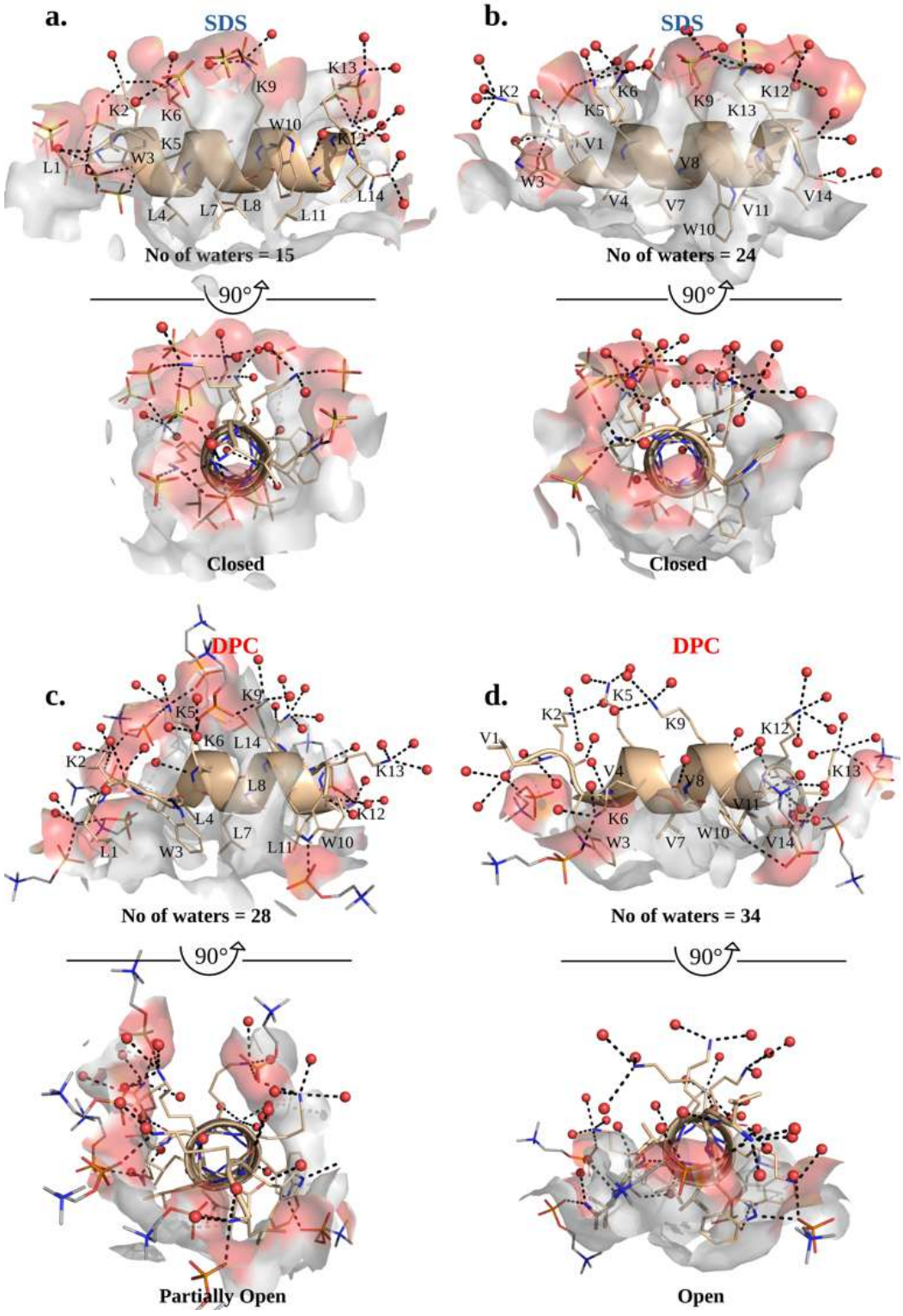

Figure 4.6: Zoomed in view from the representative MD structures of (a) LL-14: SDS , (b)VV-14: SDS, (c) LL-14: DPC, and (d) VV-14: DPC complexes. The complexes are shown by keeping the peptide in the horizontal axis (above) and rotated by 90 degree around the horizontal axis (below, N-terminal towards the reader). The peptide was found to be somewhat more deeply buried (a,b: closed conformation) relative to the DPC micelle bound form (c, d; Partially-open/open). Black dashed line indicate interaction. Peptide residues and its key interacting surfactants (polar terminals) are shown as sticks. Waters interacting with the peptide (within 0.35 nm of the peptide) is explicitly shown as red spheres.

4.3.3 LL-14 vs VV-14 Discrimination

The settled helical LL-14 peptide (**Appendix III Figure A4.5**) was deeply buried under the SDS micelle surface ("closed" pocket). In contrast, the peptide was found to be relatively less buried on the DPC micelle surface ("partially open" pocket, **Appendix III Figure A4.5**) with a noticeable loss of the helical content (**Figures 4.6** and **Appendix III A4.6**). Moreover, LL-14 was found to be more solvent-exposed in DPC micelles relative to SDS micelles (**Figure 4.6a,c**). Mutation of all leucine to valine (LL-14 → VV-14) resulted in greater solvent exposure (**Figure 4.6**). VV-14 was found to be lying on the surface of the DPC micelle ("open" pocket, **Figure 4.6d**), indicating weak VV-14:DPC binding relative to the LL-14:DPC complex ("partially open", **Figure 4.6c**). However, we did not observe complete dissociation of the VV-14 from the DPC micelle during our finite MD timescale (up to 0.55 μs). The features observed in the single N-terminal mutation (L1 → V1), namely, K2...SDS salt-bridge disruption in the SDS and broken-backbone hydrogen bond in the solvent-free hydrophobic core of DPC micelle (**Figure 4.3**), were also observed in the case of VV-14:micelle complexes (**Figure 4.6**). As expected, the disruption of $-CONH_2\cdots$SDS interaction observed in the single C-terminal mutation (L14 → V14, **Figure 4.4**) was also observed in the VV-14:SDS complex (**Figure 4.6b**).

4.4 Discussion

MDFE simulations demonstrated that the leucine-containing peptide binding to the micelle (SDS or DPC) was more favoured relative to its valine-containing analogue, indicated by positive ΔΔG (**Figure 4.2**). This was also in line with the observation that LL-14 was cytotoxic and had high antimicrobial activity relative to its valine analogue (VV-14) (Pandit et al., 2021). Another related study reported a 16-residue long valine-rich helical peptide to show weak cytotoxicity. At the same time, the leucine-rich analogue was found to be highly toxic (by 4 to 16 fold) and more potent in antimicrobial potency (Ma et al., 2011). Interestingly, the strength of relative binding affinity (ΔΔG) strongly depended on the position of the L/V mutations (**Figure 4.2**). For the first time, the results quantitatively showed how a slight decrease in the hydrophobicity of the peptide (due to the L/V mutation) at the N-terminal (first position) amplified the selectivity (highest ΔΔG ~8 kcal/mol for L1V) by altering the electrostatic interactions (**Figure 4.3b**). However, the origin of leucine selectivity compared to valine at the first position of the peptide was distinctly different for SDS and DPC micelles. In SDS micelles, a disrupted

salt-bridge interaction (K2:SDS, **Figure 4.3b**) occurred, whereas, in DPC micelles, a solvent-shielded broken-backbone hydrogen bond (0.39 nm, **Figure 4.3d**) increased the free energy of the (V1) peptide:micelle complex and ensured selectivity in favour of the L1 peptide. Thus, a small decrease in the hydrophobic content in the peptide (L1 → V1) could amplify the strength of discrimination (ΔΔG) by fine-tuning electrostatics (disruption of the salt bridge or solvent-shielded broken hydrogen bond). The highest selectivity (ΔΔG ~8 kcal/mol) associated with the N-terminal mutation of the 14-residue peptide indicated the importance of the N-terminal for micelle binding, thus likely to be crucial for its activity. Disruption of the dipole-charge electrostatic interaction ($-CONH_2$:SDS, **Figure 4.4a,b**) was also observed in response to L14/V14 mutation in the peptide in complex with SDS, resulting in ΔΔG ~4 kcal/mol (**Figure 4.2**). Owing to the electrical neutrality of the C-terminal cap ($-CONH_2$), L14/V14 mutation (**Figure 4.4b**) was much less penalized compared to the salt-bridge disruption observed in the N-terminal L1/V1 mutation (**Figures 4.2** and **4.3b**). Single or multiple L → V mutations in the middle position did not alter the peptide:micelle electrostatic interactions, and thus, the estimated ΔΔ*G*'s (L4V, L7V, L8V, L11V, and L[4,7,8,11]V) were attributed to the loss of peptide:micelle hydrophobic interactions. Loss of the hydrophobic surface area around the side chain of the peptide in response to L → V peptide mutation (at the middle portion) was found to be severe in the case of DPC relative to SDS micelles, which accounted for the higher selectivity of the former (**Figure 4.2**). Both electrostatics (multiple salt bridges) and van der Waals interactions (hydrophobic) were key components in stabilizing the peptide:SDS complex. It might be argued that the strong electrostatic interaction (i.e., peptide:SDS salt bridges) held the peptide and reduced the loss of peptide:micelle van der Waals contact in the peptide:SDS complex. On the other hand, the van der Waals interaction primarily stabilized the peptide:DPC complex. Thus, L/V mutation resulted in significant loss of peptide:DPC hydrophobic contact and strongly disfavoured the Val-containing peptide. It is worth noting that the loss of the hydrophobic surface area around the side chains in response to Leu → Val mutation was the highest at the peptide terminals, where electrostatic interactions were also disrupted as a result of the mutation. The all-valine peptide (VV-14) was indeed found to be loosely bound relative to the all-leucine peptide (LL-14) and came out from the partially open cavity in the case of DPC micelles (**Figures 4.6** and **Appendix III Figures A4.5**). Thus, increasing the hydrophobicity of the 14-residue positively charged AMP favoured micelle (SDS or DPC) binding, consistent with the experimentally observed high antimicrobial activity and toxicity of LL-14 (Pandit

et al., 2021). Moreover, the higher discriminatory power of DPC micelles (relative to SDS micelles) between LL-14 and VV-14 hinted that VV-14 might be less toxic, as suggested by our previous experimental study (Pandit et al., 2021). Thus, a threshold peptide hydrophobicity was the key for optimal antimicrobial activity and toxicity.

Saint Jean et al. studied (saint Jean et al., 2018) the effect of hydrophobic amino acid substitutions in an 18-residue AMP C18G on its antimicrobial activity, peptide–lipid interactions, bacterial membrane permeabilization, and so forth. The highest antimicrobial activity, distinctly larger binding preference toward anionic bilayer, and greater ability to disrupt lipid vesicles and bacterial membranes were confirmed for relatively higher hydrophobic variants of C18G (containing Leu/Phe) compared to the lower hydrophobic Val peptide variant. Thus, hydrophobic moieties in the AMP sequence were found to be crucial for favourable membrane binding and enhanced antibacterial activity. Wieprecht et al. studied (Wieprecht et al., 1997) the membrane activity and selectivity of magainin 2 analogues of various hydrophobicities. They showed that the increase in hydrophobicity increased the permeability of the mammalian membrane mimics, indicating cytotoxicity. Thus, in other words, an increase in the hydrophobicity decreased the discrimination in between the microbial and mammalian membranes. Ma et al. studied (Ma et al., 2011) the effect of Leu or Val substitution on 16-residue-long α-helical peptides on cell selectivity. They found that both Leu and Val peptides bound preferentially to negatively charged phospholipids (bacterial membrane mimic) compared to zwitterionic phospholipids (mammalian membrane mimic). The Leu peptide displayed stronger depolarization of the bacterial cell than its Val analogue. Moreover, the 16 residue Val peptide did not show binding with zwitterionic phospholipids, as observed in VV-14 (Pandit et al., 2021). All the above-mentioned experimental results corroborate our present observations; higher hydrophobicity of LL-14 resulted in high antimicrobial activity and cytotoxicity at the same time, whereas lesser hydrophobicity of VV-14 resulted in lesser activity and lesser toxicity.

The absolute binding affinity of LL-14 binding to SDS and DPC micelle was estimated using steered molecular dynamics simulations (SMD) combined with umbrella sampling method described the previous chapter. The results showed that LL-14:SDS and LL-14: DPC complexes were stable relative to the unbound free state by -34 kcal/mol and -12 kcal/mol respectively (**Figure 3.9** and **Appendix II Figure A3.11**). The estimated highly-selective DPC micelle (ΔΔG ~25 kcal/mol and low-selective SDS micelle (ΔΔG ~19 kcal/mol) placed the VV-14: DPC complex uphill and VV-14: SDS complex downhill from the free unbound state (**Figure 4.7**).Thus, VV-14 peptide dissociation from the DPC

micelle (eukaryotic membrane mimic) would be thermodynamically favourable (**Figure 4.7**), providing a plausible explanation for the experimentally observed noncytotoxicity of VV-14 (Pandit et al., 2021). On the other hand, LL-14 and VV-14 would spontaneously bind to the SDS (bacterial membrane mimic) micelle (downhill, **Figure 4.7**), thus correlating with the experimentally observed antimicrobial activity of both LL-14 and VV-14. Moreover, the higher stability of the former could also explain the experimentally observed higher antimicrobial potency of LL-14 relative to VV-14 (**Figure 4.7**). The stability of the II-14 (isoleucine analog of LL-14: NH_3^+-IKWIKKIIKWIKKI-$CONH_2$) peptide bound micelle is shown in **Figure 4.7**. The relative binding free energy (II-14 versus LL-14 binding SDS/DPC micelle) was estimated using alchemical free energy simulations (ΔΔG ~6 and ~10 kcal/mol for SDS and DPC micelle respectively). The II-14:SDS and II-14:DPC complex was placed relative to the LL-14:SDS and LL-14:DPC complex respectively in the free energy axis (**Figure 4.7**). Based on the intermediate stability of II-14: (SDS/DPC)-micelle complex (**Figure 4.7**), we hypothesized that II-14 is

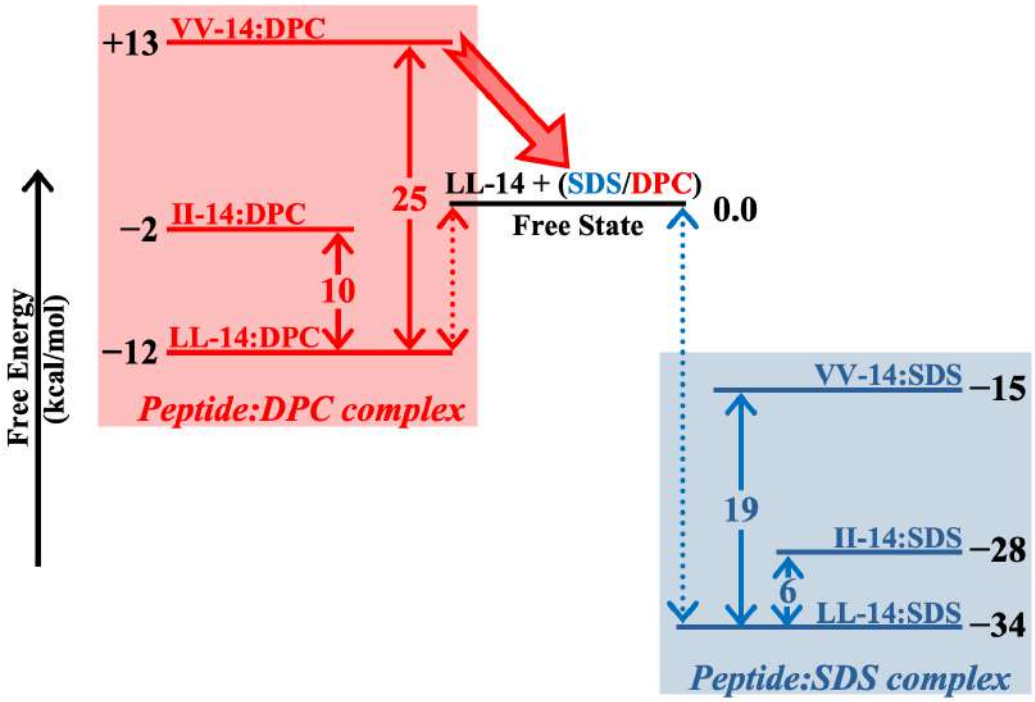

Figure 4.7: Schematic free energy (in kcal/mol) diagram for peptide: DPC (left, red) and peptide: SDS (right, blue) binding relative to the unbound (*Free State,* black) state. Absolute binding affinity (ΔG_{bind}, represented by dashed double-headed lines) estimated from umbrella sampling simulation (will be published elsewhere) place LL-14: DPC, LL-14: SDS complexes downhill relative to the free state. Estimated binding free energy differences (ΔΔG, represented by solid double-headed arrow) between LL-14 and VV-14 peptides to DPC/SDS were ~ 25/19 kcal/mol and between LL-14 and II-14 peptides to DPC/SDS were ~ 10/6 kcal/mol. The scheme illustrates that, the VV-14:DPC complex is uphill, whereas VV-14: SDS complex is downhill relative to the free state. Thermodynamically favourable dissociation of VV-14 from DPC micelle was shown as transparent red arrow.

likely to display (1) stronger antimicrobial activity relative to VV-14 and (2) less cytotoxic relative to LL-14. The predictions are subjected to experimental verification.

Ideally, a study of multiple AMP peptides binding to lipid bilayers (mimicking the lipid composition of the human or bacterial cell membrane) might be appropriate. However, micelles are minimalistic systems that mimic membranes (well-defined lipid core and flexible hydrophilic surface). They are advantageous for studying the binding affinities with relatively less computational costs (due to smaller size and faster time scales of motion) (Fernández & Wüthrich, 2003; Rakitin & Pack, 2004; Shepherd et al., 2003; Tieleman et al., 2000; Wong & Kamath, 2002). Micelles are also a popular choice for experimental studies (Campagna et al., 2007; Japelj et al., 2007; Kaluck et al., 1995; Lauterwein et al., 1979; Li, Li, Han, et al., 2006; Li, Li, Peterkofsky, et al., 2006; Porcelli et al., 2006). SDS micelles mimic bacterial membranes, which consist of an anionic exterior and a hydrophobic core, whereas DPC micelles mimic eukaryotic cell membranes (consisting of zwitterionic phospholipids) (Lim et al., 2004; Rezansoff et al., 2005; Rozek et al., 2000; van den Hooven et al., 1996; Yang et al., 2002). As we have performed our earlier computational study using SDS/DPC micelles, we have extended our present study using the same. Micelles, the simplest model systems, are certainly limited in explaining biological functions. Nonetheless, the study of peptide binding to micelles can capture the general aspects related to the activity and toxicity of peptides (Ghosh et al., 2021). Peptide binding to the microbial membrane is the first step of antimicrobial activity of membrane-active AMPs, and micelles can certainly gain insights into the initial peptide membrane binding step. In this study, we demonstrated that our adopted computational methodology could successfully estimate the binding free energy differences and establish a direct link with the atomic structures, thus acting as an excellent complement to the experiments.

4.5 Conclusion

This study demonstrated that membrane surrogates (SDS/DPC micelles) could strongly recognize the minor reduction of the peptide hydrophobicity (L → V mutation in the 14-residue peptide:NH_3^+-LKWLKKLLKWLKKL-$CONH_2$) by fine-tuning the peptide:micelle electrostatic interactions. Leu-containing peptides were always favoured relative to their Val-analogues for micelle binding, but the energetics strongly depended on the position of the mutation. In particular, we quantitatively showed how L1V mutation amplified the peptide selectivity on micelles (SDS/DPC) by fine-tuning the electrostatic interactions. Surprisingly, we found that SDS and DPC micelles recognized L1V peptide mutation by

distinctly different mechanisms. SDS micelles ensured L1V selectivity by disrupting peptide:micelle salt-bridge interaction, whereas DPC micelles shielded the broken-"peptide-backbone hydrogen bond" from the solvent in the V1 peptide:micelle complex. Discrimination of peptides by micelles based on Leu → Val mutation in the middle part of the peptide was found to be of hydrophobic origin. The DPC micelle was found to be more selective relative to SDS in favour of LL-14 binding relative to VV-14. Loss of hydrophobic contact in response to L/V mutation in the middle part of the peptide was found to be more prominent in DPC relative to SDS, resulting in higher selectivity for the former. We delineated a simple free energy diagram illustrating that the strength of discrimination could be utilized to dissociate VV-14 from the DPC micelles efficiently. We established from our studies that the (1) N-terminal of AMPs was crucial for membrane binding. Fine-tuning the hydrophobicity altered the peptide:membrane electrostatic interactions. (2) An increase in the hydrophobic content of the peptide might result in toxicity.

4.6 Supporting Information

This chapter contains supporting data provided in Appendix III.

REFERENCES

Bennett, C. H. (1976). Efficient estimation of free energy differences from Monte Carlo data. *Journal of Computational Physics*, *22*(2), 245–268. https://doi.org/10.1016/0021-9991(76)90078-4

Berglund, N. A., Piggot, T. J., Jefferies, D., Sessions, R. B., Bond, P. J., & Khalid, S. (2015). Interaction of the antimicrobial peptide polymyxin B1 with both membranes of E. coli: a molecular dynamics study. *PLoS Computational Biology*, *11*(4). https://doi.org/10.1371/JOURNAL.PCBI.1004180

Best, R. B., Zhu, X., Shim, J., Lopes, P. E. M., Mittal, J., Feig, M., & MacKerell, A. D. (2012). Optimization of the additive CHARMM all-atom protein force field targeting improved sampling of the backbone φ, ψ and side-chain χ1 and χ2 Dihedral Angles. *Journal of Chemical Theory and Computation*, *8*(9), 3257–3273. https://doi.org/10.1021/CT300400X/SUPPL_FILE/CT300400X_SI_001.PDF

Beutler, T. C., Mark, A. E., van Schaik, R. C., Gerber, P. R., & van Gunsteren, W. F. (1994). Avoiding singularities and numerical instabilities in free energy calculations based on molecular simulations. *Chemical Physics Letters*, *222*(6), 529–539. https://doi.org/10.1016/0009-2614(94)00397-1

Béven, L., Castano, S., Dufourcq, J., Wieslander, Å., & Wróblewski, H. (2003). The antibiotic activity of cationic linear amphipathic peptides: lessons from the action of leucine/lysine copolymers on bacteria of the class Mollicutes. *European Journal of Biochemistry*, *270*(10), 2207–2217. https://doi.org/10.1046/J.1432-1033.2003.03587.X

Campagna, S., Saint, N., Molle, G., & Aumelas, A. (2007). Structure and mechanism of action of the antimicrobial peptide piscidin. *Biochemistry*, *46*(7), 1771–1778. https://doi.org/10.1021/BI0620297/SUPPL_FILE/BI0620297SI20060929_065032.PDF

Chen, Y., Mant, C. T., & Hodges, R. S. (2002). Determination of stereochemistry stability coefficients of amino acid side-chains in an amphipathic alpha-helix. *The Journal of Peptide Research : Official Journal of the American Peptide Society*, *59*(1), 18–33. https://doi.org/10.1046/J.1397-002X.2001.10994.X

Deslouches, B., Phadke, S. M., Lazarevic, V., Cascio, M., Islam, K., Montelaro, R. C., & Mietzner, T. A. (2005). De novo generation of cationic antimicrobial peptides: influence of length and tryptophan

substitution on antimicrobial activity. *Antimicrobial Agents and Chemotherapy*, *49*(1), 316–322. https://doi.org/10.1128/AAC.49.1.316-322.2005

Durell, S. R., Brooks, B. R., & Ben-Naim, A. (1994). Solvent-induced forces between two hydrophilic groups. *Journal of Physical Chemistry*, *98*(8), 2198–2202. https://doi.org/10.1021/J100059A038/ASSET/J100059A038.FP.PNG_V03

Ezugwu, J. A., Okoro, U. C., Ezeokonkwo, M. A., Bhimapaka, C. R., Okafor, S. N., Ugwu, D. I., Ekoh, O. C., & Attah, S. I. (2020). Novel Leu-Val Based Dipeptide as Antimicrobial and Antimalarial Agents: Synthesis and Molecular Docking. *Frontiers in Chemistry*, *8*, 1047. https://doi.org/10.3389/FCHEM.2020.583926/BIBTEX

FAUCHERE, J. (1983). *Hydrophobic Parameters Pi of Amino-Acid Side Chains from The Partitioning Of N-Acetyl-Amino Amides*. https://pascal-francis.inist.fr/vibad/index.php?action=getRecordDetail&idt=PASCAL83X0474336

Fernández, C., & Wüthrich, K. (2003). NMR solution structure determination of membrane proteins reconstituted in detergent micelles. *FEBS Letters*, *555*(1), 144–150. https://doi.org/10.1016/S0014-5793(03)01155-4

Gapsys, V., Michielssens, S., Seeliger, D., & de Groot, B. L. (2016). Accurate and Rigorous Prediction of the Changes in Protein Free Energies in a Large-Scale Mutation Scan. *Angewandte Chemie International Edition*, *55*(26), 7364–7368. https://doi.org/10.1002/ANIE.201510054

Ghosh, S., Pandit, G., Debnath, S., Chatterjee, S., & Satpati, P. (2021). Effect of monovalent salt concentration and peptide secondary structure in peptide-micelle binding. *RSC Advances*, *11*(58), 36836–36849. https://doi.org/10.1039/D1RA06772A

Japelj, B., Zorko, M., Majerle, A., Pristovšek, P., Sanchez-Gomez, S., de Tejada, G. M., Moriyon, I., Blondelle, S. E., Brandenburg, K., Andrä, J., Lohner, K., & Jerala, R. (2007). The acyl group as the central element of the structural organization of antimicrobial lipopeptide. *Journal of the American Chemical Society*, *129*(5), 1022–1023. https://doi.org/10.1021/JA067419V/SUPPL_FILE/JA067419VSI20061212_041153.PDF

Jorgensen, W. L., Chandrasekhar, J., Madura, J. D., Impey, R. W., & Klein, M. L. (1998). Comparison of simple potential functions for simulating liquid water. *The Journal of Chemical Physics*, *79*(2), 926. https://doi.org/10.1063/1.445869

Kaluck, D. A., Tessmer, M. R., Watts, C. R., & Li, C. Y. (1995). The use of dodecylphosphocholine micelles in solution NMR. *Journal of Magnetic Resonance. Series B*, *109*(1), 60–65. https://doi.org/10.1006/JMRB.1995.1146

Kandasamy, S. K., & Larson, R. G. (2004). Binding and insertion of alpha-helical anti-microbial peptides in POPC bilayers studied by molecular dynamics simulations. *Chemistry and Physics of Lipids*, *132*(1), 113–132. https://doi.org/10.1016/J.CHEMPHYSLIP.2004.09.011

Khandelia, H., Langham, A. A., & Kaznessis, Y. N. (2006). Driving engineering of novel antimicrobial peptides from simulations of peptide-micelle interactions. *Biochimica et Biophysica Acta*, *1758*(9), 1224–1234. https://doi.org/10.1016/J.BBAMEM.2006.03.010

Klauda, J. B., Venable, R. M., Freites, J. A., O'Connor, J. W., Tobias, D. J., Mondragon-Ramirez, C., Vorobyov, I., MacKerell, A. D., & Pastor, R. W. (2010). Update of the CHARMM All-Atom Additive Force Field for Lipids: Validation on Six Lipid Types. *Journal of Physical Chemistry B*, *114*(23), 7830–7843. https://doi.org/10.1021/JP101759Q/SUPPL_FILE/JP101759Q_SI_001.PDF

la Rocca, P., Biggin, P. C., Tieleman, D. P., & Sansom, M. S. P. (1999). Simulation studies of the interaction of antimicrobial peptides and lipid bilayers. *Biochimica et Biophysica Acta*, *1462*(1–2), 185–200. https://doi.org/10.1016/S0005-2736(99)00206-0

Langham, A. A., Waring, A. J., & Kaznessis, Y. N. (2007). Comparison of interactions between beta-hairpin decapeptides and SDS/DPC micelles from experimental and simulation data. *BMC Biochemistry*, *8*. https://doi.org/10.1186/1471-2091-8-11

Lauterwein, J., Bösch, C., Brown, L. R., & Wüthrich, K. (1979). Physicochemical studies of the protein-lipid interactions in melittin-containing micelles. *Biochimica et Biophysica Acta*, *556*(2), 244–264. https://doi.org/10.1016/0005-2736(79)90046-4

Li, X., Li, Y., Han, H., Miller, D. W., & Wang, G. (2006). Solution structures of human ll-37 fragments and NMR-based identification of a minimal membrane-targeting antimicrobial and anticancer region. *Journal of the American Chemical Society*, *128*(17), 5776–5785. https://doi.org/10.1021/JA0584875/SUPPL_FILE/JA0584875SI20051222_013003.PDF

Li, X., Li, Y., Peterkofsky, A., & Wang, G. (2006). NMR studies of aurein 1.2 analogs. *Biochimica et Biophysica Acta (BBA) - Biomembranes*, *1758*(9), 1203–1214. https://doi.org/10.1016/J.BBAMEM.2006.03.032

Lim, S., Song, Y., Jang, M., Kim, Y., Hahm, K.-S., & Shin, S. (2004). Effects of two glycine residues in positions 13 and 17 of pleurocidin on structure and bacterial cell selectivity. *Protein and Peptide Letters*, *11*(1), 35–40. https://doi.org/10.2174/0929866043478383

Ma, Q.-Q., Shan, A.-S., Dong, N., Cao, Y.-P., Lv, Y.-F., & Wang, L. (2011). The Effects of Leu or Val Residues on Cell Selectivity of α-Helical Peptides. *Protein and Peptide Letters*, *18*(11), 1112–1118.

Pandit, G., Biswas, K., Ghosh, S., Debnath, S., Bidkar, A. P., Satpati, P., Bhunia, A., & Chatterjee, S. (2020). Rationally designed antimicrobial peptides: Insight into the mechanism of eleven residue peptides against microbial infections. *Biochimica et Biophysica Acta. Biomembranes*, *1862*(4). https://doi.org/10.1016/J.BBAMEM.2020.183177

Pandit, G., Chowdhury, N., Abdul Mohid, S., Bidkar, A. P., Bhunia, A., & Chatterjee, S. (2021). Effect of Secondary Structure and Side Chain Length of Hydrophobic Amino Acid Residues on the Antimicrobial Activity and Toxicity of 14-Residue-Long de novo AMPs. *ChemMedChem*, *16*(2), 355–367. https://doi.org/10.1002/CMDC.202000550

Pandit, G., Ilyas, H., Ghosh, S., Bidkar, A. P., Mohid, S. A., Bhunia, A., Satpati, P., & Chatterjee, S. (2018). Insights into the Mechanism of Antimicrobial Activity of Seven-Residue Peptides. *Journal of Medicinal Chemistry*, *61*(17), 7614–7629. https://doi.org/10.1021/ACS.JMEDCHEM.8B00353/SUPPL_FILE/JM8B00353_SI_001.CSV

Park, Y., Lee, D. G., & Hahm, K. S. (2003). Antibiotic activity of Leu-Lys rich model peptides. *Biotechnology Letters*, *25*(16), 1305–1310. https://doi.org/10.1023/A:1024995105208

Park, Y., Park, S. N., Park, S. C., Shin, S. O., Kim, J. Y., Kang, S. J., Kim, M. H., Jeong, C. Y., & Hahm, K. S. (2006). Synergism of Leu–Lys rich antimicrobial peptides and chloramphenicol against bacterial cells. *Biochimica et Biophysica Acta (BBA) - Proteins and Proteomics*, *1764*(1), 24–32. https://doi.org/10.1016/J.BBAPAP.2005.10.019

Pohorille, A., Jarzynski, C., & Chipot, C. (2010). Good practices in free-energy calculations. *Journal of Physical Chemistry B*, *114*(32), 10235–10253. https://doi.org/10.1021/JP102971X/SUPPL_FILE/JP102971X_SI_001.PDF

Porcelli, F., Buck-Koehntop, B. A., Thennarasu, S., Ramamoorthy, A., & Veglia, G. (2006). Structures of the dimeric and monomeric variants of magainin antimicrobial peptides (MSI-78 and MSI-594) in micelles and bilayers, determined by NMR spectroscopy. *Biochemistry*, *45*(18), 5793–5799. https://doi.org/10.1021/BI0601813/SUPPL_FILE/BI0601813SI20060321_021932.PDF

Rakitin, A. R., & Pack, G. R. (2004). Molecular dynamics simulations of ionic interactions with dodecyl sulfate micelles. *Journal of Physical Chemistry B*, *108*(8), 2712–2716. https://doi.org/10.1021/JP030914I/ASSET/IMAGES/LARGE/JP030914IF00006.JPEG

Rezansoff, A. J., Hunter, H. N., Jing, W., Park, I. Y., Kim, S. C., & Vogel, H. J. (2005). Interactions of the antimicrobial peptide Ac-FRWWHR-NH(2) with model membrane systems and bacterial cells. *The Journal of Peptide Research : Official Journal of the American Peptide Society*, *65*(5), 491–501. https://doi.org/10.1111/J.1399-3011.2005.00263.X

Rozek, A., Friedrich, C. L., & Hancock, R. E. W. (2000). Structure of the bovine antimicrobial peptide indolicidin bound to dodecylphosphocholine and sodium dodecyl sulfate micelles. *Biochemistry*, *39*(51), 15765–15774. https://doi.org/10.1021/BI000714M/SUPPL_FILE/BI000714M_S.PDF

saint Jean, K. D., Henderson, K. D., Chrom, C. L., Abiuso, L. E., Renn, L. M., & Caputo, G. A. (2018). Effects of Hydrophobic Amino Acid Substitutions on Antimicrobial Peptide Behavior. *Probiotics and Antimicrobial Proteins*, *10*(3), 408–419. https://doi.org/10.1007/S12602-017-9345-Z

Shai, Y. (1999). Mechanism of the binding, insertion and destabilization of phospholipid bilayer membranes by alpha-helical antimicrobial and cell non-selective membrane-lytic peptides. *Biochimica et Biophysica Acta*, *1462*(1–2), 55–70. https://doi.org/10.1016/S0005-2736(99)00200-X

Shepherd, C. M., Schaus, K. A., Vogel, H. J., & Juffer, A. H. (2001). Molecular dynamics study of peptide-bilayer adsorption. *Biophysical Journal*, *80*(2), 579–596. https://doi.org/10.1016/S0006-3495(01)76039-0

Shepherd, C. M., Vogel, H. J., & Tieleman, D. P. (2003). Interactions of the designed antimicrobial peptide MB21 and truncated dermaseptin S3 with lipid bilayers: molecular-dynamics simulations. *The Biochemical Journal*, *370*(Pt 1), 233–243. https://doi.org/10.1042/BJ20021255

Tieleman, D. P., van der Spoel, D., & Berendsen, H. J. C. (2000). Molecular dynamics simulations of dodecylphosphocholine micelles at three different aggregate sizes: Micellar structure and chain relaxation. *Journal of Physical Chemistry B*, *104*(27), 6380–6388. https://doi.org/10.1021/JP001268F/ASSET/IMAGES/MEDIUM/JP001268FE00021.GIF

Ulmschneider, J. P. (2017). Charged Antimicrobial Peptides Can Translocate across Membranes without Forming Channel-like Pores. *Biophysical Journal*, *113*(1), 73–81. https://doi.org/10.1016/J.BPJ.2017.04.056

van den Hooven, H. W., Spronk, C. A. E. M., van de Kamp, M., Konings, R. N. H., Hilbers, C. W., & van de Ven, F. J. M. (1996). Surface Location and Orientation of the Lantibiotic Nisin Bound to Membrane-Mimicking Micelles of Dodecylphosphocholine and of Sodium Dodecylsulphate. *European Journal of Biochemistry*, *235*(1–2), 394–403. https://doi.org/10.1111/J.1432-1033.1996.00394.X

van der Spoel, D., Lindahl, E., Hess, B., Groenhof, G., Mark, A. E., & Berendsen, H. J. C. (2005). GROMACS: fast, flexible, and free. *Journal of Computational Chemistry*, *26*(16), 1701–1718. https://doi.org/10.1002/JCC.20291

Wang, Q., Hong, G., Johnson, G. R., Pachter, R., & Cheung, M. S. (2010). Biophysical properties of membrane-active peptides based on micelle modeling: A case study of cell-penetrating and antimicrobial peptides. *Journal of Physical Chemistry B*, *114*(43), 13726–13735. https://doi.org/10.1021/JP1069362/SUPPL_FILE/JP1069362_SI_001.PDF

Wieprecht, T., Dathe, M., Beyermann, M., Krause, E., Maloy, W. L., MacDonald, D. L., & Bienert, M. (1997). Peptide hydrophobicity controls the activity and selectivity of magainin 2 amide in interaction with membranes. *Biochemistry*, *36*(20), 6124–6132. https://doi.org/10.1021/BI9619987/ASSET/IMAGES/LARGE/BI9619987F00005.JPEG

Wong, T. C., & Kamath, S. (2002). Molecular dynamics simulations of adrenocorticotropin (1-24) peptide in a solvated dodecylphosphocholine (DPC) micelle and in a dimyistoylphosphatidylcholine (DMPC) bilayer. *Journal of Biomolecular Structure & Dynamics*, *20*(1), 39–57. https://doi.org/10.1080/07391102.2002.10506821

Wymore, T., & Wong, T. C. (2000). The structure and dynamics of ACTH (1-10) on the surface of a sodium dodecylsulfate (SDS) micelle: a molecular dynamics simulation study. *Journal of Biomolecular Structure & Dynamics*, *18*(3), 461–476. https://doi.org/10.1080/07391102.2000.10506681

Yang, S. T., Yub Shin, S., Kim, Y. C., Kim, Y., Hahm, K. S., & Kim, J. il. (2002). Conformation-dependent antibiotic activity of tritrpticin, a cathelicidin-derived antimicrobial peptide. *Biochemical and Biophysical Research Communications*, *296*(5), 1044–1050. https://doi.org/10.1016/S0006-291X(02)02048-X

Chapter 5

Peptide Selectivity by Membrane-mimetic-bilayers in Response to Spacer Length Modification of the Cationic Side-chains

In this chapter, we estimated the difference of peptide binding affinity (ΔΔG) to the membrane-mimetic models (negatively charged POPE/POPG bilayer and zwitterionic POPC bilayer as bacterial and mammalian membrane mimic respectively) in response to the lysine side-chain modifications in LL-14 peptide (Lys → Arg, Lys → non-canonical lysine analog: Orn/Dab/Dap/Hly, Lys → non-canonical arginine analog: Agb/Agp/Hrg) using classical molecular dynamics alchemical free energy simulations. The absolute peptide: bilayer binding affinity (ΔG) was estimated by employing two popular approaches, steered molecular dynamics umbrella sampling (SMD-US) and molecular mechanics Poisson–Boltzmann surface area (MM/PBSA) method. We showed that 3 carbon spacer cationic side-chains i.e., Dab/Agb obtained by shortening the side-chain of lysine/arginine residue improves the binding affinity to both POPE/POPG and POPC bilayers, latter being prominent. Arginine and arginine-derivative peptides exhibited stronger binding affinity to the bilayers relative to the lysine analog, in line with the previous experimental studies that claims higher antimicrobial activities for the former. Homoarginine (hrg; increase in the spacer length of arginine by a single carbon) peptide binding was preferred by both the bilayers relative to the template LL-14 peptide, but displayed strongest preference for the POPE/POPG bilayer. Surprisingly, homolysine (hly; increase in the spacer length of lysine by a single carbon) peptide binding affinity to POPE/POPG bilayer was found to be comparable to that of LL-14 peptide binding, but disfavored strongly by the mammalian-membrane-mimetic POPC bilayer. Thus, we propose homolysine analog of LL-14 as a promising non-cytotoxic AMP and encourage experimental verification. Despite the strongest binding affinity of homoarginine analog of LL-14, the same is likely to be limited by cytotoxicity. The correlation between the calculated energetics (ΔΔG) and the molecule structure has been highlighted. Favourable peptide:bilayer interactions offsets the desolvation penalty and stabilize the peptide: bilayer complex. The study showed how lysine/arginine space length modification alters the energetics of peptide: bilayer binding, which might be useful for designing potent, selective and stable AMPs.

5.1 Background

The positively charged residues (Arg and Lys) are known to be very important for the activity of the cationic peptides, due to their ability to facilitate electrostatic attraction with the negatively charged bacterial membrane (Lohner et al., n.d.; Yeaman & Yount, 2003). AMPs' are known to undergo fast protease degradation, resulting in a limited stability in the serum and the gastrointestinal tract. (Karstad et al., 2012; Werle & Bernkop-Schnürch, 2006). Serine proteases such as trypsin recognizes the arginine and lysine residues for its activity. Several strategies have been adopted to improve the proteolytic stability of the AMPs (Gentilucci et al., 2010; Werle & Bernkop-Schnürch, 2006), viz., peptide cyclization, backbone or side chain modifications, terminal capping (Nguyen et al., 2010), and incorporation of D-amino acid residues (Berthold et al., 2013; Boöttger et al., 2017) etc. Space length modification of the positively charged amino acid residues is a popular approach and have been studied previously designing stable AMPs (Bagheri et al., 2016; Bagheri & Hancock, 2017; Karstad et al., 2012), in blood serum (Berthold et al., 2013; Boöttger et al., 2017; Nguyen et al., 2010) or in whole organ extracts (Karstad et al., 2012). These studies have shown that changes in the number of methylene groups of the side chain of arginine and lysine can improve the stability of the peptides by preventing fast tryptic degradation and improve the antimicrobial activity. In this chapter, we have estimated the effect of lysine and arginine space length modification on the bilayer binding affinity. The hydrophobic-hydrophilic balance of the peptide:membrane complex was shown to fine-tune the peptide binding affinity.

5.2 Materials and Methods

5.2.1 Peptide and Bilayer models

Terminal capped (N-terminal with $-NH_3^+$ and C-terminal with $-CONH_2$) linear LL-14 peptide was modelled using PyMOL (Schrödinger, LLC, 2010) and placed ~2.5 nm away from the surface of the equilibrated bacterial and mammalian membrane mimetic bilayers [bacterial membrane mimic: POPE/POPG bilayer ratio of 3:1 (which include 72 POPE and 24 POPG molecules); (Agadi et al., 2018; Lai & Kaznessis, 2020; Manzo et al., 2019; Mukherjee et al., 2017; Zou et al., 2018) and mammalian membrane mimic: POPC bilayer which include 96 lipid molecules (Benetti et al., 2019; Mukherjee et al., 2017)]. The bilayers were modelled using CHARM-GUI Membrane Builder (Jo et al., 2008; Lee et al., 2016). Water layer of 2.5 nm was placed on both sides of the bilayer. The simulation box was neutralized by adding monovalent counter ions (Na^+ or Cl^-) and the resulting simulation

setup was subjected to energy minimization followed by MD simulation employing *NPT* ensemble. Three independent simulations (3 μs each with a total of 18 μs) were performed to study LL-14: bilayer binding. The final structures from the post-equilibrated production dynamics were selected for estimating peptide:bilayer binding affinity using steered molecular dynamics umbrella Sampling. The relative binding affinity was estimated by alchemical free energy simulations. The same simulation protocol described in Chapter 2 was adopted for this work. Simulation details given in **Appendix IV Table A5.1.**

5.2.2 Absolute binding affinity

Two popular approaches Steered Molecular Dynamics-Umbrella Sampling (SMD-US) and Molecular Mechanics Poisson-Boltzmann Surface Area (MM/PBSA) were used to estimate absolute binding affinity.

Structures at various time-point from the conventional MD simulations of LL-14:bilayer binding was selected and subjected to umbrella sampling simulation. A total of 21 frames were taken as initial configuration and a harmonic potential of spring constant of 42 kJ mol^{-1} nm^{-2} was applied for the estimation of binding free energy (PMF). The weighted histogram analysis method (WHAM) (Kumar et al., 1992) was used to estimate the free energy (potential mean force) along the peptide bilayer binding event.

An alternate approach was also taken where the final structure of the LL-14:bilayer complex was selected and subjected to center of mass pulling or steered molecular dynamics (SMD) simulation (using a harmonic spring constant of 1000 kJ mol^{-1} nm^{-2} at 0.005 nm ps^{-1} pull rate). The center of mass pulling (SMD) biases the system and generates structures along the dissociation pathway. The structures generated by SMD simulations were selected for umbrella sampling and estimate the free energy profile of the dissociation event. A total of ~12.8 μs umbrella sampling simulation (150 ns each window) was performed to estimate the PMF profile (**Appendix IV Table A5.2)**.

The methodology for MM/PBSA binding affinity estimation has been described in the previous chapters (Chapter 1 and Chapter 2) and adopted for the work. The adopted dielectric constant for the peptide:bilayer were $\varepsilon = 22.2$ which is close to the experimental dielectric constant (Tian, 2010).

5.2.3 Thermodynamic cycle and Relative Binding Affinity

An appropriate thermodynamic cycle (**Figure 5.1**) was used to estimate the relative binding free energies.

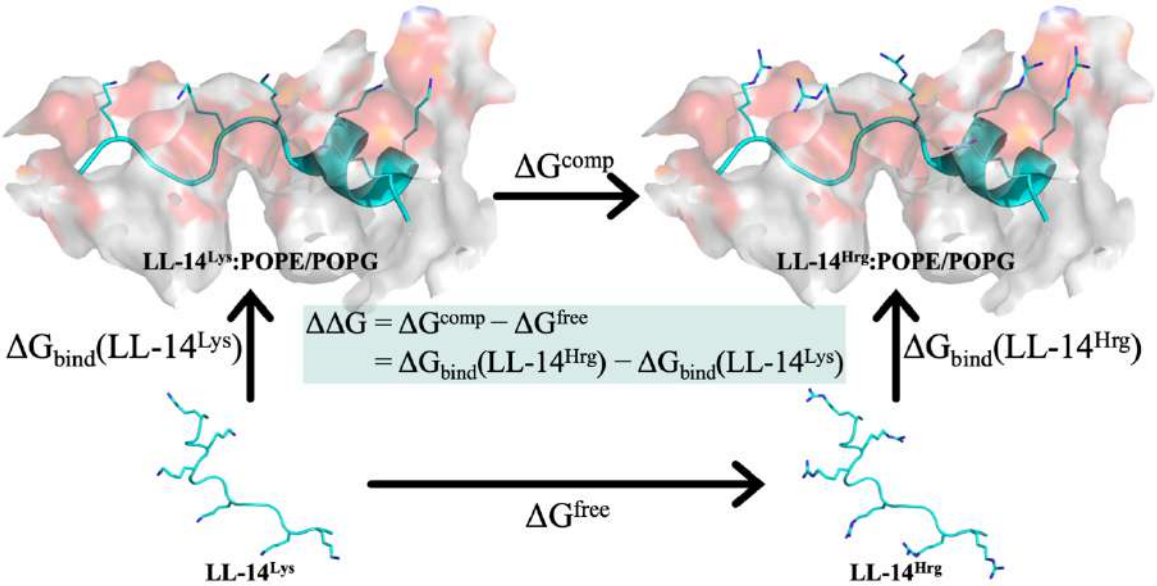

Figure 5.1: Thermodynamic cycle for studying peptide:bilayer binding. Vertical legs correspond to binding; horizontal legs correspond to the alchemical transformation of the peptide side chain from lysine (Lys) into homoarginine (Hrg), either in the bilayer (upper) or free in water (lower). The Lysine peptide(LL-14^{Lys})/Homoarginine peptide(LL-14^{Hrg}) binding free energy difference is $\Delta\Delta G = \Delta G^{comp} - \Delta G^{free} = \Delta G_{bind}(LL\text{-}14^{Hrg}) - \Delta G_{bind}(LL\text{-}14^{Lys})$. Based on our previous experiments, we confirmed that free LL-14 adopted helical conformation only after micelle binding; thus, a random coil structure was considered for lysine to homoarginine transformation in the lower horizontal arm (ΔG^{free}).

Lysine side chains of LL-14 at all the six positions (2^{nd}, 5^{th}, 6^{th}, 9^{th}, 12^{th} and 13^{th}) were transformed to Orn/Dab/Dap/Hly/Arg/Agb/Agp/Hrg in presence and absence of the bilayer. The free energy charge associated with the alchemical transformations (ΔG^{comp} and ΔG^{free}) was estimated by employing the Bennett acceptance-ratio (BAR) (Bennett, 1976) method implemented in GROMACS software (*gmx_bar*). Scripts from the PMX package (Gapsys et al., 2015) were used to generate the hybrid peptide structures and topology files. Twenty one equally spaced λ values between 0 and 1 (0.00 0.05 0.10 0.15 0.20 0.25 0.30 0.35 0.40 0.45 0.50 0.55 0.60 0.65 0.70 0.75 0.80 0.85 0.90 0.95 1.00) with a soft-core potential were used for smooth alchemical transformation. Where "λ" was coupling coordinate, to alter the Hamiltonian thus modifies the identity of the amino acid. All the 21 λ windows were simulated for 15 ns each and the free energy difference (ΔG) between the neighbouring windows were estimated using BAR method. The first 1 ns of MD trajectory at every λ window was considered as equilibration and was not considered for free energy estimation. The estimated $\Delta\Delta G$'s data given in **Appendix IV Table A5.3**.

5.3 Results

MD simulation showed that the free LL-14 peptide was unstructured (random-coil) in water (**Appendix IV Figure 5.X**) and adopted the partial helical conformation (at the C-terminal end) in response to negatively charged POPE/POPG bilayer binding (**Figure 5.2a**).

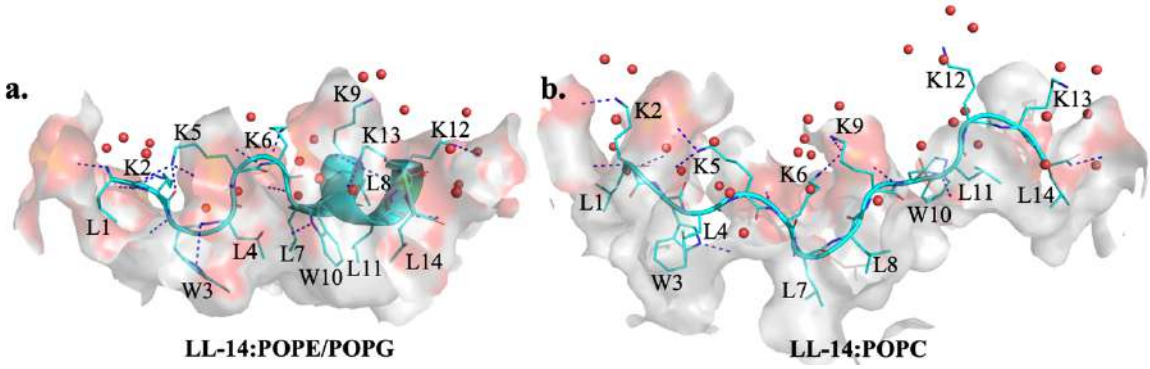

Figure 5.2: Representative MD structures. LL-14 bound to a) POPE/POPG bilayer and b) POPC bilayer within 0.35 nm. Bilayer represented as surface (Carbon light grey, Oxygen red and Phosphorus yellow color) and peptide represented as cartoon and sticks (cyan color). Peptide interacting with bilayers and waters were highlighted in blue dashed lines and red spheres. Hydrogens are not shown for clarity.

Previous CD experiments indeed reported (Ghosh et al., 2021) the coil → helix transition for LL-14 in presence of SDS/DPC micelle. Although, MD simulations could not capture the coil → helix transition for the LL-14 binding to zwitterionic POPC bilayer even after 3 μs of production dynamics, but the appearance of turns were noticeable (**Figure 5.2b**). The tryptophan residues (W3 and W10) of LL-14 were found to be buried in the similar desolvated micro-environment created by the hydrophobic lipid core of the bilayers (**Appendix IV Figure 5.1**). A single characteristic tryptophan fluorescence peak observed in the fluorescence study (Ghosh et al., 2021) indicated similar microenvironment for the both the tryptophan residues (W3, W10) of LL-14 in complex with SDS-micelle. Thus, the MD structures of LL-14:bilayer complexes corroborates the previous CD and fluorescence experiments (Ghosh et al., 2021). LL-14 satisfied the bonding requirements either by forming direct interactions (salt-bridge, hydrogen bond) with the negatively charged surface of the bilayer and water molecules (**Figure 5.2**).

5.3.1 Absolute peptide:bilayer binding affinity

The snapshots from the LL-14 binding to bilayer (at various peptide:bilayer center-of-mass distances, ξ) were selected from conventional MD trajectory. The center-of-mass of the peptide and the bilayer of the selected snapshots were harmonically restrained and subjected to molecular dynamics simulations (Umbrella sampling). The good overlap of

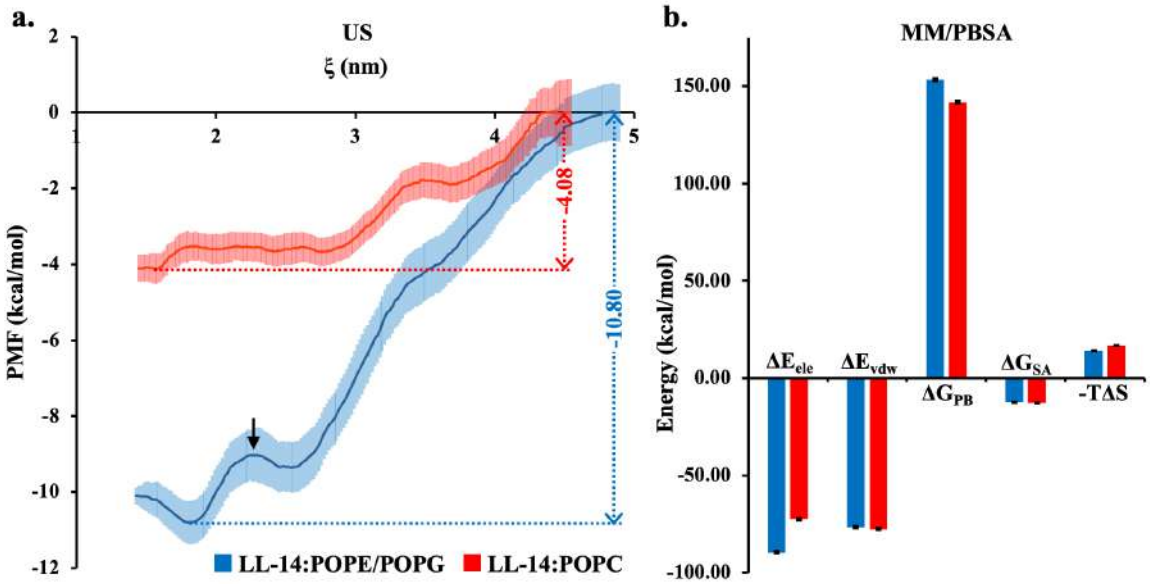

Figure 5.3: LL-14 binding energy with POPE/POPG bilayer (blue) and POPC bilayer (red). a) Potential of mean force (PMF) as a function of COM (ξ). Bootstrapping errors (100 cycles) were shown as transparent area. b) binding free energy (ΔG_{bind}) and its components: ΔE_{ele} (electrostatic energy), ΔE_{vdw} (van der Waals energy), ΔG_{PB} (polar solvation) ΔG_{SA} (non-polar solvation), and TΔS (entropy contribution) was estimated using MM/PBSA approach.

the biased equilibrium probability distribution function between the neighboring umbrella windows were ensured. PMF profile (**Figure 5.3a**) showed that the LL-14 binding is more favored for POPE/POPG bilayer (ΔG ~-4 kcal/mol) relative to the POPC bilayer (ΔG ~-8 kcal/mol). The overall negative surface charge on the POPE/POPG bilayer (contrary to zwitterionic neutral POPC bilayer) attributed to enhanced electrostatic interaction resulting in favorable LL-14:POPE/POPG binding affinity. Activation barrier at ξ = 2.27 nm (highlighted by an arrow, **Figure 5.3a**) denote the coil → helix conformational change in the LL-14 in response to POPE/POPG binding.

The LL-14:bilayer dissociation was not observed in the conventional molecular dynamics trajectories even after extending the simulation to 3 μs. Thus, to gain insight into the dissociation event we performed center of mass pulling (Steered molecular dynamics or SMD). LL-14 bound bilayer complexes (post-equilibrated converged MD structures, **Figure 5.2**) corresponds to the beginning of the simulation (t = 0 ps). Within 250-350 ps (**Appendix IV Figure A5.2**), the peptide is completely out of the bilayer and fully solvated (**Appendix IV Figure A5.2**). The force profile showed a single peak (**Appendix IV Figure A5.2**) which corresponds to the structure that preserved the interactions between the bilayer and the N-terminal of the LL-14 peptide (L1, K2, W3, L4, K5, and K6). Forces build up during the SMD simulation until a breaking point was reached (peak position in the force profile), disruption of critical interactions (N-terminal of the LL-14 and the bilayer) resulted

the peptide dissociation from the bilayer. Intact LL-14 (N-terminal):bilayer interaction in the high force point and early dissociation of the C-terminal region of LL-14 from the bilayer in response to pulling indicate the importance of N-terminal of the peptide for the stability of the peptide:bilayer complex. The series of snapshots generated from the center-of-mass pulling (SMD) were subjected to umbrella sampling (applying a harmonic biasing potential between the COM of the peptide and the bilayer: SMD-US) and the free energy of the dissociation (ΔG) was estimated from the PMF profile. As expected, the estimated the LL-14 dissociation free energy from SMD-US simulation (ΔG ~ +10 kcal/mol and +4 kcal/mol for POPE/POPG and POPC bilayer respectively) agree with the association free energy estimated from the binding event (umbrella sampling on the snapshots from unbiased conventional MD). However, the dissociation path in response to pulling (SMD-US) was found to be different from the LL-14 binding to the bilayer, evident from the PMF profiles of the binding and dissociation events (**Appendix IV Figure A5.3**). It is not surprising that the dissociation path from the SMD simulation was found to be different compared to the unbiased binding event (**Appendix IV Figure A5.3**), since the choice of the reaction coordinate "ξ" is arbitrarily and not necessarily capture the real dissociation pathway.

Peptide binding to the bilayer is penalized heavily by desolvation ($\Delta G_{pb,}$ polar term) as well as entropy ($T\Delta S$), but offsets by the favorable peptide:bilayer interaction (ΔE_{ele} and ΔE_{vdw}; former being the major component) (**Figure 5.3b**). Favorable non-polar free energy component associated with the desolvation (ΔG_{SA}) of the peptide:bilayer binding is less. Absolute binding energy difference between LL-14 bound POPE/POPG and POPC bilayer mostly come from the electrostatic energy (ΔE_{ele}) (**Figure 5.3b**).

5.3.2 Energetics of peptide binding to the membrane-mimetic-bilayer models from alchemical free energy simulations

Considering the converged MD structures LL-14:bilayer complexes (**Figure 5.2**) as template, we estimated the change in POPE/POPG bilayer binding affinity ($\Delta\Delta G$) in response to Lys $\rightarrow$ Arg mutation (in all six position of LL-14) by employing appropriate thermodynamic cycle (**Figure 5.1**). Similarly, the effect of Lys/Arg aliphatic chain length alteration on the energetics of POPE/POPG bilayer binding were examined by alchemical transformations (Lys $\rightarrow$ Orn/Dab/Dap/Hly and Lys $\rightarrow$ Arg/Agb/Agp/Hrg). Cationic residues (arginine and lysine) play a crucial role in the antimicrobial activity of most AMPs

by establishing electrostatic contacts with the negatively charged bacterial membranes. Moreover, several attempts have been made to design protease resistance, potent AMPs by systematically reducing/enhancing the side-chain-length of the positively charged amino-acid residues (Lys → Orn/Dab/Dap/Hly and Arg → Agb/Agp/Hrg; **Appendix IV Figure 5.4**). Reduction/increase of the length was shown to alter the antimicrobial activity (Arias et al., 2018; Pandit et al., 2022).

The calculated relative peptide binding affinities (ΔΔG) to the bilayer models are summarized in **Figure 5.4**. Binding of Arg-peptide and Arg-derivative peptides (Agb, Agp, Hrg) to the bilayers were found to be favored (ΔΔG ~3 to 4 kcal/mol) relative to the Lys-

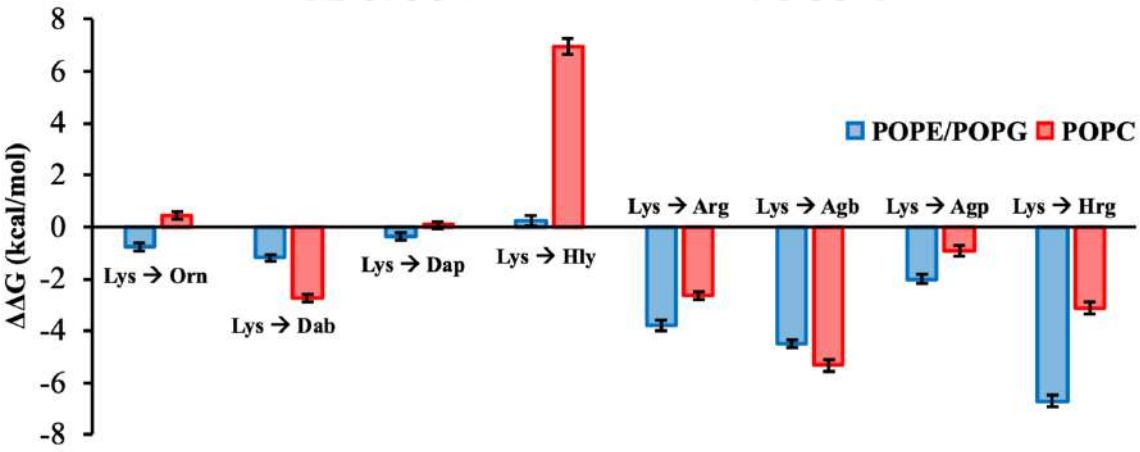

Figure 5.4: Estimated changes in binding free energy, ΔΔG, for POPE/POPG (blue) and POPC (red) as a result of Lys to Orn/Dab/Dap/Hly/Arg/Agb/Agp/Hrg transformation (at multiple positions) in the LL-14 peptide. Error bars, 1 s.e.m. Where Lys: Lysine, Orn: Ornithine, Dab: 2,4-diaminobutyric acid, Dap: 2,3-diaminopropionic acid, Hly: Homolysine, Arg: Arginine, Agb: 2-amino-4-guanidinobutyric acid, Agp: 2-amino-3-guanidinopropanoic acid, Hrg: Homoarginine.

peptide analog (**Figure 5.4**). In general, the antimicrobial assays of the peptides containing Arg- and Arg-derivatives exhibited stronger antimicrobial activities relative to their Lys- and Lys-derivative-analogs, corroborating the calculated relative binding affinities (ΔΔG). Change in the length of the aliphatic side-chain of Lysine/Arginine was found to alter the energetics of peptide:bilayer binding. Interestingly, increasing the length of the lysine side chain by one carbon (Lys → Hly: 6 carbon) is weakly/strongly disfavored by the POPE/POPG or POPC bilayer. The results indicate the LL-14 and the homo-lysine-derivative will bind the POPE/POPG bilayer with more or less equal strength, but the latter is strongly disfavored for binding to POPC bilayer. Contrary to homolysine (Hly), homoarginine-analog peptide was found to be the strongest binder to the POPE/POPG bilayer (ΔΔG ~7 kcal/mol) relative to the template LL-14 peptide. Favorable binding of homoarginine-analog to POPC bilayer was confirmed, ΔΔG ~3 kcal/mol. The results

indicated that Lys → Hrg mutation in the LL-14 peptide will enhance the peptide binding to both POPE/POPG and POPC bilayer, former being the most favorable.

The binding affinity of the peptide to the bacterial membrane mimic (POPE/POPG) was found to be weakly favored (ΔΔG < 2 kcal/mol) upon shortening the lysine side-chain (from 5 carbon of lysine → Orn:4 carbon → Dab: 3 carbon → Dap: 2 carbon), 3 carbon Dab is relatively more favorable. Similarly, bilayer binding of the 3 carbon analog of arginine (Agb) was found to be favored relative to the 2 carbon analog (Agp). Hence, 3 carbon positively charged amino-acid residues (Dab, Agb) actually appears to be somewhat favorable for bilayer binding relative to other shorter analog (Lys, Arg). This is also in line with the previous experimental studies on short AMPs (Arias et al., 2018; Pandit et al., 2022).

5.3.3 MD Structures and Energetics

5.3.3.1 Lysine versus Arginine peptide bound to Membrane-mimetic-bilayer

Favourable arginine-peptide binding relative to the lysine-peptide (LL-14) to the POPE/POPG micelles (ΔΔG ~4 kcal/mol, **Figure 5.4**) was attributed to stronger peptide:bilayer interaction for the former (**Figure 5.5**). The simulations revealed that arginine peptide interacted with larger number of phosphates and water molecules in the

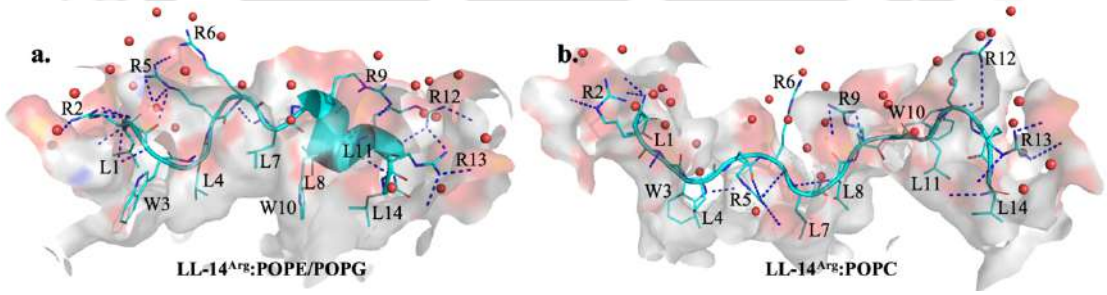

Figure 5.5: Representative MD structures. LL-14^{Arg} bound to a) POPE/POPG bilayer and b) POPC bilayer within 0.35 nm. Bilayer represented as surface (Carbon light grey, Oxygen red and Phosphorus yellow color) and peptide represented as cartoon and sticks (cyan color). Peptide interacting with bilayers and waters were highlighted in blue dashed lines and red spheres. Hydrogens are not shown for clarity.

bilayer, and stabilizes the arginine-phosphate cluster by forming 2 to 3 salt-bridges. Extensive interactions between the guanidinium moiety of arginine (five H-bond donors, whereas, amine moiety of lysine is a two H-bond donors) and sulphates of the bilayer owing to larger interaction area, higher electrostatic contact, deeper penetration. Number of water molecules around the arginine peptide (in complex with bilayer) was found be larger relative to lysine peptide (LL-14), indicated higher solvent exposer of the former peptide in complex with the bilayer. Similar to negatively charged POPE/POPG bilayer,

zwitterionic POPC bilayer ensured peptide selectivity favouring arginine-peptide relative to the lysine-peptide, however, the weaker strength of the preference (ΔΔG ~ 2.5 kcal/mol, **Figure 5.5**) was due to weaker electrostatic interactions between peptide:POPC bilayer.

5.3.3.2 MD Structures of Homolysine peptide:bilayer complexes

Lysine to homolysine mutation increases the aliphatic side-chain of the amino acid by one carbon. An increase in the hydrophobicity upon Lysine → homolysine mutation in the POPE/POPG or POPC bilayer disrupted the electrostatic interactions, thus, disfavor bilayer binding. POPE/POPG bilayer discriminate weakly between lysine- and Homolysine-peptide binding (ΔΔG ~0.25 kcal/mol, **Figure 5.4**) implying that the binding affinity is more or less independent of the Lysine → homolysine mutation. We find no major distortions of the homolysine-peptide:(POPE/POPG)-bilayer, and weak discrimination is seen to arise from a lack of peptide:bilayer contact by two units (**Figure 5.6a**). Distinctly large discrimination disfavoring homolysine peptide binding to POPC bilayer (ΔΔG ~7 kcal/mol, **Figure 5.4**) was primarily due to the significant loss of phosphate-guanidinium

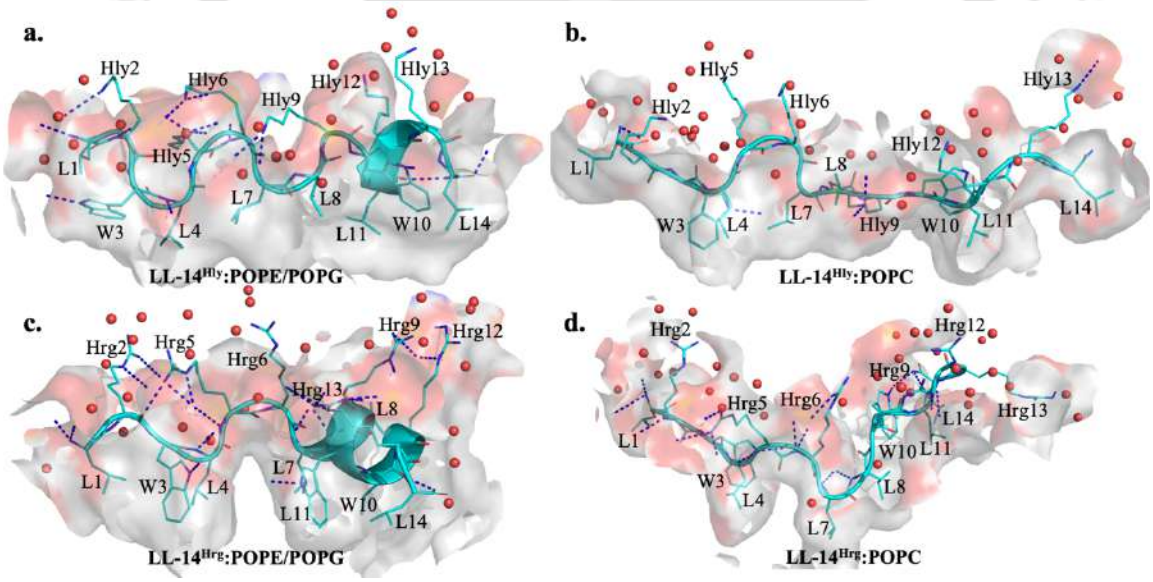

Figure 5.6: Representative MD structures. LL-14^{Hly} and LL-14^{Hrg} bound to a,c) POPE/POPG bilayer and b,d) POPC bilayer within 0.35 nm. Bilayer represented as surface (Carbon light grey, Oxygen red and Phosphorus yellow color) and peptide represented as cartoon and sticks (cyan color). Peptide interacting with bilayers and waters were highlighted in blue dashed lines and red spheres. Hydrogens are not shown for clarity.

salt-bridge interactions in response to Lysine → homolysine mutation (**Figure 5.6b**). Weakest homolysine-peptide: POPC-bilayer interaction was further evident from the highest solvent exposure ~35 water molecules.

5.3.3.3 MD Structures of Homoarginine peptide:bilayer complexes

Homoarginine-peptide binding was found to be most preferred by the POPE/POPG bilayer relative to the lysine peptide (LL-14) (ΔΔG ~7 kcal/mol, **Figure 5.4**) primarily due to extensive electrostatic contact and less desolvation penalty (**Figure 5.6c**). A total of 24 peptide:bilayer salt-bridges account for the highest stability. Weaker preference of the homoarginine-peptide relative to the lysine-peptide by the zwitterionic POPC bilayer was evident from weaker electrostatic interactions (**Figure 5.6d**).

5.4 Discussions

Free energy calculations demonstrated that the energetics of positively charged peptide binding on the bilayer (negatively charged or zwitterionic) varies dramatically upon reduction or increase in the aliphatic side-chain length of the positively charged amino-acid residues (**Figure 5.4**). In particular, 3 carbon spacer length (Dab/Agb by shortening the Lys/Arg side-chain) seems to improve the bilayer binding affinity, noticeable for zwitterionic POPC-bilayer (**Figure 5.4**). Interestingly, homolysine-analog peptide was found to be strongly disfavored relative to LL-14 (lysine-peptide) for zwitterionic POPC-bilayer binding, but very weakly disfavored for negatively charged POPE:POPG bilayer. The high free energy of the homolysine-peptide:POPC-bilayer is likely to drive the peptide dissociation from the zwitterionic POPC bilayer. (Previous chapter we established a link between estimated ΔΔG to function. hypothesis: antimicrobial but non-cytotoxic). Thus, homolysine-peptide seems to be a promising non-cytotoxic AMP and likely to bind the negatively charged bacterial membrane with more or less same affinity as its template LL-14 peptide. Arg- and Arg-derivatives were found to be exhibit stronger binding affinity relative to the lysine-analog to the bilayers due to extensive guanidinium:sulphate electrostatic contacts (**Figure 5.5**). This is also in line with the experiments (Arias et al., 2018) The homoarginine-peptide was found to be the strongest binder to the negatively charged POPE/POPG bilayer (relative to LL-14), thus likely to be the most potent AMP among the peptides reported in this work. However, homoarginine-peptide is likely to limited by cytotoxicity, indicated by the stronger binding affinity to POPC bilayer relative to the experimentally known cytotoxic LL-14 peptide. Favorable peptide: bilayer electrostatic and van der Waals interactions offsets the desolvation penalty, stabilizes the peptide: bilayer complex. The estimated energetics of the peptide selectivity (ΔΔG) to the membrane surrogates (POPE/POPG, POPC bilayers) was shown to be dependent on the aliphatic spacer length of the positively charged residues and a direct correlation between

the energetics and structures has been established. The results indicated that the synthesis and activity assays (antimicrobial, cytotoxicity) of Hly and Hrg analog of the template LL-14 is worth trying and encourage experimental verification.

5.5 Conclusion

Fourteen residue-long homo-lysine analog of the template antimicrobial peptide LL-14 (NH_3^+-LKWLKKLLKWLKKL-$CONH_2$) is proposed to be promising antimicrobial agent, potency similar to the LL-14 peptide, but likely to be non-cytotoxic in nature. The homo-arginine along is predicted to be the most potent AMP relative to the template LL-14 but likely to be cytotoxic. A three-carbon spacer length in the positively charged side-chains (lysine, arginine) favored bilayer binding. A direct link between the peptide binding affinity to the simple membrane mimic models and the molecular structures has been established. The study illustrated how side-chain mutation (Lys → Orn, Lys → Dab, Lys → Dap, Lys → Hly, Lys → Arg, Lys → Agb, Lys → Agp, Lys → Hrg) alters the hydrophobic-hydrophilic balance of the peptide:membrane complex and fine-tune the binding affinity.

5.6 Supporting information

Supporting data of this chapter is given in **Appendix IV**.

REFERENCES

Agadi, N., Vasudevan, S., & Kumar, A. (2018). Structural insight into the mechanism of action of antimicrobial peptide BMAP-28(1–18) and its analogue mutBMAP18. *Journal of Structural Biology*, *204*(3), 435–448. https://doi.org/10.1016/J.JSB.2018.10.003

Arias, M., Piga, K. B., Hyndman, M. E., & Vogel, H. J. (2018). Improving the Activity of Trp-Rich Antimicrobial Peptides by Arg/Lys Substitutions and Changing the Length of Cationic Residues. *Biomolecules 2018, Vol. 8, Page 19*, *8*(2), 19. https://doi.org/10.3390/BIOM8020019

Bagheri, M., Arasteh, S., Haney, E. F., & Hancock, R. E. W. (2016). Tryptic Stability of Synthetic Bactenecin Derivatives Is Determined by the Side Chain Length of Cationic Residues and the Peptide Conformation. *Journal of Medicinal Chemistry*, *59*(7), 3079–3086. https://doi.org/10.1021/ACS.JMEDCHEM.5B01740

Bagheri, M., & Hancock, R. E. W. (2017). High-performance liquid chromatography and mass spectrometry-based design of proteolytically stable antimicrobial peptides. *Methods in Molecular Biology*, *1548*, 61–71. https://doi.org/10.1007/978-1-4939-6737-7_5

Benetti, S., Timmons, P. B., & Hewage, C. M. (2019). NMR model structure of the antimicrobial peptide maximin 3. *European Biophysics Journal*, *48*(2), 203–212. https://doi.org/10.1007/S00249-019-01346-7/FIGURES/7

Bennett, C. H. (1976). Efficient estimation of free energy differences from Monte Carlo data. *Journal of Computational Physics*, *22*(2), 245–268. https://doi.org/10.1016/0021-9991(76)90078-4

Berthold, N., Czihal, P., Fritsche, S., Sauer, U., Schiffer, G., Knappe, D., Alber, G., & Hoffmann, R. (2013). Novel apidaecin 1b analogs with superior serum stabilities for treatment of infections by gram-negative pathogens. *Antimicrobial Agents and Chemotherapy*, *57*(1), 402–409. https://doi.org/10.1128/AAC.01923-12

Boöttger, R., Hoffmann, R., & Knappe, D. (2017). Differential stability of therapeutic peptides with different proteolytic cleavage sites in blood, plasma and serum. *PloS One*, *12*(6). https://doi.org/10.1371/JOURNAL.PONE.0178943

Gapsys, V., Michielssens, S., Seeliger, D., & de Groot, B. L. (2015). pmx: Automated protein structure and topology generation for alchemical perturbations. *Journal of Computational Chemistry*, *36*(5), 348–354. https://doi.org/10.1002/JCC.23804

Gentilucci, L., de Marco, R., & Cerisoli, L. (2010). Chemical modifications designed to improve peptide stability: incorporation of non-natural amino acids, pseudo-peptide bonds, and cyclization. *Current Pharmaceutical Design*, *16*(28), 3185–3203. https://doi.org/10.2174/138161210793292555

Ghosh, S., Pandit, G., Debnath, S., Chatterjee, S., & Satpati, P. (2021). Effect of monovalent salt concentration and peptide secondary structure in peptide-micelle binding. *RSC Advances*, *11*(58), 36836–36849. https://doi.org/10.1039/D1RA06772A

Jo, S., Kim, T., Iyer, V. G., & Im, W. (2008). CHARMM-GUI: a web-based graphical user interface for CHARMM. *Journal of Computational Chemistry*, *29*(11), 1859–1865. https://doi.org/10.1002/jcc.20945

Karstad, R., Isaksen, G., Wynendaele, E., Guttormsen, Y., de Spiegeleer, B., Brandsdal, B. O., Svendsen, J. S., & Svenson, J. (2012). Targeting the S1 and S3 subsite of trypsin with unnatural cationic amino acids generates antimicrobial peptides with potential for oral administration. *Journal of Medicinal Chemistry*, *55*(14), 6294–6305. https://doi.org/10.1021/JM3002058

Kumar, S., Rosenberg, J. M., Bouzida, D., Swendsen, R. H., & Kollman, P. A. (1992). The weighted histogram analysis method for free-energy calculations on biomolecules. I. *Journal of Computational Chemistry*, *13*(8), 1011–1021. https://doi.org/10.1002/JCC.540130812

Lai, P. K., & Kaznessis, Y. N. (2020). Insights into membrane translocation of protegrin antimicrobial peptides by multistep molecular dynamics simulations. *AIChE Annual Meeting, Conference Proceedings*, *2020-November*, 6056–6065. https://doi.org/10.1021/ACSOMEGA.8B00483/ASSET/IMAGES/LARGE/AO-2018-004837_0004.JPEG

Lee, J., Cheng, X., Swails, J. M., Yeom, M. S., Eastman, P. K., Lemkul, J. A., Wei, S., Buckner, J., Jeong, J. C., Qi, Y., Jo, S., Pande, V. S., Case, D. A., Brooks, C. L., MacKerell, A. D., Klauda, J. B., & Im, W. (2016). CHARMM-GUI Input Generator for NAMD, GROMACS, AMBER, OpenMM, and CHARMM/OpenMM Simulations Using the CHARMM36 Additive Force Field. *Journal of Chemical Theory and Computation*, *12*(1), 405–413. https://doi.org/10.1021/acs.jctc.5b00935

Lohner, K., Sevcsik, E., and, G. P.-A. in planar lipid bilayers, & 2008, undefined. (n.d.). Chapter five liposome-based biomembrane mimetic systems: Implications for lipid–peptide interactions. *Elsevier*. Retrieved January 30, 2023, from https://www.sciencedirect.com/science/article/pii/S155445160706005X

Manzo, G., Ferguson, P. M., Gustilo, V. B., Hind, C. K., Clifford, M., Bui, T. T., Drake, A. F., Atkinson, R. A., Sutton, J. M., Batoni, G., Lorenz, C. D., Phoenix, D. A., & James Mason, A. (2019). Minor sequence modifications in temporin B cause drastic changes in antibacterial potency and selectivity by fundamentally altering membrane activity. *Scientific Reports 2019 9:1*, *9*(1), 1–16. https://doi.org/10.1038/s41598-018-37630-3

Mukherjee, S., Kar, R. K., Nanga, R. P. R., Mroue, K. H., Ramamoorthy, A., & Bhunia, A. (2017). Accelerated molecular dynamics simulation analysis of MSI-594 in a lipid bilayer. *Physical Chemistry Chemical Physics*, *19*(29), 19289–19299. https://doi.org/10.1039/C7CP01941F

Nguyen, L. T., Chau, J. K., Perry, N. A., de Boer, L., Zaat, S. A. J., & Vogel, H. J. (2010). Serum stabilities of short tryptophan- and arginine-rich antimicrobial peptide analogs. *PloS One*, *5*(9), 1–8. https://doi.org/10.1371/JOURNAL.PONE.0012684

Pandit, G., Sarkar, T., S. R., V., Debnath, S., Satpati, P., & Chatterjee, S. (2022). Delineating the Mechanism of Action of a Protease Resistant and Salt Tolerant Synthetic Antimicrobial Peptide against Pseudomonas aeruginosa. *ACS Omega*. https://doi.org/10.1021/ACSOMEGA.2C01089/ASSET/IMAGES/MEDIUM/AO2C01089_M003.GIF

Schrödinger, LLC. (2010). *The PyMOL Molecular Graphics System, Version 2.4.0*. https://pymol.org/2/

Tian, P. (2010). Computational protein design, from single domain soluble proteins to membrane proteins. *Chemical Society Reviews*, *39*(6), 2071–2082. https://doi.org/10.1039/B810924A

Werle, M., & Bernkop-Schnürch, A. (2006). Strategies to improve plasma half life time of peptide and protein drugs. *Amino Acids*, *30*(4), 351–367. https://doi.org/10.1007/S00726-005-0289-3

Yeaman, M. R., & Yount, N. Y. (2003). Mechanisms of antimicrobial peptide action and resistance. *Pharmacological Reviews*, *55*(1), 27–55. https://doi.org/10.1124/PR.55.1.2

Zou, R., Zhu, X., Tu, Y., Wu, J., & Landry, M. P. (2018). Activity of Antimicrobial Peptide Aggregates Decreases with Increased Cell Membrane Embedding Free Energy Cost. *Biochemistry*, *57*(18), 2606–2610. https://doi.org/10.1021/ACS.BIOCHEM.8B00052/ASSET/IMAGES/LARGE/BI-2018-000527_0004.JPEG

Chapter 6

Overall conclusion and future perspective

Peptide:membrane interactions are critical for combating infection, signalling, ion transport, and many more. The mechanistic understanding (in terms of structure, kinetics and thermodynamics) of the peptide binding to membranes is fundamental for designing new potent selective antimicrobial agents. Despite the advancement in experiment study related to antimicrobial peptide: membrane interactions, we are far from understanding the structure-based free energy landscape of the peptide: micelle association. The ever increasing computational power and advancement of efficient software make computational analysis a powerful tool for understanding the peptide:membrane interactions on atomic scale by employing simple models. In this dissertation, classical molecular dynamics free energy calculations were used to determine the thermodynamics of peptide selectivity by membrane-mimetic-systems (micelle/bilayer). An attempt has been made to correlate computed energetics (peptide selectivity) with 3D structures of peptide: (micelle/bilayer) complexes.

In the **Chapter 1**, a brief overview of the antimicrobial peptides and the adopted methodology was discussed. Broad objectives of the thesis are described at the end of this chapter.

The **Chapter 2** discussed the principle of cationic heptapeptide selectivity (P4: NH_3^+-LKWLKKL-$CONH_2$ versus its Arginine(P5)/Histidine(P6)/Leucine(P7) analogue) by bacterial-membrane-mimetic models (SDS micelle and DOPE:DOPG bilayer). We found secondary structure of the peptides has no major role in membrane binding. Peptide:micelle interaction is sequential: electrostatic followed by hydrophobic interactions. The charge at the C-terminal end is crucial, $CONH_2$ → COO^- mutation resulted in inferior peptide:micelle interactions. The magnitude of the calculated absolute peptide binding affinity (ΔG) depends on the membrane model; however, the relative peptide binding affinities ($\Delta\Delta G$) are not. The predicted peptide binding affinity: P5 (most potent binder) > P4 > P7 >> P6 was found to be correlated with the antimicrobial activity against *P. aeruginosa* and *E. Coli* at physiological pH 7.4. Based on the computational analysis, P6 peptide was proposed to be an effective antimicrobial peptide only at low pH, which was confirmed by experiments.

The correlation between the calculated energetics and the experimental activity has been highlighted.

Chapter 3 divided into two parts (**A, B**).

Part A discusses the MD simulation of 14 residue-long antimicrobial peptides (LL-14: NH_3^+-LKWLKKLLKWLKKL-$CONH_2$, Charge = +7, obtained by doubling the length of peptide P4) in presence and absence of SDS-micelle at various monovalent salt (NaCl) concentrations (0.0%, 0.5%, 1.0% w/v). LL-14 peptide in two different conformations (random coil or unstructured: P^c, and amphipathic α-helical: P^h) were subjected to MD simulations and final MD structure of LL-14(P^h):SDS was found in line with the circular dichroism (CD) and fluorescence experiments.

Part B discussed the thermodynamics of LL-14 binding to SDS/DPC micelle at various NaCl concentrations (0.0%, 0.5%, 1.0% w/v). We found that increase in NaCl concentration systematically disfavoured the LL-14:SDS binding, primarily by stabilizing the dissociative state (i.e., free LL-14 and free micelles in water). A kinetic scheme has been proposed in which the salt-induced selective stabilization of the dissociative state increased the activation barrier for the peptide:micelle binding event resulting in reduced affinity. The N-terminal of the peptide was found to be crucial for the stability of the LL-14:SDS complex.

Chapter 4 discussed the effect of Leu → Val Mutation on the energetics of LL-14:(SDS/DPC)-micelle binding. The Leu- peptide (LL-14) was found to be preferred for micelle binding relative to the Val analogues (single or multiple Val mutants). The strength of the preference depended on the position of the Leu/Val mutation in the peptide. We have shown that, single N-terminal mutation (L1 → V1) in LL-14 fine-tune the electrostatic interactions, resulting in the highest peptide selectivity ($\Delta\Delta G$ ~8 kcal/mol for both SDS and DPC). The mechanism of L1/V1 selectivity was distinctly different for SDS and DPC micelles. SDS ensured high selectivity by disrupting the peptide:micelle salt bridge, whereas DPC desolvated the broken-peptide-backbone hydrogen bond in the V1 peptide:micelle complex. Loss of hydrophobic interaction disfavoured Leu → Val mutation in the middle of the LL-peptide. C-terminal mutation (i.e., L14V) is disfavoured by SDS micelles ($\Delta\Delta G$ ~4 kcal/mol), but not by DPC micelle. DPC micelle was found to be more selective favouring LL-14 relative to VV-14 ($\Delta\Delta G$ ~25 kcal/mol) relative to SDS micelles ($\Delta\Delta G$ ~19 kcal/mol). The high selectivity of DPC micelles provided an efficient mechanism for VV-14 dissociation from DPC micelles, thus, explain the experimentally

reported non-cytotoxicity of VV-14. On the hand, the low selectivity of SDS micelles ensured the binding of both LL-14 and VV-14.

In **Chapter 5**, discussed the effect of non-natural amino-acid substitution (Lys→ non-canonical lysine analog: Orn/Dab/Dap/Hly, Lys → non-canonical arginine analog: Agb/Agp/Hrg) on the stability of the LL-14:bilayer (POPE/POPG or POPC) complexes. Based on the estimated binding affinities of the peptides, we hypothesized (1) the homoarginine (Hrg) analogue of LL-14 as a toxic but most potent peptide, and (2) homolysine (Hly)-peptide as a non-toxic antimicrobial peptide with moderate potency (equivalent to template LL-14 peptide). This study encourage experimental verification in the future.

The overall conclusion from this thesis and the future direction is discussed in **Chapter 6**. In this thesis we have shown that the estimated peptide selectivity (employing molecular dynamics simulations) by simple membrane-mimetic-models are directly corelated to the experimental antimicrobial activity. Moreover, a direct link between the estimated free energies with the MD structures were highlighted. We think the adopted methodology and the hypothesis that emerged from our study will be helpful for the rational design of potent antimicrobial peptides. However, a transition from simple membrane models (viz., micelle or bilayer) to a multicomponent systems (including different lipids, heterogeneity, proteins, ionic environments, glycolipids etc) for modelling realistic membranes are necessary for deeper understanding of the peptide: membrane interactions. Note, accuracy of MD predictions depends on the quality of the underlying force fields and adequate sampling. Classical force fields are known to over stabilize the interactions and adequate sampling is limited by finite simulation timescale. Thus relatively more accurate force fields (viz., polarizable force fields) might be an alternative (but computationally expensive) choice for MD simulations. The convergence of the MD structures of peptide:membrane-mimetic complexes and the estimated free energies must be ensured from multiple independent MD trajectories. In short, a comprehensible understanding of the complicated peptide:membrane interactions demands use of improved models (particularly the membrane), accurate force-fields and enhanced sampling etc.

Appendix I

Content

Sl No.		Topic	Page No.
1	Table A2.1	Simulation details	148
2	Table A2.2	Binding affinity estimated from umbrella sampling.	148
3	Table A2.3	Alchemical free energy calculations and Bennett acceptance ratio method (BAR)	149-151
4	Table A2.4	Relative binding affinity ΔΔG data	151
5	Figure A2.1	Graphical representation of the simulation setup	152
6	Figure A2.2	Peptide conformations	153
7	Figure A2.3	Root mean square fluctuation (RMSF)	153
8	Figure A2.4	Membrane properties (density, deuterium order parameters)	154
9	Figure A2.5	Representative MD structures for alchemical simulation	154
10	Figure A2.6	Force profile from SMD simulations	155
11	Figure A2.7	Analytical HPLC chromatogram of **P4**	155
12	Figure A2.8	Analytical HPLC chromatogram of **P5**	155
13	Figure A2.9	Analytical HPLC chromatogram of **P6**	155
14	Figure A2.10	Analytical HPLC chromatogram of **P7**	156
15	Figure A2.11	MALDI-TOF spectra of **P4**	156
16	Figure A2.12	MALDI-TOF spectra of **P5**	157
17	Figure A2.13	MALDI-TOF spectra of **P6**	157
18	Figure A2.14	MALDI-TOF spectra of **P7**	158
19	Figure A2.15	^{1}H NMR spectra of **P4**	158
20	Figure A2.16	^{1}H NMR spectra of **P5**	159
21	Figure A2.17	^{1}H NMR spectra of **P6**	160
22	Figure A2.18	^{1}H NMR spectra of **P7**	161
23	Figure A2.19	MD structures of Peptide-micelle complexes after alchemical transformation.	162
24	Figure A2.20	Theoretical net charge on the peptide as a function of pH	163

Table A2.1: Simulation details

	Box dimension (nm^3)	No of waters/Na/ Cl	Total no of atoms	Simulation Length (ns) (Equilibration/Production Run)	No of trials
SDS#	7 × 7 × 7	9475/60/0	31005	1.875/50	1
MEMB‡	5.1 × 5.1 × 11	5488/20/0	26844	1.875/200	1
P4	5 × 5 × 5	3837/0/4	11667	0.500/200	3
P5	5 × 5 × 5	3837/0/4	11673	0.500/200	3
P6	5 × 5 × 5	3850/0/1	11688	0.500/200	3
P6*	5 × 5 × 5	3840/0/4	11664	0.500/200	3
P7	5 × 5 × 5	3845/0/4	11686	0.500/200	3
P4:SDS	7 × 7 × 7	9442/60/4	31062	1.875/100	3
P5:SDS	7 × 7 × 7	9438/60/4	31056	1.875/100	3
P6:SDS	7 × 7 × 7	9445/60/1	31053	1.875/100	3
P6*:SDS	7 × 7 × 7	9442/60/4	31050	1.875/100	3
P7:SDS	7 × 7 × 7	9442/60/4	31057	1.875/100	3
P4:MEMB	5.1 × 5.1 × 11	5454/20/4	26898	0.500/500	2
P5:MEMB	5.1 × 5.1 × 11	5452/20/4	26898	0.500/500	2

no of SDS molecules 60; ‡ no of DOPE/DOPG molecules 60/20 (including upper leaf and lower leaf)

Table A2.2: Binding affinity (ΔG) estimated from umbrella sampling. Error calculated using Bootstrap Analysis (100 cycles). Results are. They averaged from three independent MD trials. Standard error of the mean (s.e.m) after ±.

	Replicas	Simulation length of Umbrella Sampling	ΔG (kcal/mol)	$\Delta G^{Averaged}$ (kcal/mol)
P4:Micelle	Trial 1	25 windows × 200 ns = 5000 ns	16.68 ± 0.97	**16.29 ± 1.07**
	Trial 2	25 windows × 200 ns = 5000 ns	16.03 ± 1.13	
	Trial 3	25 windows × 200 ns = 5000 ns	16.15 ± 1.11	
P4:Bilayer	Trial 1	25 windows × 200 ns = 5000 ns	8.21 ± 0.75	**8.37 ± 0.69**
	Trial 2	25 windows × 200 ns = 5000 ns	8.55 ± 0.61	
	Trial 3	25 windows × 200 ns = 5000 ns	8.34 ± 0.72	

Table A2.3: Free energy (ΔG in kcal/mol, Standard error of the mean after ±.) associated with the alchemical transformation of the peptide using the Bennett acceptance ratio method (BAR) for multiple independent MD trials differing in the starting velocities (Trail 1, Trail 2, Trail 3) and/or structures (SETUP 1, SETUP 2; viz., see Figure S5). Estimated ΔG's from various trials, including forward/backward transformations, differ by less than 1 kcal/mol, thus, supporting well convergence of the data. Estimated ΔG's from various MD runs were averaged (5th column) for estimating the ΔG^{free} and ΔG^{comp} (see Figure 3a).

Free Peptide in water				
Alchemical transformation	**Trial 1 ΔG**	**Trial 2 ΔG**	**Trial 3 ΔG**	**Averaged from Three Trials ΔG^{free}**
P4 → P5	*Forward* -652.03 ± 0.16 *Backward* **652.13 ± 0.17**	-651.92 ± 0.23	-651.98 ± 0.19	**-651.98 ± 0.20**
P4 → P6	*Forward* 366.48 ± 1.59 *Backward* **-366.59 ± 1.42**	366.73 ± 1.54	366.63 ± 1.63	**366.61 ± 1.58**
P4 → P6*	*Forward* 60.85 ± 0.28 *Backward* **-60.98 ± 0.19**	61.03 ± 0.14	60.91 ± 0.23	**60.93 ± 0.22**
P6* → P6	*Forward* 291.81 ± 1.09 *Backward* **-292.03 ± 0.96**	291.73 ± 1.10	291.93 ± 0.99	**291.82 ± 1.06**
P4 → P7	*Forward* -36.19 ± 0.05 *Backward* **36.08 ± 0.04**	-36.33 ± 0.09	-36.07 ± 0.06	**-36.20 ± 0.07**
Peptide bound to bilayer				
Alchemical transformation	**Different structures (SETUP 1, SETUP 2) selected from two other MD runs are subjected to MD (Trail 1, Trail 2)**	**Trial 1 ΔG**	**Trial 2 ΔG**	**Averaged from Three Trials ΔG^{comp}**
P4 → P5	**SETUP 1**	*Forward* -654.15 ± 0.78 *Backward* **654.41 ± 0.47**	-654.44 ± 0.57	**-654.24 ± 0.60**
	SETUP 2	*Forward* -654.39 ± 0.49 *Backward* **654.07 ± 0.63**	-653.99 ± 0.54	
P4 → P6	**SETUP 1**	*Forward* 376.72 ± 1.06 *Backward*	377.21 ± 1.36	**377.01 ± 1.14**

		-376.88 ± 1.15		
	SETUP 2	*Forward* 377.11 ± 1.13 *Backward* **-376.95 ± 1.09**	376.98 ± 1.01	
P4 → P6*	**SETUP 1**	*Forward* 61.33 ± 0.33 *Backward* **-61.43 ± 0.41**	61.54 ± 0.37	**61.46 ± 0.32**
	SETUP 2	*Forward* 61.46 ± 0.25 *Backward* **-61.57 ± 0.23**	61.51 ± 0.29	
P6* → P6	**SETUP 1**	*Forward* 301.93 ± 1.17 *Backward* **-302.02 ± 1.13**	301.76 ± 1.21	**301.85 ± 1.20**
P4 → P7	**SETUP 1**	*Forward* -33.85 ± 0.11 *Backward* **33.64 ± 0.16**	-33.60 ± 0.18	**-33.73 ± 0.15**
	SETUP 2	*Forward* -33.78 ± 0.13 *Backward* **33.81 ± 0.17**	-33.69 ± 0.16	
Peptide bound to micelle				
Alchemical transformation	**Different structures (SETUP 1, SETUP 2) selected from two different MD runs are subjected to MD (Trail 1, Trail 2)**	**Trial 1** **ΔG (kcal/mol)**	**Trial 2** **ΔG**	**Average ΔG^{comp}**
P4 → P5	**SETUP 1**	-654.48 ± 0.21	-654.37 ± 0.31	**-654.42 ± 0.27**
	SETUP 2	-654.29 ± 0.29	-654.53 ± 0.28	
P4 → P6	**SETUP 1**	378.06 ± 2.79	378.19 ± 2.41	**378.22 ± 2.59**
	SETUP 2	378.08 ± 2.62	378.57 ± 2.54	
P4 → P6*	**SETUP 1**	61.16 ± 0.24	61.34 ± 0.28	**61.20 ± 0.25**
	SETUP 2	61.09 ± 0.15	61.22 ± 0.31	

P6* → P6	**SETUP 1**	303.23 ± 1.22	302.87 ± 1.31	**303.09 ± 1.26**
	SETUP 2	303.25 ± 1.29	302.96 ± 1.22	
P4 → P7	**SETUP 1**	-33.98 ± 0.19	-34.09 ± 0.15	**-34.03 ± 0.17**
	SETUP 2	-34.03 ± 0.17	-34.03 ± 0.16	

Table A2.4: Relative binding affinities (ΔΔG, in kcal/mol) estimated from alchemical (BAR) and MM/PBSA approach. ΔΔG (BAR) = ΔG^{comp} -ΔG^{free} (See 5th column of Table S3 and Figure 3a of the main text). ΔΔG(MM/PBSA) was estimated using a single trajectory approach (See Table 1 of main text). Standard error of the mean (s.e.m) after ±.

	Micelle (BAR)	**Bilayer (BAR)**	**Micelle (MM/PBSA)**	**Bilayer (MM/PBSA)**
P4 to P5	-2.44 ± 0.21	-2.26 ± 0.48	-3.51 ± 0.45	-3.28 ± 0.39
P4 to P6	11.61 ± 0.43	10.4 ± 0.61	14.96 ± 0.62	14.13 ± 0.69
P4 to P6*	0.27 ± 0.13	0.53 ± 0.33	1.6 ± 0.37	1.45 ± 0.38
P4 to P7	2.17 ± 0.26	2.47 ± 0.15	2.97 ± 0.38	3.19 ± 0.29

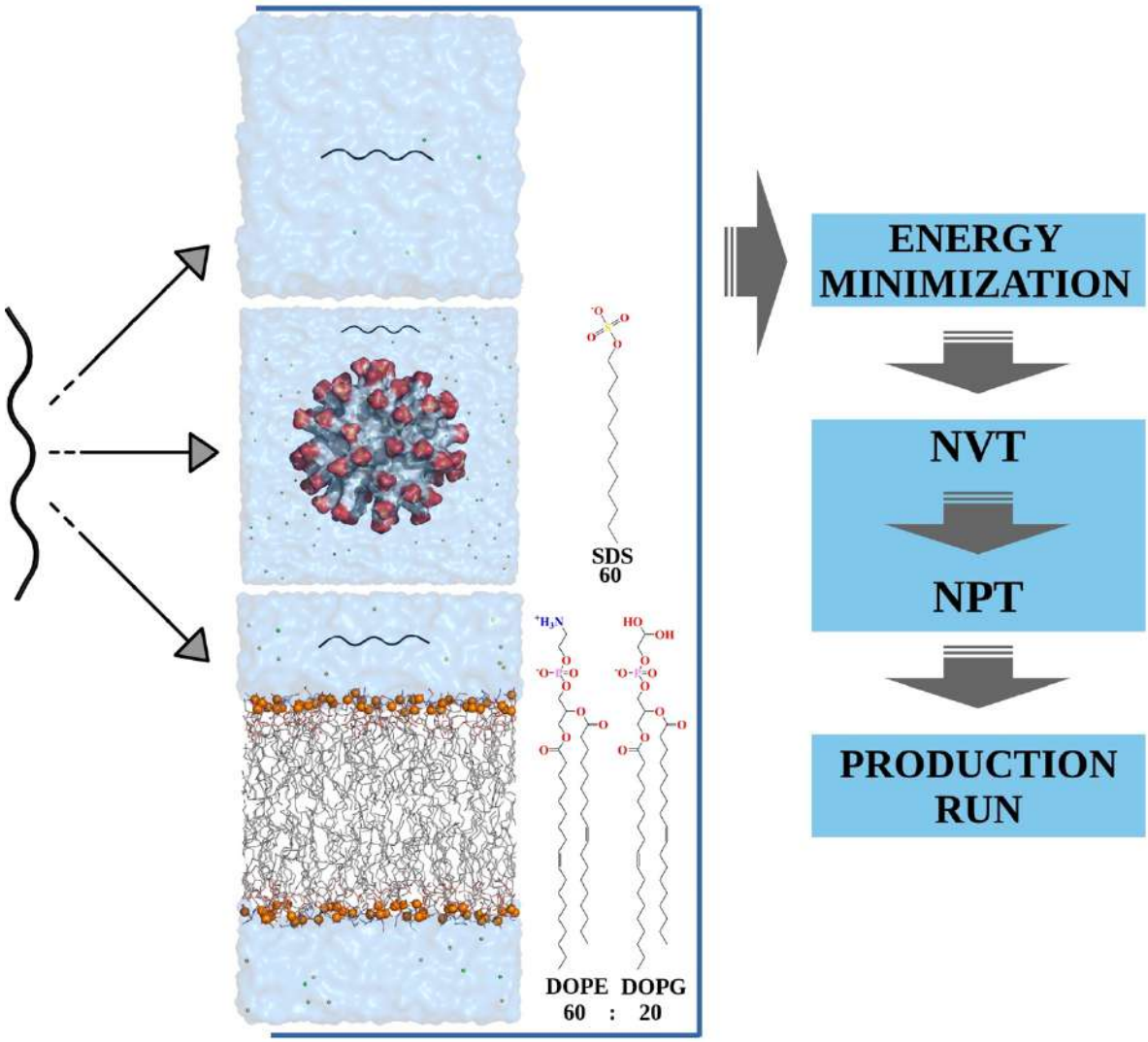

Figure A2.1: A graphical representation of the simulation setup where the extended peptide is placed: at the centre of a water box (top), above the surface of the pre-equilibrated solvated SDS micelle (middle), DOPE/DOPG bilayer (bottom). Each model was minimized, equilibrated (using NVT followed by NPT ensemble), and subjected to production MD employing NPT ensemble (P = 1 bar, T = 310 K).

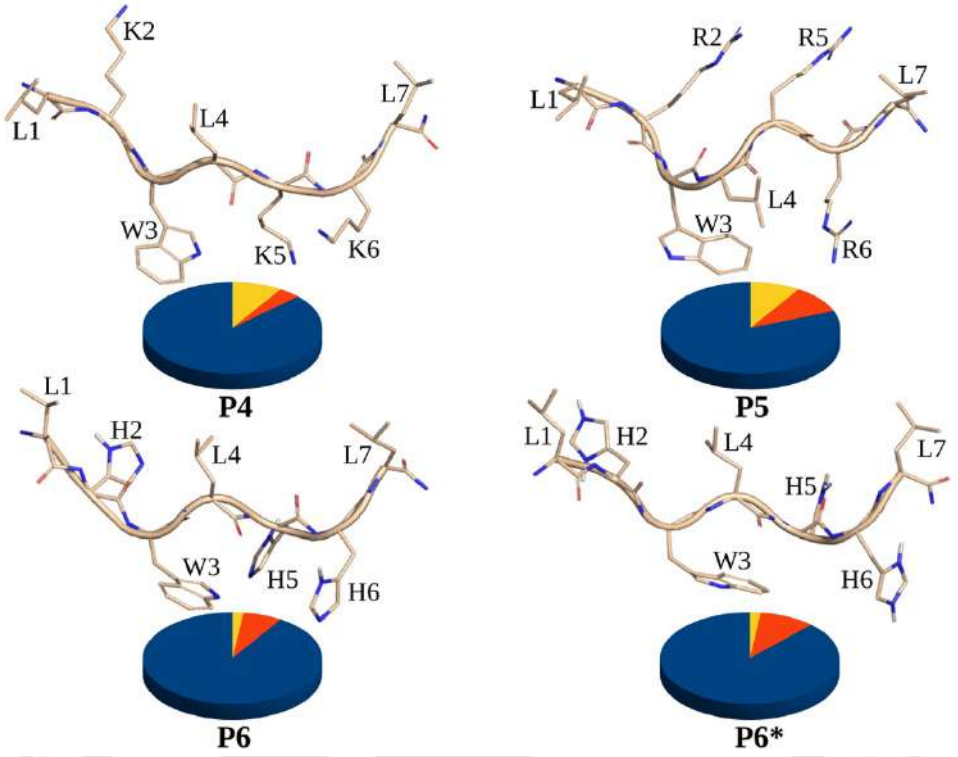

Figure A2.2: Peptide conformation after 200 ns simulation in water. The pie chart represents the secondary structure percentage obtained from the MD trajectory (blue represents coil, orange represents bend, and yellow represents turn).

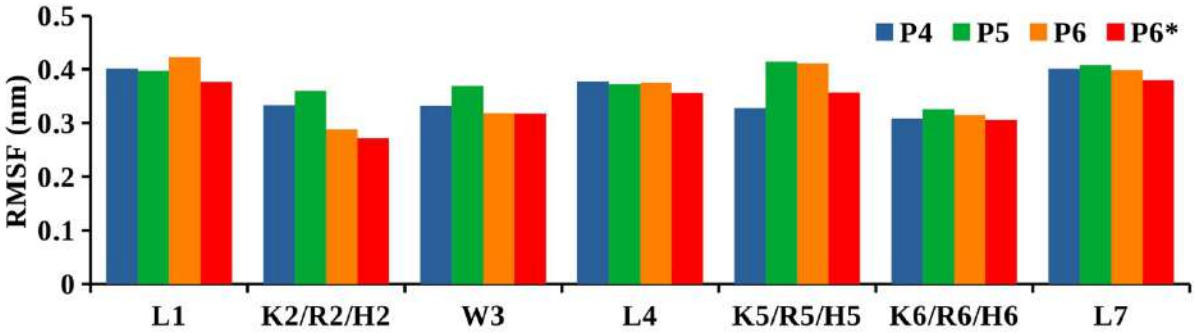

Figure A2.3: Residue wise Root-mean-square-fluctuation (RMSF) of the free peptide in water. The last 50 ns of the 200 ns MD trajectory was post-processed for estimating the average residue-wise RMSF.

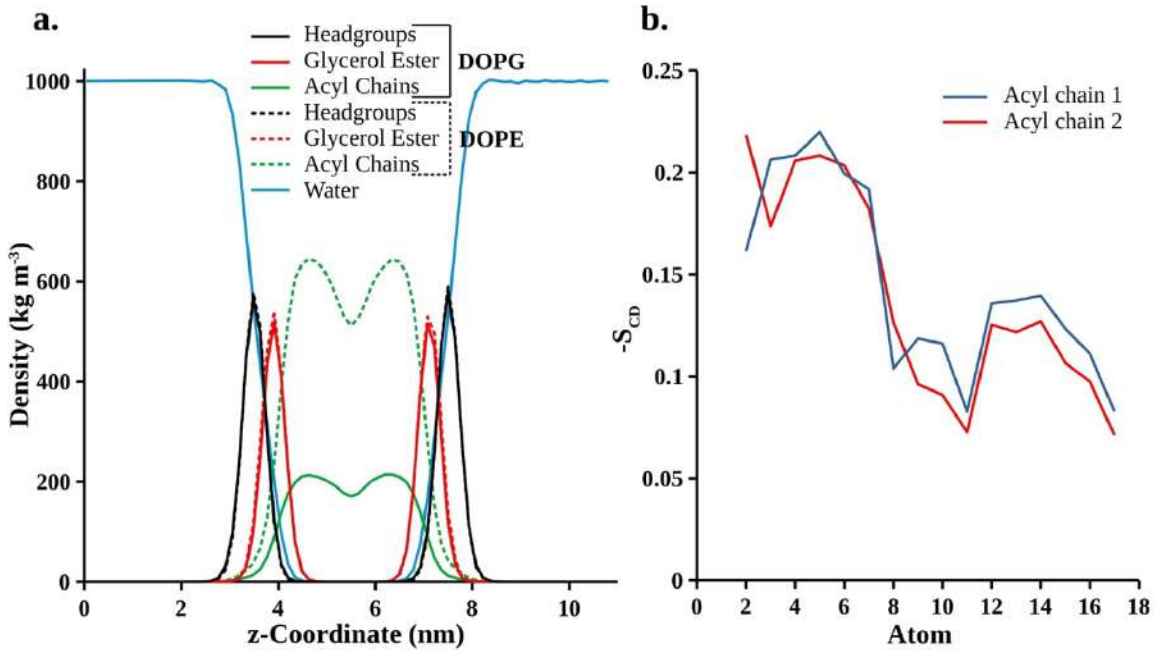

Figure A2.4: (a) Density analysis of the bilayer (b) Deuterium order parameters confirmed that the simulated bilayer entered a gel phase. The last 150 ns of the 200 ns MD trajectory (of the bilayer in a water box) was used for estimating density and order parameters.

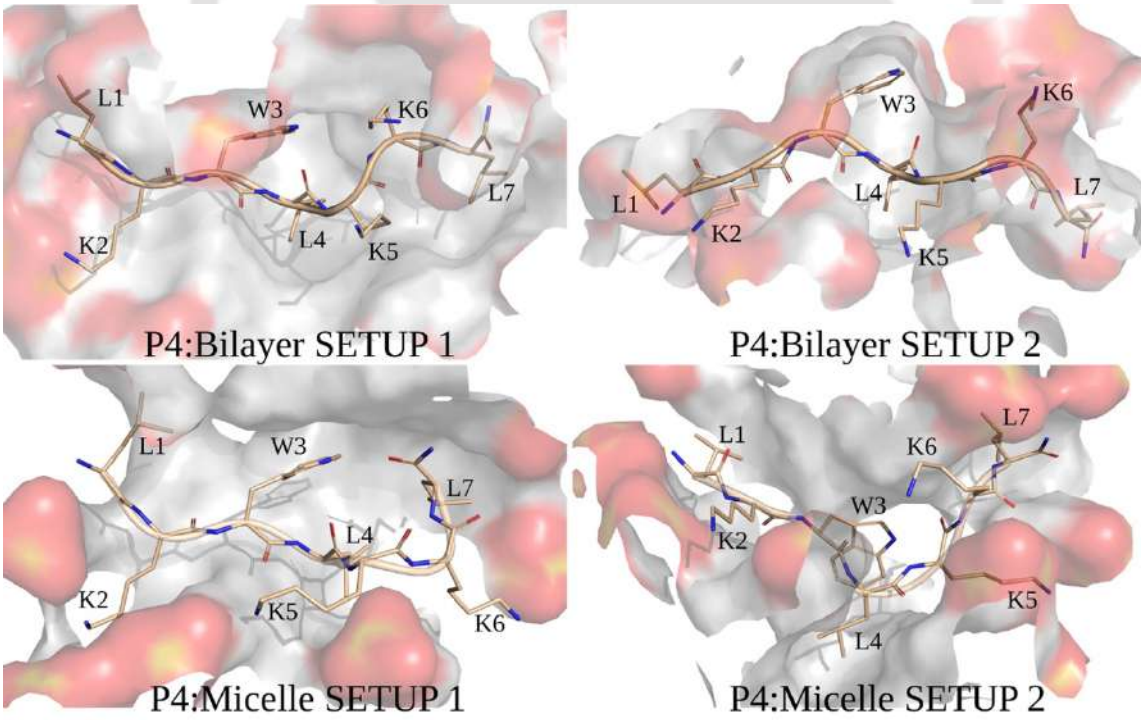

Figure A2.5: Representative initial structures (SETUP 1 and SETUP 2) of the peptide-bilayer (upper panel) and peptide-micelle (lower panel) complexes obtained from two independent MD simulations are subjected to alchemical free energy simulations.

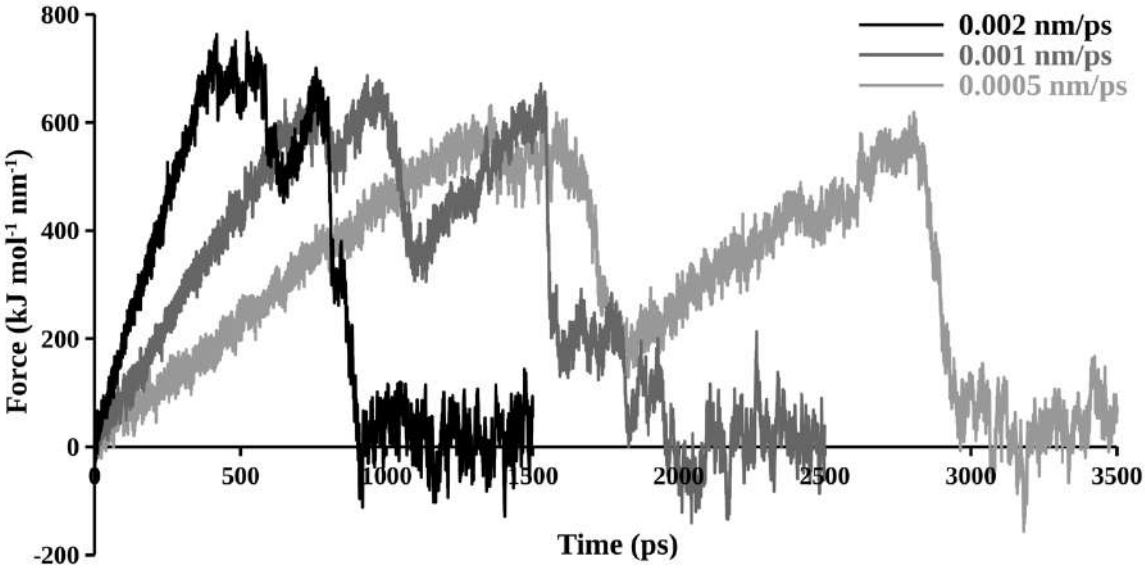

Figure A2.6: Force profile (Force versus time plots) obtained Steered Molecular Dynamics (SMD) simulations of P4:Bilayer complex at different pull rates (0.002 nm/ps, 0.001 nm/ps, and 0.0005 nm/ps). The shape of the force profile was independent of the pull rates.

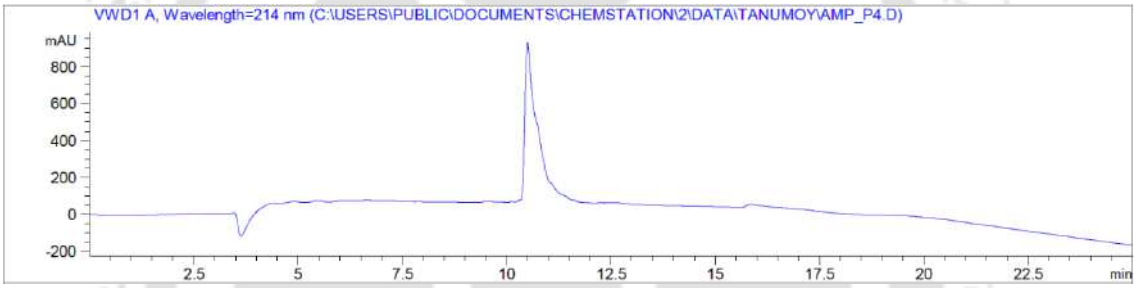

Figure A2.7: Analytical HPLC chromatogram of **P4** at 214 nm. Retention time: 10.504 min.

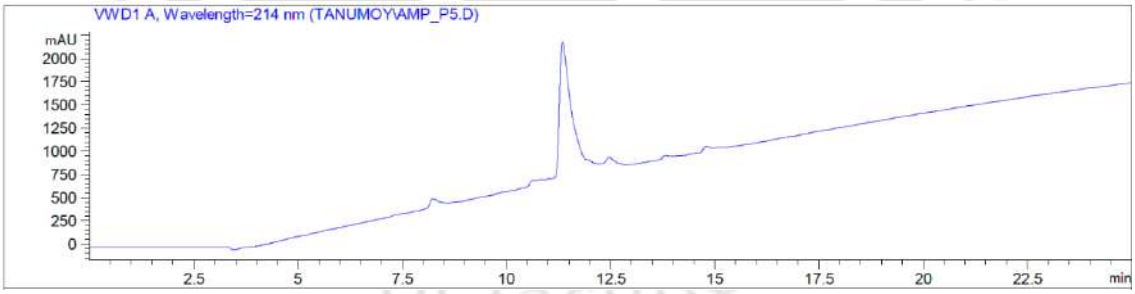

Figure A2.8: Analytical HPLC chromatogram of **P5** at 214 nm. Retention time: 11.351 min.

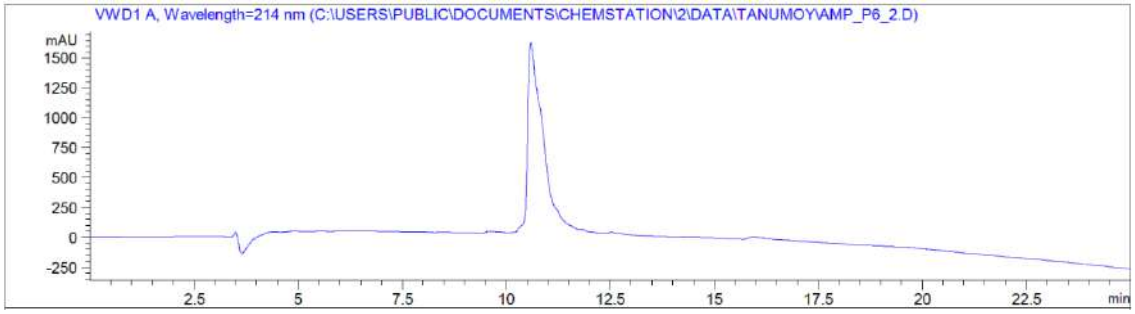

Figure A2.9: Analytical HPLC chromatogram of **P6** at 214 nm. Retention time: 10.589 min.

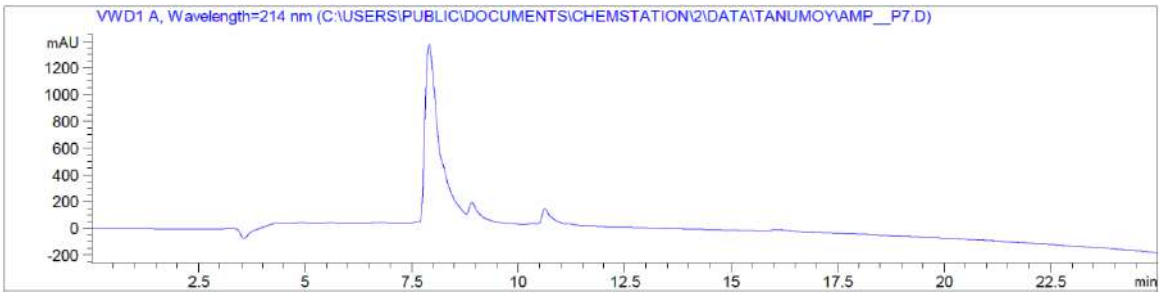

Figure A2.10: Analytical HPLC chromatogram of **P7** at 214 nm. Retention time: 7.912 min.

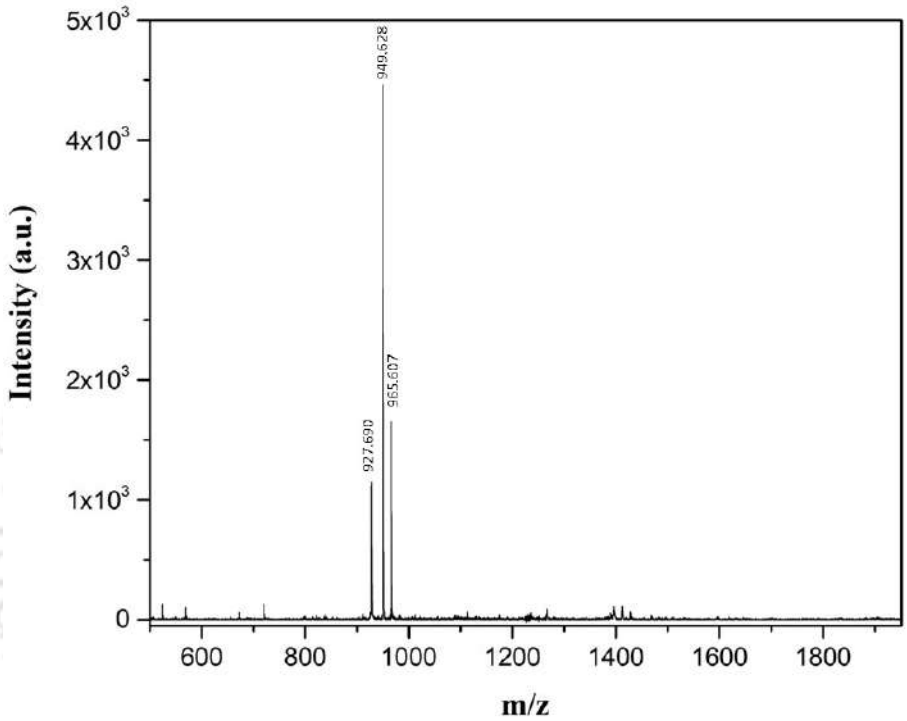

Figure A2.11: MALDI-TOF spectra of **P4**. Calc. $(M+H)^+$ for **P4** = 927.642 Da ; Obs. $(M+H)^+$= 927.690 Da, $(M+Na)^+$= 949.628 Da, $(M+K)^+$= 965.607 Da.

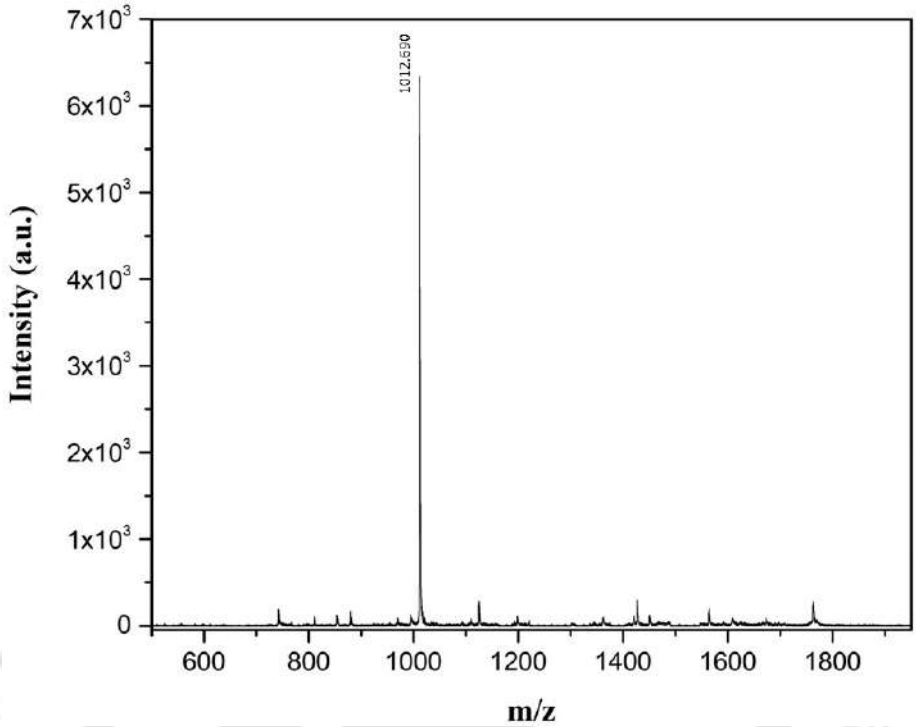

Figure A2.12: MALDI-TOF spectra of **P5**. Calc. $(M+H)^+$ for **P5** = 1011.661 Da ; Obs. $(M+H)^+$= 1012.690 Da.

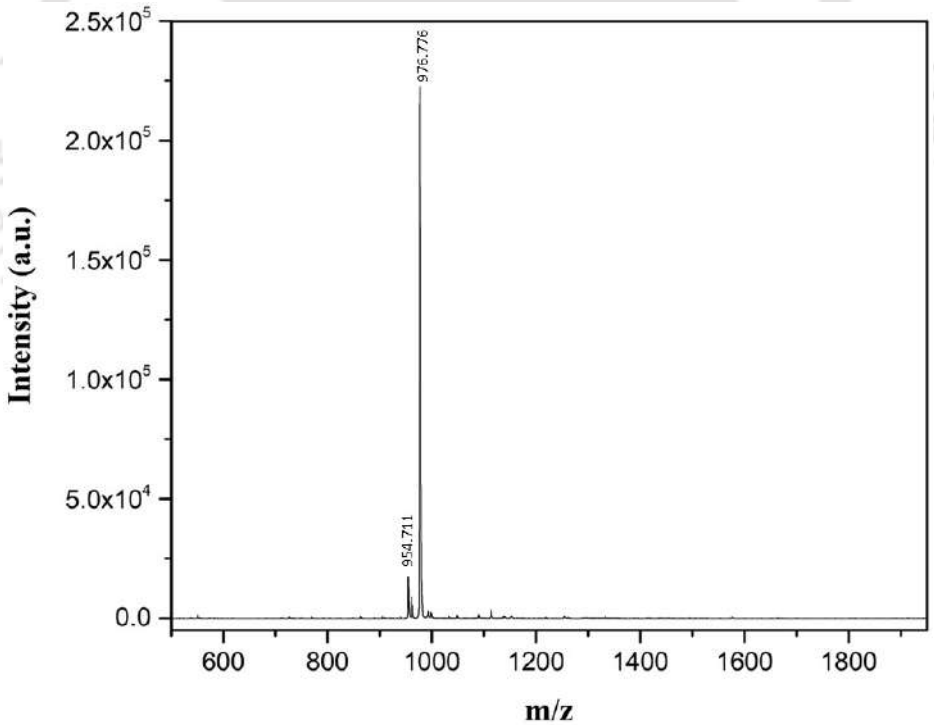

Figure A2.13: MALDI-TOF spectra of **P6**. Calc. $(M+H)^+$ for **P6** = 954.534 Da ; Obs. $(M+H)^+$= 954.711 Da, $(M+Na)^+$= 976.776 Da.

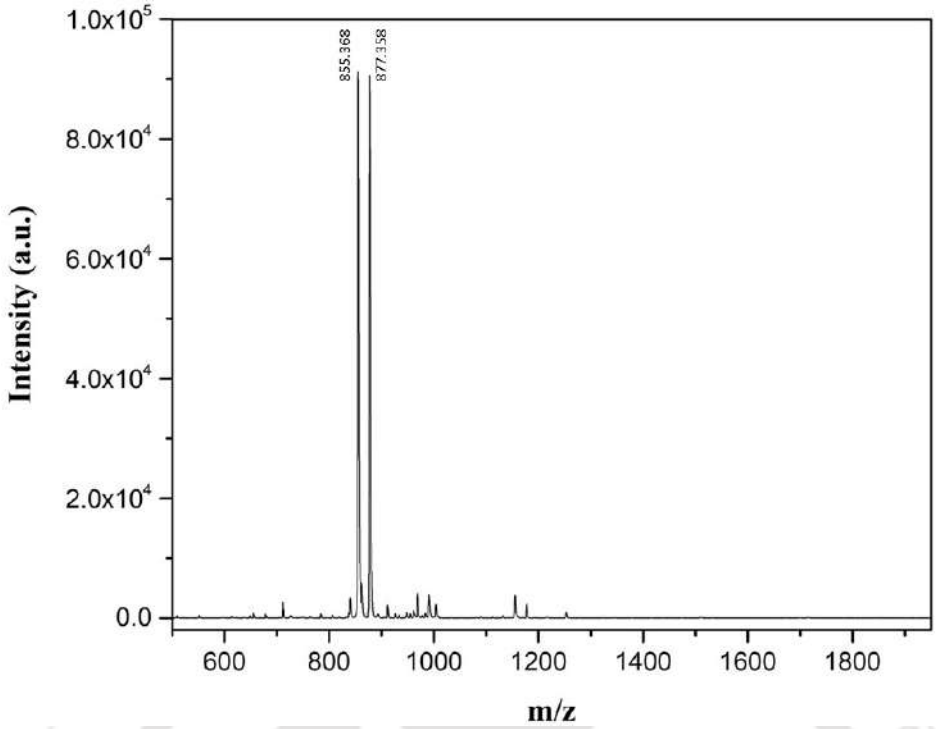

Figure A2.14: MALDI-TOF spectra of **P7**. Calc. $(M+H)^+$ for **P7** = 854.647Da ; Obs. $(M+H)^+$= 855.363 Da, $(M+Na)^+$= 877.358 Da.

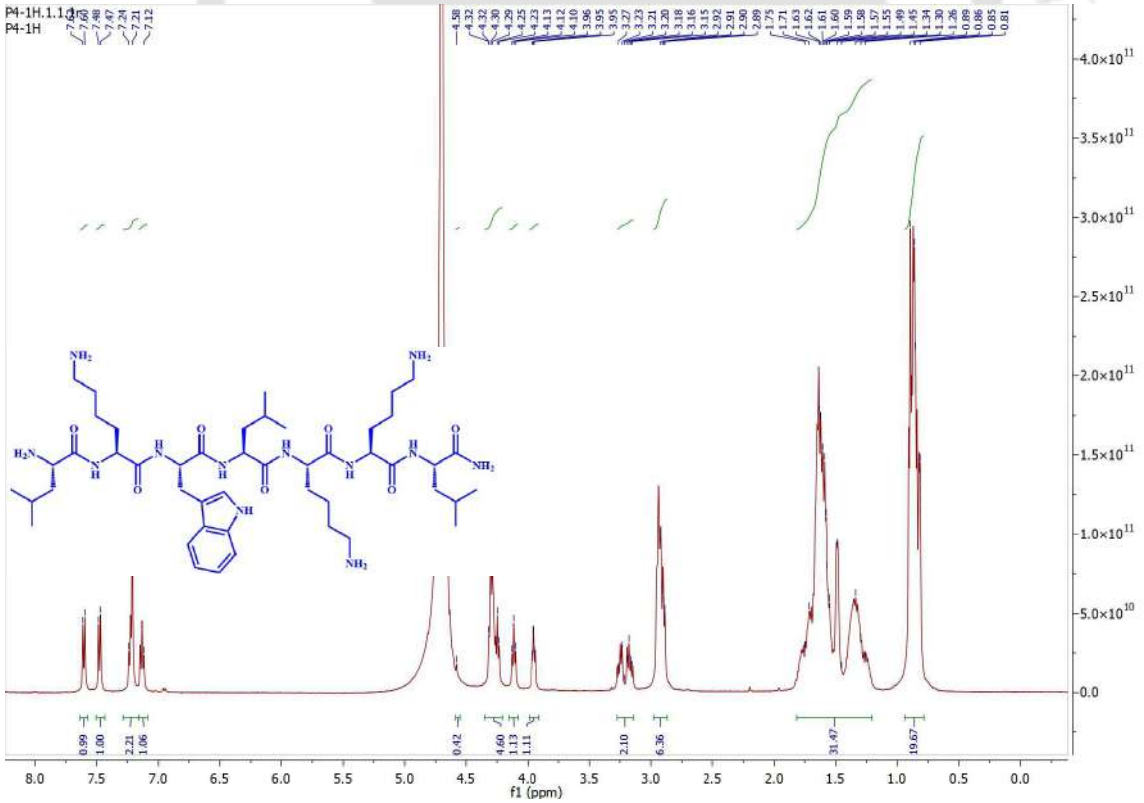

Figure A2.15: ^{1}H NMR spectra of **P4** at room temperature in D_2O. ^{1}H NMR (500 MHz, D_2O) δ 0.78-0.94 (18H, Leucine), δ 1.21-1.82 (27H, Leucine and Lysine), δ 2.87-3.29 (8H, Lysine and Tryptophan), δ 3.91-4.60 (7 αH), 7.11-7.64 (5H, Tryptophan).

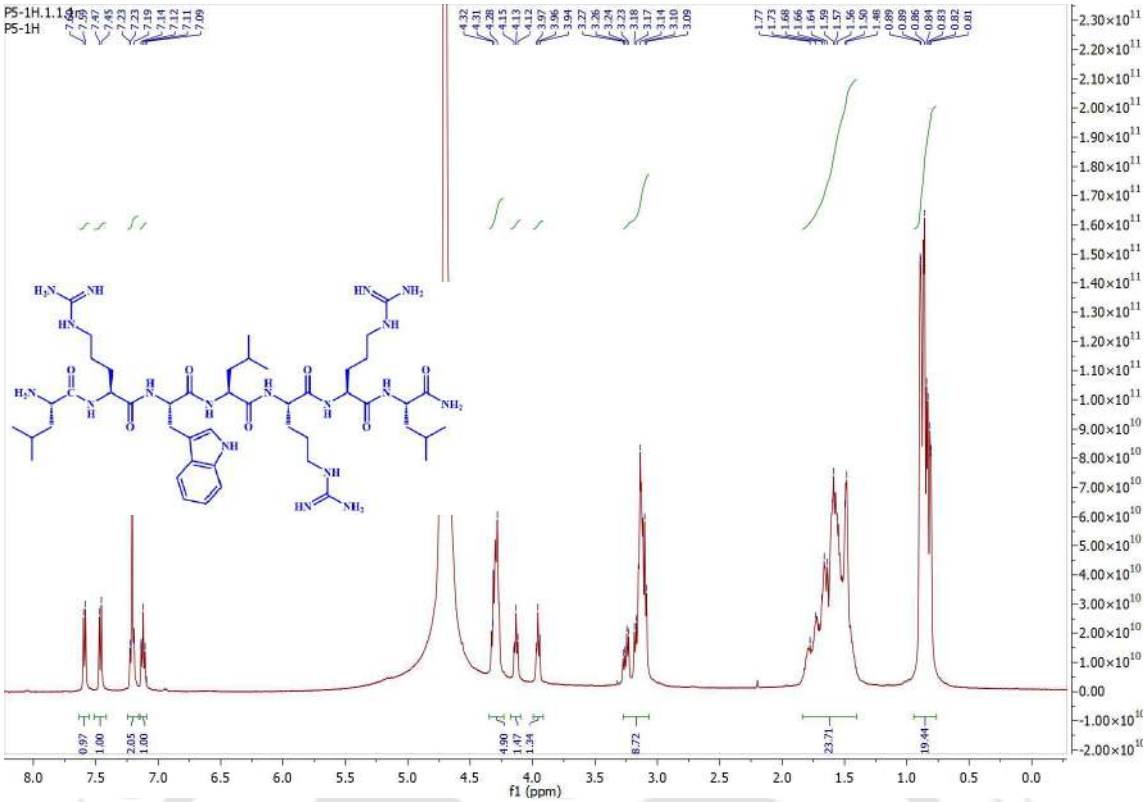

Figure A2.16: ^{1}H NMR spectra of **P5** at room temperature in D_2O. ^{1}H NMR (500 MHz, D_2O) δ 0.76-0.94 (18H, Leucine), δ 1.41-1.84 (21H, Leucine and Arginine), δ 3.06-3.27 (8H, Arginine and Tryptophan), δ 3.91-4.35 (7 αH), 7.09-7.64 (5H, Tryptophan).

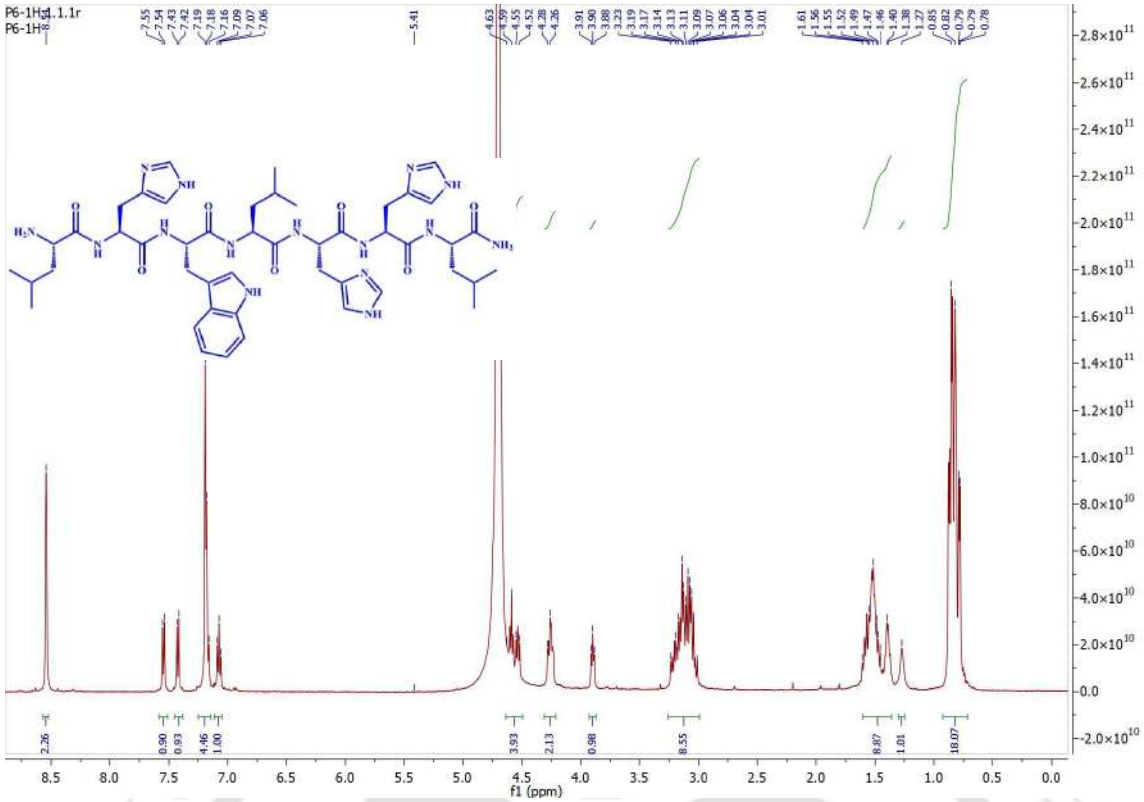

Figure A2.17: ^{1}H NMR spectra of **P6** at room temperature in D_2O. ^{1}H NMR (500 MHz, D_2O) δ 0.75-0.91 (18H, Leucine), δ 1.25-1.61 (9H, Leucine), δ 3.87-4.64 (8H, Histidine and Tryptophan), δ 3.91-4.35 (7 αH), 7.85-8.07 (11H, Histidine and Tryptophan).

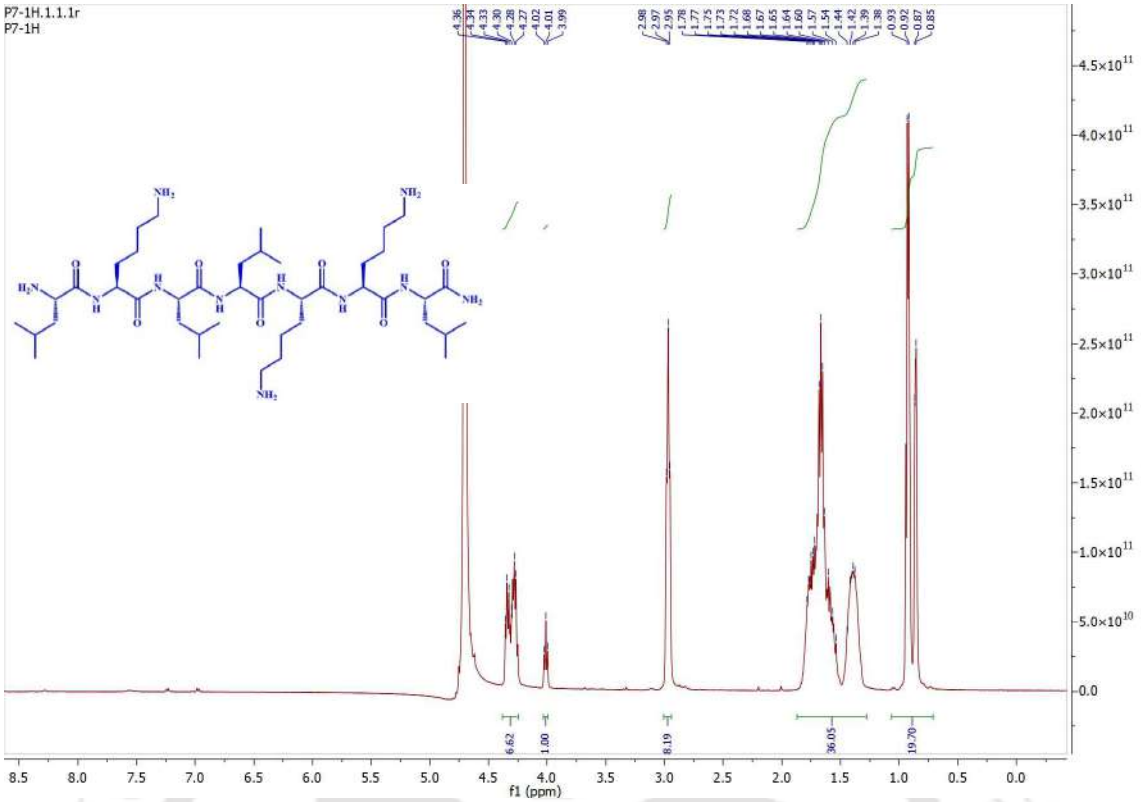

Figure A2.18: ^{1}H NMR spectra of **P7** at room temperature in D_2O. ^{1}H NMR (500 MHz, D_2O) δ 0.70-1.07 (24H, Leucine), δ 1.28-1.87 (33H, Leucine and lysine), δ 2.93-3.01 (6H, Lysine), δ 3.99-4.38 (7 αH).

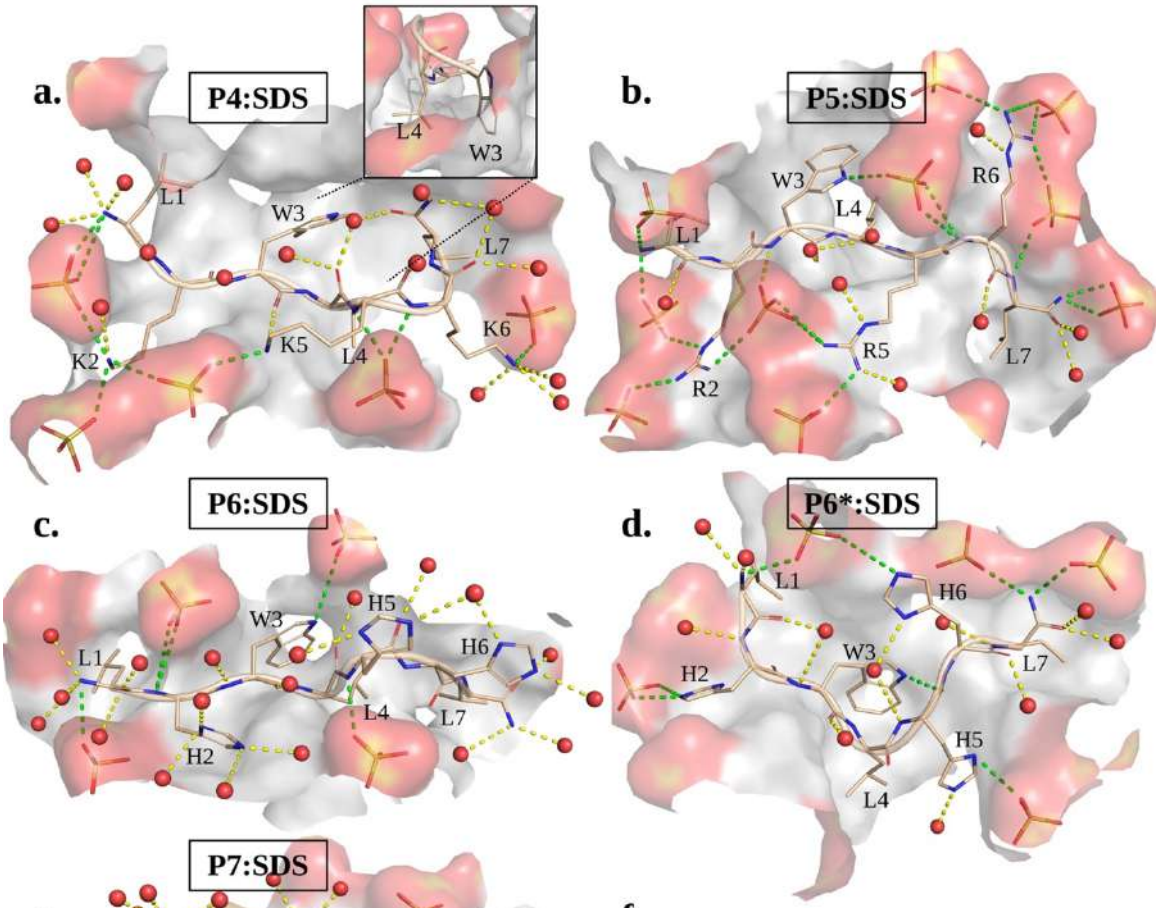

f.

	P4	P5	P6	P6*	P7
Interaction area (Å²)	781 ± 71	866 ± 74	651 ± 75	814 ± 63	769 ± 74
Number of peptide (NH) … SDS (O) interaction (<3.5 Å)	9.1 ± 1.8	17.3 ± 2.3	4.8 ± 1.9	7.8 ± 1.3	8.6 ± 1.9
Water molecules within 3.5 Å of the peptide	14.7 ± 2.9	9.8 ± 2.0	19.5 ± 4.1	11.4 ± 3.2	15.4 ± 3.1

Figure A2.19: (a-e) Representative MD structures of Peptide-micelle complexes after alchemical transformation. (f) Properties of the peptide-micelle complexes averaged from the MD trajectories. Standard deviation is indicated as an error.

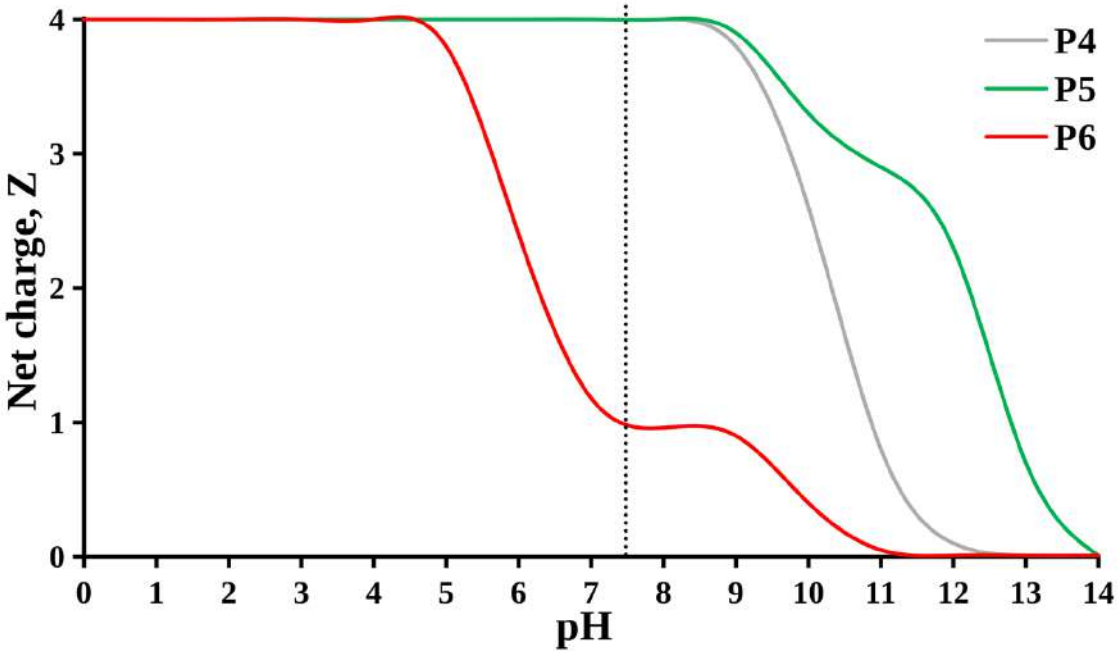

Figure A2.20: The theoretical charge carried by each peptide at different pH (dotted line indicates the cumulative charge of that particular peptide at physiological pH 7.4). The plots were generated by using an online peptide calculator tool (BACHEM, http://www.bachem.com/service-support/peptide-calculator/)

Appendix II

Content

Sl. no.		Topic	Page No.
1	Table A3.1	Size of MD simulation models	166
2	Table A3.2	Number of independent replicas (varying the initial velocities) considered for each simulation model and the post-equilibrated production MD run-length.	166
3	Table A3.3	Micelle eccentricity (averaged from the last 20 ns of the first 50 ns trajectory) independent of salt concentration.	168
4	Table A3.4	Simulation setup details for umbrella sampling.	168
5	Table A3.5	Sampling and run length for Umbrella sampling simulations of LL-14:SDS complex at different salt concentration	169
6	Table A3.6	Sampling and run length for Umbrella sampling simulations of LL-14:DPC complex	170
7	Figure A3.1	Relative position of LL-14 and SDS micelle considered as initial model for MD simulations. (b) Representative snapshot from MD simulation highlighting the initial contact between LL-14 and SDS micelle. Center of mass represented by grey sphere.	171
8	Figure A3.2	Eccentricity vs Time plot (NaCl =0.0%). Secondary structural content of the peptide (P^c or P^h) estimated from the MD trajectory in presence of SDS micelle at various salt concentrations.	172
9	Figure A3.3	Lines in the Figure 3 of the main-text has been divided into three groups (based on salt-concentrations). 5 independent replicas (obtained from Setup C of Fig. S1a, d_{COM} = 5.8 nm) were considered to calculated the temporal average for each simulation models. Error are reported as s.e.m from 5 replicas and shown as vertical bars. The same trend has been confirmed starting with various other setups (Figure A3.1a).	173
10	Figure A3.4	"d" is the distance between positively charged nitrogen of the LL-14 residues and the centre of mass of SDS micelle. Distance plot (d vs. time) is shown along the MD trajectories (0% NaCl). Different colours represent different $-NH_3^+$ containing residues. N-terminal (L1, blue) and side-chain of K2 (red) forms the initial contact (represented as vertical arrow) with the micelle	174

		surface. The trend is same for simulations in presence of salt (not shown).	
11	Figure A3.5	Peptide backbone of P^c satisfied its hydrogen bonding requirement by forming H-bond with water molecules or sulphates of the SDS micelle or both. Snapshot after 50ns of MD. Peptide in sticks, water in red sphere, SDS (surface representation, lines represent sulphate).	174
12	Figure A3.6	Final structure of the peptide: micelle complex after 50 ns of MD simulations from three different NaCl-concentrations: 0.0% (given also in the main-text), 0.5% , and 1.0% w/v.	175
13	Figure A3.7	Force versus time plots from various SMD simulations (pull rates = 0.01nm/ps, 0.005 nm/ps, and 0.001 nm/ps). The shape of the force profile was independent of the pull rates. Structures from various time-points shown in the boxes (**red** : 0.005 nm/ps pull-rate, **green** : 0.001 nm/ps pull-rate).	175
14	Figure A3.8	Center-of-mass pulling simulation (d_{COM} vs. time plot, pulling rate = 0.01 nm/ps). d_{COM} = Distance between the center-of-mass of the LL-14 and SDS micelle. "d_{COM}" range (Minimum = 1.14 nm, Maximum = 6.31nm)	176
15	Figure A3.9	Probability distribution at each umbrella sampling window (Total windows = 43, shown in different colours) from the LL-14:SDS PMF profile at various salt-concentrations (NaCl = 0%, 0.5%, and 1.0% w/v). The overlap of probability distribution (between two neighbouring windows) was evident.	176
16	Figure A3.10	Ramachandran Plot of LL-14 peptide obtained from different trajectory segment during the centre-of-mass pulling (SMD, pull rate= 0.01 nm/ps, NaCl = 0% w/v). SMD trajectory segment (a) 0 - 263 ps, (b) 264 – 351 ps, and (c) 352 - 500 ps. ϕ and Ψ angles were plotted from -180° to 180°. Dispersion of red points from "a" → "c" indicates helical → random-coil transition. Blue regions exhibit either zero or little likelihood of the peptide adopting such a conformation.	177
17	Figure A3.11	(a) Force vs. time plots of LL-14:DPC micelle complex (pull rate 0.01nm/ps, NaCl = 0% w/v). Structures at different time-points (grey, red, blue, and green) were overlaid (shown in surface-cartoon representations). (b) LL-14:DPC binding free energy (ΔG) estimated from the potential of mean force (PMF) versus reaction coordinate "ξ" plot. Simulation details were given in Table A3.6.	178

Table A3.1: Size of MD simulation models.

	P^c*	P^c_SDS (NaCl= 0.0% w/v)	P^c_SDS (NaCl= 0.5% w/v)	P^c_SDS (NaCl= 1.0% w/v)	P^h*	P^h_SDS (NaCl= 0.0% w/v)	P^h_SDS (NaCl= 0.5% w/v)	P^h_SDS (NaCl= 1.0% w/v)
Total no of atoms	98307	268911	268062	267241	98295	268833	268038	266918
Water molecules	32667	88675	88300	87933	32663	88649	88292	87925
Na^+	-	60	198	338	-	60	198	338
Cl^-	7	7	145	285	7	7	145	285

	SDS (NaCl= 0.0% w/v)	SDS (NaCl= 0.5% w/v)	SDS (NaCl= 1.0% w/v)	DPC (NaCl= 0.0% w/v)
Total no of atoms	269046	268494	267934	270642
Water molecules	88822	88546	88266	88994
Na^+	60	198	338	-
Cl^-	-	138	278	-

Table A3.2: Number of independent replicas (varying the initial velocities) considered for each simulation model and the post-equilibrated production MD run-length. Multiple relative orientation has been considered for studying LL-14:micelle binding (Setup A, Setup B, Setup C: see Figure A3.1). Total MD run-lenth= 14.2 μs.

Salt (NaCl)	**Free in Water** Replica (Run-length)				**LL-14: Micelle interaction** Replica (Run-length)			
	P^c	P^h	SDS	DPC		P^c:SDS	P^h:SDS	P^c:DPC
0.0%	Rep1 (200ns) Rep2 (500ns) Rep3 (1μs)	Rep1 (200ns) Rep2 (500ns) Rep3 (1μs)	Rep1 (20 ns)	Rep1 (20ns)	Setup A	Rep1 (50ns) Rep2 (50ns) Rep3 (50 ns)	Rep1 (50ns) Rep2 (50ns) Rep3 (50 ns)	Rep1 (1μs)
					Setup B	Rep1 (50ns) Rep2 (50ns)	Rep1 (50ns) Rep2 (50ns)	
					Setup C	Set1(d_{com} = 5.8 nm) Rep1 (6 μs) Rep2 (50ns) Rep3 (50ns)	Set1(d_{com} = 5.8 nm) Rep1(50ns) Rep2 (50ns) Rep3 (50ns)	

						Rep4 (50ns) Rep5 (50ns) Set2 (d_{com} = 5.1 nm) Rep1 (50ns) Rep2 (10ns) Rep3 (10ns) Set 3 (d_{com} = 8.6 nm) Rep1 (50ns)	Rep4 (50ns) Rep5 (50ns) Set2 (d_{com} = 5.1 nm) Rep1 (50ns) Rep2 (10ns) Rep3 (10ns) Set 3 (d_{com} = 8.6 nm) Rep1 (50ns)	
0.5%			20 ns		Setup A	Rep1 (50ns) Rep2 (50ns) Rep3(50 ns)	Rep1 (50ns) Rep2 (50ns) Rep3(50 ns)	
					Setup B	Rep1 (50ns) Rep2 (50ns)	Rep1 (50ns) Rep2 (50ns)	
					Setup C	Set1(d_{com} = 5.8 nm) Rep1 (50ns) Rep2 (50ns) Rep3 (50ns) Rep4 (50ns) Rep5 (50ns) Set2 (d_{com} = 5.1 nm) Rep1 (50ns) Rep2 (10ns) Rep3 (10ns) Set2 (d_{com}= 8.6 nm) Rep1 (50ns)	Set1(d_{com} = 5.8 nm) Rep1 (50ns) Rep2 (50ns) Rep3 (50ns) Rep4 (50ns) Rep5 (50ns) Set2 (d_{com} = 5.1 nm) Rep1 (50ns) Rep2 (10ns) Rep3 (10ns) Set2 (d_{com} = 8.6 nm) Rep1 (50ns)	
1.0%			20 ns		Setup A	Rep1 (50ns) Rep2 (50ns) Rep3(50 ns)	Rep1 (50ns) Rep2 (50ns) Rep3(50 ns)	
					Setup B	Rep1 (50ns) Rep2 (50ns)	Rep1 (50ns) Rep2 (50ns)	
					Setup C	Set1(d_{com} = 5.8 nm) Rep1 (50ns) Rep2 (50ns) Rep3 (50ns) Rep4 (50ns) Rep5 (50ns)	Set1(d_{com} = 5.8 nm) Rep1 (50ns) Rep2 (50ns) Rep3 (50ns) Rep4 (50ns) Rep5 (50ns)	

						Set2 (d_{com} = 5.1 nm) Rep1 (50ns) Rep2 (10ns) Rep3 (10ns) Set3 (d_{com} = 8.6 nm) Rep1 (50ns)	Set2 (d_{com} = 5.1 nm) Rep1 (50ns) Rep2 (10ns) Rep3 (10ns) Set3 (d_{com} = 8.6 nm) Rep1 (50ns)	

Table A3.3: Micelle eccentricity (averaged from the last 20 ns of the first 50 ns trajectory) independent of salt concentration.

System (Salt concentration)	**Eccentricity**	**I_{min}/I_{max}**
SDS:P^c (NaCl = 0.0% w/v)	0.15 ± 0.06	1.34 ± 0.15
SDS:P^c (NaCl = 0.5% w/v)	0.17 ± 0.05	1.38 ± 0.18
SDS:P^c (NaCl = 1.0% w/v)	0.16 ± 0.06	1.39 ± 0.18
SDS:P^h (NaCl = 0.0% w/v)	0.22 ± 0.08	1.53 ± 0.21
SDS:P^h (NaCl = 0.5% w/v)	0.21 ± 0.08	1.52 ± 0.22
SDS:P^h (NaCl = 1.0% w/v)	0.22 ± 0.07	1.52 ± 0.20

Table A3.4: Simulation setup details for umbrella sampling.

	LL-14:SDS (NaCl = 0.0% w/v)	**LL-14:SDS (NaCl = 0.5% w/v)**	**LL-14:SDS (NaCl = 1.0% w/v)**
Total no of atoms	268833	268038	266918
No of Water molecules	88649	88292	87925
Na+ ions	60	198	338
Cl- ions	7	145	285
USMD parameters			
Integrator and time step for integration (dt)	md (leap-frog algorithm) and 0.002 ps		
Periodic boundary condition (pbc)	xyz (all directions)		
Long range electrostatics (coulombtype)	Particle Mesh Ewald (PME(Darden et al., 1993))		
Short-range neighbour list cut-off (rlist)	1.2 nm		
Short-range electrostatic cut-off (rcoulomb)	1.2 nm		
Short-range van der Waals cut-off (rvdw)	1.2 nm		
constraint_algorithm (h-bonds)	Lincs (Hess et al., 1997)		
Temperature control (Tcoupl)	velocity rescaling algorithm (V-rescale (Bussi et al., 2007))		
Pressure control (Pcoupl)	Parrinello-Rahman(Parrinello & Rahman, 1982)		

REFERENCES

Bussi, G., Donadio, D., & Parrinello, M. (2007). Canonical sampling through velocity rescaling. *The Journal of Chemical Physics*, *126*(1), 014101. https://doi.org/10.1063/1.2408420

Darden, T., York, D., & Pedersen, L. (1993). Particle mesh Ewald: An N·log(N) method for Ewald sums in large systems. *The Journal of Chemical Physics*, *98*(12), 10089–10092. https://doi.org/10.1063/1.464397

Hess, B., Bekker, H., Berendsen, H. J. C., & Fraaije, J. G. E. M. (1997). LINCS: A linear constraint solver for molecular simulations. *Journal of Computational Chemistry*. https://doi.org/10.1002/(SICI)1096-987X(199709)18:12<1463::AID-JCC4>3.0.CO;2-H

Parrinello, M., & Rahman, A. (1982). Strain fluctuations and elastic constants. *The Journal of Chemical Physics*, *76*(5), 2662–2666. https://doi.org/10.1063/1.443248

Table A3.5: No restraint applied for SDS micelle during umbrella Sampling. Run-length (in ns) and estimated binding free energy from each independent replica are given. $\Delta G^{Averaged}$ is the average over multiple replicas. $\Delta\Delta G^{Averaged}$ = $\Delta G^{Averaged}$(0.5% or 1% NaCl) - $\Delta G^{Averaged}$(0% NaCl). Total Simulation length =(33745 ns *umbrella sampling* + 120.6 ns *equilibration* + 8 ns *SMD*) = 33873.6 ns ~33.87 µs. Error is in SEM given after ±.

	Replicas	Run-length of Umbrella Sampling	ΔG (kcal/mol)	$\Delta G^{Averaged}$ (kcal/mol)	$\Delta\Delta G^{Averaged}$ (kcal/mol)
LL-14:SDS (NaCl = 0.0%)	**Trial 1**	43 windows × 50 ns = 2150 ns	-33.85 ± 0.97	-33.53 ± 0.86	0.0
	Trial 2	43 windows × 55 ns = 2365 ns	-34.15 ± 1.16		
	Trial 3 (Highest Sampling)	**43 windows × 250 ns = 10750 ns**	**-33.19 ± 0.75**		
LL-14:SDS (NaCl = 0.5%)	**Trial 1**	43 windows × 50 ns = 2150 ns	-25.58 ± 0.86	-25.61 ± 0.93	-7.92
	Trial 2	43 windows × 55 ns = 2365 ns	-25.79 ± 1.12		
LL-14:SDS (NaCl = 1.0%)	**Trial 1**	43 windows × 50 ns = 2150 ns	-21.54 ± 0.98	-21.58 ± 1.02	-11.95
	Trial 2	43 windows × 55 ns = 2365 ns	-21.80 ± 1.16		

Alternate Approach In each window, "d_{COM}" and SDS micelle were harmonically restrained, employing a force constant of 1000 kJ mol^{-1} nm^{-2} relative to the starting coordinate. Snapshots selected from fast pulling simulations, pulling rate = 0.01 nm ps^{-1}). In trial 4, umbrella sampling was performed by choosing the snapshots from a slow pull (pulling rate = 0.005 nm ps^{-1}) simulation. The SDS micelle was modelled as an immobile reference (restrained) during the umbrella sampling simulations.

Alternate Approach*	Replicas	Run-length of Umbrella Sampling	ΔG (kcal/mol)	$\Delta G^{Averaged}$ (kcal/mol)	$\Delta\Delta G^{Averaged}$ (kcal/mol)
LL-14:SDS (NaCl = 0.0%)	**Trial 1**	43 windows × 10 ns = 430 ns	-61.95 ± 0.95	-61.09 ± 0.85	0.0
	Trial 2	43 windows × 50 ns = 2150 ns	-60.09 ± 0.88		
	Trial 3	43 windows × 10 ns = 430 ns	-61.03 ± 0.97		
	Trial 4 *(Slow Pull SMD)*	44 windows × 10 ns = 440 ns	-61.29 ± 0.93		

LL-14:SDS (NaCl = 0.5%)	**Trial 1**	43 windows × 10 ns = 430 ns	-46.14 ± 0.52	-46.04 ± 0.45	-15.04
	Trial 2	43 windows × 50 ns = 2150 ns	-45.94 ± 0.44		
LL-14:SDS (NaCl = 1.0%)	**Trial 1**	43 windows × 10 ns = 430 ns	-42.58 ± 0.49	-42.34 ± 0.32	-18.77
	Trial 2	43 windows × 50 ns = 2150 ns	-42.09 ± 0.31		

The absolute value of estimated free energies (ΔG) was strongly dependent on the adopted approach (Restrained or unrestrained SDS micelle). However, the salt-induced systematic change in the binding affinity, disfavouring LL-14 binding to SDS micelle, was a robust feature independent of the adopted approach.

Table A3.6: LL-14:DPC micelle binding free energy estimated from umbrella sampling (Approach 2: No restraint on the DPC micelle, Snapshot selected from COM pull rate = 0.01 nm/ps). SEM given after ±.

Approach 2	Replicas	Run-length of Umbrella Sampling	ΔG (kcal/mol)
LL-14:DPC (NaCl = 0.0%)	**Trial 1**	42 windows × 20 ns = 840 ns	-11.58 ± 0.98

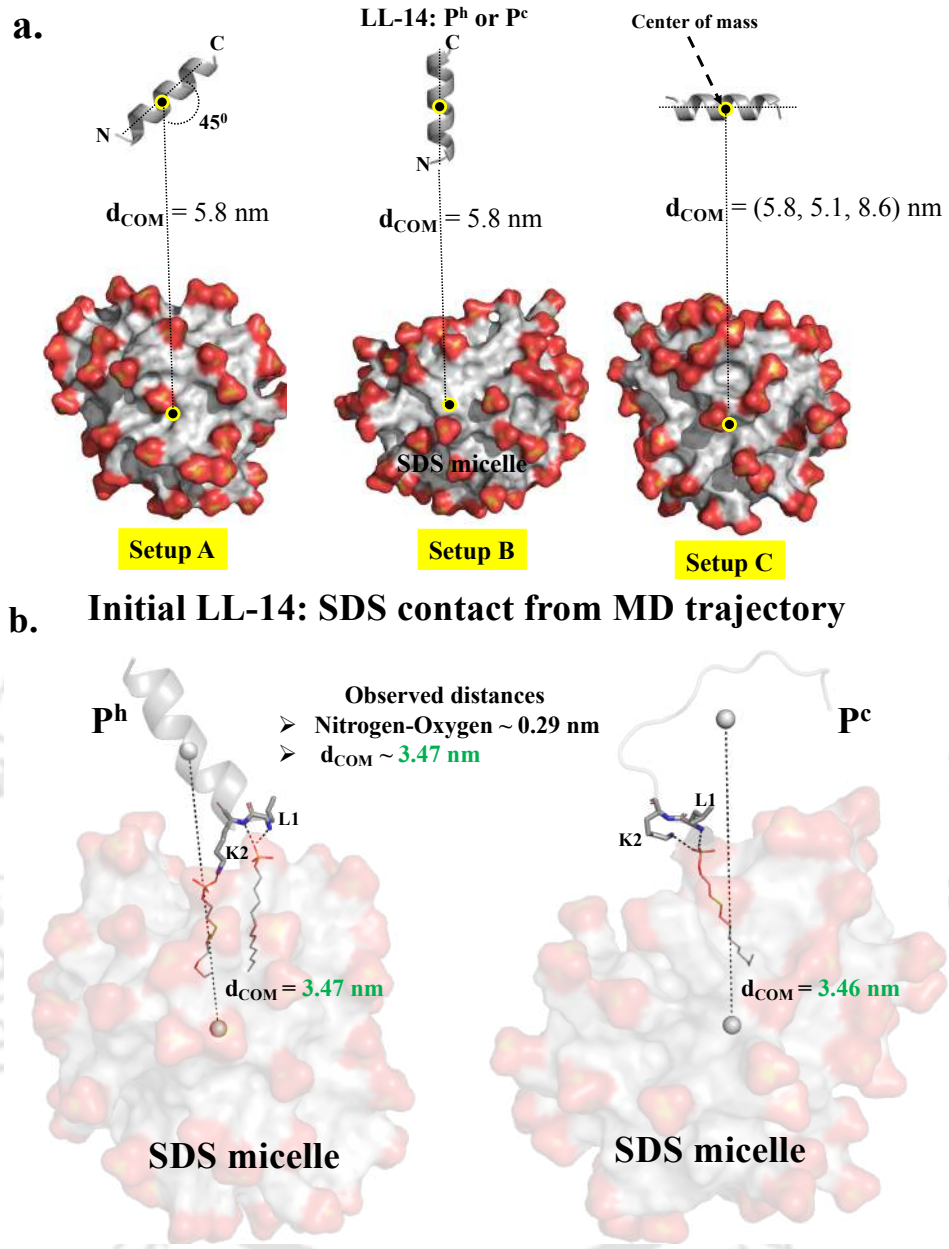

Figure A3.1: (a) Relative position of LL-14 and SDS micelle considered as initial model for MD simulations. (b) Representative snapshot from MD simulation highlighting the initial contact between LL-14 and SDS micelle. Center of mass represented by grey sphere.

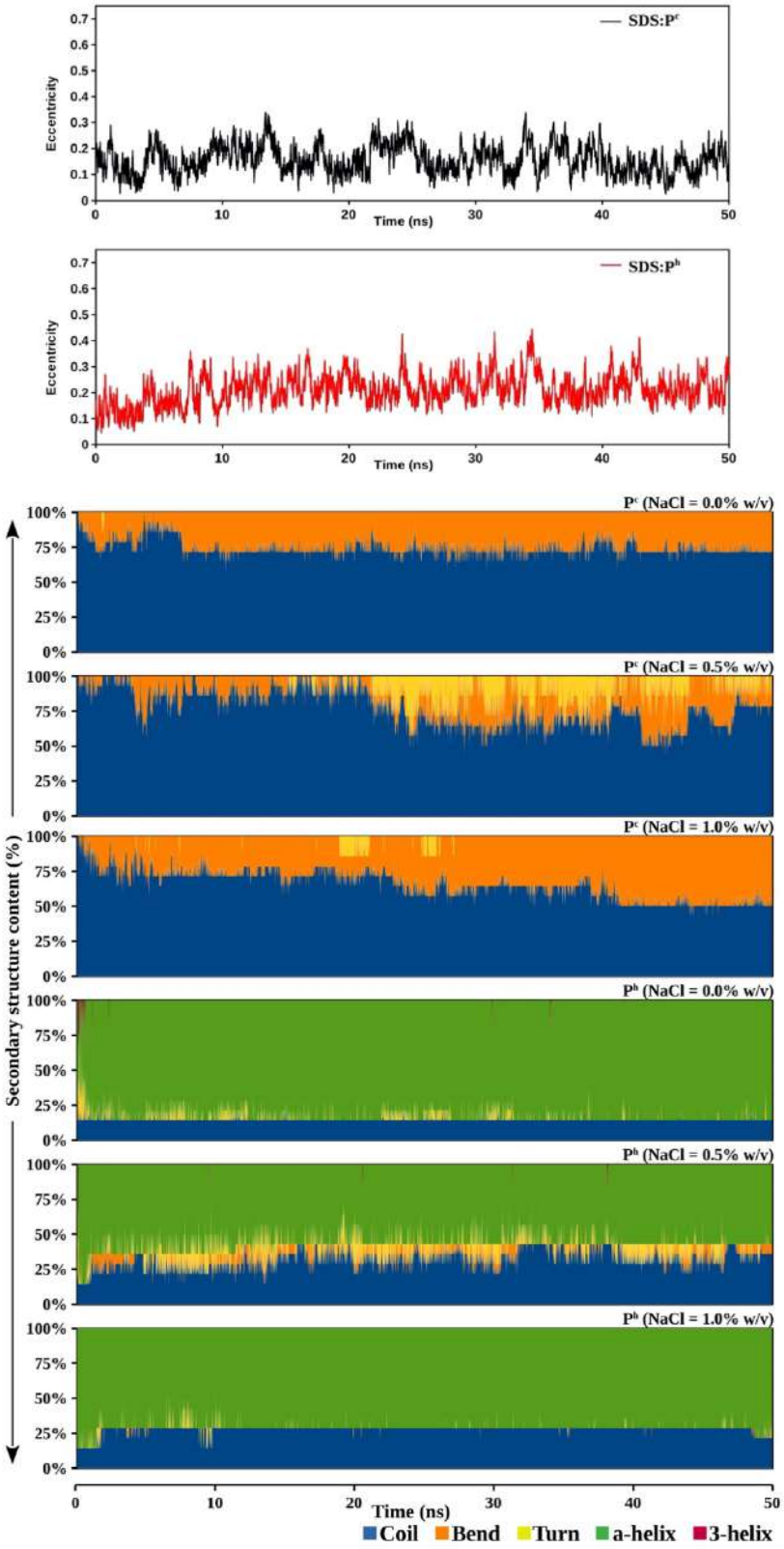

Figure A3.2: Eccentricity vs Time plot (NaCl =0.0%). Secondary structural content of the peptide (P^c or P^h) estimated from the MD trajectory in presence of SDS micelle at various salt concentrations.

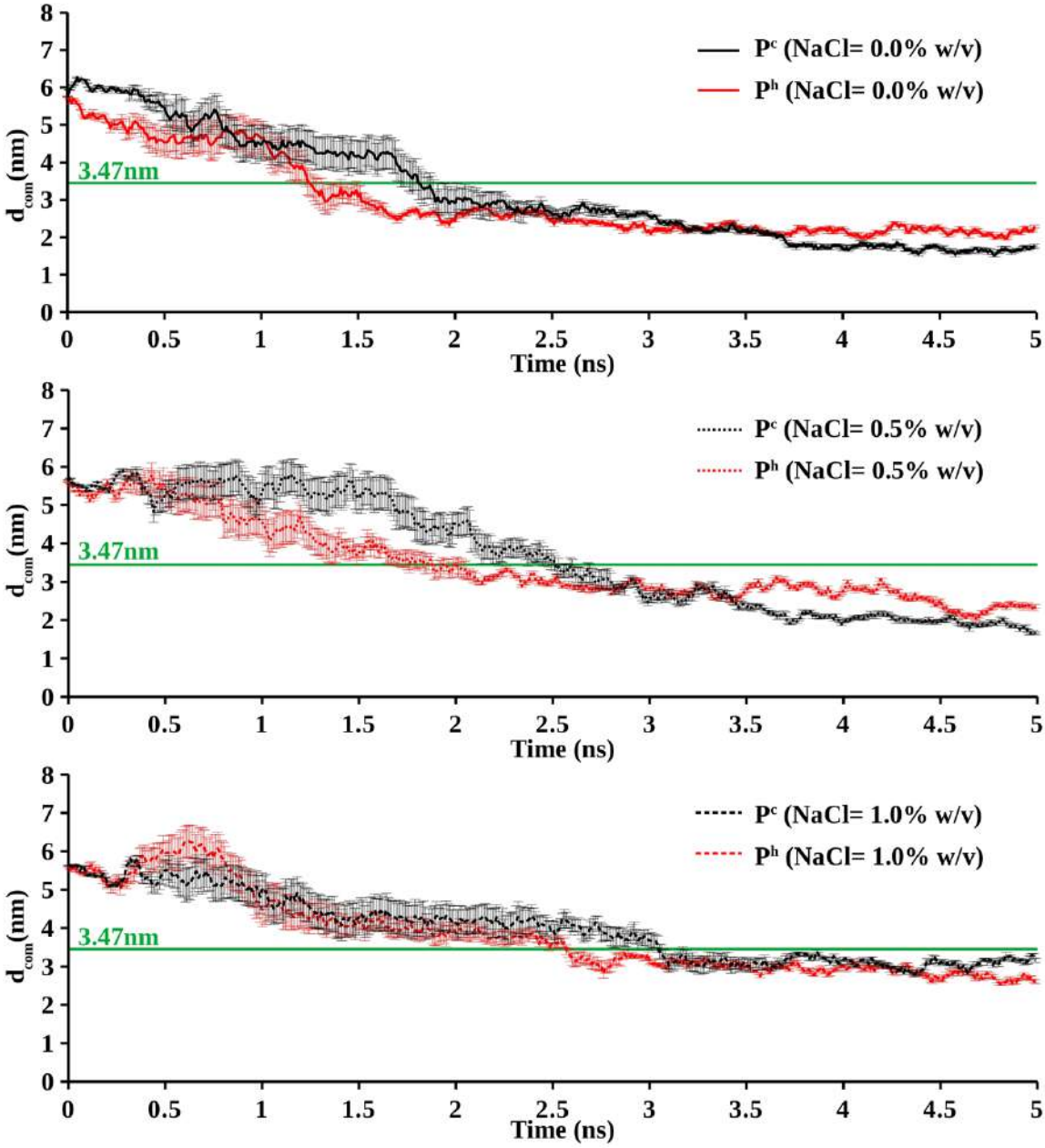

Figure 3.3 Lines in the Figure 3 of the main-text has been divided into three groups (based on salt-concentrations). 5 independent replicas (obtained from Setup C of Fig. S1a, d_{COM} = 5.8 nm) were considered to calculated the temporal average for each simulation models. Error are reported as s.e.m from 5 replicas and shown as vertical bars. The same trend has been confirmed starting with various other setups (Figure A3.1a).

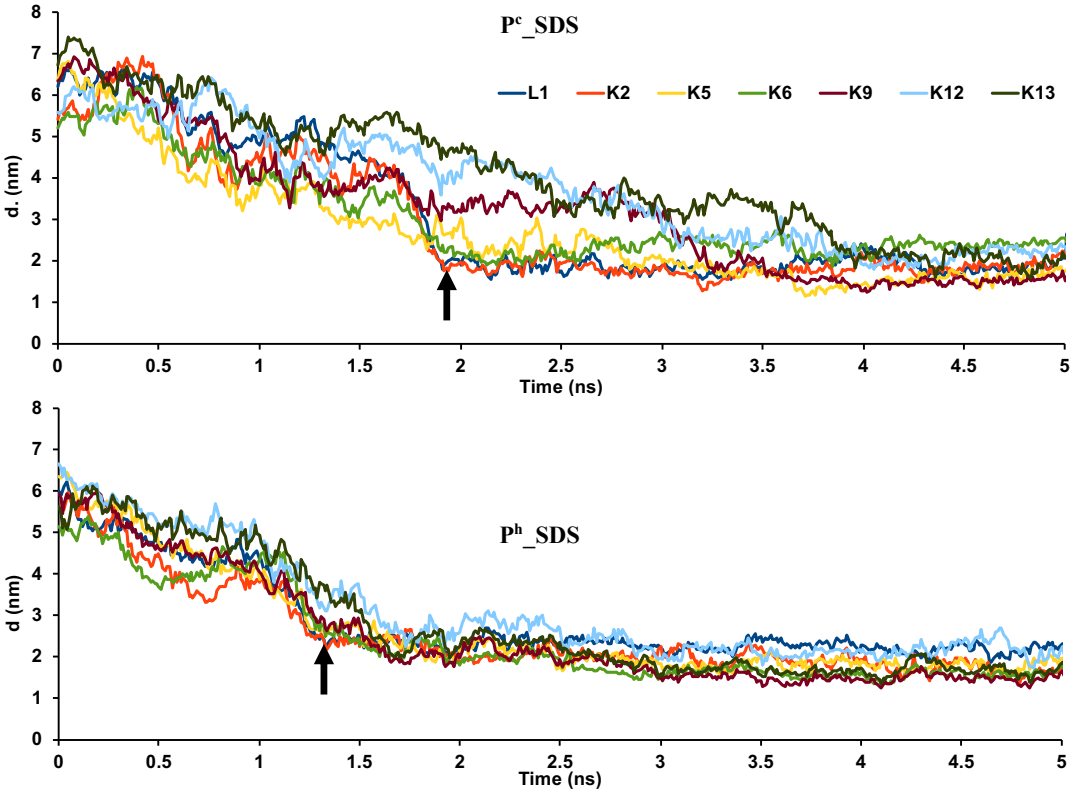

Figure 3.4: "d" is the distance between positively charged nitrogen of the LL-14 residues and the centre of mass of SDS micelle. Distance plot (d vs. time) is shown along the MD trajectories (0% NaCl). Different colours represent different -NH_3^+ containing residues. N-terminal (L1, blue) and side-chain of K2 (red) forms the initial contact (represented as vertical arrow) with the micelle surface. The trend is same for simulations in presence of salt (not shown).

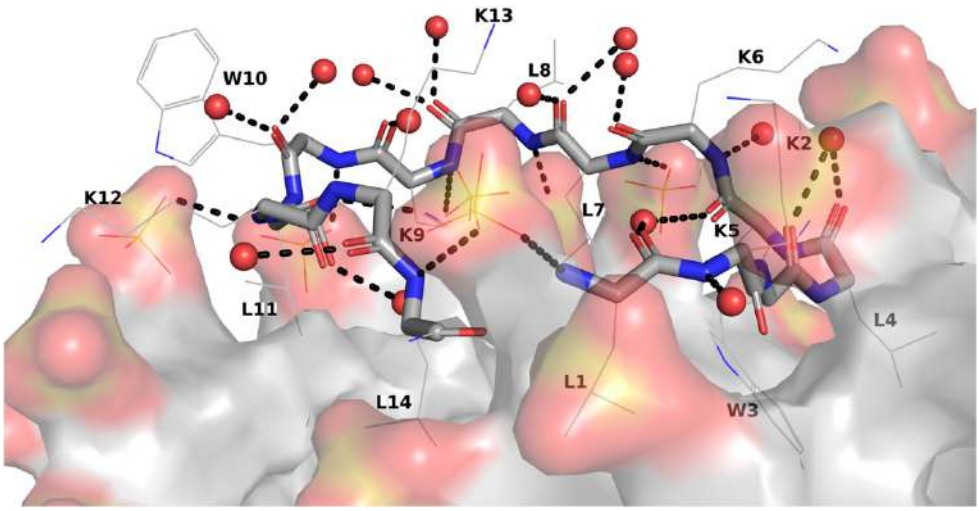

Figure A3.5: Peptide backbone of P^c satisfied its hydrogen bonding requirement by forming H-bond with water molecules or sulphates of the SDS micelle or both. Snapshot after 50ns of MD. Peptide in sticks, water in red sphere, SDS (surface representation, lines represent sulphate).

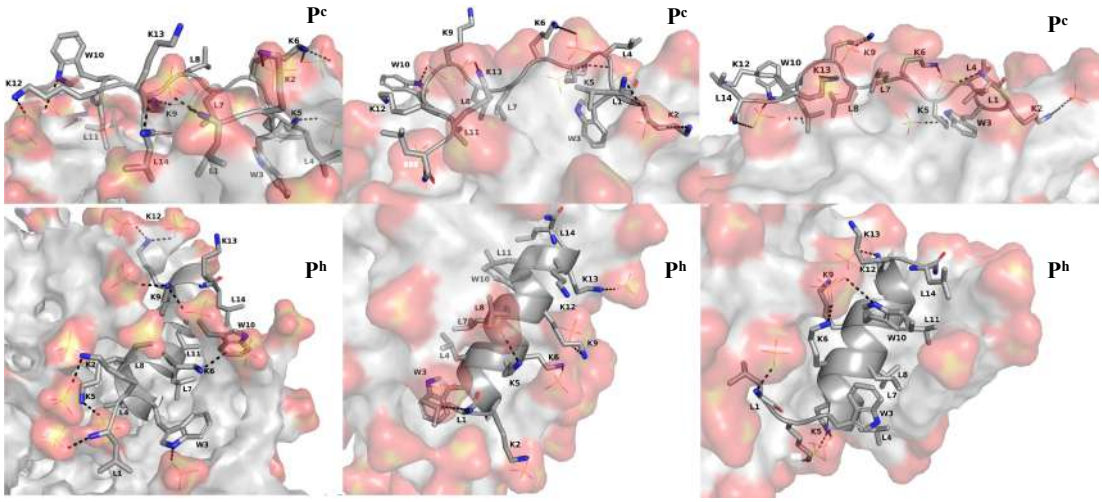

Figure A3.6: Final structure of the peptide:micelle (SDS) complex after 50 ns of MD simulations from three different NaCl-concentrations: 0.0% (given also in the main-text), 0.5% , and 1.0% w/v.

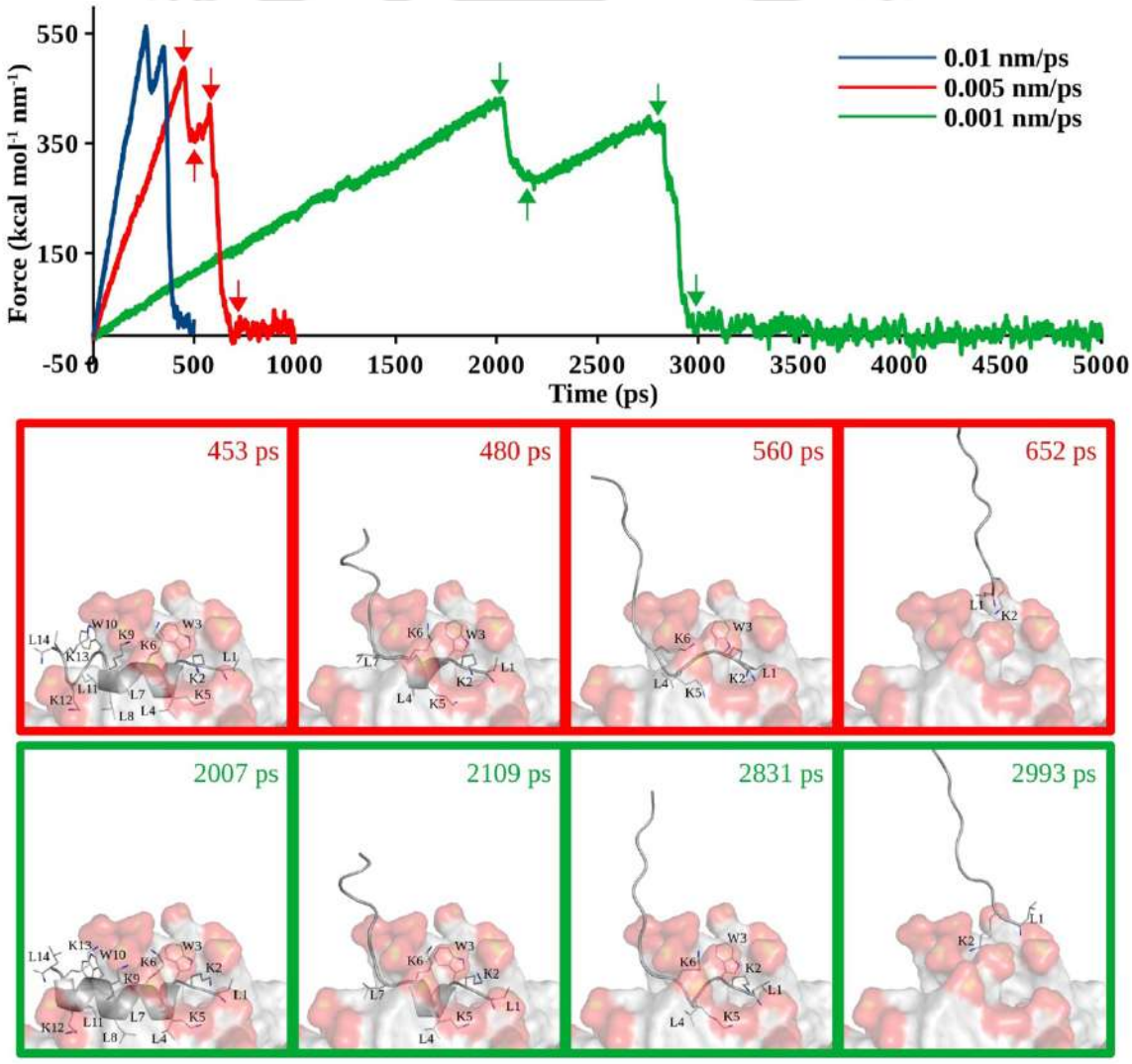

Figure A3.7: Force versus time plots from various SMD simulations (pull rates = 0.01nm/ps, 0.005 nm/ps, and 0.001 nm/ps). The shape of the force profile was independent of the pull rates. Structures from various time-points shown in the boxes (**red** : 0.005 nm/ps pull-rate, **green** : 0.001 nm/ps pull-rate).

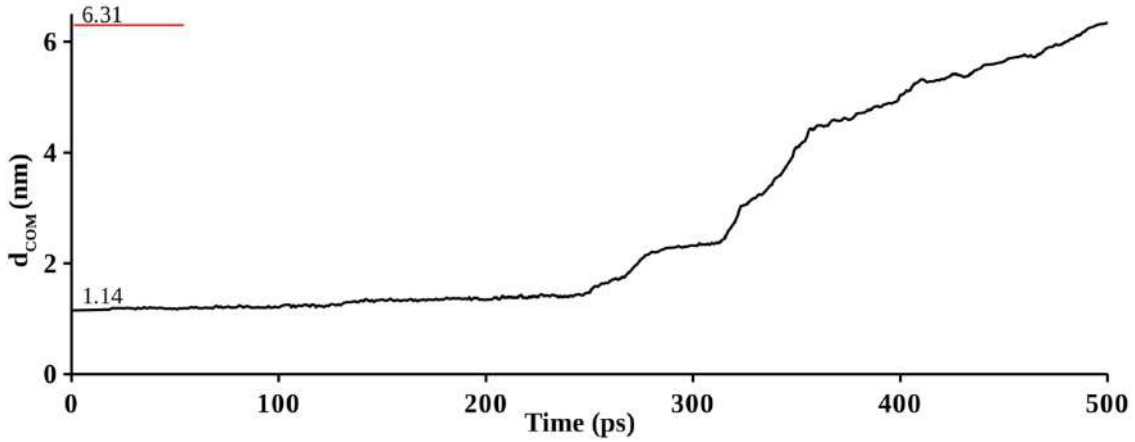

Figure A3.8: Center-of-mass pulling simulation (d_{COM} vs. time plot, pulling rate = 0.01 nm/ps). d_{COM} = Distance between the center-of-mass of the LL-14 and SDS micelle. "d_{COM}" range (Minimum = 1.14 nm, Maximum = 6.31nm).

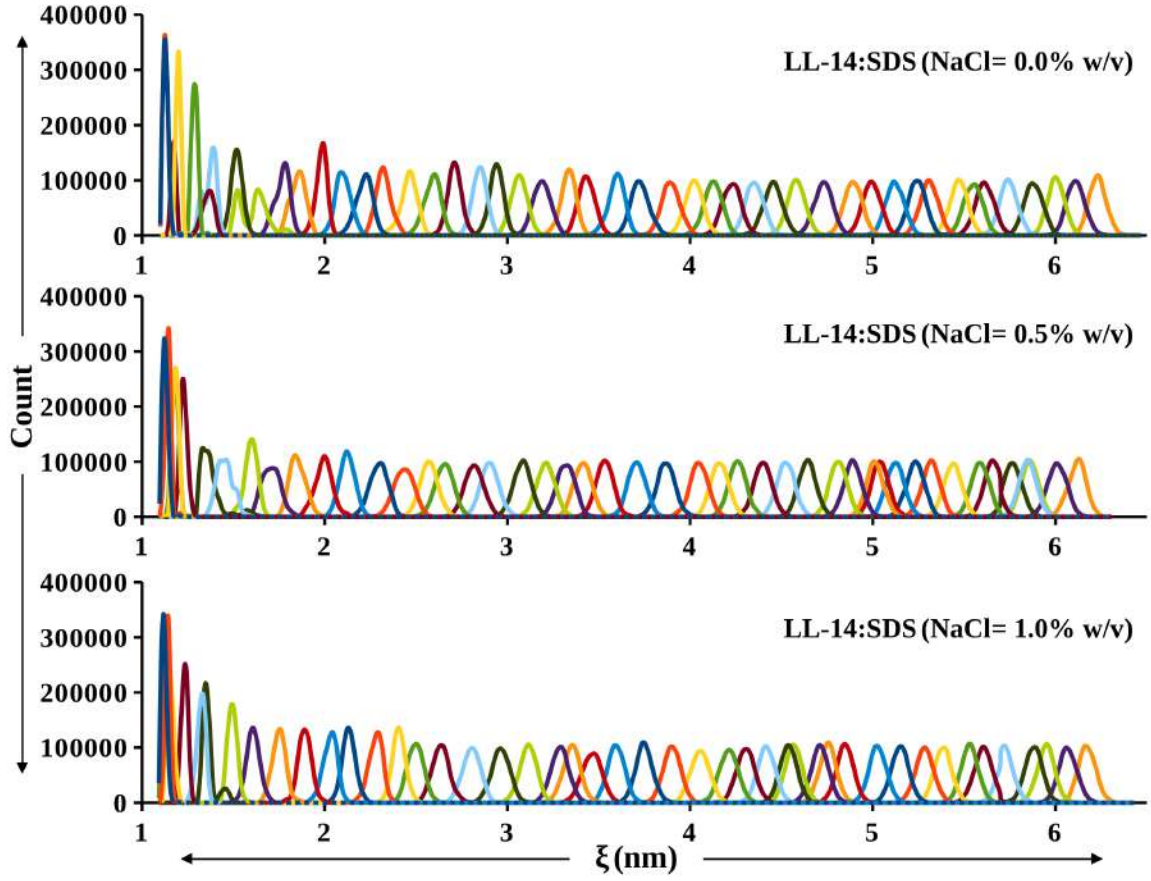

Figure A3.9: Probability distribution at each umbrella sampling window (Total windows = 43, shown in different colours) from the LL-14:SDS PMF profile at various salt-concentrations (NaCl = 0%, 0.5%, and 1.0% w/v). The overlap of probability distribution (between two neighbouring windows) was evident.

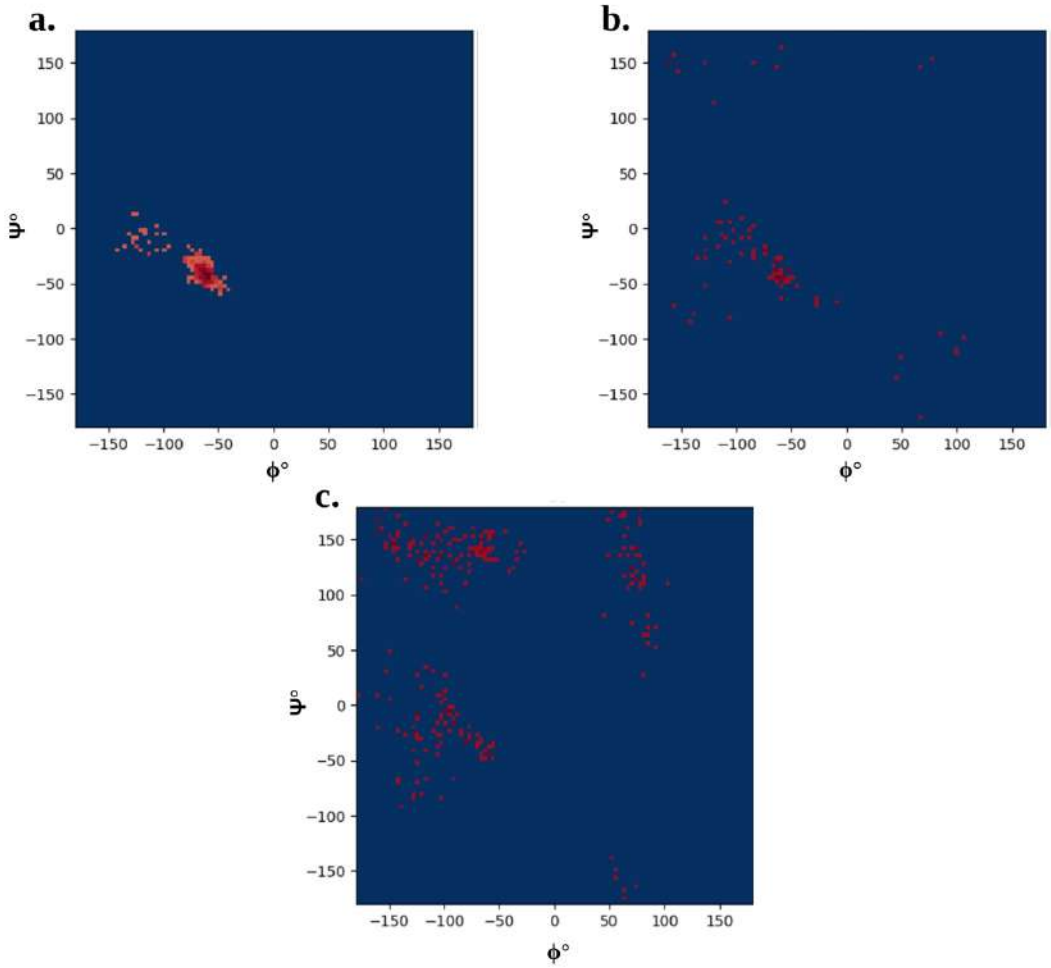

Figure A3.10: Ramachandran Plot of LL-14 peptide obtained from different trajectory segment during the centre-of-mass pulling (SMD, pull rate= 0.01 nm/ps, NaCl = 0% w/v). SMD trajectory segment (a) 0 - 263 ps, (b) 264 – 351 ps, and (c) 352 - 500 ps. ϕ and Ψ angles were plotted from -180° to 180°. Dispersion of red points from "a" → "c" indicates helical → random-coil transition. Blue regions exhibit either zero or little likelihood of the peptide adopting such a conformation.

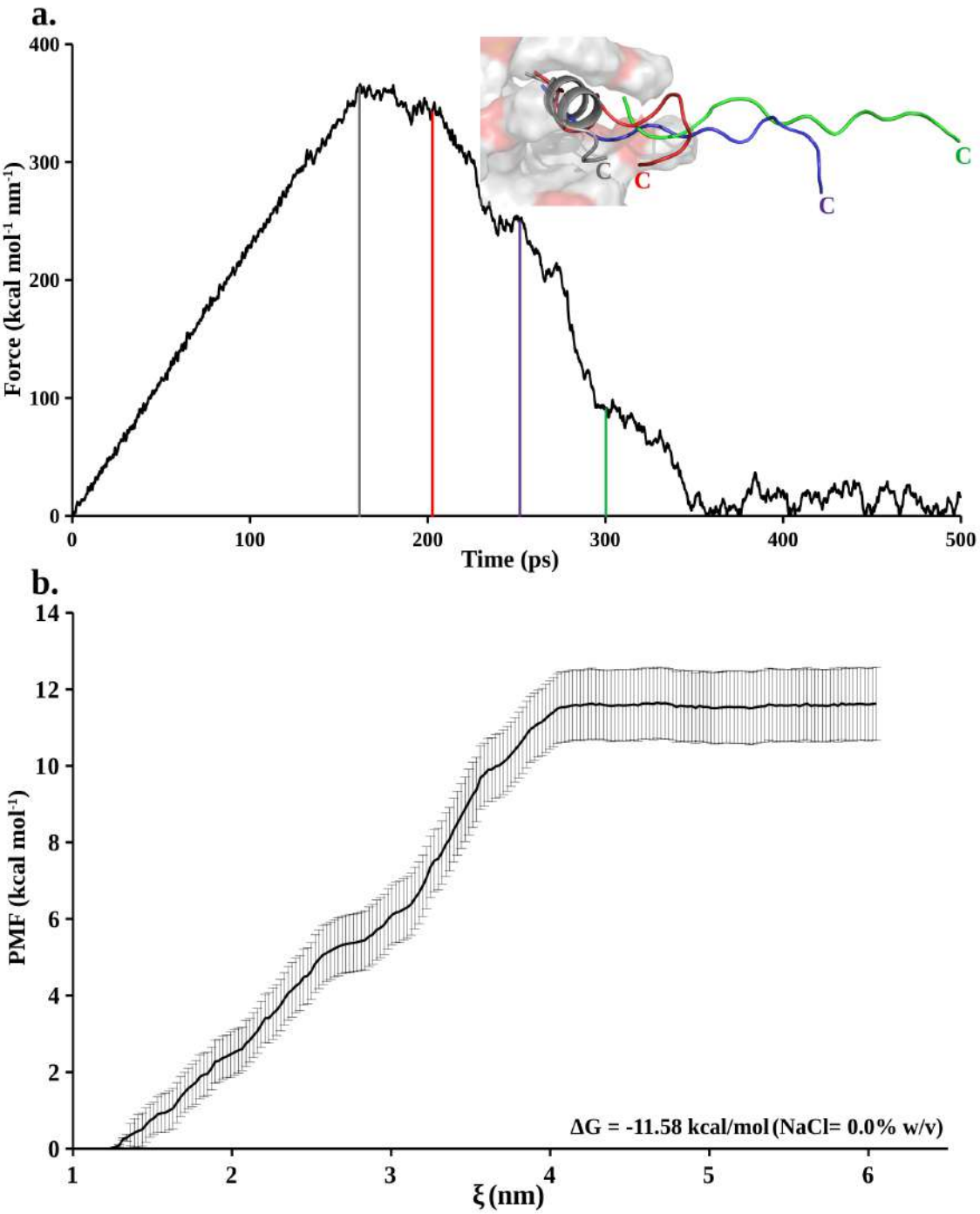

Figure A3.11: (a) Force vs. time plots of LL-14:DPC micelle complex (pull rate 0.01nm/ps, NaCl = 0% w/v). Structures at different time-points (grey, red, blue, and green) were overlaid (shown in surface-cartoon representations). (b) LL-14:DPC binding free energy (ΔG) estimated from the potential of mean force (PMF) versus reaction coordinate "ξ" plot. Simulation details were given in Table A3.6.

Appendix III

Content

Sl. no.		Topic	Page No.
1	Table A4.1	Molecular Dynamics Parameters	180
2	Table A4.2	Sampling (multiple replicas) and free energy estimates from independent replicas.	181
3	Table A4.3	ΔΔG (kcal/mol) values corresponding to the alchemical transformation (Leu→Val) at various position of LL-14 peptide. Standard error given after '±'	183
6	Figure A4.1	Probability distribution function at each λ window	184
7	Figure A4.2	MD structures from the end-points of backward "alchemical transformation (λ=1;Valine→ λ=0;Leucine)".	185
8	Figure A4.3	Illustration of the amino-acid side-chain (L1 and K2) flexibility of LL-14 and its single mutant L1V peptide in complex with SDS/DPC micelle	185
9	Figure A4.4	Illustration of the amino-acid side-chain (L14 and V14) flexibility of LL-14 and its single mutant L14V peptide in complex with SDS/DPC micelle	186
10	Figure A4.5	Peptide burial depth in the micelle	187
11	Figure A4.6	Secondary structural analysis of the peptide in complex with SDS/DPC micelle	188

Table A4.1: Parameters used in MD simulations.

Molecular Dynamics Parameters (NPT ensemble)	
Integrator and time steps	Leap-frog (velocity verlet algorithm), 2 fs
Long range electrostatics short range electrostatic cut-off	Particle Mesh Ewald (PME)(Darden et al., 1993) 1.2 nm
EWALD parameters *pme_order (interpolation order for PME)* *ewald_rtol (relative strength of the Ewald-shifted direct potential)*	 6 1e-06
Short range van der Waals cut-off	1.2 nm
Boundary Condition	Periodic Boundary Condition (PBC)
Hydrogen Bonds Constraints-algorithm	Lincs (Hess et al., 1997)
Temperature control, coupling constant	Velocity rescaling algorithm (v-rescale) (Bussi et al., 2007), 0.1 ps
Pressure control, coupling constant	Parrinello-Rahman (Parrinello & Rahman, 1982), 5.0 ps
Temperature	300 K
Pressure	1 bar

References

Bussi, G., Donadio, D., & Parrinello, M. (2007). Canonical sampling through velocity rescaling. *The Journal of Chemical Physics*, *126*(1), 014101. https://doi.org/10.1063/1.2408420

Darden, T., York, D., & Pedersen, L. (1993). Particle mesh Ewald: An N·log(N) method for Ewald sums in large systems. *The Journal of Chemical Physics*, *98*, 10089–10092. https://doi.org/10.1063/1.464397

Hess, B., Bekker, H., Berendsen, H. J. C., & Fraaije, J. G. E. M. (1997). LINCS: A linear constraint solver for molecular simulations. *Journal of Computational Chemistry*. https://doi.org/10.1002/(SICI)1096-987X(199709)18:12<1463::AID-JCC4>3.0.CO;2-H

Parrinello, M., & Rahman, A. (1982). Strain fluctuations and elastic constants. *The Journal of Chemical Physics*, *76*(5), 2662–2666. https://doi.org/10.1063/1.443248

Table A4.2: Trial 1, Trail 2, Trail 3: Replicas differ in the initial velocity distribution. The coordinates of LL-14:SDS/DPC structure is same. [#](Trail 4): Initial structure LL-14:SDS/DPC complex is distinctly different from (Trail 1, Trail 2, Trail 3). *Forward*: Leu(λ=0) → Val (λ=1); ***Backward***: Val(λ=1) → Leu (λ=0). ΔG in kcal/mol. standard error given after '±'. Total simulation time ~ **7.43 μs** for free energy estimation preceded by 14.2 ns equilibration.

		LL-14(P^h):SDS complex				**LL-14(P^h):DPC complex**			
Position and Alchemical Transformation	**Simulation length (ns). Total = 21 λ windows**	**Trial 1** ΔG (Kcal/mol)	**Trial 2** ΔG	**Trial 3** ΔG	**Average** ΔG^{Comp}	**Trial 1** ΔG	**Trial 2** ΔG	**Trial 3** ΔG	**Average** ΔG^{Comp}
L1→V1 (L1V)	2 ns/window Total = 21×2 = 42	**28.93 ± 0.43**	–	–	–	**27.54 ± 0.33**	–	–	–
	5 ns/window Total = 21×5 = 105	*Forward* 26.86 ± 0.19 ***Backward*** **-26.49 ± 0.10**	26.79 ± 0.12	26.78 ± 0.22	**26.81 ± 0.21**	26.21 ± 0.12	26.16 ± 0.31	26.47 ± 0.19	**26.28 ± 0.26**
	10 ns/window Total = 21×10 = 210	**26.71 ± 0.21**	–	–	–	–	–	–	–
L1→V1[#] (Trail 4) (L1V)	5 ns/window Total = 21×5 = 105	**26.68 ± 0.20**	–	–	–	**26.29 ± 0.21**	–	–	–
L4→V4 (L4V)	5 ns/window Total = 21×5 = 105	*Forward* 20.27 ± 0.06 ***Backward*** **-20.46 ± 0.10**	20.51 ± 0.13	20.48 ± 0.12	**20.42 ± 0.15**	21.18 ± 0.07	21.11 ± 0.10	21.14 ± 0.14	**21.14 ± 0.11**
L7→V7 (L7V)	5 ns/window Total = 21×5 = 105	*Forward* 20.70 ± 0.07 ***Backward*** **-20.79 ± 0.11**	20.25 ± 0.11	20.27 ± 0.20	**20.41 ± 0.25**	22.53 ± 0.11	22.56 ± 0.20	22.52 ± 0.21	**22.54 ± 0.18**
L8→V8 (L8V)	5 ns/window Total = 21×5 = 105	*Forward* 19.74 ± 0.09 ***Backward*** **-19.46 ± 0.49**	19.55 ± 0.18	19.67 ± 0.15	**19.66 ± 0.16**	21.95 ± 0.12	21.98 ± 0.14	21.98 ± 0.19	**21.97 ± 0.15**
L11→V11 (L11V)	5 ns/window Total = 21×5 = 105	*Forward* 21.01 ± 0.06 ***Backward*** **-20.89 ± 0.32**	20.83 ± 0.15	21.08 ± 0.05	**20.97 ± 0.14**	21.69 ± 0.19	21.53 ± 0.15	21.52 0.21	**21.58 ± 0.20**
L14→V14 (L14V)	5 ns/window Total = 21×5 = 105	*Forward* 23.20 ± 0.41 ***Backward*** **-23.43 ± 0.49**	23.18 ± 0.38	23.11 ± 0.47	**23.16 ± 0.42**	18.87 ± 0.17	18.98 ± 0.25	18.99 ± 0.24	**18.95 ± 0.23**
LL-14→VV-L[all]V	5 ns/window Total = 21×5 = 105	131.84 ± 0.29	131.89 ± 0.38	131.87 ± 0.33	**131.87 ± 0.34**	137.89 ± 0.50	137.34 ± 0.33	137.71 ± 0.41	**137.58 ± 0.43**
LL-14→VV-14 L[all]V	5 ns/window (**Total = 41 λ**)	**131.41 ± 0.42**	–	–	–	–	–	–	–

Multiple mutations (All)	Total = **41**×5 = 205								
LL-14→VV-14 Multiple mutations (positions 4th, 7th, 8th and 11th)	5 ns/window Total = 21×5 = 105	82.04 ± 0.28	81.92 ± 0.34	_	**81.98 ± 0.33**	91.39 ± 0.32	91.27 ± 0.29	_	**91.33 ± 0.32**
Unstructured random-coil LL-14 in Water									
L1→V1 (L1V)	5 ns/window Total = 21×5 = 105	**18.69 ± 0.08**							
L4→V4 (L4V)	5 ns/window Total = 21×5 = 105	*Forward* 18.76 ± 0.11 ***Backward*** **-18.73 ± 0.09**	18.81 ± 0.09	18.79 ± 0.05	ΔG^{free} = **18.78 ± 0.09**				
L7→V7 (L7V)	5 ns/window Total = 21×5 = 105	**18.75 ± 0.11**							
L8→V8 (L8V)	5 ns/window Total = 21×5 = 105	**18.82 ± 0.10**							
L11→V11 (L11V)	5 ns/window Total = 21×5 = 105	**18.77 ± 0.12**							
L14→V14 (L14V)	5 ns/window Total = 21×5 = 105	**18.91 ± 0.09**							
LL-14→VV-14 Multiple mutations (All)	5 ns/window Total = 21×5 = 105	113.08 ± 0.16	112.98 ± 0.17	113.01 ± 0.17	ΔG^{free} = **113.02 ± 0.17**				
LL-14→VV-14 Multiple mutations (positions 4th, 7th, 8th and 11th)	5 ns/window Total = 21×5 = 105	75.68 ± 0.11	75.61 ± 0.12	_	ΔG^{free} = **75.64 ± 0.12**				

Table A4.3: ΔΔG (kcal/mol) values corresponding to the alchemical transformation (Leu→Val) at various position of LL-14 peptide. Standard error given after '±'

	LL-14(P^h):SDS complex	**LL-14(P^h):DPC complex**
Position and Alchemical Transformation		
L1→V1 L1V	8.12 ± 0.05	7.59 ± 0.17
L4→V4 L4V	1.64 ± 0.13	2.36 ± 0.04
L7→V7 L7V	1.66 ± 0.26	3.79 ± 0.02
L8→V8 L8V	0.84 ± 0.10	3.15 ± 0.02
L11→V11 L11V	2.20 ± 0.13	2.81 ± 0.10
L14→V14 L14V	4.25 ± 0.04	0.04 ± 0.07
LL-14→VV-14 Multiple mutations (positions 4^{th}, 7^{th}, 8^{th} and 11^{th}) L[4,7,8,11]V	6.34 ± 0.12	15.69 ± 0.08
LL-14→VV-14 Multiple mutations (All) L[all]V	18.84 ± 0.04	24.59 ± 0.39

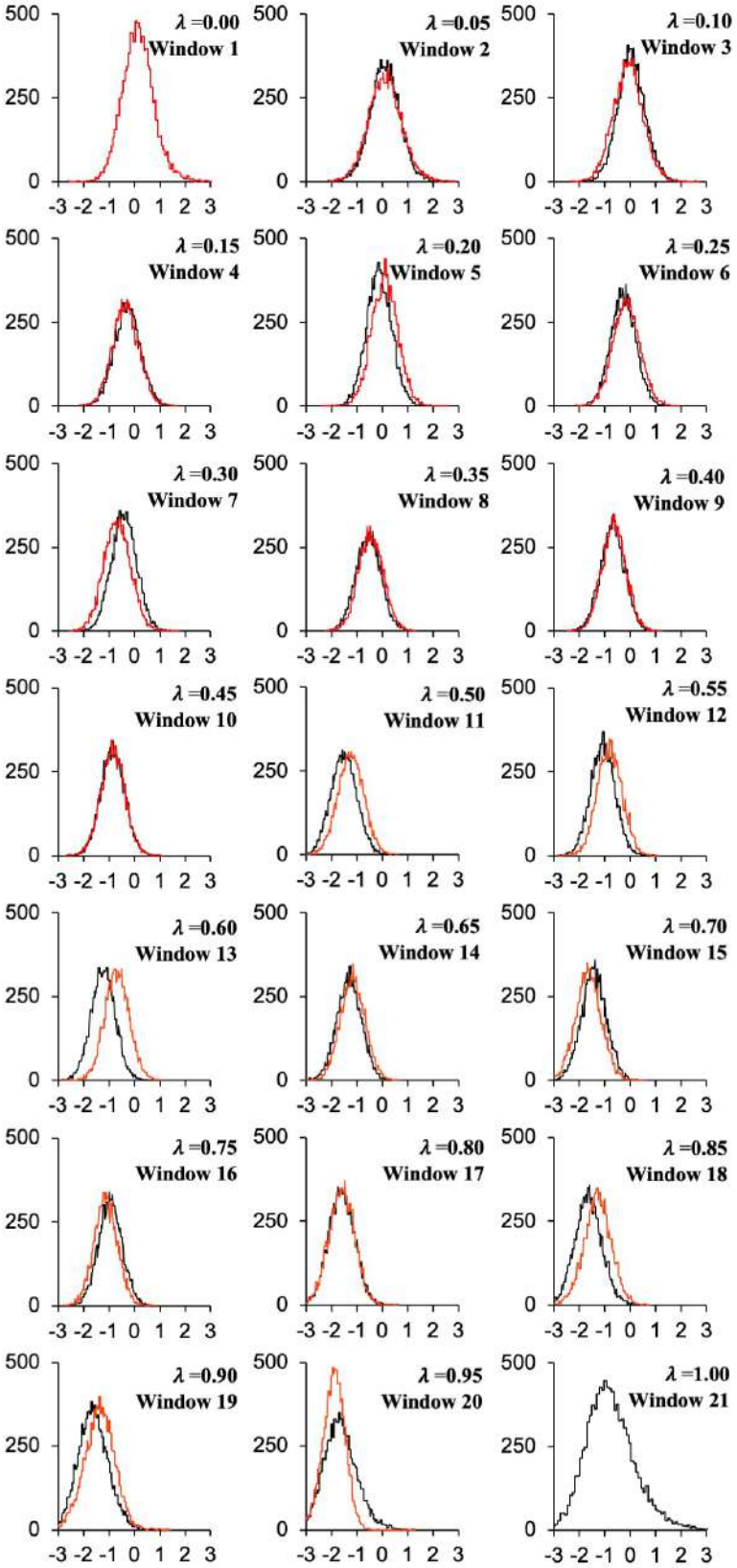

Figure A4.1: Probability distribution function (Y-axis) characterizing the forward (black lines) and the backward (red) transformations for all 19 intermediate states in the total 21 λ window simulation strategy. X-axis indicates the difference in potential energy (in kJ/mol) between two neighbouring windows. Note that, the significant overlap between the forward (black lines) and the backward (red) probability distributions ensured reversibility.

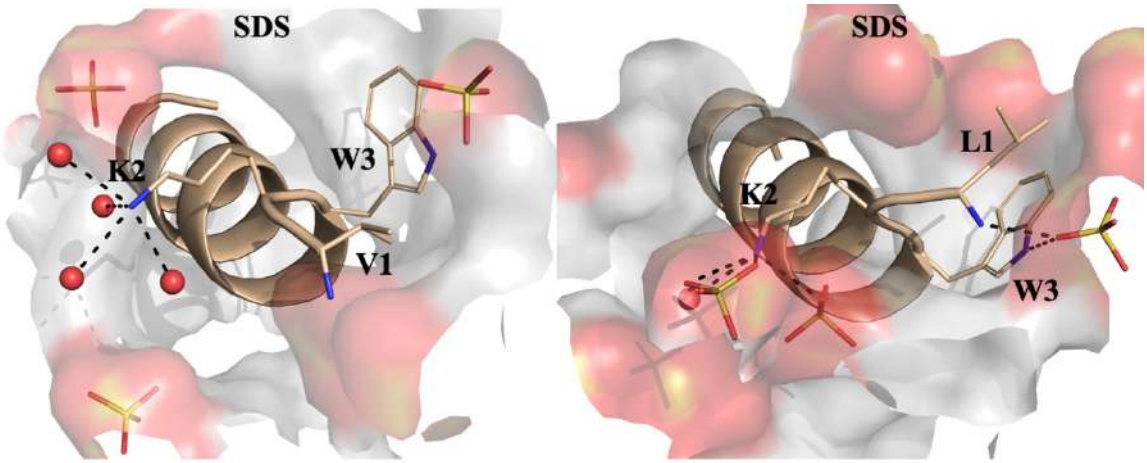

Figure A4.2: Left: Single mutant peptide (Valine at 1st position) bound to SDS micelle. Representative MD structure from the end-point of forward alchemical transformation, i.e, λ=1 window. K2 is exposed to water. **Right**: Representative structure of peptide (Leucine at 1st position) bound SDS after the end of backward alchemical transformation, i.e, λ=0 window. Salt-bridge interaction formed K2:SDS. Interaction indicated by black-dashed line.

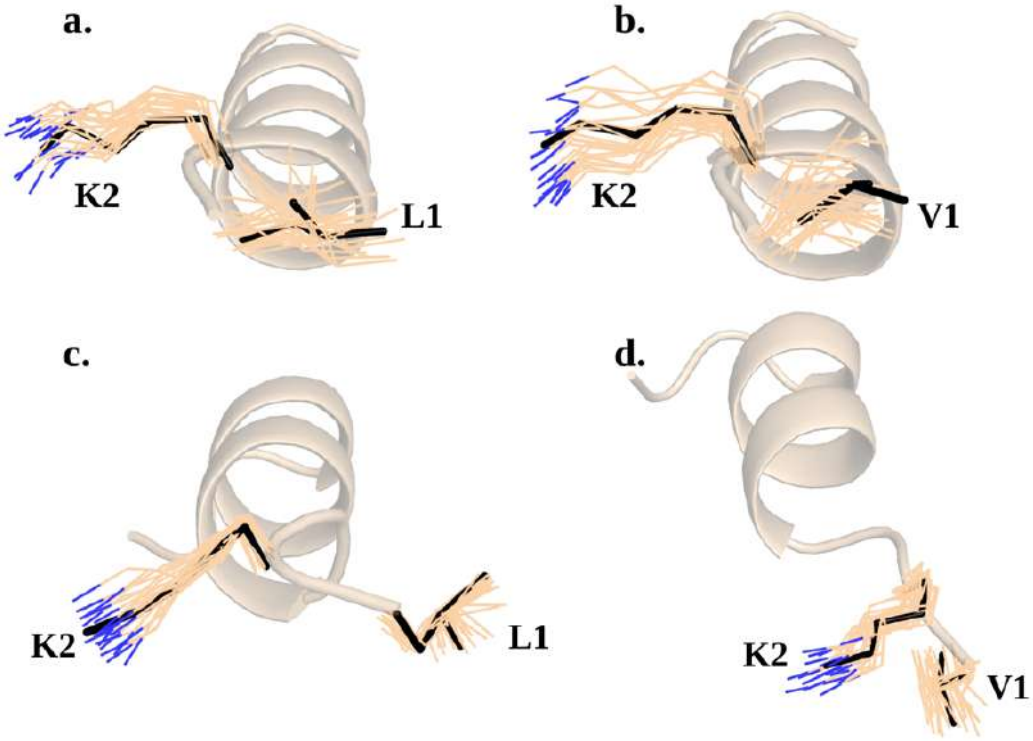

Figure A4.3: Illustration of the amino-acid side-chain (L1 and K2) flexibility. LL-14 (left) and its single mutant L1V (right) in complex with SDS (a, b) and DPC (c, d) micelle. MD snapshots of the amino-acid side chain are shown as lines (wheat) compared to the trajectory averaged structure (black stick); 25 snapshots with a 0.2 ns spacing from 5 ns MD trajectory. Hydrogens and the micelle are not shown for clarity.

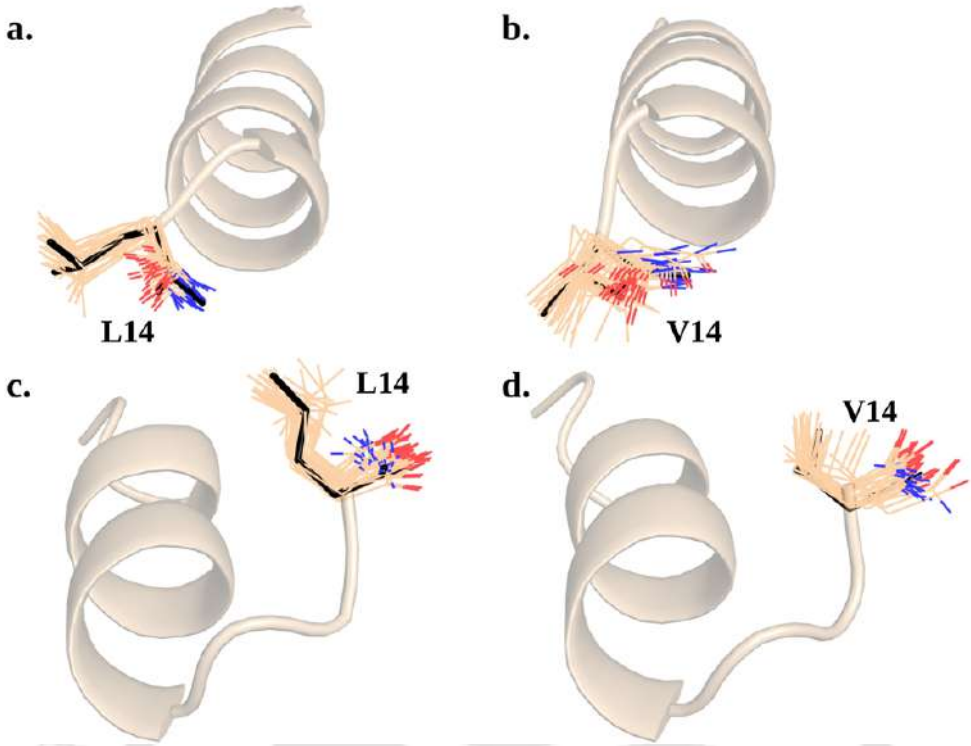

Figure A4.4: Illustration of the flexibility of the side-chain of leucine-14 (left) and Valine-14(right) side-chains of the LL-14 and L14V peptide respectively in complex with SDS (a, b) and DPC (c, d) micelle. MD snapshots of the amino-acid side chain are shown as lines (wheat) compared to the trajectory averaged structure of the side-chain (black stick); 25 snapshots with a 0.2 ns spacing from 5 ns MD trajectory. Hydrogens and the micelle are not shown for clarity.

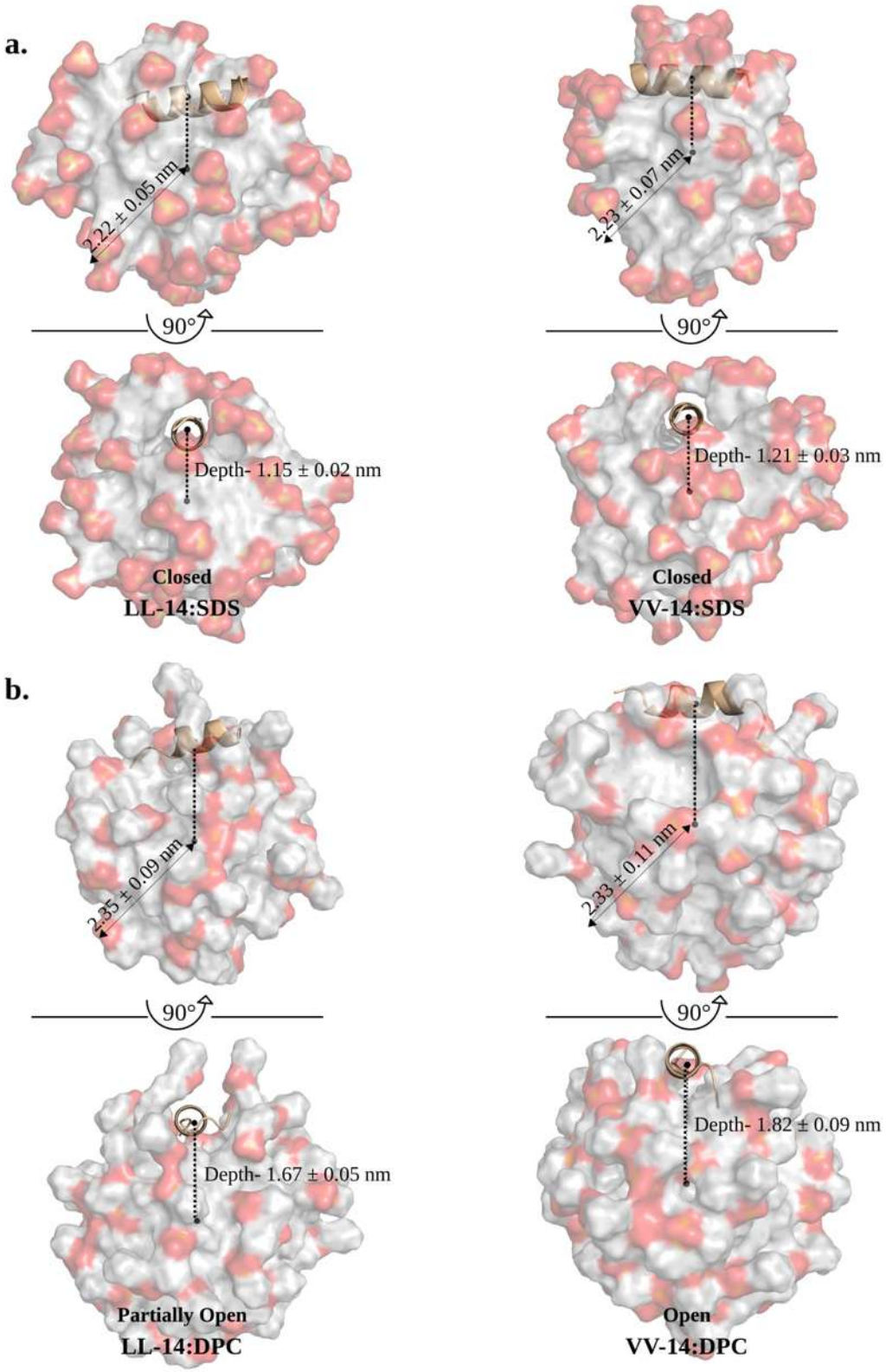

Figure A4.5: LL-14 (left) and VV-14 (right) burial depth analysis in complex with (a) SDS and (b) DPC micelle. Peptide burial depth is the trajectory averaged distance between the centre of mass of the micelle and the peptide (indicated by dashed line, Standard deviation is given as error). Top and bottom images are rotated with respect to each other by 90 degrees along the depth axis. Three independent MD replicas (5 ns each) of the end-states (λ= 0 and λ= 1) of alchemical transformation were used for calculating the averages.

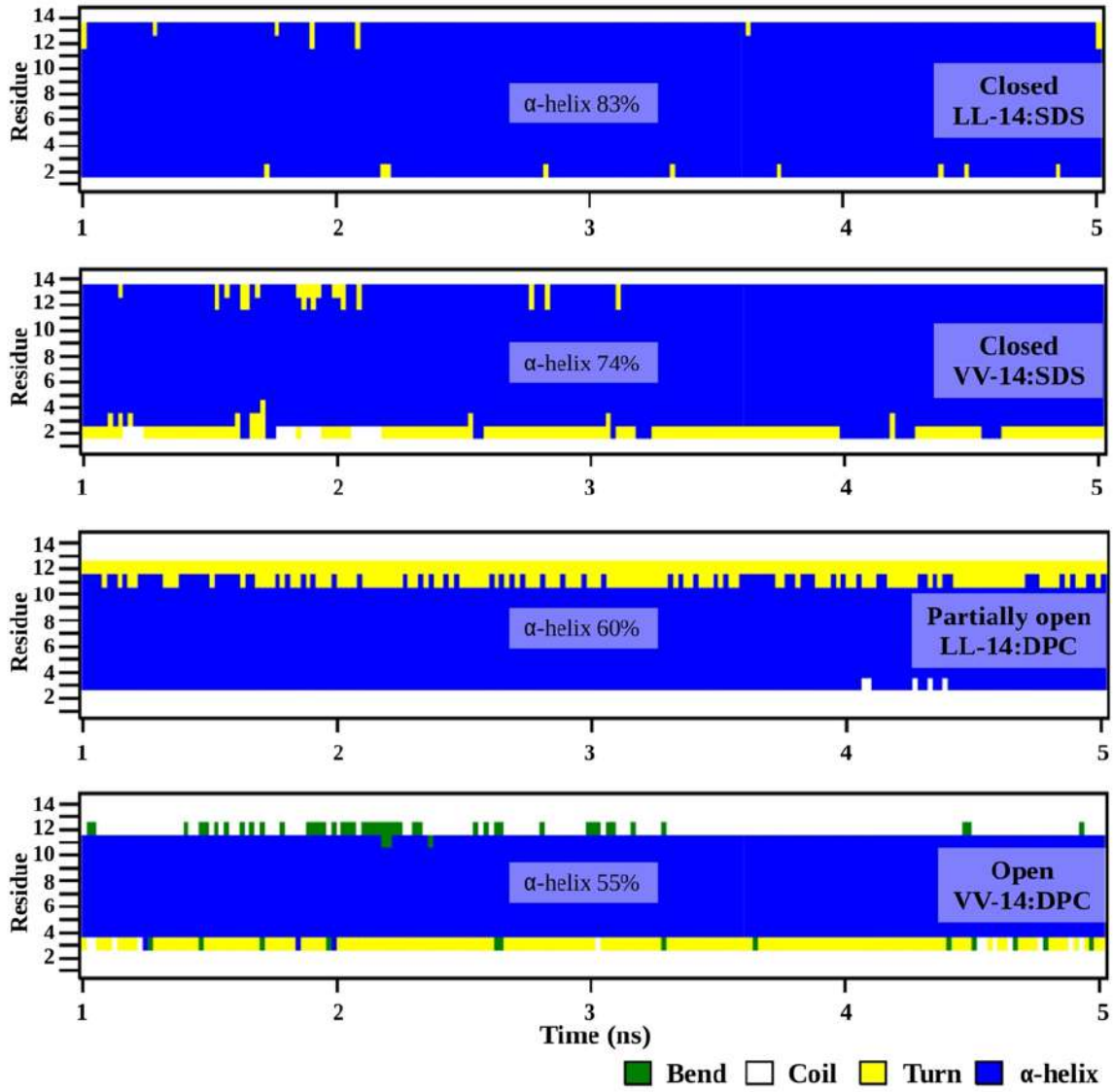

Figure A4.6: Secondary structure of the peptides (estimated by invoking DSSP program implemented in GROMACS) at every time frame during the 5ns MD simulation of the end-states (λ= 0 and λ= 1) associated with the alchemical transformation. α-helical content of the micelle bound VV-14 peptide is less than its LL-14 analogue.

Appendix IV

Content

Sl No.		Topic	Page No.
1	Table A5.1	Simulation details	190
2	Table A5.2	Binding affinity (ΔG) estimated from umbrella sampling. Error calculated using Bootstrap Analysis (100 cycles). Results are. They averaged from three independent MD trials. Standard error of the mean (s.e.m) after ±.	190
3	Table A5.3	Table A5.3: Relative binding affinities (ΔΔG, in kcal/mol) estimated from alchemical (BAR) approach. ΔΔG (BAR) = ΔG^{comp} - ΔG^{free} (See and Figure 5.1 of the main text). Standard error of the mean (s.e.m) after ±.	191
5	Figure A5.1	Peptide:bilayer complex and the magnified top view of peptide:bilayer local environment. The local environment around W3 and W10 are explicitly shown in square box.	191
6	Figure A5.2	Figure A5.2: Force profile (Force vs. Time plot) obtained from Steered Molecular Dynamics (SMD) simulations of LL-14:bilayer complex. Fully dissociation time shown by arrows.	192
7	Figure A5.3	Potential of mean force (PMF) as a function of COM (ξ) generated from SMD data (black color). Bootstrapping errors (100 cycles) were shown as transparent grey lines.	192
8	Figure A5.4	Figure A5.4: Structures of Lysine and arginine analogs.	193

Table A5.1: Simulation details

	Box dimension (nm^3)	No of waters/Na/ Cl	Total no of atoms	Simulation Length (ns) (Equilibration/Production Run)	No of trials
POPE/POPG	5.5 × 5.5 × 12	6965/24/0	32967	0.50/500	1
POPC	5.7 × 5.7 × 12	7989/0/0	36831	0.50/500	1
LL-14	8 × 8 × 8	16240/0/7	49026	0.25/1000	2
LL-14:POPE/POPG	5.5 × 5.5 × 12	6898/24/7	33072	0.20/3000	3
LL-14:POPC	5.7 × 5.7 × 12	7917/0/7	36921	0.20/3000	3

Table A5.2: Binding affinity (ΔG) estimated from umbrella sampling. Error calculated using Bootstrap Analysis (100 cycles). Results are. They averaged from three independent MD trials. Standard error of the mean (s.e.m) after ±.

PMF data calculated from US				
	Replicas	**Simulation length of Umbrella Sampling**	**ΔG (kcal/mol)**	**$\Delta G^{Averaged}$ (kcal/mol)**
LL-14:POPE/POPG	Trial 1	21 windows × 150 ns = 3150 ns	-10.80 ± 0.53	**-10.73 ± 0.53**
	Trial 2	21 windows × 150 ns = 3150 ns	-10.62 ± 0.47	
	Trial 3	21 windows × 150 ns = 3150 ns	-10.77 ± 0.58	
LL-14:POPC	Trial 1	21 windows × 150 ns = 3150 ns	-4.12 ± 0.39	**-4.15 ± 0.38**
	Trial 2	21 windows × 150 ns = 3150 ns	-4.24 ± 0.41	
	Trial 3	21 windows × 150 ns = 3150 ns	-4.09 ± 0.35	
PMF data calculate from SMD-US				
	Replicas	**Simulation length of Umbrella Sampling**	**ΔG (kcal/mol)**	**$\Delta G^{Averaged}$ (kcal/mol)**
LL-14:POPE/POPG	Trial 1	21 windows × 150 ns = 3150 ns	-11.29 ± 0.45	**-11.16 ± 0.51**
	Trial 2	21 windows × 150 ns = 3150 ns	-11.06 ± 0.54	
	Trial 3	21 windows × 150 ns = 3150 ns	-11.14 ± 0.55	
LL-14:POPC	Trial 1	21 windows × 150 ns = 3150 ns	-3.94 ± 0.30	**-3.94 ± 0.31**
	Trial 2	21 windows × 150 ns = 3150 ns	-4.02 ± 0.27	
	Trial 3	21 windows × 150 ns = 3150 ns	-3.86 ± 0.36	

Table A5.3: Relative binding affinities (ΔΔG, in kcal/mol) estimated from alchemical (BAR) approach. ΔΔG (BAR) = ΔG^{comp} - ΔG^{free} (See and Figure 5.1 of the main text). Standard error of the mean (s.e.m) after ±.

	POPE/POPG	POPC
LL-14^{Lys} to LL-14^{Orn}	-0.76 ± 0.13	0.46 ± 0.16
LL-14^{Lys} to LL-14^{Dab}	-1.18 ± 0.12	-2.73 ± 0.17
LL-14^{Lys} to LL-14^{Dap}	-0.36 ± 0.15	0.09 ± 0.13
LL-14^{Lys} to LL-14^{Hly}	0.25 ± 0.21	6.95 ± 0.31
LL-14^{Lys} to LL-14^{Arg}	-3.79 ± 0.18	-2.62 ± 0.16
LL-14^{Lys} to LL-14^{Agb}	-4.48 ± 0.15	-5.32 ± 0.22
LL-14^{Lys} to LL-14^{Agp}	-2.01 ± 0.19	-0.9 ± 0.21
LL-14^{Lys} to LL-14^{Hrg}	-6.7 ± 0.24	-3.13 ± 0.23

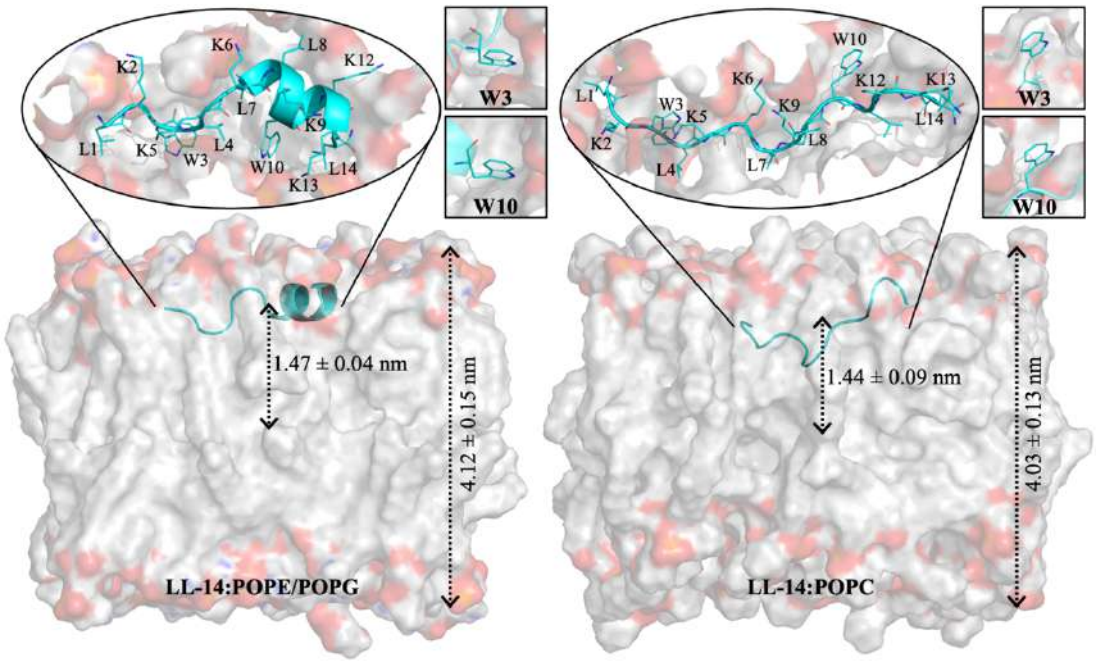

Figure A5.1: Peptide:bilayer complex and the magnified top view of peptide:bilayer local environment. The local environment around W3 and W10 are explicitly shown in square box.

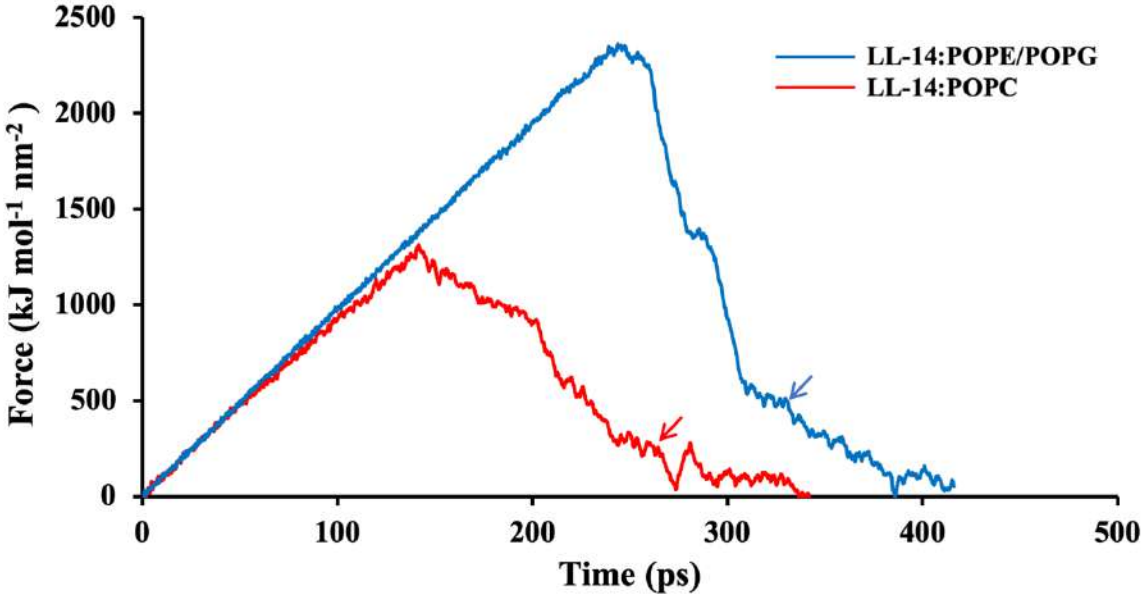

Figure A5.2: Force profile (Force vs. Time plot) obtained from Steered Molecular Dynamics (SMD) simulations of LL-14:bilayer complex. Fully dissociation time shown by arrows.

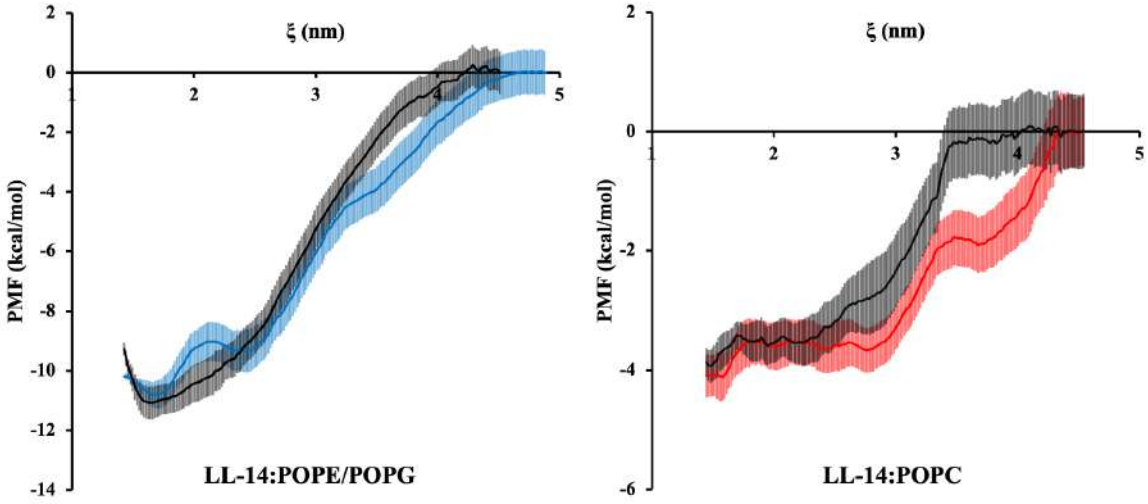

Figure A5.3: Potential of mean force (PMF) as a function of COM (ξ) generated from SMD data (black color). Bootstrapping errors (100 cycles) were shown as transparent grey lines.

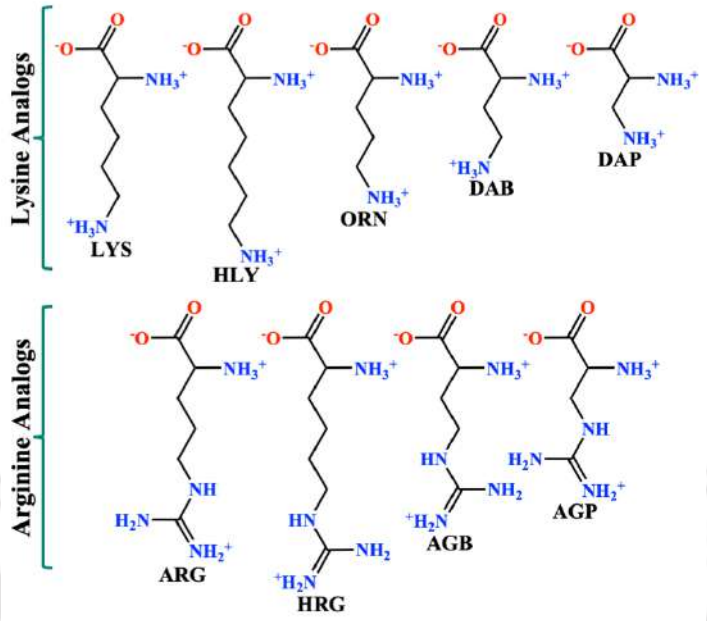

Figure A5.4: Structures of Lysine and arginine analogs. Where Lys: Lysine, Orn: Ornithine, Dab: 2,4-diaminobutyric acid, Dap: 2,3-diaminopropionic acid, Hly: Homolysine, Arg: Arginine, Agb: 2-amino-4-guanidinobutyric acid, Agp: 2-amino-3-guanidinopropanoic acid, Hrg: Homoarginine.

Publications

From the thesis work

1. Gopal Pandit, Humaira Ilyas, **Suvankar Ghosh**, Anil P. Bidkar, Sk Abdul Mohid, Anirban Bhunia*, Priyadarshi Satpati*, and Sunanda Chatterjee*. Insights into the Mechanism of Antimicrobial Activity of Seven-Residue Peptides. *Journal of medicinal chemistry*, 61, 17 (2018): 7614-7629.

2. **Suvankar Ghosh**, Swapna Debnath, Gopal Pandit, Sunanda Chatterjee* and Priyadarshi Satpati*. Effect of Monovalent Salt Concentration and Peptide Secondary Structure in Peptide-Micelle Binding. *RSC Adv*., 11 (2021): 36836-36849.

3. **Suvankar Ghosh**, Sunanda Chatterjee* and Priyadarshi Satpati*. Effect of Monovalent Salt on the Energetics of Antimicrobial-Peptide:Micelle Dissociation. *Phys. Chem. Chem. Phys* (2022): 24, 23669-23678.

4. **Suvankar Ghosh**, Sunanda Chatterjee* and Priyadarshi Satpati*. Effect of Leu/Val Mutation of the Energetics of Anti-microbial Peptide:Micelle Binding. *J. Phys. Chem. B* (2022): 126, 28, 5262–5273.

5. **Suvankar Ghosh**, Tanumoy Sarkar, Sunanda Chatterjee* and Priyadarshi Satpati*. Bridging Thermodynamics, Antimicrobial Activity, and pH Sensitivity of Cationic Membranolytic Peptides – A Computational and Experimental Study. *J. Chem. Inf. Model.* 2023, 63, 8, 2393-2408

6. **Suvankar Ghosh**, Sunanda Chatterjee* and Priyadarshi Satpati*. Peptide Selectivity by Membrane-mimetic-bilayers in Response to Spacer Length Modification of the Cationic Side-chains. (Manuscript under preparation)

7. **Suvankar Ghosh**, Tanumoy Sarkar, Sunanda Chatterjee* and Priyadarshi Satpati*. Effect of Aromatic Amino Acid (Trp/Phe/Tyr) in the Antimicrobial activity of the Cationic Hepta-Peptide. (Manuscript under preparation)

Other Publications

8. **Suvankar Ghosh**, T. Atchuta Ramarao, Pralok K. Samanta, Anjali Jha*, Priyadarshi Satpati*, and Anik Sen*. Triazole Based Isatin Derivatives as Potential Inhibitor of Key Cancer promoting Kinases-Insight from Electronic Structure, Docking and Molecular Dynamics Simulations. *Journal of Molecular Graphics and Modelling*, (2021): 107944.

9. **Suvankar Ghosh**, Debojit Bhattacherjee, Priyadarshi Satpati*, and Krishna Pada Bhabak*.Venetoclax: A Promising Repurposed Drug Against SARS-CoV-2 Main Protease. *Journal of Biomolecular Structure & Dynamics*, (2021): 1-12.

10. Karabi Roy, **Suvankar Ghosh**, Monikha Chetia, Priyadarshi Satpati*, and Sunanda Chatterjee*. Dicyclohexylurea derivatives of amino acids as dye absorbent organogels and anion sensors. *Organic & biomolecular chemistry* 17, no. 11 (2019): 3026-3039.

11. Gopal Pandit, Karishma Biswas, **Suvankar Ghosh**, Swapna Debnath, Anil P. Bidkar, Priyadarshi Satpati*, Anirban Bhunia*, and Sunanda Chatterjee*. Rationally designed antimicrobial peptides: Insight into the mechanism of eleven residue peptides against microbial infections. *Biochimica et Biophysica Acta (BBA)-Biomembranes* 1862, no. 4 (2020): 183177.

12. Nasim Akhtar, Nirmalya Pradhan, Ganesh Kumar Barik, Soumya Chatterjee, **Suvankar Ghosh**, Abhishek Saha, Priyadarshi Satpati, Arindam Bhattacharyya, Manas Kumar Santra, and Debasis Manna*. Quinine-Based Semisynthetic Ion Transporters with Potential Antiproliferative Activities. *ACS Applied Materials & Interfaces* 12, no. 23 (2020): 25521-25533.

13. Swapna Debnath, **Suvankar Ghosh**, Gopal Pandit, Priyadarshi Satpati*, and Sunanda Chatterjee*. Effect of Differential Geminal Substitution of γ Amino Acid Residues at the (i+2) Position of αγ Turn Segments on the Conformation of Template β-Hairpin Peptides. *The Journal of Organic Chemistry*, 86, 17 (2021): 11310-11323.

14. Swapna Debnath, **Suvankar Ghosh**, Dinesh Kumar, Prema G Vasudev*, Priyadarshi Satpati*, and Sunanda Chatterjee*. Effect of differential backbone di-substitution of gamma amino acid residues on the conformation and assembly of their Fmoc derivatives in solid and solution states, *Chemistry–An Asian Journal*, 17, 14 (2022): e202200356.